

1. Report No. FHWA/TX-5/9-1520-3	2. Government Accession No.	3. Recipient's Catalog No.	
4. Title and Subtitle <b>CHARACTERIZATION OF DESIGN PARAMETERS FOR FIBER REINFORCED POLYMER COMPOSITE REINFORCED CONCRETE SYSTEMS</b>		5. Report Date September 2003	Resubmitted: June 2005
		6. Performing Organization Code	
7. Author(s) David Trejo, Francisco Aguiñiga, Robert L. Yuan, Ray W. James, and Peter B. Keating		8. Performing Organization Report No. Report 9-1520-3	
9. Performing Organization Name and Address Texas Transportation Institute The Texas A&M University System College Station, Texas 77843-3135		10. Work Unit No. (TRAIS)	11. Contract or Grant No. Project 9-1520
12. Sponsoring Agency Name and Address Texas Department of Transportation Research and Technology Implementation Office P. O. Box 5080 Austin, Texas 78763-5080		13. Type of Report and Period Covered Technical Report: August 1999 – June 2003	14. Sponsoring Agency Code
15. Supplementary Notes Project performed in cooperation with the Texas Department of Transportation and the Federal Highway Administration. Project Title: FRP Reinforcing Bars in Bridge Decks URL: <a href="http://tti.tamu.edu/documents/9-1520-3.pdf">http://tti.tamu.edu/documents/9-1520-3.pdf</a>			
16. Abstract  Fiber-reinforced polymers (FRP) are being increasingly used in the construction industry. One application is to use FRP bars as reinforcement in concrete. It is thought that FRP bars do not exhibit the type of expansive corrosion exhibited by steel reinforcing bars; FRP bar reinforcement embedded in concrete will result in longer service-life expectancies. This report presents results from research performed on three types of glass fiber-reinforced polymer (GFRP) reinforcing bars. The results indicate that some current predictive equations for evaluating long-term properties may overestimate actual performance of GFRP reinforcing bars and GFRP-bar reinforced concrete systems. By unconservatively underestimating GFRP characteristics, key design requirements such as strength, deflection, crack width, and bond may not be adequately addressed in the design of GFRP-bar reinforced concrete elements. As such, recommendations are made to modify existing design methodologies.			
17. Key Words FRP, GFRP, Concrete, Composite, Fiber, Polymer, Degradation, Cracking, Deflection, Crack Width, Strength, Bond		18. Distribution Statement No restrictions. This document is available to the public through NTIS: National Technical Information Service Springfield, Virginia 22161 <a href="http://www.ntis.gov">http://www.ntis.gov</a>	
19. Security Classif.(of this report) Unclassified	20. Security Classif.(of this page) Unclassified	21. No. of Pages 276	22. Price



**CHARACTERIZATION OF DESIGN PARAMETERS FOR FIBER  
REINFORCED POLYMER COMPOSITE REINFORCED  
CONCRETE SYSTEMS**

by

David Trejo  
Assistant Professor and Assistant Researcher  
Texas A&M University and Texas Transportation Institute

Francisco Aguiñiga  
Graduate Research Assistant  
Texas A&M University and Texas Transportation Institute

Robert L. Yuan  
Professor  
University of Texas at Arlington

Ray W. James  
Manager, Highway Structures Program  
Texas Transportation Institute

and

Peter B. Keating  
Associate Professor  
Texas A&M University

Report 9-1520-3  
Project 9-1520  
Project Title: FRP Reinforcing Bars in Bridge Decks

Performed in cooperation with the  
Texas Department of Transportation  
and the  
Federal Highway Administration

September 2003  
Resubmitted: June 2005

TEXAS TRANSPORTATION INSTITUTE  
The Texas A&M University System  
College Station, Texas 77843-3135



## **DISCLAIMER**

The contents of this report reflect the views of the authors who are responsible for the facts and the accuracy of the data presented herein. The contents do not necessarily reflect the official view or policies of the Federal Highway Administration (FHWA) or the Texas Department of Transportation (TxDOT). This report does not constitute a standard, specification, or regulation. The researcher in charge of the project was David Trejo.

## **ACKNOWLEDGMENTS**

This project was performed in cooperation with the Federal Highway Administration and the Texas Department of Transportation. This report is based on the dissertation of Francisco Aguiñiga, performed under the direction of Drs. David Trejo, Joseph Bracci, and Jose Roesset. Drs. Robert L. Yuan, Ray W. James, Eugene W. Buth, and Peter B. Keating assisted with the research. Financial support for the research was provided by the Federal Highway Administration, Texas Department of Transportation, and the Texas Transportation Institute.

The authors wish to express their gratitude to:

**Project Coordinator:**

Ronald E. Koester, P.E., TxDOT, Waco District

**Project Director:**

Timothy E. Bradberry, P.E., TxDOT, Bridge Division

**Project Advisors:**

Don Harley, P.E., Federal Highway Administration  
Mary Lou Ralls, P.E., State Bridge Engineer, TxDOT  
Joe Chappell, P.E., TxDOT, Amarillo District  
Mark Bloschock, P.E., TxDOT, Bridge Division  
Kevin Pruski, P.E., TxDOT, Bridge Division  
Robert Sarcinella, TxDOT, Construction Division  
Paul McDad, TxDOT, Construction Division

**Project Advisors from Texas A&M University:**

David Trejo, Assistant Professor, Department of Civil Engineering, Texas A&M University  
Joseph Bracci, Associate Professor, Department of Civil Engineering, Texas A&M University  
Jose Roesset, Professor, Associate Department Head, and Wofford Cain '13 Chair, Department of Civil Engineering, Texas A&M University  
Robert L. Yuan, Professor, Department of Civil and Environmental Engineering, The University of Texas at Arlington  
Ray W. James, Associate Professor, Department of Civil Engineering, Texas A&M University  
Peter B. Keating, Associate Professor, Department of Civil Engineering, Texas A&M University

## TABLE OF CONTENTS

	<b>Page</b>
LIST OF FIGURES.....	x
LIST OF TABLES .....	xiii
I. INTRODUCTION .....	1
II. RELATED LITERATURE REVIEW .....	5
Diffusion Concepts.....	5
Fick's First Law of Diffusion.....	6
Fick's Second Law of Diffusion .....	6
Issue I. Change of Tensile Properties of GFRP Reinforcing Bars Over Time.....	7
Issue II. Direct Shear Strength of GFRP Bars.....	12
Issue III. Creep-Induced Deflections of GFRP-Reinforced Concrete Elements.....	13
Issue IV. Cracking of GFRP-Reinforced Concrete Structures.....	15
Issue V. Deflections of GFRP-Reinforced Concrete Elements due to Cyclic Loading.....	21
Issue VI. Degradation of Bond between GFRP Bars and Concrete.....	22
Issue VII. Cracking of GFRP-Reinforced Concrete Elements due to Thermal Expansion.....	23
III. MATERIALS, EXPERIMENTAL PROGRAM, AND TEST PROCEDURES .....	27
Materials .....	27
GFRP Reinforcing Bars.....	27
Concrete.....	31
Materials Used in the Cracking of Concrete Slabs Test.....	32
Materials Used in the Cyclic Loading of Concrete Beams Test .....	34
Materials Used in the Bond Test .....	35
Materials Used in the Thermal Expansion of Concrete Slabs Test .....	36
Experimental Program.....	36
Tension Test .....	37
Moisture Absorption Test.....	42
Direct Shear Strength Test .....	45
Creep Test.....	48
Cracking of Concrete Slabs Test.....	50
Cyclic Loading of Concrete Beams Test.....	54
Bond Test .....	56
Thermal Expansion of Concrete Slabs Test .....	60

## TABLE OF CONTENTS (CONT.)

IV. RESULTS .....	63
Tension Test.....	63
Unexposed Tensile Strength and Modulus of Elasticity Results .....	63
Exposed Tensile Strength and Modulus of Elasticity Results.....	66
Tension Test of Notched Bars .....	82
Moisture Absorption Test.....	86
Test Results for Bars with Uncapped Ends .....	86
Test Results for Bars with Capped Ends .....	87
Diffusion Analysis.....	91
Tensile Strength Degradation Analysis.....	100
Direct Shear Strength Test .....	106
Direct Shear Strength Test Results.....	107
Shear Modulus of Elasticity Test Results.....	109
Failure Analysis.....	111
Creep Test.....	114
Definitions .....	114
Creep Test Results .....	115
Time-Dependent Deformation Analysis .....	118
Cracking of Concrete Slabs Test.....	137
Test Results .....	137
Comparison between Test Results and Available Equations to Predict Maximum Crack Width .....	144
Correlation of Test and Predicted Results .....	149
Cyclic Loading of Concrete Beams Test.....	155
Constant Load Rate Tests.....	155
Cyclic Load Tests.....	157
Constant Load Rate after Cyclic Load Tests.....	167
Bond Test .....	169
Thermal Expansion of Concrete Slabs .....	177
Cracking Temperature of Bar Type P Specimen.....	178
Cracking Temperature of Bar Type V1 Specimen.....	181
Cracking Temperature of Bar Type V2 Specimen.....	182
V. REVIEW OF ACI 440 DESIGN GUIDELINES .....	187
ACI 440 Section 7.2 Design Material Properties.....	187
ACI 440 Section 8.3.1 Cracking .....	190
ACI 440 Section 8.3.2 Deflections.....	193
ACI 440 Section 8.3.2.3 Calculation of Deflection (Direct Method) .....	194
ACI 440 Section 11.1 Development Length of a Straight Bar.....	195

## TABLE OF CONTENTS (CONT.)

Minimum Concrete Cover.....	198
Introduction to Design Example .....	199
Design Example .....	199
Objective .....	199
VI. PROPOSED REVISIONS TO THE AASHTO LRFD BRIDGE DESIGN SPECIFICATIONS.....	225
Introduction .....	225
Proposed Revisions .....	225
VII. CONCLUSIONS, RECOMMENDATIONS, AND FUTURE WORK .....	239
Conclusions and Recommendations.....	239
Future Work .....	243
REFERENCES.....	245
APPENDIX A: ABSORPTION DATA.....	255
APPENDIX B: CREEP TEST DATA .....	259

## LIST OF FIGURES

	<b>Page</b>
Fig. 1 Test Data, Faza and GangaRao Equation, and ACI 440 Equation .....	20
Fig. 2 Surface of GFRP Bar Types P1, V1, and V2 (Modified from Schaefer [2002]) .....	28
Fig. 3 Cross Section of GFRP Bar Types P, V1, and V2 (Modified from Schaefer [2002]) .....	29
Fig. 4 SEM Photograph of the Surface of a V1 Bar (Modified from Schaefer [2002]) .....	30
Fig. 5 SEM Photograph of the Surface of a V1 Bar (Modified from Schaefer [2002]) .....	30
Fig. 6 Average Concrete Compressive Strengths at 7, 28, and 56 Days .....	32
Fig. 7 Setup for Exposure of GFRP Bars.....	39
Fig. 8 Strain Gage Attached to Surface of FRP Bar .....	40
Fig. 9 Test Specimen Layout for Tensile Tests .....	42
Fig. 10 Direct Shear Strength Test Apparatus .....	47
Fig. 11 Elevation View of Creep Frame .....	49
Fig. 12 Half Bridge Used in Strain Gage Setup for Creep Test.....	50
Fig. 13 Layout of Slabs with 0.625-Inch Diameter Bars in Top Mat .....	52
Fig. 14 Layout of Slabs Reinforced with 0.75-Inch Diameter Bars on Top Mat.....	53
Fig. 15 Slab Cracking Test Setup.....	53
Fig. 16 Beam Loading Setup.....	55
Fig. 17 Dimensions of Bond Specimens Reinforced with (a) 0.5-Inch Diameter Bars and (b) 0.75-Inch Diameter Bars .....	59
Fig. 18 Loading Setup of Bond Specimens.....	60
Fig. 19 Dimensions and Reinforcement of Thermal Expansion Specimens.....	62
Fig. 20 Typical Stress-Strain Plot .....	65
Fig. 21 Strength of Bar Type P after Distilled Water Exposure .....	68
Fig. 22 Strength of Bar Type P after Alkaline Solution Exposure .....	68
Fig. 23 Modulus of Elasticity of Bar Type P after Distilled Water Exposure .....	70
Fig. 24 Modulus of Elasticity of Bar Type P after Alkaline Solution Exposure .....	70
Fig. 25 Strength of Bar Type V1 after Distilled Water Exposure.....	72
Fig. 26 Strength of Bar Type V1 after Alkaline Solution Exposure.....	72
Fig. 27 Strength of Bar Type V2 after Distilled Water Exposure.....	74
Fig. 28 Strength of Bar Type V2 after Alkaline Solution Exposure.....	74
Fig. 29 Modulus of Elasticity of Bar Type V1 after Distilled Water Exposure .....	77
Fig. 30 Modulus of Elasticity of Bar Type V1 after Alkaline Solution Exposure.....	77
Fig. 31 Modulus of Elasticity of Bar Type V2 after Distilled Water Exposure .....	79
Fig. 32 Modulus of Elasticity of Bar Type V2 after Alkaline Solution Exposure.....	79
Fig. 33 Summary of Tensile Strength Results .....	81
Fig. 34 Summary of Young's Modulus Results.....	82
Fig. 35 Average Relative Weight of Specimens in Distilled Water .....	89

## LIST OF FIGURES (CONT.)

	Page
Fig. 36 Average Relative Weight of Specimens in Alkaline Solution.....	90
Fig. 37 Heterogeneous Distribution of Fibers within the Matrix.....	91
Fig. 38 Main Types of Diffusion .....	92
Fig. 39 Weight of Bars in Distilled Water as a Fraction of Weight at Saturation .....	93
Fig. 40 Weight of Bars in Alkaline Solution as a Fraction of Weight at Saturation.....	93
Fig. 41 Typical Trend of Computed Diffusion Coefficients.....	96
Fig. 42 Predicted Weight Gain for Distilled Water Specimens Using Computed Diffusion Coefficients.....	97
Fig. 43 Predicted Weight Gain for Alkaline Solution Specimens Using Computed Diffusion Coefficients.....	98
Fig. 44 Comparison between Average Predicted and Measured Absorption in Distilled Water.....	99
Fig. 45 Comparison between Average Predicted and Measured Absorption in Alkaline Solution.....	99
Fig. 46 Schematic of Degradation Model .....	100
Fig. 47 Measured and Predicted Residual Relative Tensile Strength .....	102
Fig. 48 Relative Shear Strength versus Exposure Condition .....	109
Fig. 49 Relative Shear Modulus of Elasticity versus Exposure Condition .....	111
Fig. 50 Failure of Bars Type P .....	111
Fig. 51 Failure of Bars Type V1 .....	112
Fig. 52 Failure of Bars Type V2 .....	112
Fig. 53 Elastic and Creep Strains of a Bar Under Constant Load.....	116
Fig. 54 Creep Test Results .....	118
Fig. 55 Relaxation of Prestressing Steel Tendon .....	119
Fig. 56 Prestress Losses due to Prestressing Steel Relaxation in a Loaded Beam .....	120
Fig. 57 Prestressed Concrete Beam Deflections .....	121
Fig. 58 Creep of FRP Reinforcement in a Loaded Concrete Beam .....	126
Fig. 59 Analysis of a Cracked Cross Section.....	127
Fig. 60 Initial and Time Dependent Strains and Curvatures .....	130
Fig. 61 Elastic, Shrinkage, and Creep Strains Developed in Concrete.....	133
Fig. 62 Deflections of a Simple Beam .....	136
Fig. 63 Stress versus Maximum Crack Width of Specimens with 1.21-Inch Cover .....	143
Fig. 64 Stress versus Maximum Crack Width of Specimens with 2.18-Inch Cover .....	143
Fig. 65 Stress versus Maximum Crack Width of Specimens with 3.18-Inch Cover .....	144
Fig. 66 Comparison of Predicted and Measured Values for Specimens with 1.21-Inch Cover .....	148

## LIST OF FIGURES (CONT.)

	<b>Page</b>
Fig. 67 Comparison of Predicted and Measured Values for Specimens with 2.18-Inch Cover .....	148
Fig. 68 Comparison of Predicted and Measured Values for Specimens with 3.18-Inch cover .....	149
Fig. 69 Comparison of Equations Analyzed for Specimens with 1.21-Inch Cover....	150
Fig. 70 Comparison of Equations Analyzed for Specimens with 2.18-Inch Cover....	151
Fig. 71 Comparison of Equations Analyzed for Specimens with 3.18-Inch Cover....	151
Fig. 72 Cyclic Loading Results of Beams Reinforced with 0.75-Inch Diameter Bars .....	160
Fig. 73 Cyclic Loading Results of Beams Reinforced with 0.5-Inch Diameter Bars .....	161
Fig. 74 Influence of Concrete Cover on Rate of Beam Deflection Increase .....	162
Fig. 75 Deflections of All Specimens .....	163
Fig. 76 Selected Deflections of Specimens with 0.5- and 0.75-Inch Diameter Bars .....	164
Fig. 77 Regression Analysis Results.....	165
Fig. 78 Bar Rupture Failure .....	175
Fig. 79 Pullout Failure .....	176
Fig. 80 Specimen with Bars Type P after Testing (Modified from Schaefer [2002]) .....	179
Fig. 81 Temperature Profile of Slab at Cracking for Bars Type P.....	180
Fig. 82 Temperature Profile of Slab at Cracking for Bars Type V1 .....	181
Fig. 83 Specimen with Bars Type V1 after Testing (Modified from Schaefer [2002]) .....	182
Fig. 84 Specimen with Bars Type V2 after Testing (Modified from Schaefer [2002]) .....	183
Fig. 85 Temperature Distribution of Slab at Cracking for Bars Type V2 .....	184
Fig. 86 Comparison between Equation 81 (C=0.09) and Other Equations for a 1.21-Inch Cover.....	193
Fig. 87 Design Example .....	200

## LIST OF TABLES

<b>TABLE</b>	<b>Page</b>
1 Measured Area and Diameter of Bars .....	31
2 Concrete Compressive Strengths.....	33
3 Concrete Compressive Strengths on Test Date for Cracking Slabs .....	34
4 Concrete Compressive Strengths on Test Date for Beams .....	35
5 Concrete Compressive and Tensile Strengths .....	36
6 Number of Tension Test Specimens.....	38
7 Cracking Test Parameters .....	51
8 Parameters to Investigate in Bond Test .....	57
9 Number of Bond Specimens with 0.5-Inch Diameter Bars .....	58
10 Number of Bond Specimens with 0.75-Inch Diameter Bars .....	58
11 Unexposed Tensile Strength Results .....	64
12 Unexposed Modulus of Elasticity Results.....	64
13 Tensile Strength of Bar Type P After Exposure to Distilled Water .....	66
14 Tensile Strength of Bar Type P After Exposure to Alkaline Solution .....	67
15 Modulus of Elasticity of Bar Type P After Exposure to Distilled Water.....	69
16 Modulus of Elasticity of Bar Type P After Exposure to Alkaline Solution ....	69
17 Tensile Strength of Bar Type V1 After Exposure to Distilled Water.....	71
18 Tensile Strength of Bar Type V1 After Exposure to Alkaline solution.....	71
19 Tensile Strength of Bar Type V2 After Exposure to Distilled Water.....	73
20 Tensile Strength of Bar Type V2 After Exposure to Alkaline Solution.....	73
21 Young's Modulus of Bar V1 After Exposure to Distilled Water .....	75
22 Young's Modulus of Bar V1 After Exposure to Alkaline Solution .....	76
23 Young's Modulus of Bar V2 After Exposure to Distilled Water .....	78
24 Young's Modulus of Bar V2 After Exposure to Alkaline Solution .....	78
25 Tensile Strength of Bar Type P Notched .....	83
26 Tensile Strength of Bar Type V1 Notched .....	84

## LIST OF TABLES (CONT.)

TABLE	Page
27 Tensile Strength of Bar Type V2 Notched .....	85
28 Average Relative Weight from Test of Bars with Uncapped Ends .....	87
29 Average Relative Weight from Test of Capped-End Bars in Distilled Water.....	88
30 Average Relative Weight from Test of Capped-End Bars in Alkaline solution .....	88
31 Diffusion Coefficients .....	96
32 Comparison of Relative Residual Tensile Strength Results of Unstressed Specimens .....	105
33 Shear Strength Values of Bar Type P .....	107
34 Shear Strength Values of Bar Type V1 .....	107
35 Shear Strength Values of Bar Type V2 .....	108
36 Shear Modulus of Elasticity Values of Bar Type P .....	109
37 Shear Modulus of Elasticity Values of Bar Type V1 .....	110
38 Shear Modulus of Elasticity Values of Bar Type V2 .....	110
39 Creep strain of GFRP Bars at Six Months.....	118
40 Cracking and Ultimate Loads of Specimens .....	139
41 Midspan GFRP Bar Stresses and Maximum Crack Widths for 1.21-Inch Cover.....	140
42 Midspan GFRP Bar Stresses and Maximum Crack Widths for 2.18-Inch Cover (Part A).....	140
43 Midspan GFRP Bar Stresses and Maximum Crack Widths for 2.18-Inch Cover (Part B).....	141
44 Midspan GFRP Bar Stresses and Maximum Crack Widths for 3.18-Inch Cover (Part A).....	141
45 Midspan GFRP Bar Stresses and Maximum Crack Widths for 3.18-Inch Cover (Part B).....	142
46 Variables Used in the ACI 440 Expression .....	146
47 Values of the Variables Used in the Equation of Faza and GangaRao .....	147

## LIST OF TABLES (CONT.)

TABLE	Page
48 Values of SSE of Several Equations Normalized to SSE of Least Squares Line .....	153
49 Observations within $\pm$ 30 Percent Range.....	153
50 Failure Loads of Beams with 0.5-Inch Diameter Bars .....	156
51 Failure Loads of Beams with 0.75-Inch Diameter Bars .....	156
52 GFRP Bar Stresses at Midspan.....	158
53 Number of Cycles and Midspan Beam Deflections (Part A) .....	158
54 Number of Cycles and Midspan Beam Deflections (Part B).....	159
55 Number of Cycles and Midspan Beam Deflections (Part C).....	159
56 Failure Loads with and without Cyclic Loading for 0.75-Inch Diameter Bar Specimens .....	168
57 Failure Loads with and without Cyclic Loading for 0.5-Inch Diameter Bar Specimens .....	168
58 Average Bond Stresses at Failure for the 0.5-Inch Diameter Bars.....	170
59 Average Bond Stresses at Failure for the 0.75-Inch Diameter Bars .....	170
60 Average Pullout Failure Stresses for 0.75-Inch Diameter Bars.....	171
61 Computed Development Length for 0.75-Inch Diameter Bars .....	172
62 Average Slip at Loaded End of 0.5-Inch Diameter Bars at Failure.....	175
63 Average Slip at Loaded End of 0.75-Inch Diameter Bars at Failure.....	175
64 Comparison of Temperatures at Cracking.....	185
65 Tensile Strength Results and Predicted Values .....	189
A1 Moisture Absorption of Uncapped End Specimen.....	255
A2 Moisture Absorption of Capped End Specimens in Distilled Water.....	256
A3 Moisture Absorption of Capped End Specimens in Alkaline Solution.....	256
B1 Creep Test Data.....	259



## I. INTRODUCTION

There are approximately 500,000 bridges in the Federal Highway System and an estimated one trillion dollars needs to be invested in the system to rehabilitate those bridges that are classified as insufficient ([Nystrom 2003](#)). Corrosion of steel reinforcement is a primary problem afflicting the concrete bridges in the United States. Considerable research efforts have been made worldwide to mitigate the damage caused by corrosion of steel reinforcement in concrete. The use of fiber-reinforced-polymer (FRP) bars to reinforce concrete has been researched since the 1970s and this material has shown promise as an alternative reinforcement for steel ([Nawy and Neuwerth 1971](#)). Glass Fiber-Reinforced Polymer (GFRP) bars are lightweight, non-conductive, exhibit high tensile strength, and have been reported to be non-corrosive when compared with conventional steel reinforcement. As a result of these characteristics, FRP reinforcement has been used to reinforce prestressed concrete bridge beams, bridge decks, tunnel linings, waterfront structures, buildings near waterfronts, electrical substations, marine aquariums, as well as to retrofit historic buildings ([Trejo et al. 2000](#), [Hughes Brothers 2002](#)).

FRP reinforcing bars and tendons are composite materials made up of unidirectional fibers embedded in a polymeric matrix. The fiber materials used to make reinforcing bars for civil applications are glass, aramid, and carbon. The most commonly used polymeric resins are polyester, epoxy, vinyl ester, and polyimide. Of particular interest are GFRP bars because they have the lowest initial costs.

Although GFRP reinforcing bars may provide potential benefits for the performance of reinforced concrete structures, problems have been identified with these types of bars. There are a number of gaps in existing knowledge regarding the performance of GFRP bars as reinforcement for concrete. The mechanical properties of

the GFRP bars degrade with time, and the residual properties have not been fully characterized. The methods available for the prediction of long-term deflections of GFRP-reinforced concrete members due to creep may be unconservative, and further creep tests are necessary. The equations available for the prediction of maximum crack width of GFRP-reinforced concrete members have not been thoroughly investigated. The increase in deflections of FRP-reinforced concrete members due to cyclic loading are supported by limited tests, and only a limited number of tests were conducted on GFRP bars. Limited information exists on the degradation of the bond strength of GFRP bars in concrete after exposure. The information available to determine whether concrete structures can crack due to stresses induced by differential thermal expansion between GFRP bars and concrete is inconclusive. This research will address each of these issues.

The construction of the Sierrita de la Cruz Creek Bridge, built for the Texas Department of Transportation in Amarillo, Texas, motivated most of the research questions addressed in this report. The Sierrita de la Cruz Creek Bridge incorporated hybrid concrete decks in two of the spans. In the spans containing GFRP reinforcement, the bottom mat of the deck consisted of a combination of epoxy coated steel reinforcement, uncoated steel bars, and uncoated steel strands, and the top mat consisted of GFRP reinforcement.

[Section II](#) presents a review of the existing literature pertaining to the degradation of the tensile strength of variously conditioned FRP bars over time, the characterization of the direct shear strength of GFRP bars, the prediction of long-term deflections of GFRP-reinforced concrete members, the prediction equations for maximum crack width of GFRP-bar reinforced concrete elements, the increase in deflections of GFRP-bar reinforced concrete elements due to cyclic loading, the degradation of bond strength between GFRP bars and concrete, and the cracking of concrete structures due to thermal expansion.

[Section III](#) describes the materials used in this research, the experimental program, research test specimens, and the test procedures used in this research. This section describes the following tests: axial tension test, moisture absorption test, direct shear strength test, creep test, cracking of concrete slabs test, cyclic loading of concrete beam test, bond test, and thermal expansion of concrete slabs test.

The results of the tests described in [Section III](#) are presented in [Section IV](#). An analysis of the results is presented for each test.

[Section V](#) contains a review of the ACI 440 design guidelines analyzed in the light of the results of this investigation. A design example showing how the recommendations from this research can be implemented into the existing design methodology is presented. [Section VI](#) contains recommendations for including GFRP reinforcement into American Association of State Highway and Transportation Officials (AASHTO) Load and Resistance Factor Design (LRFD) specifications for the design of bridges.

Although preliminary recommendations are made here, the reader is cautioned that some recommendations are based on the results of this research program only. [Section VII](#) summarizes the document by presenting the conclusions, recommendations, and required future work.



## **II. RELATED LITERATURE REVIEW**

As described in the introduction, the topics addressed in this document are aimed toward improving the current knowledge for the application of GFRP bars in reinforced concrete elements. This section will begin with an introduction to diffusion concepts and their application toward predicting moisture absorption by GFRP bars. Following this, issues involving the change of tensile properties of GFRP reinforcing bars over time due to the moisture absorption and diffusion into GFRP bars, direct shear strength of GFRP bars, creep-induced deflections of GFRP-reinforced concrete elements, cracking of GFRP-reinforced concrete structures, deflections of GFRP-reinforced concrete elements due to cyclic loading, degradation of bond between GFRP bars and concrete, and cracking of GFRP-reinforced concrete elements due to thermal expansion. Each of these issues has been identified as an issue that has not been thoroughly investigated or that requires further investigation to better assist engineers in the design of GFRP-reinforced concrete structures.

### **DIFFUSION CONCEPTS**

The change in the mechanical properties of GFRP bars depends on the transport rates and mechanisms resulting from the migration of elements that degrade the properties of the polymeric matrix and glass fibers. Mass transport in solution is a function of diffusion of molecules due to a concentration gradient ([Shackelford 1996](#)), diffusion of charged particles under the influence of an electrical potential ([Girifalco 1964](#)), and hydrodynamic transport ([Rossier 2003](#)). In the case of GFRP bars embedded in concrete, the hydrodynamic transport factor would be negligible. According to Soles et al. ([2000](#)), the polarity of the resin may be an important factor in the moisture transport in epoxy resins, even though they did not measure the polarity of the resins used in their study. The same researchers verified that moisture uptake of a polymer could be modeled by applying Fick's second law of diffusion. A review of Fick's laws as they apply to diffusion of a substance into a cylinder is presented next.

## Fick's First Law of Diffusion

Fick's first law of diffusion, as it applies to one-dimensional transport, is given by:

$$J = -D \frac{\partial c}{\partial x} \quad (1)$$

where,

- $J$  = Flux in one dimension with the concentration gradient being constant with time,
- $D$  = Diffusion coefficient for the substance considered, usually assumed to be constant for a given medium, temperature, and pressure ( $cm^2 sec^{-1}$ ),
- $c$  = Concentration of the solution,
- $x$  = Direction of flux.

## Fick's Second Law of Diffusion

For three-dimensional linear diffusion:

$$\frac{\partial c}{\partial t} = D \left( \frac{\partial^2 c}{\partial x^2} + \frac{\partial^2 c}{\partial y^2} + \frac{\partial^2 c}{\partial z^2} \right) \quad (2)$$

where the terms are as defined above,  $t$  is time, and  $y$  and  $z$  are directions of flux.

Fick's second law of diffusion applies to cases where the concentration gradient is not constant with time. The first law is obtained by reducing [Equation 2](#) to one-dimensional flow for the case of no change in concentration with time, i.e.,

$$\frac{\partial c}{\partial t} = 0 \quad (3)$$

and the following is obtained:

$$D \frac{\partial^2 c}{\partial x^2} = 0, \frac{\partial c}{\partial x} = \text{constant}, c = c_0 + c_1 x \quad (4)$$

Fick's second law can be rewritten in cylindrical coordinates by using the appropriate divergence operator:

$$\text{div}F = \frac{1}{r} \frac{\partial}{\partial r} (r \cdot F_r) + \frac{1}{r} \frac{\partial F_\theta}{\partial \theta} + \frac{\partial F_z}{\partial z} \quad (5)$$

obtaining:

$$\frac{\partial c}{\partial t} = \frac{D}{r} \left( \frac{\partial}{\partial r} \left( r \frac{\partial c}{\partial r} \right) + \frac{\partial}{\partial \theta} \left( \frac{1}{r} \frac{\partial c}{\partial \theta} \right) + \frac{\partial}{\partial z} \left( r \frac{\partial c}{\partial z} \right) \right) \quad (6)$$

assuming that the diffusion coefficient remains constant (linear diffusion).

If it is further assumed that the concrete pore solution has a constant concentration at the surface of the GFRP bar, that the bar can be modeled to be homogeneous and cylindrical, and that migration into the cylindrical bar occurs in the radial direction only, the diffusion equation simplifies to the following expression:

$$\frac{\partial c}{\partial t} = D \left( \frac{\partial^2 c}{\partial r^2} + \frac{1}{r} \left( \frac{\partial c}{\partial r} \right) \right) \quad (7)$$

This equation can then be used to determine the rate of transport of compounds or elements that can influence the mechanical characteristics of GFRP bars.

## ISSUE I. CHANGE OF TENSILE PROPERTIES OF GFRP REINFORCING BARS OVER TIME

Corrosion of steel reinforcement reduces the useful life of a structure, resulting in high economic losses and safety hazards. It has been reported that the estimated service life of a deck reinforced with conventional reinforcing steel is 10 years, that of a deck with two layers of epoxy-coated steel reinforcement is 40 years, and that of a deck with two layers of stainless steel reinforcement ranges from 75 to 100 years ([Yunovich and Thompson 2003](#)). The service life of GFRP-reinforced concrete structures is not known. Nevertheless, the interest in using GFRP reinforcing bars has been mostly driven by the fact that these reinforcing bars do not exhibit conventional corrosion, similar to that of steel reinforcement. As such, these bars are becoming a potential substitute for steel reinforcement, conceivably eliminating or reducing the safety and serviceability issues associated with corrosion of steel reinforcement.

It is well known that polymers absorb moisture and the polymer matrix softens as a result of this moisture absorption (Trejo et al. 2000). Because the pore humidity in concrete seldom drops below 72 percent (Pyé 1998), GFRP bars are continually exposed to a moist environment. Beginning with the onset of hydration, concrete exhibits a high pH (Mindess and Young 1981), usually between 12 and 12.5 (in the absence of carbonation). In addition, glass fibers have been reported to deteriorate in alkaline environments (Tannous and Saadatmanesh 1999). As a result, the mechanical characteristics of GFRP bars embedded in concrete would be expected to change over time, since concrete is a moist environment with a high pH solution. Although the fundamental reason for implementing the use of FRP bars has been to eliminate conventional steel reinforcement deterioration due to corrosion, FRP bars, especially GFRP bars, could exhibit significant loss of tensile strength.

Katsuki and Uomoto (1995) found that the residual tensile strength of GFRP bars after exposure to alkaline solutions could be predicted based on the hypothesis that GFRP bars degrade due to the attack on the glass fibers by alkalis present in the concrete pore solution that diffuses into the bar. They observed and measured the depth of penetration of the alkaline solution into the bars with an Electron Probe Microscope Analyzer, and proposed the use of the following expression to compute the depth of penetration:

$$x = \sqrt{2Dct} \quad (8)$$

where  $x$ ,  $D$ ,  $c$ , and  $t$ , as reported by the authors, indicate depth from the surface of the bar ( $cm$ ), diffusion coefficient of the FRP bar for the concrete pore solution ( $cm^2 h^{-1}$ ), alkaline concentration ( $mol/l$ ), and time ( $h$ ), respectively. The authors stated that the above expression was obtained using Fick's first law. However, rearranging Equation 8, it can be shown that the concentration is a function of time and of the penetration distance to the second power. Thus, the authors did not use Fick's first law of diffusion to model the penetration of the concrete pore solution into the GFRP bar. The authors assumed the alkali-penetrated area of the bar could be modeled as a ring. To predict the

residual tensile strength, the authors assumed the ring-like alkali-penetrated area to have no strength and the core of the bar to have the original strength. As a result, the authors obtained the following expression for the computation of the residual tensile strength:

$$\sigma_t = \left(1 - \frac{\sqrt{2Dct}}{R_0}\right)^2 \sigma_0 \quad (9)$$

where the terms are as described earlier and  $\sigma_t$ ,  $\sigma_0$ , and  $R_0$  are the tensile strength at any given age (MPa), the tensile strength before exposure (MPa), and the bar radius (cm), respectively. Katsuki and Uomoto (1995) exposed GFRP bars to a 39,006 ppm aqueous solution of NaOH at 104 °F. The diffusion coefficient computed was  $2.8 \times 10^{-6}$  cm<sup>2</sup>/h. The authors appear to have obtained good agreement between the predicted residual tensile strength and the measured strength. Since the degradation study was based on specimens exposed to high temperature, it is not clear whether the results from such accelerated exposure conditions would be applicable to normal concrete exposure conditions.

Gurtin and Yatomi (1979) proposed a two-phase diffusion model to predict the moisture absorption of composite materials. However, for classical non-steady-state diffusion (Fick's second law), the diffusion coefficient is independent of the length of the specimen. As such, because the model proposed by Gurtin and Yatomi depends on the length of the specimen, the validity of the model is questionable.

Carter and Kibler (1978) proposed another diffusion model. Their model fits experimental data well for specimens 0.038 inch thick made with a specific resin (type 5208). The authors stated that their model could be applied to other composites although they conducted their tests on only one type of epoxy resin.

Although polymers are heterogeneous materials, Dejke (2001) carried out moisture absorption tests on GFRP bars and used Fick's second law of diffusion to model the moisture absorption of the bars. However, the author did not verify whether

the model was applicable to FRP bars, probably because the author used a solution of Fick's second law of diffusion that yields concentration as a function of penetrated distance and time, and could not correlate that with the weight gain measurements from the experimental program, since a method to measure the concentration at different depths has not yet been developed. Dejke (2001) also developed a service life prediction model; however, the author compared the model predictions of residual strength of GFRP bars with results from another model and not with actual test results.

In another study, Tannous and Saadatmanesh (1999) found that the strength of GFRP bars degraded and the modulus of elasticity increased over six months of exposure to different environments. The authors recorded the moisture absorption of GFRP bars with 0.375-inch and 0.75-inch diameters. The researchers used the models by Gurtin and Yatomi (1979) and Carter and Kibler (1978), among others, to develop one- and two-phase diffusion models. The researchers conducted moisture absorption tests for a period of 417 days. The researchers' moisture absorption models agree reasonably well with the initial portion of the moisture absorption curves that they recorded from the test data. However, the predicted moisture absorption curves depart from the actual data at 26 days for one specimen and at 150 days for the other three specimens studied. As indicated by the authors, the models used to predict moisture absorption become invalid when the predictions and the measured data depart. Although none of the specimens reached complete saturation when the test was stopped, the highest recorded weight moisture absorption was approximately 100, 425, 240, and 200 percent of the maximum moisture absorbed predicted by the models for 0.375-inch diameter glass-polyester bar, 0.375-inch diameter glass-vinylester bar, 0.75-inch diameter glass-polyester bar, and 0.75-inch diameter glass-vinylester bar, respectively. Tannous and Saadatmanesh (1999) used the moisture absorption data to find a diffusion coefficient and the model proposed by Katsuki and Uomoto (1995) to predict the residual tensile strength of the GFRP bars. The authors' predictions were between 8 percent below and 15 percent above the measured ultimate strength of the GFRP bars exposed for six months. The good

agreement between the predicted and measured tensile strength losses may result from the good agreement between the moisture absorption models and the moisture absorption test results up to approximately 150 days. The bars used in the tension tests were exposed for only six months. The model used by the authors to make residual tensile strength predictions may not be valid for exposure periods longer than six months, due to the large discrepancies between the measured and predicted moisture absorption data after 150 days.

The present literature demonstrates the need to conduct tension tests and moisture absorption tests on GFRP bars exposed over longer periods of time in order to gain confidence in making long-term predictions. A model that relates results from tensile strength degradation of GFRP bars to the moisture absorption that takes place in the bars is required to improve existing models for the prediction of the rate of change of the mechanical properties of the bars. To fill this gap, the authors implemented a study to evaluate the influence of six-month and one-year exposure periods on the mechanical properties of GFRP bars. Tension tests were performed at the end of these exposure times. Moisture absorption tests on GFRP bars also were performed until the bars were near saturation.

In addition to possible degradation of GFRP bars exposed to concrete pore solution, there is concern in the design community that GFRP bars may be damaged by construction equipment and regular construction practices. Deitz (1998) made an assessment of the constructability of bridge decks with GFRP bars and concluded that construction tools such as shovels and vibrators could scratch the surface of the bars, but that no major damage was observed. Nonetheless, Deitz (1998) pointed out that the scratches could lead to long-term deterioration. Thus, there is also a need for degradation tests to be conducted on “damaged” GFRP bars exposed to simulated concrete pore solution. To address this issue, the authors of this project notched GFRP and exposed them to a simulated concrete pore solution. The bars were then tested, and the moduli of

elasticity and tensile strengths were measured after exposure to evaluate any changes in mechanical properties.

## **ISSUE II. DIRECT SHEAR STRENGTH OF GFRP BARS**

GFRP bars could be subjected to direct shear when used to reinforce concrete elements that are connected by a construction joint crossed by the reinforcement. GFRP bars have been proposed to reinforce bridge barriers and their connection to concrete decks. It is typical in the construction of bridge decks to cast the deck prior to casting the barrier, leaving the connecting bars to the barrier protruding from the concrete. The reinforcement for the barrier is later tied and finished and the barrier concrete cast. GFRP bars connecting the barrier and the deck across this construction joint could be subjected to a combination of tension and direct shear in the case of a vehicle impact. GFRP dowel bars that connect a bridge deck to the concrete pavement are another example where GFRP bars can be subjected to direct shear. Nevertheless, limited information exists on the shear strength of GFRP bars and on the deterioration of the direct shear strength of GFRP bars exposed to concrete environments. Ueda et al. (1995) conducted shear tests on aramid FRP bars subjected simultaneously to tension and shear and developed failure envelopes. Dejke (2001) evaluated the interlaminar shear strength of FRP bars by testing them in three-point bending after exposure to neutral, alkaline, and concrete environments at room and high temperatures for up to 421 days. Dejke found the largest interlaminar shear strength reductions ranged from approximately 20 to 80 percent for specimens exposed to alkaline and concrete environments at 140 °F for approximately 390 days. Up to 82 percent reductions in interlaminar shear strength were reported for specimens exposed to alkaline solution and concrete for exposure to 68 °F for approximately 390 days.

Structural elements without shear reinforcement such as bridge decks or slabs are other applications where GFRP bars may fail in direct shear or a combination of tension and direct shear. In an experimental study on the behavior of one-way concrete slabs

reinforced with FRP bars, Michaluk et al. (1998) conducted flexural tests. The researchers found that one of their specimens collapsed after shear rupture occurred on GFRP bars at a crack. Therefore, the direct shear strength of GFRP bars can be an important parameter to consider in design and requires further evaluation.

Since limited test data on the degradation of the direct shear strength exists, this research focused on testing and evaluating the direct shear strength of GFRP bars and determining the change in direct shear strength and direct shear stiffness as a function of exposure time to simulated concrete pore solutions.

### **ISSUE III. CREEP-INDUCED DEFLECTIONS OF GFRP-REINFORCED CONCRETE ELEMENTS**

A reinforced concrete structure must be designed to meet strength and serviceability requirements. Strength requirements indicate that a structural member must be able to sustain the factored design loads. Regarding serviceability requirements, GFRP-reinforced concrete elements are required to develop small deformations under service (unfactored) loads to maintain the function of the structure, to limit damage to nonstructural elements, to give the users confidence in the structure, and to prevent the structural behavior from being different from that assumed (Park and Paulay 1975). GFRP bars have higher tensile strengths and lower tensile and shear stiffnesses than conventional steel reinforcing bars. As a result of the lower axial stiffness of the GFRP bars, GFRP-reinforced concrete members deform more than typical steel-reinforced concrete members. Consequently, the design of GFRP-reinforced concrete members is typically governed by serviceability requirements. Allowable deflections are thus common governing requirements for GFRP-reinforced concrete elements. Deflections of structures are of two types: immediate and long-term. The contribution of creep and shrinkage of concrete, as well as creep of GFRP bars account for the total long-term deflections. Based on the research of Brown (1997), Kage et al. (1995), and Vijay and GangaRao (1998), the current American Concrete Institute (ACI) 440 (2001) design

guidelines provided the following equation for the computation of the long-term deflections of FRP-reinforced concrete elements:

$$\Delta_{(cp+sh)} = 0.6\xi(\Delta_i)_{sus} \quad (10)$$

where,

$\Delta_{(cp+sh)}$  = Additional deflection due to creep and shrinkage under sustained loads (*mm, inch*),

$(\Delta_i)_{sus}$  = Immediate deflection due to sustained loads (service loads) (*mm, inch*),

$\xi$  = Time-dependent factor for sustained load defined in the ACI 318 Building Code (2000).

[Equation 10](#) is believed to yield inaccurate predictions for GFRP-reinforced concrete elements under sustained load, as demonstrated by tests conducted by Kage et al. (1995) and by Brown (1997). [Equation 10](#) does not consider the contribution of creep of FRP bars to the total deflection. Gere and Timoshenko (1990) define creep as the increase in length of a bar loaded with a constant force over time, beyond the initial (elastic) deformation. The original equation to compute long-term deflections of steel-reinforced concrete members due to creep and shrinkage of the concrete alone was developed by Branson (1977). In [Equation 10](#), the factor of 0.6 was likely proposed because this number fit data obtained from tests conducted by Brown (1997). However, creep and shrinkage deflections computed using the 0.6 factor overestimated the measured deflections for a carbon FRP-reinforced concrete beam by 350 percent, and by 360 percent for a glass FRP-reinforced concrete beam after one year (Kage et al. 1995). Tests conducted by Brown (1997) showed that the deflections of one beam specimen were accurately predicted using [Equation 10](#). However, the ACI 440 (2001) method for computing long-term deflections underestimated the six-month deflections of two other beam specimens by 24 percent. Summarizing, [Equation 10](#) does not specifically account for the creep of FRP bars, and the factor of 0.6 may not be adequate to account for long-term creep.

In an attempt to improve the methods available to predict deflections of FRP-reinforced concrete elements due to creep, this project included tests to measure creep of FRP bars and proposes a new method for evaluating the strains and curvatures of FRP-reinforced concrete elements, accounting for creep of FRP bars. The proposed method of analysis is derived from a method used in the prediction of deflections of prestressed concrete elements, where simplified methods similar to the one described above fail to provide accurate predictions ([Gilbert and Mickleborough 1990](#)). The ACI 440 ([2001](#)) method for predicting long-term deflections of FRP-reinforced concrete elements may be used to make order-of-magnitude estimates of long-term deflections. However, more accurate predictions of long-term deflections could be obtained by accounting for creep and shrinkage of concrete and creep of FRP bars.

#### **ISSUE IV. CRACKING OF GFRP-REINFORCED CONCRETE STRUCTURES**

The design of steel-reinforced concrete elements is sometimes governed by strength requirements. Concrete members with a given geometry reinforced with bars that have a lower elastic modulus than steel bars will deform more and develop wider cracks than concrete members with the same geometry reinforced with the same configuration and area of steel bars. For this reason, the design of GFRP-reinforced concrete elements is typically governed by serviceability requirements such as allowable maximum crack widths and allowable deflections. Maximum crack widths in steel-reinforced concrete members have typically been limited in design codes to preserve visual appearance and because of reinforcement corrosion concerns ([ACI 1996](#)). Although the 1995 version of the ACI 318 code does not explicitly mention that crack width limits were chosen because of corrosion concerns, the corrosion concern is evidenced by the fact that different crack width limits are indicated for concrete elements subjected to interior exposure and exterior exposure ([ACI 1996](#)). As MacGregor ([1992](#)) points out, crack width has traditionally been related to corrosion of steel reinforcement. However, since the 1999 version of the ACI 318 code, the requirements for crack width limitations have been eliminated and no distinction is made between structural elements

subjected to interior or exterior exposure (ACI 2000). The crack width limitations were eliminated because the relationship between cracks and corrosion of steel reinforcement is controversial (ACI 2000). Nevertheless, the spacing of reinforcement requirement that replaced the crack width limitations in the 1999 version of the ACI 318 code still implicitly limits the surface crack widths.

Maximum crack widths in FRP-reinforced concrete structures are implicitly limited in concrete building codes, such as the ACI 318 Building Code (1996), to maintain visual appearance, to reduce the possibility of deterioration of the reinforcement, and to limit stiffness reductions. No publication has been identified that links crack width to durability of GFRP bars. Schmuck and de Tourreil (2003) have reported that over 100 “brittle fractures” have occurred in composite bars used as insulators in distribution lines and transmission systems. Schmuck and de Tourreil (2003) reported that the hardener used for the impregnation of the glass fibers used to manufacture the bars could be transformed into an acid by moisture and degrade the glass fibers up to a point that causes brittle failure of the bars while in service. As such, GFRP bars exposed to moisture at a crack in a concrete element may degrade and rupture. Therefore, until the influence of maximum crack width on the deterioration of GFRP bars is studied and the mechanisms governing the deterioration of GFRP bars in concrete elements under service conditions are further explored, the maximum implicit crack width limit remains a useful design parameter for GFRP-reinforced concrete elements.

In the current ACI 440 (2001) design guidelines, Equation 8-9b given for maximum crack width prediction is based on an equation developed by Gergely and Lutz (1973) for steel-reinforced concrete elements. ACI committee 440 (2001) adapted the Gergely and Lutz (1973) equation for FRP-reinforced concrete members. The ACI 440 (2001) design guidelines recommended using the Gergely and Lutz (1973) equation after reviewing three investigations, one of which was conducted by Faza and GangaRao

(1993), another by Masmoudi et al. (1998), and a technical report by the civil engineering department of the University of Sherbrooke that could not be obtained by the authors. To better understand the topic, a basic description of the cracking phenomenon will be provided next, followed by an analysis of the investigations that led to Equation 8-9b reported in the ACI 440 (2001) design guidelines.

When a reinforced concrete member is loaded in flexure, an internal couple will develop to balance the applied moment. The internal couple is the result of stresses developed by the concrete and the reinforcement. The concrete will develop compressive and tensile stresses. The reinforcement will develop tensile stresses, as well. However, the fraction of the tensile load taken by the reinforcement will be small compared to the load sustained by the concrete in tension. This behavior will continue until the applied moment causes tensile stresses in the concrete larger than the tensile strength of the concrete, and the concrete will crack. After cracking, almost all of the tensile force is transferred to the reinforcement at the cracked section. As the applied moment increases, the stresses in the reinforcement will continue to increase, and the crack will widen. If the applied moment is further increased, more cracks will develop, the stresses in the reinforcement will increase, and the width of the first crack will change. When several cracks develop in a reinforced concrete element, the widths of the cracks will be different at different load stages, and usually one of the cracks will be the widest. The widest crack at one load level may not be the widest at another load level. At a given load level, the widths of all of the cracks can be measured, the average crack width can be computed, and the maximum crack width identified.

Gergely and Lutz (1973) proposed the following expression for estimating the most probable maximum crack width,  $W_{\max}$ , at a given reinforcement stress level on the bottom (tensile side) of a steel-reinforced concrete specimen:

$$W_{\max} = 0.076\beta \cdot f_s \cdot \sqrt[3]{d_c A} \quad (11)$$

where,

$W_{max}$  = Maximum crack width (*inch*),

$\beta$  =  $h_2/h_1$ ,

$h_1$  = Distance from the centroid of the reinforcement to the neutral axis (*inch*),

$h_2$  = Distance from the extreme tension fiber to the neutral axis (*inch*),

$f_s$  = Stress in the reinforcement (*ksi*),

$d_c$  = Bottom cover measured from the center of lowest bar (*inch*),

$A$  = Twice the difference between the total and effective depths multiplied by the width of the section (effective area of concrete surrounding the main reinforcement) divided by the number of bars (*inch*<sup>2</sup>).

Gergely and Lutz (1973) conducted a statistical evaluation of the results of five different investigations on crack width. As reported by Gergely and Lutz (1973), the maximum crack width measured at a certain stress level is considered statistically as an observation. The researchers evaluated 24 different possible equations to be used to predict the maximum bottom crack width. The investigators concluded that the most relevant parameters influencing maximum crack width were the reinforcement stresses, the concrete cover, the effective area of concrete surrounding the reinforcement, and the number of bars. The reinforcement stress was deemed the most important variable by the researchers. The investigators identified scatter in the data such that approximately two-thirds of the maximum crack widths were within 25 percent of the most probable value. The researchers also found that perfect correlation could not be obtained even for a single beam using  $f_s$  or any other variable.

The research conducted by Faza and GangaRao (1993) was one of the investigations reviewed by the ACI 440 (2001) guidelines before proposing Equation 8-9b. Faza and GangaRao (1993) proposed to use the following equation to predict maximum flexural crack width in a beam:

$$W_{\max} = \frac{f_f}{E_f} \frac{2f_t'}{\mu_m} \frac{A}{\pi D} \quad (12)$$

where,

$W_{\max}$  = Maximum crack width (*inch*),

$f_t' = 7.5 (f_c')^{1/2}$ ,

$f_c'$  = Compressive strength of concrete (*psi*),

$f_f$  = Maximum FRP bar stress at service load level (*ksi*),

$E_f$  = Modulus of elasticity of FRP bar (*ksi*),

$\mu_m$  = Maximum bond stress (*psi*),

$D$  = Bar diameter (*inch*),

$A$  = Twice the difference between the total and effective depths multiplied by the width of the section (effective area of concrete surrounding the main reinforcement) divided by the number of bars (*inch*<sup>2</sup>).

The expression proposed by Faza and GangaRao (1993) was derived from an equation used to compute average crack spacing developed by Watstein and Bresler (1974). Although the equation proposed by Faza and GangaRao (1993) is based on an average crack width expression, Faza and GangaRao reported their equation to predict maximum crack widths. Equation 12 tends to predict larger crack widths than the crack widths predicted with Equation 11. This can be seen in Figure 1, which is a plot of the values reported in Table 2 of the study conducted by Faza and GangaRao. As mentioned by Gergely and Lutz (1973), concrete cover is one of the important variables to predict maximum crack width. Unfortunately, the information provided by Faza and GangaRao is limited and neither the specimens' dimensions nor the concrete cover were reported. Since the number of observations is limited and because crack width behavior usually exhibits large scatter, it would be difficult to determine whether the equation proposed by Faza and GangaRao reliably predicts maximum crack widths for specimens with different concrete covers. A larger number of observations are required to gain

confidence in the accuracy of the proposed expression to compute maximum crack widths in FRP-reinforced concrete members.

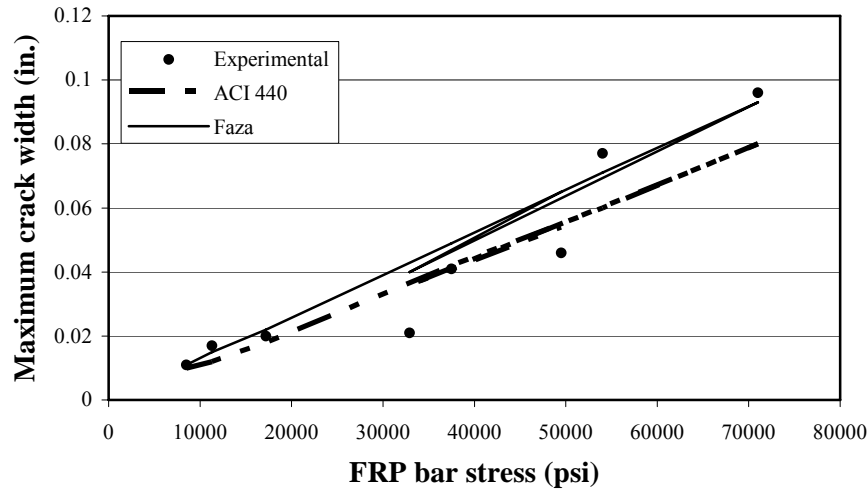


**Figure 1. Test Data, Faza and GangaRao Equation, and ACI 440 Equation.**

Masmoudi et al. (1998) tested 12 GFRP-reinforced concrete beams. All of the beams were reinforced with 0.5-inch diameter bars. The specimens were made in groups with three different reinforcement ratios, namely: 0.5, 0.7, and 1.07 percent. All of the specimens had a clear concrete cover of 1.18 inches. The authors found good “correlation” between predictions made with the Gergely and Lutz (1973) expression and a European equation. However, only a visual comparison between the results of two of the 12 specimens and the equations mentioned was made, with no quantitative analysis. It would have been quite useful to have the data obtained from all of the specimens compared with the theoretical predictions. Measurement of a data set of 21 bridge decks by Weyers et al. (2003) showed an average cover depth of 2.56 inches and a standard deviation of 0.36 inch. An additional data set of 31 bridge decks showed an average cover depth of 2.6 inches and a standard deviation of 0.38 inch. The measured cover depths result from a requirement by the AASHTO Specifications (1998) that deck

slabs exposed to deicing salts have a cover depth of not less than 2.5 inches. Thus, it is common to find concrete covers larger than 2.5 inches in bridge decks. However, the study conducted by Masmoudi et al. (1998) was limited to a concrete cover of 1.18 inches, and it is, therefore, necessary to verify the applicability of the Gergely and Lutz expression for GFRP-reinforced concrete elements with concrete covers of 2.5 inches or larger.

Limited information is available from maximum crack width tests on FRP-reinforced concrete elements. Correlation between maximum crack width data and the equations given by the ACI 440 (2001) design guidelines and by Faza and GangaRao (1993) have not been validated. This investigation will fill that gap by conducting tests that evaluate the cracking behavior of FRP-reinforced concrete elements with different concrete covers. The test sample configuration will be similar to typical bridge decks built in Texas, such as the Sierrita de la Cruz Creek Bridge deck built in Amarillo, Texas. In addition, this research will provide a correlation between the observed data and the different equations proposed.

## **ISSUE V. DEFLECTIONS OF GFRP-REINFORCED CONCRETE ELEMENTS DUE TO CYCLIC LOADING**

The low modulus of elasticity of GFRP bars compared to steel reinforcement typically results in either allowable maximum crack widths or allowable deflections being the governing design criterion for GFRP-reinforced concrete elements.

Iwamoto et al. (1993) carried out cyclic loading tests on concrete beams prestressed with aramid FRP bars. Deflections in some beams doubled and in others increased five times after approximately 1.5 million cycles. Benmokrane et al. (1999) subjected a concrete slab reinforced with carbon FRP mesh to 4 million cycles of loading, and the slab showed an increase in deflection of 44 percent from the initial deflection.

The research conducted by Iwamoto et al. (1993) and Benmokrane et al. (1999) was limited and did not account for the effects of bar size, bar texture, and concrete cover. Equations have not been developed to predict deflections due to cyclic loading. Current ACI 440 (2001) design guidelines do not account for deflections due to repeated loading, perhaps because few cyclic loading studies have been made.

The research conducted by Iwamoto et al. (1993) and Benmokrane et al. (1999) indicates that deflections of FRP-reinforced concrete members due to cyclic loading can be significant and should be accounted for in design. The research studies mentioned were carried out on specimens made with prestressed aramid FRP bars and a slab reinforced with non-prestressed carbon FRP mesh. It is necessary to conduct cyclic load tests on non-prestressed specimens made with GFRP bars due to the limited availability of test data. It has not been reported how bar size, concrete cover, and surface finish of the bar influence the deflections of FRP-reinforced concrete elements due to cyclic loading. To address these issues, concrete beams were tested by the authors in cyclic loading, and the test results were used to develop an expression to predict deflections due to cyclic loading. As shown by Iwamoto et al. (1993) and Benmokrane et al. (1999), deflections of FRP-reinforced concrete members due to cyclic loading can be significant and should be accounted for in the prediction of long-term deflections.

## **ISSUE VI. DEGRADATION OF BOND BETWEEN GFRP BARS AND CONCRETE**

A number of studies have been made to characterize the bond strength and behavior of FRP bars in concrete (Trejo et al. 2000). However, only a few studies have been performed to evaluate the changes in bond properties over time. Mashima and Iwamoto (1993) concluded that freeze-thaw cycles do not significantly degrade the bond strength of FRP bars. Al-Dulaijan et al. (1996) found considerable reduction in bond strength of FRP bars immersed in an alkaline solution for 28 days.

Bond is important to maintain the integrity of a reinforced concrete structure. Excessive bond degradation could cause slippage in the development length region of FRP bars and the eventual collapse of a structural element. As such, it is necessary to carry out longer-term studies to evaluate the bond performance of GFRP bars to judge whether bond failure due to degradation could be an issue at later ages for FRP-reinforced concrete elements. The following expression given by ACI committee 440 (2001) to compute the development length of FRP bars has not been verified for long-term exposure of FRP bars embedded in concrete (ACI 2001):

$$l_{bf} = \frac{d_b f_{fu}}{2700} \quad (13)$$

where,

$l_{bf}$  = Development length of an FRP bar (inch),

$d_b$  = Bar diameter (inch),

$f_{fu}$  = Tensile strength of FRP bar considering reductions for service environment (psi).

To address the possible issue of long-term bond degradation, this project will investigate the degradation of bond strength of GFRP bars embedded in concrete beams exposed to high relative humidity for a period of 16 months.

## **ISSUE VII. CRACKING OF GFRP-REINFORCED CONCRETE ELEMENTS DUE TO THERMAL EXPANSION**

Another concern with FRP bars arises from the fact that the transverse coefficient of thermal expansion of the bars ranges from four to nine times that of concrete (Gentry and Husain 1999). Several researchers have performed theoretical and experimental studies. Aiello (1999) performed analytical and experimental studies, and provided an analytical solution to predict the maximum temperature rise that can be sustained by the concrete before cracking for a given ratio between the coefficient of thermal expansion (CTE) of the FRP bar and the CTE of the concrete, and for a given bar diameter and

concrete cover. Although the author did not specify the reference temperature with respect to which the temperature rise should be measured, the model predicts that the minimum allowable concrete cover increases as the ratio of the CTE of the FRP bar to the CTE of the concrete increases. The experimental study was limited to 0.375-inch diameter aramid FRP bars with concrete covers varying from 0.375 inch to 0.89-inch and the tests were carried out in specimens 3.94 inches deep by 5.91 inches wide by 39.4 inches long. The author did not indicate the setting temperature of the concrete specimens built and did not indicate the reference temperature against which a temperature rise was measured. The analytical predictions showed good agreement with the experimental results in predicting the temperature increase required for cracking of the concrete to occur for values of concrete cover to diameter ratios of 1.0, 1.19, and 1.25. However, for larger values of the cover to diameter ratios, such as 1.67, 2.0, and 2.27, the agreement was poor. Another limitation of the research is that the authors used aramid FRP bars only. Aramid FRP bars are polymeric fibers and, thus, have a larger coefficient of thermal expansion in the transverse direction than glass fibers.

Gentry and Husain (1999) developed an analytical solution for a cylindrical bar confined by a cylinder of concrete. The solution provided by Gentry and Husain (1999) predicts that the concrete surrounding the bar will crack for 0.5-inch and 0.75-inch diameter bars for a temperature rise of 72 °F regardless of concrete cover. An obvious limitation of the model developed by the researchers arises from the fact that it predicts the concrete to crack for a given temperature and for any concrete cover size. Additionally, for ease of computation, the researchers utilized a model consisting of an FRP bar placed concentrically in a concrete cylinder. The boundary conditions in typical reinforced concrete structures differ significantly from those assumed.

Rahman et al. (1995) proposed an analytical solution to compute the stresses in a cylinder of concrete with an FRP bar in its center. The researchers analyzed the thermal behavior of carbon and carbon-glass FRP bars embedded in a concrete cylinder. The

authors assumed square bars to be cylindrical. The model predicted the concrete cylinder surrounding the FRP bars with a compressive strength of 5075 psi to crack for a 0.31-inch diameter bar and a concrete cover of 0.75 inch for a temperature increase of 54 °F. The reference temperature considered by the authors was 68 °F. A limitation of the model considered by the researchers is the assumption that a concrete cylinder would concentrically enclose the FRP bar. This boundary condition differs considerably from the boundary conditions encountered in real structural elements. The authors did not verify their theoretical predictions with experiments.

Due to the lack of realistic models, engineers designing GFRP-reinforced concrete structures are still not sure of temperature limits that result in cracking caused by the large transverse coefficient of thermal expansion of these bars ([Gisiner and Bradberry 2003](#)). This project will provide more realistic test data by studying the behavior of concrete slabs under high temperature changes for a typical bridge deck and common concrete covers. The test specimens for this project are 8 inch deep by 12 inch wide by 60 inch long concrete bridge deck sections reinforced with 0.75-inch diameter bars with covers of 1, 2, and 3 inches. The tests carried out in this project will provide a lower-bound value for safe concrete covers to be used in concrete structures reinforced with 0.75-inch diameter or smaller GFRP bars.



### **III. MATERIALS, EXPERIMENTAL PROGRAM, AND TEST PROCEDURES**

As indicated in [Section II](#), several experiments are required to address the many issues associated with using FRP bars in concrete. This section will describe the materials used in the experiments. The experimental program used to evaluate the characteristics of the materials, including tensile properties, moisture absorption properties, direct shear strength properties, creep properties, cracking behavior of GFRP-reinforced concrete slabs, response of GFRP-reinforced concrete beams to cyclic loading, bond properties, and thermal expansion of GFRP-reinforced concrete slabs will be described in this section as well. Finally, this section will describe the test procedures followed to perform all of the necessary tests.

#### **MATERIALS**

The main materials used in this research were GFRP bars and concrete.

##### **GFRP Reinforcing Bars**

GFRP bars with diameters of 0.5 inch, 0.625 inch, and 0.75 inch provided by three different manufacturers were used in the experiments. The bars contained approximately 70 percent unidirectional glass fibers by volume and 30 percent resin. Three different bar types, representing three manufacturers, were evaluated. The bars are identified as bar P, V1, and V2, and were manufactured by Marshall Industries, Hughes Brothers, and Pultrall, respectively.

As indicated by Schaefer ([2002](#)), bar type P is made with polyethylene terephthalate (PET) polyester matrix and E-glass fibers. The manufacturer did not report either the chemical composition of the bar nor the type of filler material used in the resin matrix. Bar type P has a noncircular cross section due to the impression of surface lugs.

The surface of bar type P was finished with lugs and had no sand coating. Figures 2 and 3 show the surface and cross section of each bar type (modified from Schaefer [2002]).

Bar type V1 contains E-glass fibers embedded in a vinyl ester resin (Schaefer 2002). Bar type V1 is made with external helical fiber wrapping with an average spacing of 1.04 inches. The surface of the bar is coated with fine sand. Figures 2 and 3 (modified from Schaefer [2002]) show the surface and cross section of this bar type.

Bar type V2 is composed of E-glass fibers embedded in a vinyl ester resin (Schaefer 2002). Bar type V2 has a circular cross section and is coated with coarse sand. Figures 2 and 3 (modified from Schaefer [2002]) show the surface and cross section of this bar type.

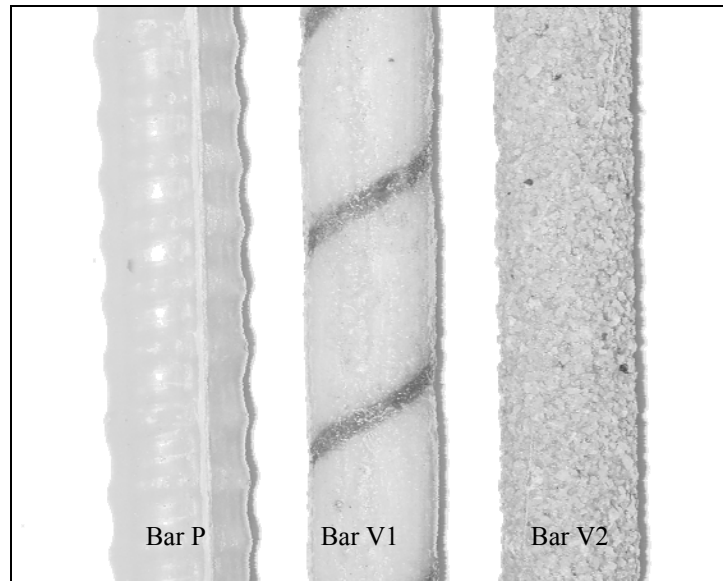


**Figure 2. Surface of GFRP Bar Types P1, V1, and V2 (Modified from Schaefer [2002]).**

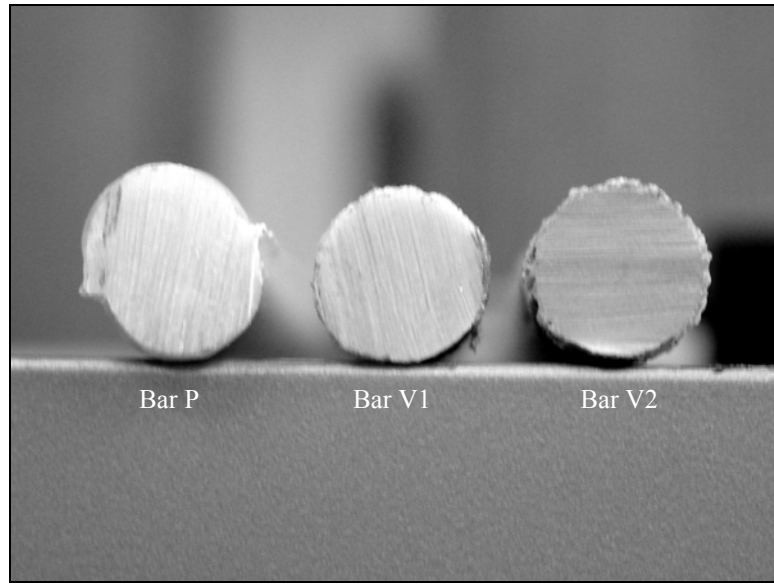


**Figure 3. Cross Section of GFRP Bar Types P, V1, and V2 (Modified from Schaefer [2002]).**

Schaefer (2002) conducted an examination of the bars under a scanning electron microscope (SEM). The SEM observations indicated that the thickness of the resin around the circumference of all three bar types was non-uniform. A layer of resin that protects the fibers is present on most of the surface of the bars and is more prevalent on one side. This occurs because the uncured resin made by pultrusion flows downward due to gravity before entering the heated die and setting. As such, portions of the bar where the glass fibers are exposed can be found. None of the bar types exhibited a uniform resin matrix cover over the glass fibers. Figure 4 (modified from Schaefer [2002]) illustrates how some glass fibers are exposed on the surface of a bar. Figure 5 (modified from Schaefer [2002]) shows the same type of bar where a rich resin layer covers the fibers.

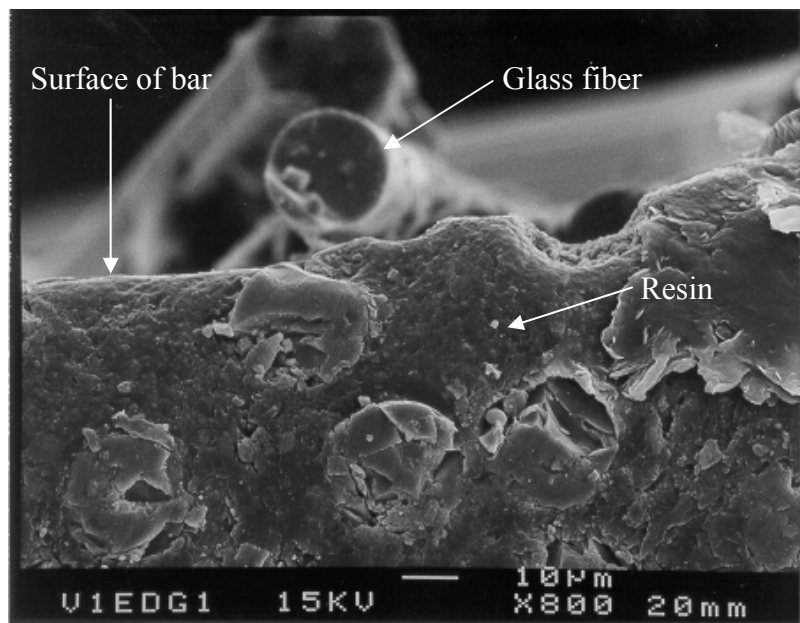


Figure 4. SEM Photograph of the Surface of a V1 Bar (Modified from Schaefer [2002]).

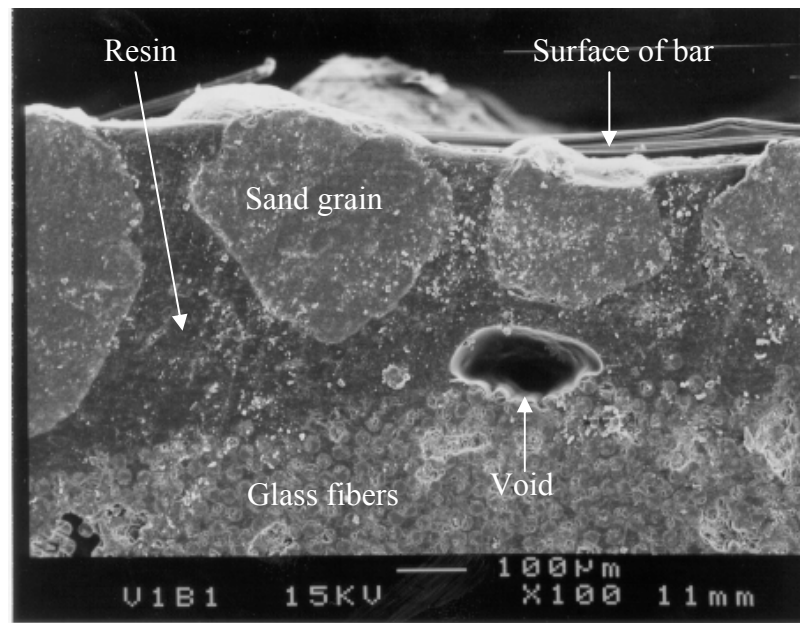


Figure 5. SEM Photograph of the Surface of a V1 Bar (Modified from Schaefer [2002]).

It is necessary to determine the area of the bars to compute engineering stresses in the reinforcement. Since the surface of the bars are irregular, the cross-sectional area of the bars was measured by immersing the samples in water. Water was placed in a graduated measuring cylinder; then the FRP bar was introduced in the cylinder, and the displaced volume was measured. To obtain the average cross-sectional area, the volume was divided by the measured bar length. The computed area and diameter of the bars are indicated in [Table 1](#).

**Table 1. Measured Area and Diameter of Bars.**

Bar type	Nominal diameter (in.)	Bar	Avg. area (in. <sup>2</sup> )	Avg. diameter (in.)
P	0.750	1	0.44	0.751
		2		
	0.625	1	0.34	0.661
		2		
	0.500	1	0.20	0.508
		2		
V1	0.750	1	0.43	0.743
		2		
	0.625	1	0.33	0.651
		2		
	0.500	1	0.20	0.503
		2		
V2	0.750	1	0.47	0.775
		2		
	0.625	1	0.34	0.660
		2		
	0.500	1	0.21	0.520
		2		

## Concrete

The specimens used in the different tests were made with a TxDOT class “S” concrete. The design 28-day compressive strength was 4000 psi, and the target

water/cement ratio was 0.35. The design mix contained the following proportions per cubic yard:

- 1895 lb. of limestone with maximum size of 1 inch;
- 1180 lb. of sand, 488 lb. of TxDOT type-1-3 aggregate;
- 116 lb. of Type C fly ash, 210 lb. of water;
- 4 fl. oz. of air entraining (type AE90);
- 24 fl. oz. of superplasticizer; and
- 603 lb. of cement.

The target concrete slump was 5 inches. The compressive strength of the concrete cylinders was measured at 7 days, 28 days, 56 days, and on test dates following ASTM C 39-96 (1998). The specimens were cast on five different dates. The results of the concrete compressive strengths at 7, 28, and 56 days are shown in [Figure 6](#) and summarized in [Table 2](#).

### Materials Used in the Cracking of Concrete Slabs Test

GFRP bars, 0.75 and 0.625 inch in diameter, were used to reinforce the slabs. Concrete from casts 1, 3, and 4 was used to make the slabs. The compressive strength of the concrete cylinders corresponding to the day of the test is indicated in [Table 3](#).

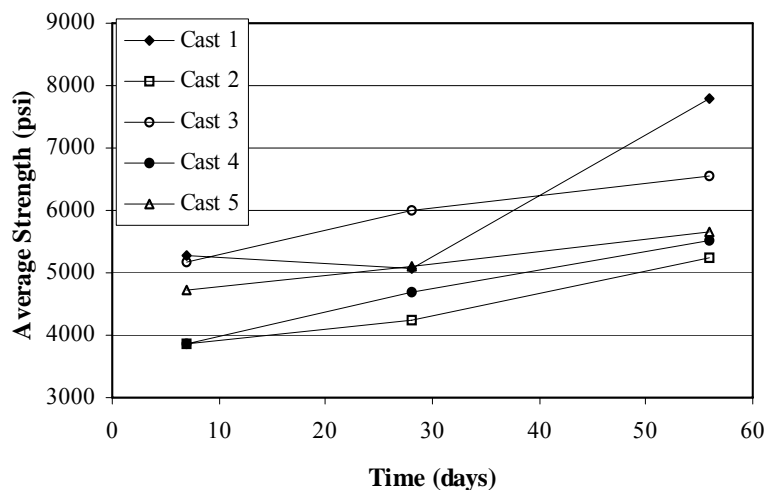


**Figure 6. Average Concrete Compressive Strengths at 7, 28, and 56 Days.**

**Table 2. Concrete Compressive Strengths.**

Cylinder number	Compressive strength cast 1, slump 5.5 in.		
	7 days (psi)	28 days (psi)	56 days (psi)
1	5728	5505	7383
2	4757	5807	8019
3	5322	3850	7940
Average	5269	5054	7780
Cylinder number	Compressive strength cast 2, slump 4.5 in.		
	7 days (psi)	28 days (psi)	56 days (psi)
1	3397	5569	5235
2	4344	2912	5171
3	3882	4288	5322
Average	3874	4256	5243
Cylinder number	Compressive strength cast 3, slump 5 in.		
	7 days (psi)	28 days (psi)	56 days (psi)
1	5871	6698	7208
2	5927	5418	7669
3	3763	5855	4789
Average	5187	5990	6555
Cylinder number	Compressive strength cast 4, slump 5.5 in.		
	7 days (psi)	28 days (psi)	56 days (psi)
1	3771	4479	5187
2	4097	5147	6197
3	3683	4439	5203
Average	3850	4688	5529
Cylinder number	Compressive strength cast 5, slump 5 in.		
	7 days (psi)	28 days (psi)	56 days (psi)
1	4360	5107	5394
2	4924	5012	5975
3	4940	5155	5632
Average	4741	5091	5667

**Table 3. Concrete Compressive Strengths on Test Date for Cracking Slabs.**

Cylinder number	Compressive strength cast 1, slump 5.5 in.
	274 days (psi)
1	9208
2	7086
3	7796
4	8090
5	8476
6	7663
Average	8053
Cylinder number	Compressive strength cast 3, slump 5 in.
	270 days (psi)
1	7438
2	9098
3	8984
4	7937
5	8258
6	8547
Average	8377
Cylinder number	Compressive strength cast 4, slump 5.5 in.
	249 days (psi)
1	5415
2	6749
3	6129
Average	6098

### Materials Used in the Cyclic Loading of Concrete Beams Test

GFRP bars, 0.5 and 0.75 inch in diameter, were used to reinforce the beam specimens. The beams were made with the TxDOT class "S" concrete. Concrete from casts 2, 3, 4, and 5 was used to make the beams. The compressive strength of the concrete cylinders corresponding to the day of the test is shown in [Table 4](#).

**Table 4. Concrete Compressive Strengths on Test Date for Beams.**

Cylinder number	Compressive strength cast 2, slump 4.5 in.
	365 days (psi)
1	6254
2	6202
3	6240
Average	6232
Cylinder number	Compressive strength cast 3, slump 5 in.
	270 days (psi)
1	8572
2	8228
3	8840
Average	8546
Cylinder number	Compressive strength cast 4, slump 5.5 in.
	319 days (psi)
1	6186
2	6356
3	6715
Average	6419
Cylinder number	Compressive strength cast 5, slump 5 in.
	292 days (psi)
1	5810
2	6790
3	6643
Average	6414

### Materials Used in the Bond Test

GFRP bars 0.5 and 0.625 inch in diameter were embedded in the concrete beams. The bond specimens were made with the TxDOT class "S" concrete. Concrete from casts 2 and 5 was used to make the bond specimens. The compressive strength of the concrete cylinders corresponding to the day of the test is the same as that indicated in [Table 4](#) for casts 2 and 5.

## **Materials Used in the Thermal Expansion of Concrete Slabs Test**

A thermal expansion test was performed on GFRP bars embedded in concrete slabs. The bars used had a diameter of 0.75 inch, and the slabs were made with the TxDOT class “S” concrete. Concrete from cast 1 was used to make the thermal expansion slabs. The compressive and tensile strength of the concrete was evaluated on the test date, following ASTM C 39-96 (1998) and ASTM C 496-96 (1998), respectively. The results of the concrete compressive and tensile strengths evaluated on the day of the test are shown in [Table 5](#).

**Table 5. Concrete Compressive and Tensile Strengths.**

Cylinder number	Compressive strength cast 1, slump 5.5 in.	Tensile strength
	372 days (psi)	372 days (psi)
1	8122	659
2	8267	410
3	7687	733
Average	8025	601

## **EXPERIMENTAL PROGRAM**

The objectives of the experimental program are to address each of the issues described in [Section II](#). Several tests need to be conducted to address these issues. The tests to be conducted are the following:

- [tension test](#) of GFRP bars,
- [moisture absorption test](#) of GFRP bars,
- [direct shear strength](#) of GFRP bars,
- [creep test](#) of GFRP bars,
- [cracking](#) of GFRP-reinforced concrete slabs,
- [cyclic loading](#) of GFRP-reinforced concrete beams,
- [bond](#) between GFRP bars and concrete, and
- [thermal expansion](#) of GFRP-reinforced concrete slabs.

In this section, the objective of each test will be stated, the test will be discussed, the equipment and instrumentation required for the test will be described, and the procedures followed to fabricate, condition, and test the specimens will be described.

## **Tension Test**

### *Test Objective*

Tension tests on environmentally conditioned GFRP bars simulating exposure to concrete environments are necessary to evaluate the change of tensile strength and modulus of elasticity of the bars with exposure time. The results of the tests are necessary to predict, using degradation models, the residual tensile strength of GFRP bars over time. In this investigation, the influence of temperature, solution pH, moisture, bar composition, and time on the change of tensile strength and Young's modulus of GFRP bars over time will be evaluated.

Since GFRP bars are relatively new materials in the civil engineering market, the degradation of their tensile properties is a concern in the design community, as evidenced in the high strength reduction factors suggested by ACI 440 design guidelines ([ACI 2001](#)). Glass fibers corrode by either etching or leaching ([Adams 1984](#)). Etching is characterized by alkaline attack and leaching by acid attack ([Adams 1984](#)). As indicated by Paul ([1982](#)), the pH and the nature of the attacking solution are the factors that govern the chemical durability of glasses. All silicate glasses become especially susceptible to decomposition when in contact with a solution with pH values higher than approximately 9 or 10 ([Paul 1982](#)). Vitreous silica will be attacked at a pH of 10 or higher. Thus, the glass fibers used in GFRP bars may be susceptible to corrosion when the high pH concrete pore solution diffuses through the GFRP bar. This condition can result in tensile strength degradation of the GFRP bars. However, since the rate of glass degradation is not known, simulated exposure tests are required to estimate the tensile strength degradation of GFRP bars used to reinforce concrete elements.

### *Test Description*

GFRP bar specimens, 41 inches long, were cut from 0.625 inch diameter, 20 ft long, bars for all three bar types. Five bars from each manufacturer were tested as received at room temperature. Sets of five bars from each manufacturer were placed into two exposure conditions: distilled water and a solution with a pH of 12. Each set of specimens was exposed to three different temperatures for periods of six months and one year as indicated in [Table 6](#). Because temperature can influence the migration of ions, elements, or compounds into a material, the samples were tested at different temperatures. After exposure, the bars were allowed to air dry for two days and then tested at room temperature. A total of 65 bars from each manufacturer were tested. Schaefer ([2002](#)) conducted the exposure and testing of all of the specimens.

**Table 6. Number of Tension Test Specimens.**

Bar type	No exposure (control specimens)	Temperature	26 weeks		50 weeks	
			pH			
			7	12	7	12
P	5	Low (52 °F)	5	5	5	5
		Room (70 °F)	5	5	5	5
		High (95 °F)	5	5	5	5
V1	5	Low (52 °F)	5	5	5	5
		Room (70 °F)	5	5	5	5
		High (95 °F)	5	5	5	5
V2	5	Low (52 °F)	5	5	5	5
		Room (70 °F)	5	5	5	5
		High (95 °F)	5	5	5	5

Plastic containers were utilized to expose the bars in the solutions. Only the middle 16-inch portion of the bar was exposed to the solution. Only a portion of the bar was exposed to the solution to avoid a potential loss of bond between the bars and the

pipes grouted on the bar ends during testing. A solution with a pH of approximately 12 was used in the containers to simulate the alkalinity of the concrete pore solution. The high pH was obtained by adding 0.055 lb. of calcium hydroxide to 3.96 gallons of distilled water. The pH of the solution was monitored every two weeks and adjusted as needed to keep it close to the target pH value of 12. [Figure 7](#) shows the exposure setup.

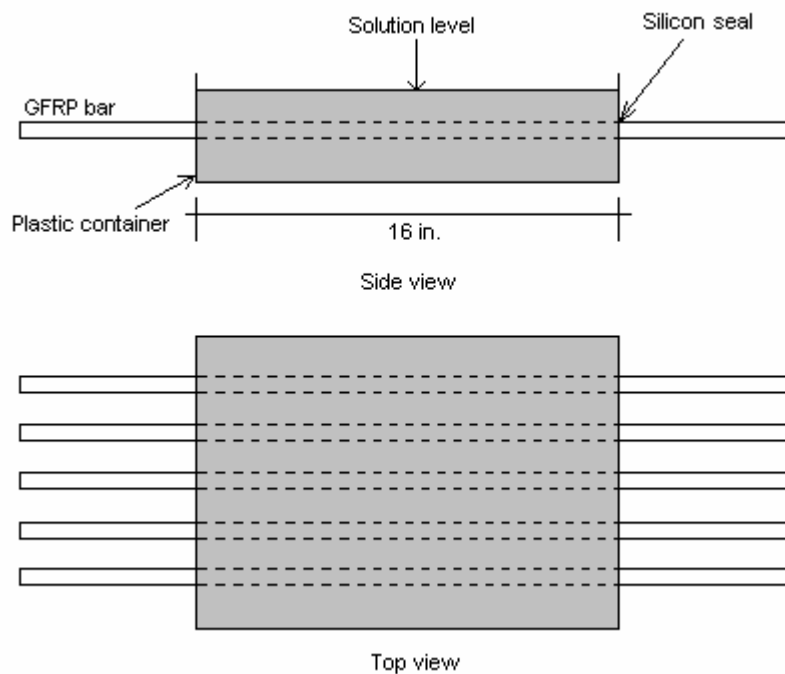


**Figure 7. Setup for Exposure of GFRP Bars.**

The average temperature of the specimens stored at room temperature was 70 °F. The average temperatures in the hot and cold rooms were 95 °F and 51 °F, respectively. Daily readings of the temperature were recorded.

### *Test Equipment and Instrumentation*

A 110 kip MTS load frame loaded the specimens. The frame components included an MTS 410 function generator, an MTS 442 controller, and an MTS 413 master control panel. The load accuracy of the load cell was 0.05 kips. The 1994 version of the Labtech NotebookPro® software was used to collect the data.

An MTS extensometer was used to measure the strain on the bar during the tension test. The extensometer had a gage length of 1 inch, a range of  $\pm 0.15$  inch, and an accuracy of 0.125 percent.

In addition to the extensometer, CEA-06-250UW-350 strain gages from Micro-Measurements® were attached to the bar sides as illustrated in [Figure 8](#), to form a quarter bridge and measure the strain in the bars.

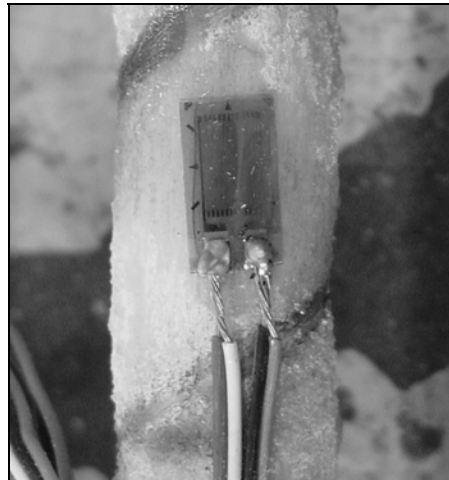


**Figure 8. Strain Gage Attached to Surface of FRP Bar.**

### *Notched Bar Testing*

Notches in three bars from each manufacturer simulated possible damage during construction and were tested at room temperature. Another three bars from each

manufacturer were notched and exposed to a solution with a pH of 12 for six months at room temperature before testing. The same containers and calcium hydroxide solution as used in the tension test were used for the notched bar tests.

#### *Test Procedure*

The bar ends were grouted in 1.5-inch diameter steel pipe to prevent crushing of the bar during testing.

The specimen preparation, as described by Schaefer ([2002](#)), is as follows:

- The bars and steel pipes were cut to length using a 12 inch disk cutoff saw.
- After exposure, specimens were removed from the exposure environment and dried in air at 70 °F for 24 hours.
- To cap the bars, plastic cylinder molds 2 inches by 4 inches were utilized. The molds were drilled at the center of the bottom to align the FRP bar in the steel pipe.
- The capped bar and pipe were then placed in an alignment rack, cast with grout, and allowed to cure for 24 hours before testing.
- The bars were marked at the center to identify the location for the strain gage installation. The protective cover of the bar was removed with a Dremmel® tool, and the surface was sanded sequentially with 220 and 320 sand paper. Fiber damage was avoided during sanding. The surface of the bar was then cleaned with ethyl alcohol.
- The strain gage was then glued to the bar following the manufacturer's specifications using M-bond AE-10 adhesive. Once the glue had cured, wires were soldered to the strain gage tabs in order to make a quarter bridge installation.
- The knife-edges of the extensometer were pressed against the sides of the bar with a rubber band. Then the edges of the extensometer were glued to the side of the bar with cyanoacrylate adhesive.

A schematic of the dimensions of the test specimen is illustrated in [Figure 9](#).



**Figure 9. Test Specimen Layout for Tensile Tests.**

As described by Schaefer (2002), the specimen testing was conducted as follows:

- The bar ends were mounted on grips specifically designed for the test.
- A preload of 500 lb. was applied to the bar, the grips were tightened, and the load was then released.
- The extensometer was then glued on the bar and the pin removed.
- The data acquisition was started, and then loading of the bar began. Once the bar reached the ultimate load, the machine was stopped and then the data acquisition was stopped.
- The bars were loaded in displacement-controlled mode up to failure. The loading rate was 0.11 inch/min.

#### *Test Procedure for Notched Bars*

Rotating a pipe cutter around the FRP bar created a notch on the bars. In order to obtain uniform notch depths, a fixed number of rotations were applied with the pipe cutter. Five trial specimens were notched, and the notches were measured to determine the average notch depth. The average notch depth was 0.057 inch for bar type P, 0.055 inch for bar type V1, and 0.055 inch for bar type V2. All tension tests were conducted on 0.625-inch nominal diameter bars. The reduced bar diameters were 0.547 inch for bar type P, 0.541 inch for bar type V1, and 0.55 inch for bar type V2. To measure the strain, an MTS extensometer was mounted on the bar across the notch.

### **Moisture Absorption Test**

#### *Test Objective*

GFRP bars are composed of unidirectional glass fibers embedded in a polymer matrix. It is known that polymers absorb moisture and the polymer matrix softens as a result of this moisture uptake. GFRP reinforcing bars are typically exposed to a moist

concrete environment, which usually exhibits a degree of saturation above 72 percent (Pyé 1998). Thus, it is necessary to investigate whether moisture absorption affects the tensile strength and/or modulus of elasticity of GFRP bars. In order to do this, a series of moisture absorption tests were performed. The results of the moisture absorption tests were compared with results from tension tests of GFRP bars to determine how moisture absorption affects the tensile strength or modulus of elasticity of the bars over time.

As mentioned in the discussion of the tension test, the corrosion of glass fibers depends on the pH and the nature of the attacking exposure solution surrounding the GFRP bars. However, the attacking solution needs to be transported through the matrix of the GFRP bars before reaching the glass fibers. Thus, it is necessary to obtain the diffusion coefficient of a simulated concrete pore solution diffusing into a GFRP bar in order to make estimates of the tensile strength degradation of GFRP bars embedded in concrete.

#### *Test Description*

Some manufacturers require protecting the cut ends of GFRP bars while others have no requirements for protecting the ends. There is no consensus in the field as to whether end capping is needed to prevent moisture uptake at the bar ends. As such, mass gain tests on capped and uncapped specimens were conducted to determine how much solution uptake could be expected. The test with capped ends may better reflect the transport mechanisms that take place between the concrete and FRP bars since, in the case of a specimen with capped ends, the transport of solution into the bar from the ends would not be significant. This would also be the case in a GFRP-reinforced concrete structural element where the moisture absorption of the midspan section is not affected by any moisture uptake that takes place at the ends of the member.

*Moisture Absorption of Bars with Capped Ends.*

Tests were performed on three bar types with 0.50-, 0.625-, and 0.75-inch bar diameters. For each bar type, one set of bars was exposed to distilled water, and another set was exposed to a simulated concrete pore solution made with 1.98 gallons of distilled water and 0.028 lb. of calcium hydroxide. Prior to exposure, all bars were weighed. Five bars of each diameter were then exposed to both solutions for a period of 97 weeks at an average temperature of 70 °F. Bars were then removed and reweighed, and data were recorded to evaluate mass gain. Since the moisture absorption of capped end bars was considered more representative of the actual absorption phenomenon occurring in GFRP bars used in concrete structures, the diffusion coefficient of the simulated concrete pore solution that diffused into the GFRP bar was obtained for this test only. The results section describes how the diffusion coefficient was determined. The weight gain of the specimens used in this project was measured periodically until the bars were near saturation.

*Moisture Absorption of Bars with Uncapped Ends.*

Tests were performed on three bar types with three bar diameters, namely: 0.50, 0.625, and 0.75 inch for each bar type. Four solutions were used to simulate different environments. Solution 1 was distilled water. Solution 2 was a high pH solution made with 3.96 gallons of distilled water and 0.055 lb. of calcium hydroxide to simulate the concrete environment. Solution 3 was made with distilled water and 3.5 percent of sodium chloride content. Solution 4 was a high pH solution made with 3.96 gallons of distilled water, 0.055 lb. of calcium hydroxide, and with 3.5 percent sodium chloride content. Prior to exposure, all bars were weighed. Three bars of each diameter were exposed in each solution at an average temperature of 70 °F. Bars of type P were exposed for 48 weeks, and bars of type V1 and V2 were exposed for 68 weeks. These exposure times resulted from the fact that bars V1 and V2 were received from the manufacturers 20 weeks before the type P bars. Bars were then removed and reweighed, and data were recorded to evaluate weight gain.

### *Test Equipment and Instrumentation*

The bars were weighed before and after exposure with an electronic balance with a precision of  $2.20 \times 10^{-6}$  lb.

### *Test Procedure*

The bars with capped ends were cut to a length of 6 inches, tagged and identified, and protected on the ends with two layers of a sprayed polymer before placing them in the solutions indicated in the experimental program section. The bars were weighed at 0.7, 2.4, 15.9, 68, and 88.7 weeks. Before weighing the bars, they were dried to a saturated surface dry condition. The bars air-dried for approximately five minutes at 69.8 °F before being weighed. In the case of the uncapped bars, type P bars were weighed at 48 weeks and bar types V1 and V2 at 68 weeks.

## **Direct Shear Strength Test**

### *Test Objective*

The direct shear strength of GFRP bars may be necessary to design some structural elements, such as a concrete bridge rail that is connected to a concrete bridge deck with GFRP bars. The failure of GFRP bars by direct shear strength has also been the cause of failure of GFRP-reinforced concrete structural elements ([Michaluk et al. 1998](#)). As indicated in [Section II](#), limited information is available on the direct shear strength of GFRP bars and on the degradation of the direct shear strength of exposed GFRP bars. Thus, GFRP bars were tested at a constant load rate in direct shear. The degradation over time of the direct shear strength and shear modulus of elasticity of GFRP bars was also determined by testing specimens previously exposed to different solutions in uncapped ends conditions. Studies on unidirectional Kevlar®-epoxy and carbon-epoxy composites, conducted by Kaddour et al. ([1995](#)), showed that FRP laminates have a higher shear strength and shear modulus of elasticity at high strain rates (80/sec) than at low strain rates (5/sec). Since a similar behavior can be expected from glass FRP unidirectional composites, this research will focus on determining the shear strength and shear modulus

of elasticity at low strain rates (0.062/sec). Designing with the quasi-static shear strength obtained in this project will be conservative, since higher shear strengths should be developed by GFRP bars when subjected to impact from a vehicle on a bridge barrier or for dowel pavement bars. As such, high strain rate shear strength tests were not conducted as part of this project. The results of these tests will provide design engineers with values of the direct shear strength for GFRP bars used in the design of connections between structural elements where the bars are subjected to direct shear loads.

According to the American Concrete Pavement Association (ACPA), the longevity of concrete pavements is greatly affected by joints with poor performance ([ACPA 2003](#)). Typical distress, such as faulting, pumping, and corner breaks, develop partly as a result of poor load transfer efficiency. When joints deflect significantly under loads, all of the problems mentioned above are aggravated. An isolation joint, which has a maximum joint opening of 1 inch, is a typical joint type that can undergo serious shear displacements. Isolation joints are normally used where the pavement connects to a bridge.

#### *Test Description*

The 6-inch long specimens with uncapped ends exposed to the four different solutions in the moisture absorption gain test to 48 and 68 weeks were tested in a direct shear test apparatus. Bars with a 0.625-inch diameter were investigated. The shear span was 0.0197 inch.

#### *Test Equipment and Instrumentation*

A direct shear apparatus as shown in [Figure 10](#) was used to test the 0.625-inch diameter GFRP bars. The test apparatus was fabricated following the Japanese recommendation for design and construction of concrete structures using continuous fiber reinforcing materials ([Japanese Society of Civil Engineers1997](#)) and modified so that bars could be tested with variable shear gaps. A metallic gage was used to measure the

0.0197-inch gap between the loading block and the support block. A 110-kip MTS machine was used to load the specimens, and the 1994 version of the Labtech® Notebook computer program was used to collect the data. The shear displacement was measured using the frame crosshead displacement.

### *Test Procedure*

After exposure to the solutions, bars were placed in plastic bags to prevent drying and tested within two hours at a temperature of 74 °F. The specimen was placed in the direct shear test apparatus, and a 200 lb. preload was applied. The gap between the sliding block and the bearing blocks of the shear test apparatus was confirmed with a metallic gage. The specimen was then loaded in displacement-controlled mode with a loading rate of 0.11 inch/min. The applied strain rate was 0.062/sec. The shear deformation was obtained from the measured crosshead displacement. During the test, the bars were loaded until a reduction in the applied load was observed.

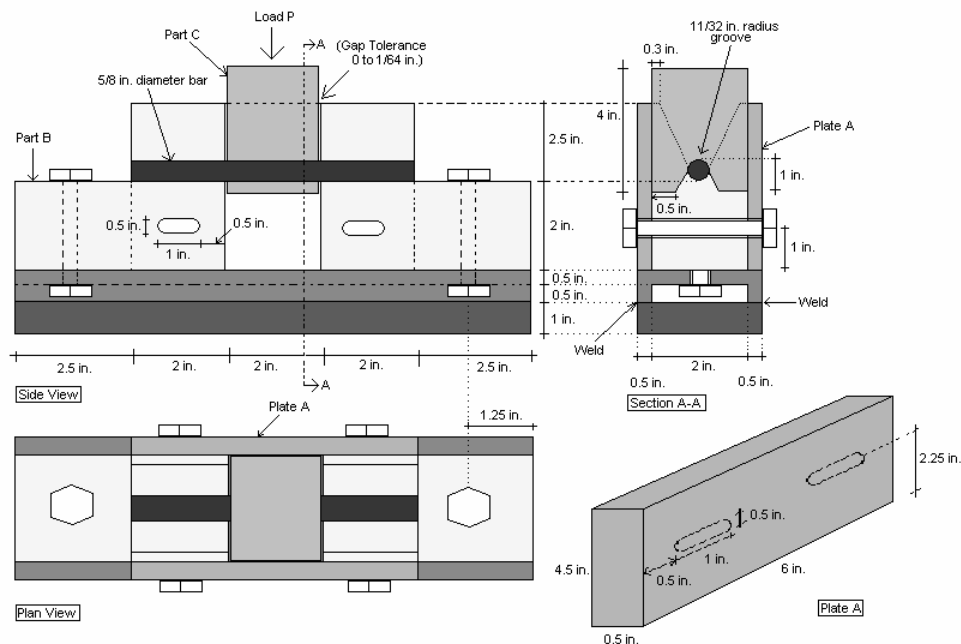


**Figure 10. Direct Shear Strength Test Apparatus.**

## **Creep Test**

### *Test Objective*

Composite materials creep under constant load and can fracture due to creep-rupture under sustained high loads. For a GFRP-reinforced concrete element, this could situation lead to catastrophic failure. Even if a GFRP-reinforced concrete element does not fail by creep rupture, creep of GFRP bars increases the long-term deflections of GFRP-reinforced concrete elements as noted in [Section II](#). As such, creep tests were conducted on GFRP bars to investigate whether creep rupture would occur at service loads for a typical bridge deck overhang and to obtain the creep properties of GFRP bars. Bar specimens from three manufacturers were instrumented and loaded under controlled temperature and relative humidity conditions, and after a six-month exposure period, the performance of these bars was determined.

### *Test Description*

Six steel creep frames were fabricated to apply a service load equivalent of approximately 23 percent of the design tensile strength of the GFRP bars for a period of six months. The specimens were loaded to 23 percent of the design tensile strength of the bars because the design of GFRP-reinforced concrete elements is typically governed by serviceability requirements, and the GFRP bars will be subjected to stresses considerably smaller than the design tensile strength of the bar. The design example shown at the end of [Section V](#) shows that a typical sustained stress experienced by GFRP bars is approximately 9.4 percent of the design tensile strength of the bar, and the service load stress is approximately 23 percent of the design tensile strength of the bar. These stress levels are larger than those expected to occur in service. Creep of the GFRP bars was monitored continually by recording the strain in the bars with a data acquisition system.

### *Test Equipment and Instrumentation*

Steel creep frames were used to load the GFRP bars as indicated in [Figure 11](#). The specimens were wired to a computer with a data acquisition system controlled with

LabView® software. Strain gages type CEA-06-250UW-350 made by Micro-Measurements® with a 350-ohm resistance and a gage factor of 2.09 were used to measure the strain in the bars. Coupled with the strain gages, 350-ohm precision resistors from Micro-Measurements® with a precision of 0.01 percent and wide bandwidth strain gage signal conditioners (model 1B31, made by Analog Devices) were used to monitor the strain in the bars. An AC1222 mounting card and an ATMIO 16-bit data acquisition card were used to acquire the data.

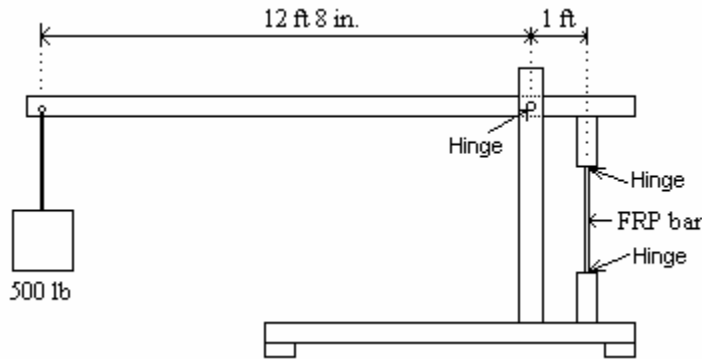


**Figure 11. Elevation View of Creep Frame.**

#### *Test Procedure*

The creep frames were located in a temperature-controlled room. The average temperature was 88 °F, and the average relative humidity was 67 percent. Two strain gages were attached on opposite sides at the middle portion of the bar using M-bond AE-10 adhesive and aligned in the longitudinal direction. The gages were connected with the 350-ohm precision resistors to form a half bridge as shown in [Figure 12](#). This setup was designed to cancel any strain due to bending of the bar. The half bridge was connected to a wide bandwidth strain gage signal conditioner model 1B31 made by Analog Devices, which was mounted on an AC1222 mounting card. The output from the signal conditioning cards was connected to a multi-channel connector box connected to the

computer port. A 1994 Version of LabView® software and an ATMIO 16-bit data acquisition card was used to acquire the data. The entire system was calibrated by mounting the strain gages and precision resistors on a steel bar. The strain was verified using an MTS extensometer model 632.11B-20, and the bar was loaded with a 110-kip MTS machine. The system was then recalibrated using the GFRP specimens before placing them in the creep frames. The GFRP bars were placed in the creep frames located in the environmentally controlled room, and the data acquisition was run to collect the data. A rocker connector was placed in the connection between the creep frame and the bar end to prevent bending moments from being transferred to the bars. Creep data were recorded every three hours for a period of six months.

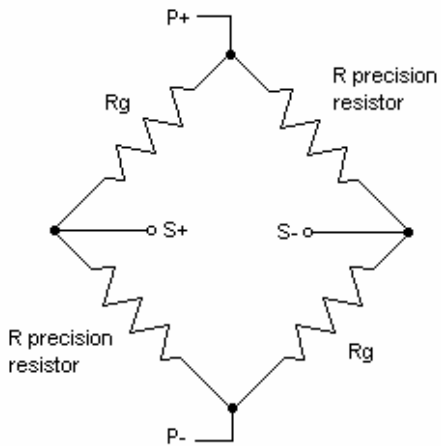


**Figure 12. Half Bridge Used in Strain Gage Setup for Creep Test.**

## Cracking of Concrete Slabs Test

### *Test Objective*

Because the modulus of elasticity of FRP bars is only approximately one-fifth that of steel, it is expected that GFRP-reinforced concrete members with a given geometry will deform more than steel-reinforced concrete members, with the same area of

reinforcement and geometry, after cracking. Crack widths in the GFRP-reinforced concrete members are expected to be larger than in their steel-reinforced concrete counterparts. This makes maximum crack width one of the governing design criteria in GFRP-reinforced concrete elements. This project provides extensive testing results and evaluates the appropriateness of existing equations to predict the maximum crack width of GFRP-reinforced concrete elements.

#### *Test Description*

In order to investigate the effects of concrete cover, bar diameter, and bar type in the cracking of typical bridge decks built in Texas, a series of slabs having the same reinforcement type, diameter, and spacing as those of the Sierrita de la Cruz Creek bridge deck built in Amarillo, Texas, were fabricated and tested. Thirty-six concrete slabs reinforced with GFRP bars were fabricated as indicated in [Table 7](#). For each cover and bar size reinforcement, two identical specimens were built for the three different bar types. The parameters investigated were bar diameter and concrete cover. [Figure 13](#) illustrates the reinforcement configuration for the slabs reinforced with 0.625-inch diameter GFRP bars, and [Figure 14](#) shows the configuration for the slabs with 0.75-inch diameter GFRP bars. All of the specimens are hybrid in the sense that 0.625-inch diameter epoxy-coated steel (ECS) bars were placed on the compression side of the slabs.

**Table 7. Cracking Test Parameters.**

Cover (in.)	Number of specimens (two identical slabs for each of three bar types)	Bar diameter (in.)	Bar spacing (in.)
1	6	0.625	4.13
	6	0.75	5.51
2	6	0.625	4.13
	6	0.75	5.51
3	6	0.625	4.13
	6	0.75	5.51

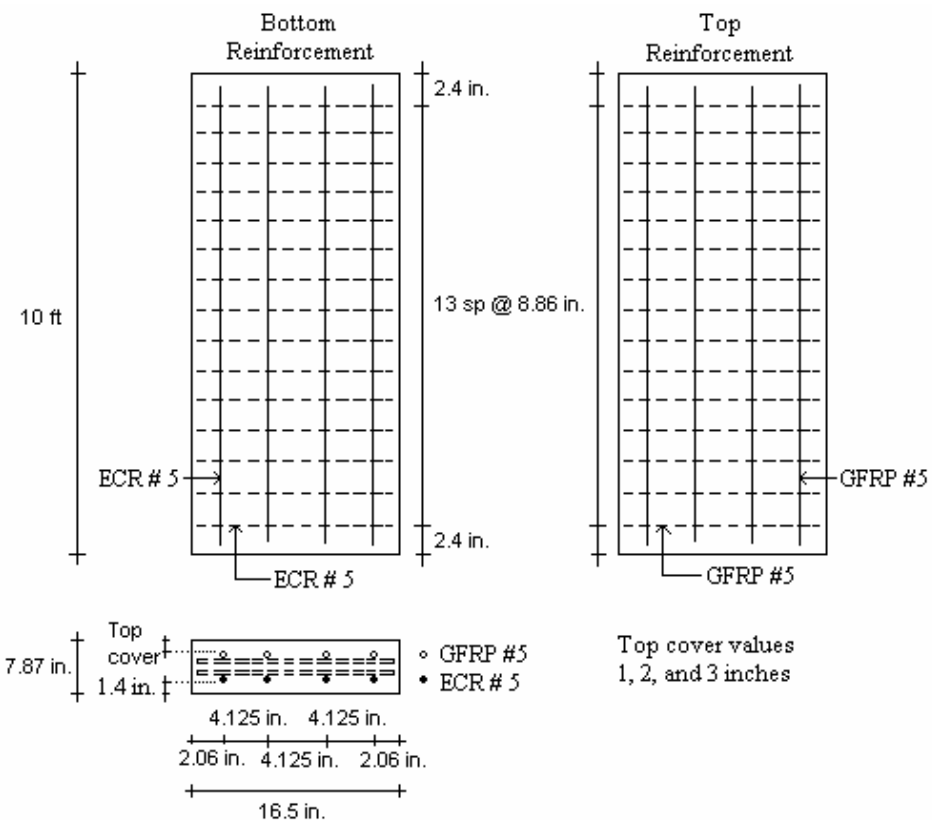


**Figure 13. Layout of Slabs with 0.625-inch Diameter Bars in Top Mat.**

The concrete used to make the slabs was TxDOT class “S,” with a 28-day design compressive strength of 4000 psi as described in the [materials section](#). The slabs were kept continuously wet using burlap for a period of 28 days. The slabs were tested approximately one year after being cast. The dimensions of the specimens were 120 inches long by 16.5 inches wide by 7.87 inches deep. [Figure 15](#) shows the test setup and indicates where the FRP reinforcement and the epoxy coated steel reinforcement are located.

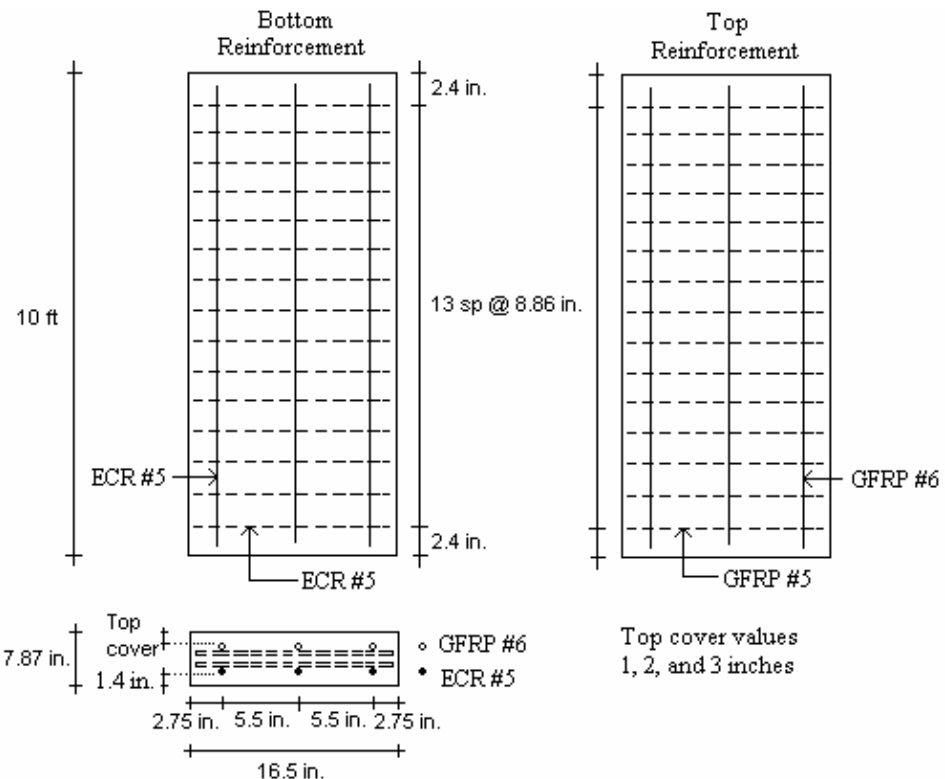


**Figure 14.** Layout of Slabs Reinforced with 0.75-inch Diameter Bars on Top Mat.

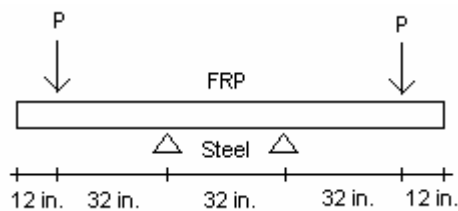


**Figure 15.** Slab Cracking Test Setup.

#### *Test Equipment and Instrumentation*

Two strain gages were installed, as indicated in the tension test, on the longitudinal GFRP bars at the middle section of each slab. The specimens were loaded with a 100-kip hydraulic actuator in four-point bending. The displacements of the slabs were measured by placing Linear Variable Differential Transformers (LVDTs) at the load

points and at midspan. A crack microscope was used to measure crack widths at several load levels.

#### *Test Procedure*

Each slab was placed on simple supports and loaded in four-point bending. The specimens were loaded statically per ASTM C 78-75 ([1975](#)) with a load rate between 125 and 175 psi/min. A mixture of plaster was made following the manufacturer's instructions and placed on top of the two flat steel plates where the slab rested. The plates were placed on top of the simple supports to reduce stress concentrations. The slab was then placed on top of the fresh plaster, and the plaster was allowed to set for 20 minutes. A 0.75-inch thick neoprene pad was placed between the slab and the top steel bearings to reduce stress concentrations. The time to failure at continuous loading was estimated to be approximately three minutes. Loading of the slabs was stopped between 8 to 10 times to measure crack widths, and thus, the actual test time was approximately one hour. The loading was applied in the displacement-controlled mode with a stroke rate of 0.5 inch/min. Crack widths were measured at several load levels with a crack microscope.

### **Cyclic Loading of Concrete Beams Test**

#### *Test Objective*

Bridge decks are subjected to repeated loading due to traffic. Thus, GFRP bars embedded in concrete bridge decks are subjected to repeated loading. Cyclic loading has been reported to increase deflections of FRP-reinforced concrete elements

([Iwamoto et al. 1993](#), [Benmokrane et al. 1999](#)). Thus, cyclic loading tests were conducted to simulate bridge loading and to document the behavior of GFRP-reinforced concrete sections under repeated loading.

#### *Test Description*

Beams were constructed to study the influence of varying bar diameters (0.5 and 0.75 inch) and covers of 1.5 and 2 inches on the response of GFRP-reinforced concrete

beams to repeated loading. Bars from three different manufacturers were evaluated. The beam dimensions were 84 inches long, 5.5 inches wide, and 7.87 inches deep. Twenty-seven beams were fabricated for this test. Twelve beams were tested at constant load rate. Fifteen beams were subjected to 2 million cycles of loading at simulated service load and then tested at constant load rate to failure. The beam loading setup is shown in [Figure 16](#). Eight of the specimens subjected to cyclic load were reinforced with 0.75- inch diameter bars, and seven of the specimens were reinforced with 0.5-inch diameter bars. The upper load magnitude was 4.1 kips, and the lower load magnitude was 200 lb. for the beams reinforced with 0.75-inch diameter bars. Thus, the load range was 3.9 kips. The upper load magnitude was 2.1 kips, and the lower load magnitude was 200 lb. for the beams reinforced with 0.5-inch diameter bars. Thus, the load range was 1.9 kips. Therefore, beams reinforced with 0.75-inch diameter bars were cyclically loaded with an upper load of approximately 25 percent of the ultimate load of the beams, and beams reinforced with 0.5-inch diameter bars were loaded to approximately 16 percent of the ultimate load of the beams. By loading the 15 beams subjected to cyclic loading to failure after being subjected to 2 million cycles of load, the residual load capacity of the beams could be determined.

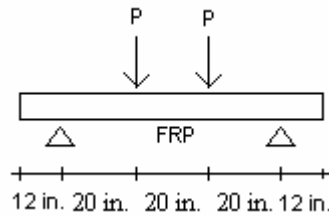


**Figure 16. Beam Loading Setup.**

#### *Test Equipment and Instrumentation*

The beams were instrumented with a strain gage attached, as indicated in the tension test, to the FRP bar at midspan. Beam displacements were measured with an LVDT placed at midspan. The 12 beams loaded at a constant displacement rate were

loaded with a 110-kip MTS machine. The beams subjected to cyclic loading were loaded with a 50-kip MTS machine. The beams that survived the cyclic loading test were tested at a constant load rate to failure with a 110-kip MTS machine. Strain, load, and displacement were recorded during testing.

#### *Test Procedure*

The beams were cast using TxDOT class “S” concrete with a 28-day design compressive strength of 4000 psi as described in the [materials section](#). The beams were then kept continuously wet using burlap for a period of 28 days. The beams were exposed outdoors and tested approximately one year after being cast. The beams were loaded with simple supports in four-point bending. The constant rate load was applied in the displacement-controlled mode. The static load rate was 0.5 inch/min. The frequency of application of the cyclic load was 10 Hertz.

### **Bond Test**

#### *Test Objective*

The bond strength between GFRP bars and concrete is difficult to characterize because it depends on many factors. These factors include concrete strength, surface finish of the bar, strength of the matrix of the bar, concrete cover, environmental effects, etc. Of particular concern are environmental effects. Al-Dulaijan et al. (1996) detected considerable reduction in the bond strength of pullout specimens (GFRP bars embedded in concrete) immersed in a saturated calcium hydroxide solution with a pH of 12.3 at 140 °F for 28 days. This reduction seems to be a result of degradation of the resin. Based on the findings of the previously mentioned study and the potential impact on performance of GFRP-reinforced concrete elements, a study investigating the reduction in bond strength of GFRP bars embedded in concrete was performed.

### *Test Description*

The influence of bar diameter, bond length, and exposure as indicated in [Table 8](#) was studied. The specimen dimensions are illustrated in [Figure 17](#). The ends of the GFRP bars were first cast in steel pipes. The bars were then placed in the molds and steel shear reinforcement was placed around the FRP bars. PVC pipes were placed at the ends of the bars to obtain the desired bond length as indicated in [Figure 17](#). The specimens were cast using TxDOT class “S” concrete with a design 28-day compressive strength of 4000 psi as described in the [materials section](#). The specimens were kept continuously wet using burlap for a period of 28 days. After curing, the specimens with 0.5-inch diameter bars were left outdoors for three months, and the specimens with 0.75- inch diameter bars were left outdoors for 1.5 months. After that outdoor exposure, nine specimens with two 0.5-inch diameter bars each and nine specimens with two 0.75-inch diameter bars each were placed in a room with temperature and humidity controls for a period of 16 months. The room had an average temperature of 95 °F and a relative humidity of 88 percent. Another set of 20 bond specimens with two 0.5-inch diameter bars each was left outdoors for the entire period of time. A total of 38 specimens were fabricated for this test.

Sets of bond specimens with two bars each were exposed as indicated in [Tables 9](#) and [10](#) for the specimens with 0.5-inch and 0.75-inch diameter bars, respectively. The average clear concrete covers were 3.15 inches and 2.33 inches for the 0.5-inch and 0.75-inch diameter bars, respectively.

**Table 8. Parameters to Investigate in Bond Test.**

Exposure condition	Bar diameter (in.)	Bond length (in.)	Duration of exposure (months)
Outdoors	0.5	5, 15, 30	16
Indoors	0.5	5, 15, 30	
95 F 88% RH	0.75	7.5, 22.5, 45	

**Table 9. Number of Bond Specimens with 0.5-Inch Diameter Bars.**

Bond length (in.)	Outdoor exposure			Indoor exposure		
	Bar P	Bar V1	Bar V2	Bar P	Bar V1	Bar V2
5	3	3	4	1	1	1
15	3	3	2	1	1	1
30	2	0	0	1	1	1

**Table 10. Number of Bond Specimens with 0.75-Inch Diameter Bars.**

Bond length (in.)	Outdoor exposure			Indoor exposure		
	Bar P	Bar V1	Bar V2	Bar P	Bar V1	Bar V2
7.5	0	0	0	1	1	1
22.5	0	0	0	1	1	1
45	0	0	0	0	2	1

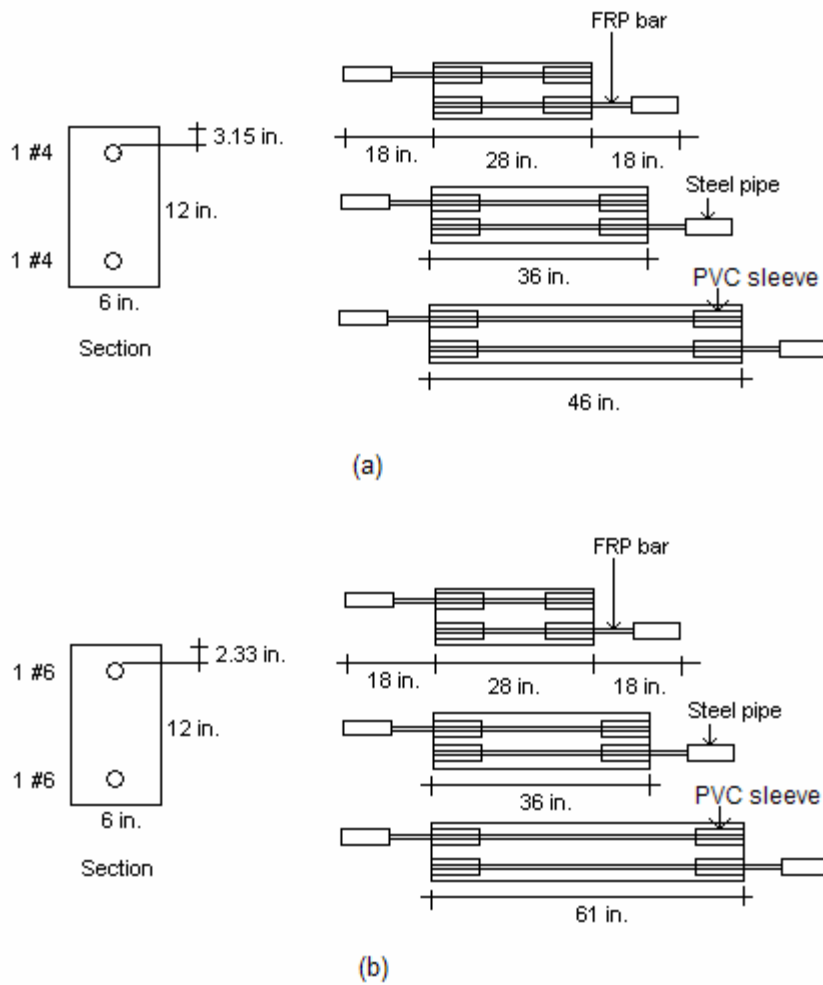


**Figure 17. Dimensions of Bond Specimens Reinforced with (a) 0.5-Inch Diameter Bars and (b) 0.75-Inch Diameter Bars.**

#### *Test Equipment and Instrumentation*

A 100-kip actuator was used to load the specimens, and an LVDT was used to measure the bond slip at the loaded end of the specimen. The same grip used in the tension test was used in the bond test to connect the specimens to the actuator. A bearing frame was built and mounted on the laboratory floor to hold the concrete specimen while the bar was being loaded. The test setup is depicted in [Figure 18](#).



**Figure 18. Loading Setup of Bond Specimens.**

### *Test Procedure*

The end of the specimen to be loaded was placed in the groove of the grip described in the [tension test section](#). The nuts were slightly tightened, followed by centering the concrete block of the specimen on the bearing frame. After centering, the bar was preloaded with a 500 lb. load. The nuts were then securely tightened with a pneumatic wrench, and the preload was released before actual testing began. The LVDT was attached to the side of the loading grip via a magnet. The specimens were loaded at constant rate in pullout to failure at room temperature. The specimens were loaded in displacement-controlled mode at a rate of 0.18 inch/min. After one end of the specimen was tested, the specimen was turned, and the other end was loaded.

## **Thermal Expansion of Concrete Slabs Test**

### *Test Objective*

The coefficient of thermal expansion of concrete is approximately  $6 \times 10^{-6}/^{\circ}\text{F}$  ([Beer and Johnston 1981](#)), that of E-glass fibers is approximately  $1 \times 10^{-6}/^{\circ}\text{F}$  ([Agarwal and Broutman 1990](#)), and that of polyester is approximately  $69 \times 10^{-6}/^{\circ}\text{F}$  ([Agarwal and Broutman 1990](#)). The coefficient of thermal expansion of the FRP composite bars is governed in the longitudinal direction primarily by the thermal properties of the glass fibers and in the transverse direction completely by the thermal properties of the matrix. Thus, there is concern in the design community that GFRP bars may cause spalling of the concrete on structures exposed to high temperatures such as bridge decks. The main objectives of this test are to determine whether thermal expansion is a concern for

reinforced concrete structures and to determine a minimum concrete cover that would not cause spalling of the concrete under typical service temperature.

#### *Test Description*

Bars with 0.75-inch diameters were cast in a slab with the typical thickness of a TxDOT bridge deck. The bar diameter used was selected because this size was the largest diameter used in the deck of the Sierrita de la Cruz Creek Bridge built in Amarillo, Texas. The specimens were cured for 28 days and stored outdoors for 372 days. The materials used in the thermal expansion test were as described in the [materials section](#).

The concrete specimen dimensions were 8 inches thick, 12 inches wide, and 60 inches long. Each concrete slab contained nine 0.75-inch diameter and 10-inch long GFRP bars. The bars were placed in groups of three at three different depths to investigate the effects of cover depth on cracking. The clear cover for each bar depth was 1, 2, and 3 inches. One thermocouple was attached to the side of the bar, with a plastic tie, at the depth of the centroid for each of the three depths. Three specimens were fabricated for this test, one for each bar type. [Figure 19](#) illustrates the reinforcement configuration of the specimens.

#### *Test Equipment and Instrumentation*

Fastoria Sun-Nite® infrared heat lamps, model CH-212-A, were used to heat the slabs. Copper and constantan thermocouples were used to monitor the temperature. A 2176A Fluke digital thermometer, model No. 2414065, with 10 channels and a precision of 0.2 °F was used to read the output temperature from the thermocouples.

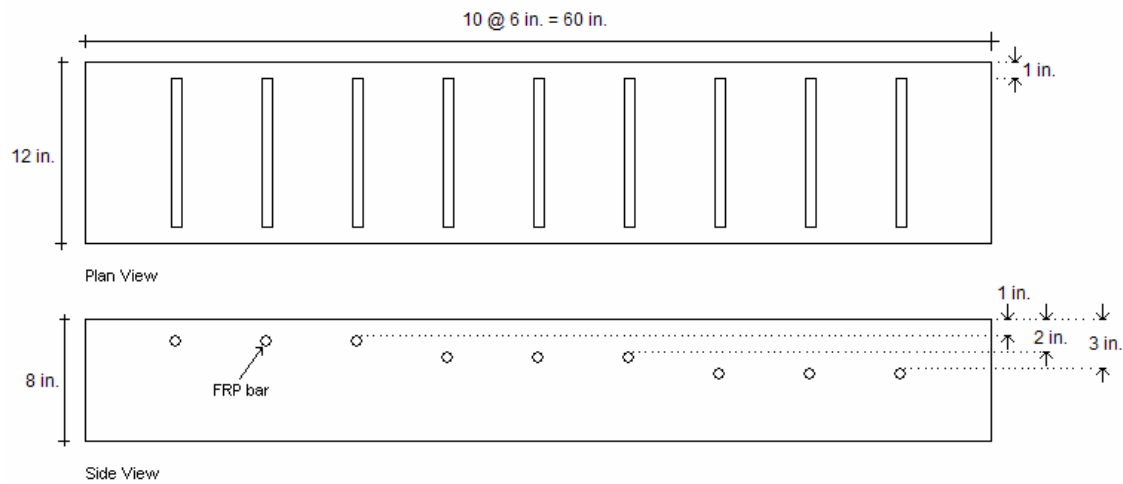


**Figure 19. Dimensions and Reinforcement of Thermal Expansion Specimens.**

#### *Test Procedure*

The specimens were tested 372 days after casting. The temperature at the time the concrete set was approximately 95 °F. Thermocouples were tied to the surface of the middle bars for each of the three cover depths during casting. Thermocouples were also attached to the top and bottom surfaces of the slabs. The slabs were then heated with two infrared heat lamps located 3 inches above the top surface of the slab. The slabs were heated until cracking on the surface of the slab was observed. The temperature at which cracking on the surface of the slab occurred was recorded. The specimens were inspected for cracking at regular intervals. The slab inspections were made visually. When cracks were detected on the surface of the slab, the temperature was recorded, a line was drawn next to the cracks with a marking pen, and the temperature was marked on the slab next to the line.

All of the specimens were first heated with the infrared heat lamps placed 5.25 inches above the surface of the slab. Since no cracks were observed for any of the three slab specimens, the lamps were lowered to a distance of 0.5 inch from the surface of the slab, and the test was repeated.

## IV. RESULTS

This section presents the results of the tests described in the experimental program. The results to be presented correspond to the tension tests, moisture absorption tests, direct shear strength tests, creep tests, cracking of concrete slab tests, cyclic loading of concrete beam tests, bond tests, and thermal expansion of concrete slab tests.

### TENSION TEST

This section summarizes the results of the tension tests. Only 0.625-inch diameter bars were evaluated in the tension tests. The characteristics of the bars, as well as the exposure conditions and test procedures, were described in [Section III](#). The properties of interest in the tension test are the tensile strength and Young's modulus. Schaefer ([2002](#)) conducted all of the testing and obtained the raw data used in this section. The results of the modulus of elasticity were taken directly from Schaefer's work and are presented here for completeness. The tensile strength results from Schaefer's work were reanalyzed and are presented in this document. Finally, additional analyses were carried out for both the tensile strength and the modulus of elasticity results. The unexposed tensile strength and modulus of elasticity of the bars will be presented first, followed by the results of the effects of exposure on the tensile strength and modulus of elasticity of the GFRP bars. Results of the tensile tests on notched GFRP bars will be presented at the end of this section.

#### Unexposed Tensile Strength and Modulus of Elasticity Results

The bars used for these tests were not exposed to any solution and were tested as received from the manufacturers. The unexposed tensile strength results are summarized in [Table 11](#) for each bar type. The unexposed moduli of elasticity obtained for each bar type are summarized in [Table 12](#).

**Table 11. Unexposed Tensile Strength Results.**

Bar	P (psi)	V1 (psi)	V2 (psi)
1	86,125	76,393	76,670
2	85,414	93,258	77,096
3	81,286	96,778	75,099
4	87,265	90,766	71,673
5	82,851	85,339	71,816
Average	84,588	88,507	74,471
Standard Deviation	2,456	7,951	2,598
Coefficients of Variation	0.03	0.09	0.03

**Table 12. Unexposed Modulus of Elasticity Results.**

Bar	P (psi)	V1 (psi)	V2 (psi)
1	6,236,745	6,952,246	6,912,379
2	4,854,173	5,920,664	6,878,169
3	5,846,400	6,451,806	6,320,454
4	5,197,169	5,865,517	6,103,352
5	-	6,203,626	5,656,034
Average	5,533,622	6,278,772	6,374,078
Standard Deviation	623,716	443,896	532,830
Coefficients of Variation	0.11	0.07	0.08

In general, the coefficients of variation (COV) of the moduli of elasticity are larger than the COV of the tensile strength. Only bar V1 has a higher COV for the tensile strength than for the modulus of elasticity. Castro and Carino (1998) conducted tension tests on GFRP bars and reported coefficients of variation for the tensile strength that ranged from 8.3 to 9.9 percent for sand-coated GFRP bars spiral-wrapped with a fiber bundle with a pitch of 1.18 inches. Castro and Carino (1998) reported that a COV of 9 percent is high, and in that case, five test specimens do not provide a reliable

estimate of the true mean tensile strength. The authors used the relationship given by ASTM E 122-72 (1975) to compute the likely relative error,  $e$ , at the 0.05 risk level, between the true mean tensile strength and the mean tensile strength obtained from  $n$  test specimens. The ASTM expression is presented next.

$$e = \pm \frac{1.96 COV}{\sqrt{n}} \quad (14)$$

Castro and Carino (1998) analyzed the case for a COV of 9 percent and five test specimens, obtaining a computed relative error of  $\pm 7.9$  percent. The authors also analyzed the case of reducing the relative error to  $\pm 2$  percent, obtaining that over 70 specimens would need to be tested for a risk level of 0.05. More than five specimens are necessary to obtain a computed relative error of less than 5 percent. However, due to limitations of budget and time, only five specimens were used for these tests. A typical stress-strain plot is shown in Figure 20.

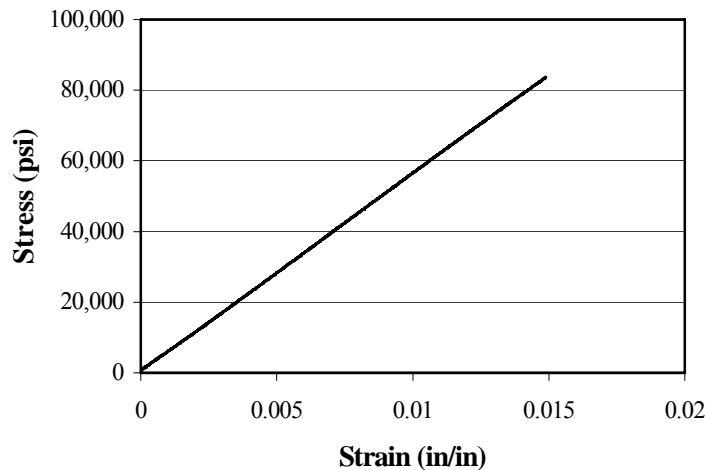


**Figure 20. Typical Stress-Strain Plot.**

## Exposed Tensile Strength and Modulus of Elasticity Results

The results from the tensile strength and Young's modulus measurements are presented next. The terms LT, RT, and HT will be used to indicate low temperature exposure conditions, room temperature exposure conditions, and high temperature exposure conditions, respectively.

During testing of some bars, several fibers snapped directly underneath the strain gages, damaging the gage and data acquisition process required for the determination of the Young's modulus. In other instances, the strain gages debonded and precluded the determination of the Young's modulus of those bars. Thus, only the modulus of elasticity data from specimens where the strain gage stayed bonded to the bar surface could be used.

### *Tensile Strength of Bar Type P*

[Table 13](#) shows the strength results for bar type P after exposure to distilled water, and [Table 14](#) shows the strength results after exposure to the high pH solution. The data in Tables 13 and 14 indicate that the tensile strength test results have high variability as indicated by the coefficients of variation. The highest COV is 7 percent. As discussed in the unexposed tension tests, this is a high COV.

**Table 13. Tensile Strength of Bar Type P after Exposure to Distilled Water.**

Specimen	Unexposed (psi)	Low temperature (psi)		Room temperature (psi)		High temperature (psi)	
		26 weeks	50 weeks	26 weeks	50 weeks	26 weeks	50 weeks
1	86,125	88,389	73,004	89,405	89,405	86,792	73,004
2	85,414	90,421	71,553	93,033	80,406	86,502	76,343
3	81,286	86,357	77,649	95,936	91,727	89,840	72,424
4	87,265	88,824	70,827	88,824	87,228	88,679	68,650
5	82,851	85,631	77,794	88,244	89,115	86,792	76,923
Avg.	84,588	87,954	74,165	91,001	87,663	87,663	73,440
S. D.	2,456	1,930	3,701	3,295	4,311	1,466	3,353
COV	0.03	0.02	0.05	0.04	0.05	0.02	0.05

**Table 14. Tensile Strength of Bar Type P after Exposure to Alkaline Solution.**

Specimen	Unexposed (psi)	Low temperature (psi)		Room temperature (psi)		High temperature (psi)	
		26 weeks	50 weeks	26 weeks	50 weeks	26 weeks	50 weeks
1	86,125	90,397	82,508	79,933	84,488	85,627	76,303
2	85,414	89,187	85,222	90,752	92,176	85,200	71,890
3	81,286	91,108	80,222	87,905	80,929	85,271	77,015
4	87,265	89,114	85,008	83,207	85,200	88,973	80,645
5	82,851	94,525	79,222	83,919	76,018	87,763	73,740
Avg.	84,588	90,866	82,436	85,143	83,762	86,567	75,918
S. D.	2,456	2,211	3,002	4,227	5,945	1,706	3,341
COV	0.03	0.02	0.03	0.05	0.07	0.02	0.04

Figures 21 and 22 illustrate the relative strength results of the samples exposed to distilled water and alkaline solution, respectively. It can be seen in these figures that the tensile strength increased on average, in some cases, by as much as 8 percent of the reference strength after 26 weeks of exposure. Nevertheless, after 50 weeks of exposure, most of the exposure conditions degraded the GFRP bar strength, the maximum mean reduction being 13 percent. The specimens studied do not follow a consistent degradation pattern linked to an exposure condition. Exposure time appears to be the only significant factor evaluated in this project affecting the change in strength of bar type P. It is not clear why the tensile strength increased at 26 weeks of exposure. The fact that the distilled water exposure condition seems to degrade the tensile strength of the bars more than the alkaline exposure condition at 50 weeks may result from a difference in diffusion coefficients, especially since the diffusion rate of distilled water through the resin is faster than the diffusion rate of the calcium hydroxide solution.

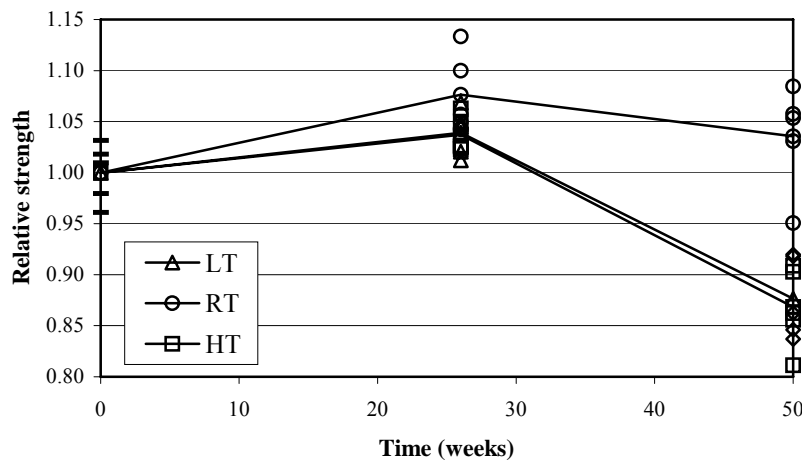


**Figure 21.** Strength of Bar Type P after Distilled Water Exposure.

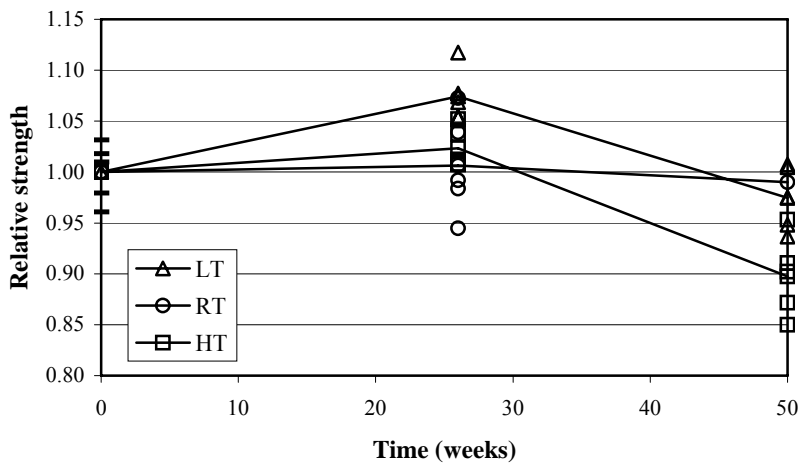


**Figure 22.** Strength of Bar Type P after Alkaline Solution Exposure.

#### *Young's Modulus of Bar Type P*

Tables 15 and 16 show the Young's modulus data for bar type P exposed to distilled water and the high pH solution, respectively. These data indicate that Young's moduli have more variability as compared to tensile strength results. In this case, the

highest COV is 17 percent, a very high value when compared with the coefficients of variation of the tensile strength results.

**Table 15. Modulus of Elasticity of Bar Type P after Exposure to Distilled Water.**

Specimen	Unexposed (ksi)	Low temperature (ksi)		Room temperature (ksi)		High temperature (ksi)	
		26 weeks	50 weeks	26 weeks	50 weeks	26 weeks	50 weeks
1	6,241	6,749	6,865	5,806	5,051	5,428	6,110
2	4,862	6,125	6,851	5,849	4,993	5,689	5,980
3	5,849	7,170	6,430	5,660	5,225	5,443	7,460
4	5,196	6,430	7,126	5,559	5,210	5,994	6,168
5	-	6,488	8,258	5,980	4,993	6,096	7,126
Avg.	5,537	6,592	7,106	5,771	5,094	5,730	6,569
S. D.	623	392	691	164	115	308	675
COV	0.11	0.06	0.10	0.03	0.02	0.05	0.10

**Table 16. Modulus of Elasticity of Bar Type P after Exposure to Alkaline Solution.**

Specimen	Unexposed (ksi)	Low temperature (ksi)		Room temperature (ksi)		High temperature (ksi)	
		26 weeks	50 weeks	26 weeks	50 weeks	26 weeks	50 weeks
1	6,241	6,299	6,967	5,167	-	6,081	6,168
2	4,862	-	6,328	6,299	6,792	5,559	7,634
3	5,849	-	8,882	4,746	5,907	6,183	6,720
4	5,196	5,980	5,718	5,196	7,562	6,343	6,546
5	-	6,284	6,792	-	6,517	5,646	6,096
Avg.	5,537	6,188	6,938	5,352	6,694	5,962	6,633
S. D.	623	180	1,190	664	686	343	617
COV	0.11	0.03	0.17	0.12	0.10	0.06	0.09

Figures 23 and 24 depict the relative modulus of elasticity results for the distilled water and high pH solution exposure conditions, respectively. The only clear pattern observed in Figures 23 and 24 is that the Young's moduli of bars tend to increase with longer exposure times irrespective of the solution or temperature. The maximum relative stiffness increase was 28 percent, on average, at 50 weeks.

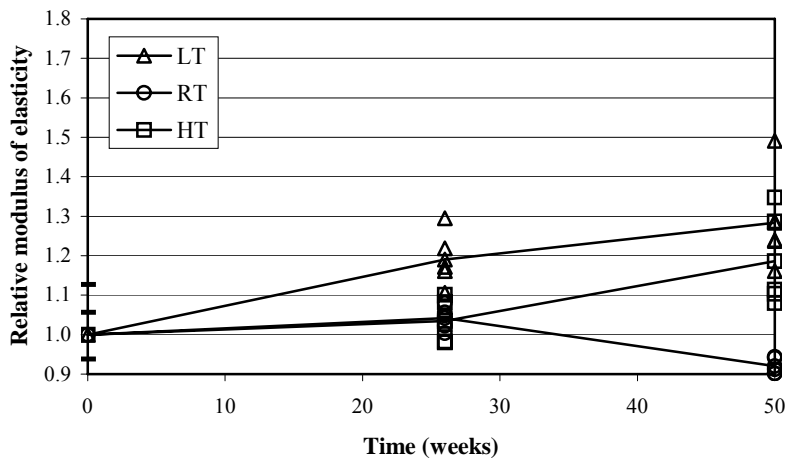


**Figure 23. Modulus of Elasticity of Bar Type P after Distilled Water Exposure.**

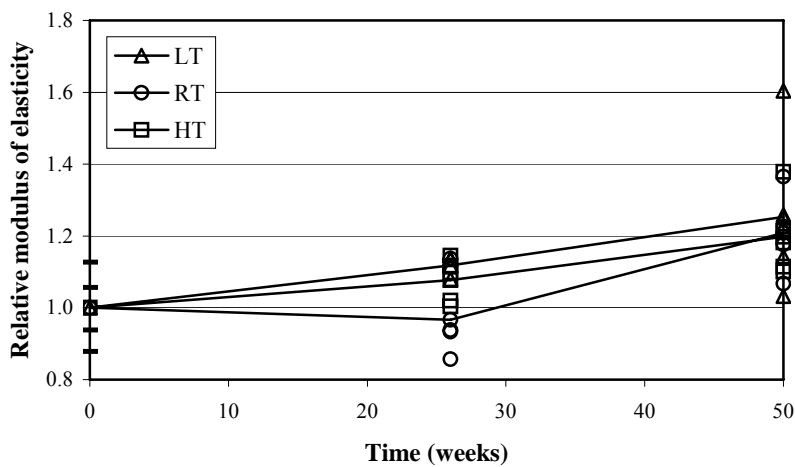


**Figure 24. Modulus of Elasticity of Bar Type P after Alkaline Solution exposure.**

#### *Tensile Strength of Bar Types VI and V2*

Tables 17 and 18 summarize the tensile strength results of bar type V1 exposed to distilled water and the high pH solution, respectively. From the data in Tables 17 and 18, it can be observed that the tensile strength results have relatively high variability,

with the highest COV being 9 percent. High temperature exposure conditions seem to degrade the bars more in distilled water, while low temperature caused more degradation in the specimens exposed to the alkaline solution.

**Table 17. Tensile Strength of Bar Type V1 after Exposure to Distilled Water.**

Specimen	Unexposed (psi)	Low temperature (psi)		Room temperature (psi)		High temperature (psi)	
		26 weeks	50 weeks	26 weeks	50 weeks	26 weeks	50 weeks
1	76,393	89,444	81,436	91,058	-	77,788	84,753
2	93,258	81,159	72,936	82,993	91,571	92,158	80,427
3	96,778	95,237	92,152	80,134	91,058	77,861	83,726
4	90,766	80,502	86,294	95,677	79,987	91,058	78,594
5	85,339	92,670	83,008	90,398	80,647	80,207	82,847
Avg.	88,507	87,802	83,165	88,052	85,816	83,814	82,069
S. D.	7,951	6,691	7,766	6,344	6,358	7,191	2,516
COV	0.09	0.08	0.08	0.07	0.07	0.09	0.03

**Table 18. Tensile Strength of Bar Type V1 after Exposure to Alkaline Solution.**

Specimen	Unexposed (psi)	Low temperature (psi)		Room temperature (psi)		High temperature (psi)	
		26 weeks	50 weeks	26 weeks	50 weeks	26 weeks	50 weeks
1	76,393	77,494	73,578	88,272	86,072	76,541	77,421
2	93,258	82,407	85,080	86,292	77,201	88,932	79,254
3	96,778	78,081	82,865	81,014	93,404	90,838	89,885
4	90,766	84,386	73,007	80,940	77,788	90,838	70,969
5	85,339	87,905	83,079	82,260	95,310	83,726	85,779
Avg.	88,507	82,055	79,522	83,756	85,955	86,175	80,662
S. D.	7,951	4,370	6,349	3,336	8,461	6,121	7,377
COV	0.09	0.05	0.07	0.04	0.10	0.07	0.09

The strength results for bar type V1 are plotted in Figures 25 and 26 for the distilled water and high pH solutions, respectively. As observed in Figures 25 and 26, all exposure conditions led to deterioration of the bars at 26 and 50 weeks. All of the exposure conditions at 50 weeks, except the room temperature exposure condition, had

more deterioration than the 26 weeks exposure. Thus, bar type V1 shows a clear pattern of increased degradation with time. The maximum and minimum degradation at 26 weeks were 7 and 1 percent, on average, respectively. The maximum and minimum degradation at 50 weeks were 10 and 3 percent, on average, respectively.

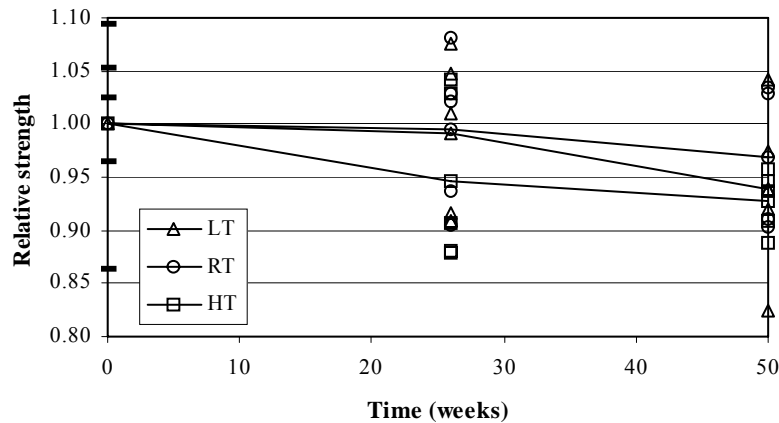


**Figure 25. Strength of Bar Type V1 after Distilled Water Exposure.**

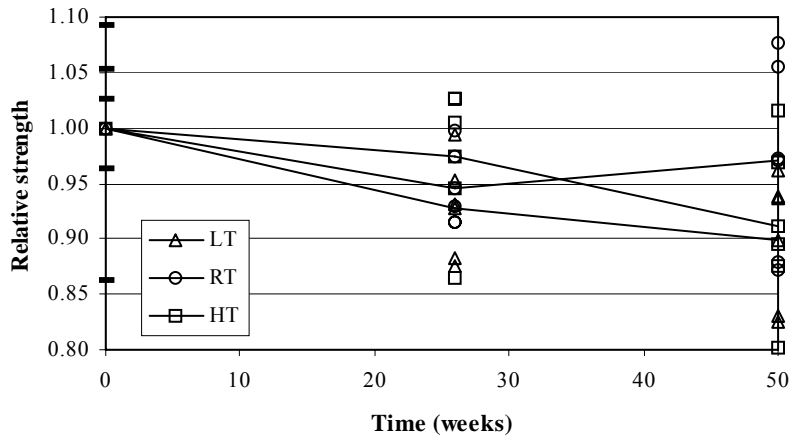


**Figure 26. Strength of Bar Type V1 after Alkaline Solution Exposure.**

The data in Tables 19 and 20 show the tensile strength results from bar type V2 after exposure to the distilled water and the high pH solution, respectively.

**Table 19. Tensile Strength of Bar Type V2 after Exposure to Distilled Water.**

Specimen	Unexposed (psi)	Low temperature (psi)		Room temperature (psi)		High temperature (psi)	
		26 weeks	50 weeks	26 weeks	50 weeks	26 weeks	50 weeks
1	76,670	-	66,435	76,240	76,455	68,388	67,460
2	77,096	71,172	65,363	74,099	74,741	69,887	62,534
3	75,099	69,102	66,721	74,384	70,244	65,033	67,674
4	71,673	71,957	61,220	74,456	73,314	71,386	62,534
5	71,816	72,243	67,721	73,742	72,600	70,315	66,318
Avg.	74,471	71,118	65,492	74,584	73,471	69,002	65,304
S. D.	2,598	1,419	2,793	968	2,330	2,466	2,580
COV	0.03	0.02	0.04	0.01	0.03	0.04	0.04

**Table 20. Tensile Strength of Bar Type V2 after Exposure to Alkaline Solution.**

Specimen	Unexposed (psi)	Low temperature (psi)		Room temperature (psi)		High temperature (psi)	
		26 weeks	50 weeks	26 weeks	50 weeks	26 weeks	50 weeks
1	76,670	70,530	64,721	76,707	72,742	67,460	64,747
2	77,096	72,243	68,292	79,464	69,958	67,817	66,532
3	75,099	72,100	70,435	80,094	68,317	72,171	64,105
4	71,673	70,815	67,935	79,464	69,887	69,958	56,609
5	71,816	74,313	69,578	74,581	72,314	68,459	63,819
Avg.	74,471	72,000	68,192	78,062	70,644	69,173	63,162
S. D.	2,598	1,499	2,410	2,346	1,848	1,929	3,812
COV	0.03	0.02	0.03	0.03	0.03	0.03	0.06

Figures 27 and 28 show the tensile strength results of bar type V2 after exposure to the distilled water and the high pH solution, respectively. Most exposure conditions led to strength degradation at 26 weeks of exposure, with an average maximum degradation of 7 percent. However, the specimens stored at room temperature showed an average strength increase of 5 percent. At 50 weeks, all of the exposure conditions

reduced the strength of the specimens, with a minimum strength reduction of 2 percent and a maximum strength reduction of 15 percent, on average.

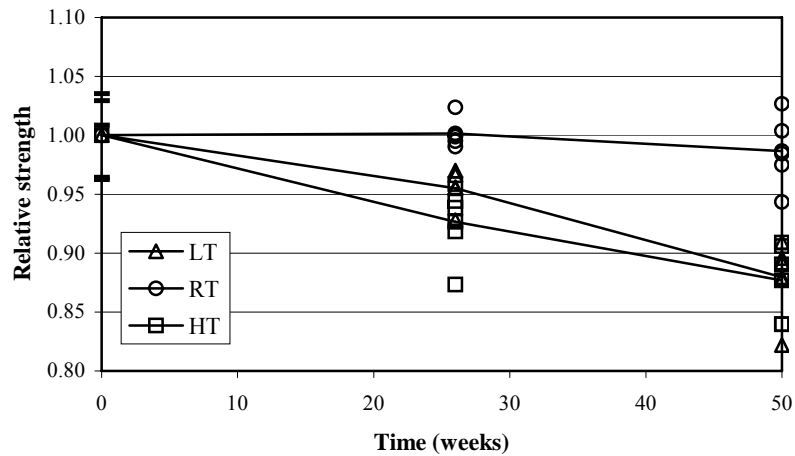


**Figure 27. Strength of Bar Type V2 after Distilled Water Exposure.**

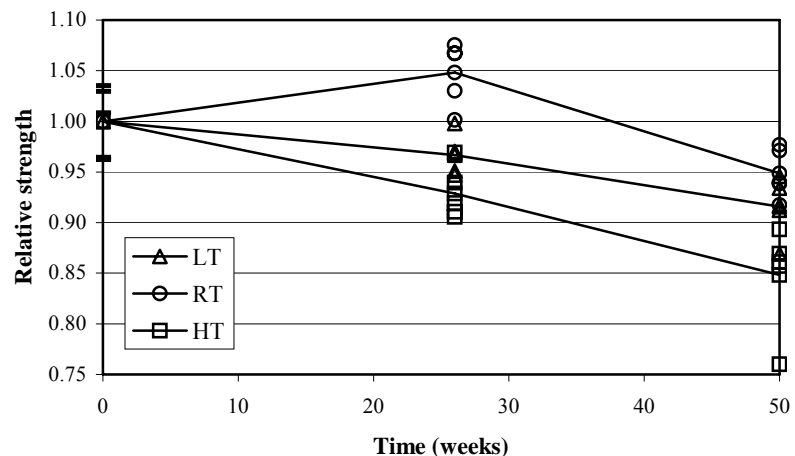


**Figure 28. Strength of Bar Type V2 after Alkaline Solution Exposure.**

In the case of bar type V2, the highest COV from the tensile strength results is 6 percent. Alkaline solution exposure caused more tensile strength reduction than the distilled water exposure condition for room and high temperature exposures at 50 weeks. Thus, GFRP bars embedded in the alkaline environment of concrete could potentially suffer considerable tensile strength deterioration. No marked difference was observed at 26 weeks of exposure between the distilled water and alkaline solution exposure conditions.

#### *Young's Modulus of Bar Types V1 and V2*

Tables 21 and 22 show the results of the modulus of elasticity data for bar type V1 exposed to distilled water and the high pH solution, respectively.

**Table 21. Young's Modulus of Bar V1 after Exposure to Distilled Water.**

Specimen	Unexposed (ksi)	Low temperature (ksi)		Room temperature (ksi)		High temperature (ksi)	
		26 weeks	50 weeks	26 weeks	50 weeks	26 weeks	50 weeks
1	6,952	6,792	7,315	5,980	-	7,620	7,126
2	5,922	7,591	6,792	6,125	7,518	6,821	7,489
3	6,459	6,952	6,763	6,038	8,070	7,388	6,792
4	5,864	7,518	7,170	6,284	7,083	6,401	7,576
5	6,212	6,894	7,591	6,081	7,388	7,170	6,517
Avg.	6,282	7,149	7,126	6,102	7,515	7,080	7,100
S. D.	444	375	352	115	413	480	451
COV	0.07	0.05	0.05	0.02	0.05	0.07	0.06

**Table 22. Young's Modulus of Bar V1 after Exposure to Alkaline Solution.**

Specimen	Unexposed (ksi)	Low temperature (ksi)		Room temperature (ksi)		High temperature (ksi)	
		26 weeks	50 weeks	26 weeks	50 weeks	26 weeks	50 weeks
1	6,952	6,313	7,997	-	7,213	7,547	7,010
2	5,922	6,894	6,676	5,907	-	6,778	7,010
3	6,459	7,184	7,997	6,255	7,141	6,531	7,054
4	5,864	6,081	9,390	6,168	7,141	7,678	5,864
5	6,212	6,241	6,807	-	-	6,749	7,300
Avg.	6,282	6,543	7,774	6,110	7,165	7,057	6,848
S. D.	444	472	1,101	181	42	518	563
COV	0.07	0.07	0.14	0.03	0.01	0.07	0.08

Figures 29 and 30 depict the behavior of the modulus of elasticity of bar type V1 after exposure to distilled water and high pH solution, respectively. Bar type V1 showed modulus of elasticity gain, in general, regardless of exposure condition at 50 weeks. The maximum modulus of elasticity gain was 24 percent and the minimum was 9 percent. No modulus of elasticity reductions were observed at 50 weeks. There is high variability in the Young's moduli exhibited by bar type V1. The highest COV was 14 percent. There are no marked differences between the distilled water and alkaline solution exposure conditions.

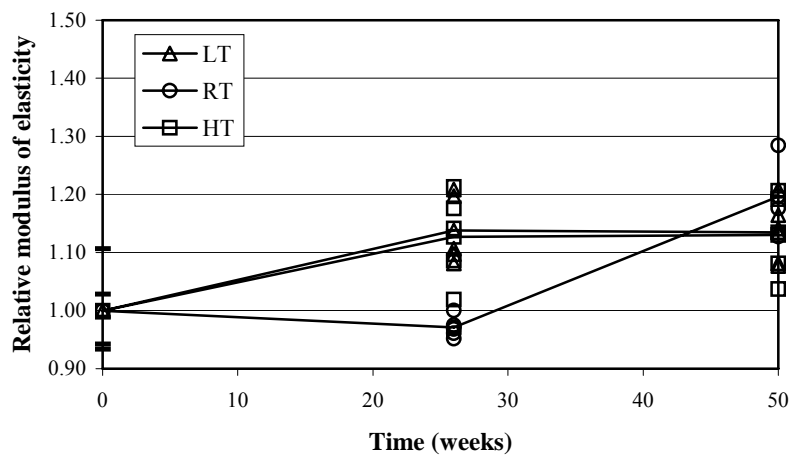


**Figure 29. Modulus of Elasticity of Bar Type V1 after Distilled Water Exposure.**

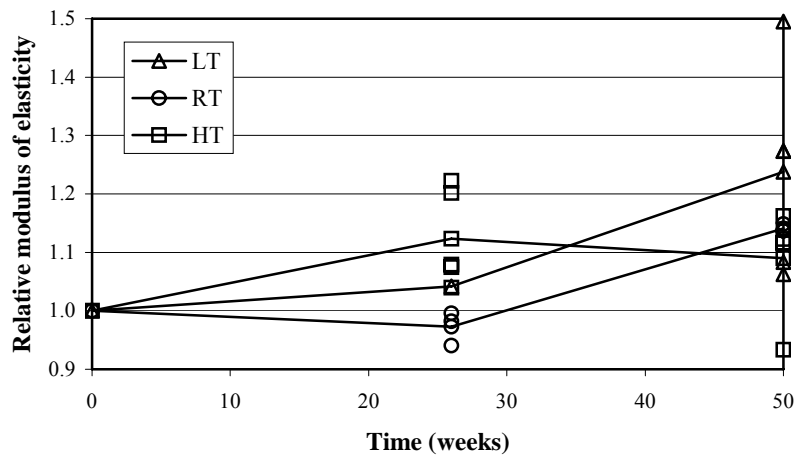


**Figure 30. Modulus of Elasticity of Bar Type V1 after Alkaline Solution Exposure.**

Tables 23 and 24 show the Young's moduli of bar type V2 after exposure to distilled water and the high pH solution, respectively.

**Table 23. Young's Modulus of Bar V2 after Exposure to Distilled Water.**

Specimen	Unexposed (ksi)	Low temperature (ksi)		Room temperature (ksi)		High temperature (ksi)	
		26 weeks	50 weeks	26 weeks	50 weeks	26 weeks	50 weeks
1	6,923	-	6,401	6,038	5,849	4,078	6,720
2	6,880	6,473	6,081	5,864	5,864	5,428	6,139
3	6,328	6,096	6,720	5,878	6,923	4,514	6,125
4	6,110	5,747	6,459	6,212	8,157	6,705	4,122
5	5,660	5,718	6,212	5,747	6,923	5,617	5,414
Avg.	6,380	6,009	6,374	5,948	6,743	5,269	5,704
S. D.	533	354	245	180	953	1,024	998
COV	0.08	0.06	0.04	0.03	0.14	0.19	0.18

**Table 24. Young's Modulus of Bar V2 after Exposure to Alkaline Solution.**

Specimen	Unexposed (ksi)	Low temperature (ksi)		Room temperature (ksi)		High temperature (ksi)	
		26 weeks	50 weeks	26 weeks	50 weeks	26 weeks	50 weeks
1	6,923	6,154	5,660	4,673	5,254	5,835	5,399
2	6,880	6,197	5,951	6,517	5,109	5,515	6,183
3	6,328	5,806	6,096	5,980	5,051	5,065	5,922
4	6,110	5,936	6,560	5,704	4,731	5,820	6,154
5	5,660	6,502	6,241	6,067	5,109	5,791	5,806
Avg.	6,380	6,119	6,102	5,788	5,051	5,605	5,893
S. D.	533	267	334	688	194	329	318
COV	0.08	0.04	0.05	0.12	0.04	0.06	0.05

Figures 31 and 32 illustrate the results for exposure to distilled water and high pH solution, respectively. From Figures 31 and 32 it can be observed that the modulus of elasticity was reduced for all times under alkaline exposure conditions and for all times except the room temperature condition at 50 weeks in the distilled water exposure. The maximum observed average reduction was 21 percent for the 50-week room temperature exposure condition.

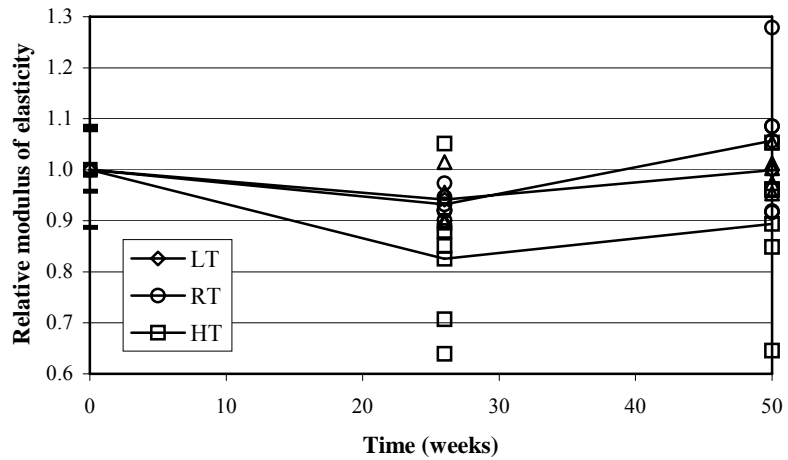


**Figure 31. Modulus of Elasticity of Bar Type V2 after Distilled Water Exposure.**

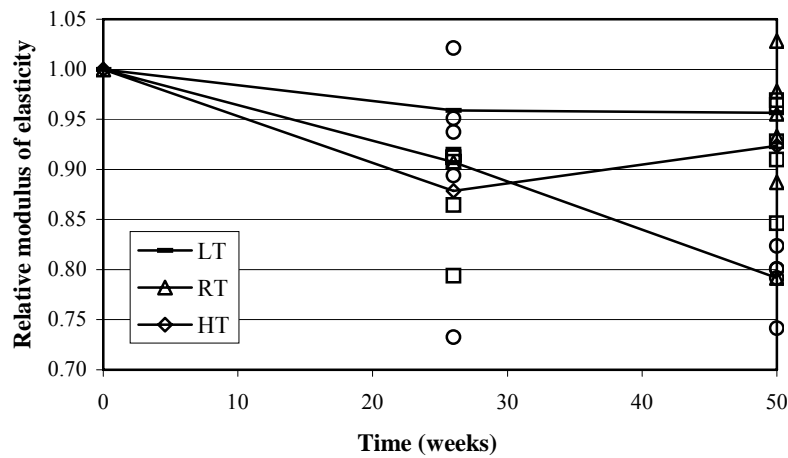


**Figure 32. Modulus of Elasticity of Bar Type V2 after Alkaline Solution Exposure.**

Once again, high variability is observed in the Young's moduli results. In the case of bar type V2, the maximum COV is 19 percent. It is not clear why the modulus of elasticity decreased at 26 weeks for the specimens exposed to distilled water, and then increased at 50 weeks.

A summary of the tensile strength test results is illustrated in [Figure 33](#). A circular data marker indicates the average values of the results obtained from each exposure condition for 26 and 50 weeks. Thus, 18 circular markers corresponding to 3 bar types with 6 exposure conditions each are drawn for the times of 26 and 50 weeks. An overall average value of the relative tensile strength was obtained using the average values from the relative tensile strength of each of the exposure conditions mentioned. The middle line shown in [Figure 33](#) shows the location of the overall average relative tensile strength. The overall average tensile strength values are 0.99 at 26 weeks and 0.93 at 50 weeks. The top line in [Figure 33](#) connects the maximum relative tensile strengths observed from all of the specimens tested for each test time. The maximum relative tensile strength values observed were 1.09, 1.13, and 1.09 at 0, 26, and 50 weeks of exposure, respectively. The lower line in [Figure 33](#) connects the minimum relative tensile strengths observed from all of the specimens tested for each test time. The minimum relative tensile strength values observed were 0.86, 0.86, and 0.76, for 0, 26, and 50 weeks of exposure, respectively. The overall standard deviations for the relative strength at 0, 26, and 50 weeks were 0.054, 0.063, 0.070, respectively. The overall coefficients of variation at 0, 26, and 50 weeks were 0.054, 0.063, and 0.075, respectively. An analysis of the results obtained in this section will be presented at the end of the moisture absorption test section, where a method to predict long-term degradation of the GFRP bars is described.

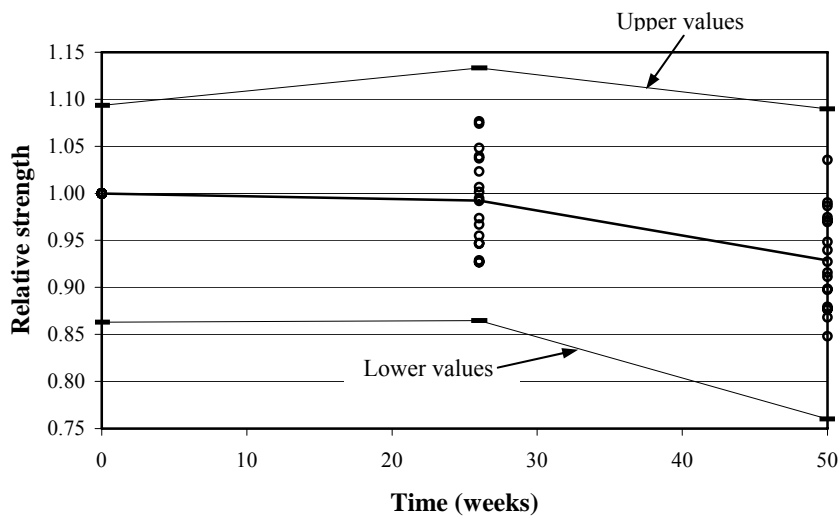


**Figure 33. Summary of Tensile Strength Results.**

A summary of the Young's modulus test results is illustrated in Figure 34. A circular data marker indicates the average values of the results obtained for each exposure condition at 26 weeks and 50 weeks. As for the tensile strength case, an overall average value of the relative Young's modulus was obtained using the average values from the relative Young's modulus of each of the exposure conditions mentioned. The middle line shown in Figure 34 indicates the location of the overall average relative Young's modulus. The overall average Young's modulus values are 1.01 at 26 weeks and 1.09 at 50 weeks. The top line in Figure 34 connects the maximum relative Young's modulus observed from all of the specimens tested for each test time. The maximum relative Young's modulus values observed were 1.13, 1.29, and 1.60 at 0, 26, and 50 weeks of exposure, respectively. The bottom line in Figure 34 connects the minimum relative Young's modulus observed from all of the specimens tested for each test time. The minimum relative Young's modulus values observed were 0.88, 0.64, and 0.65, for 0, 26, and 50 weeks of exposure, respectively. The overall standard deviations for the relative modulus of elasticity at 0, 26, and 50 weeks were 0.081, 0.12, 0.17, respectively.

The overall coefficients of variation at 0, 26, and 50 weeks were 0.081, 0.12, and 0.16, respectively.

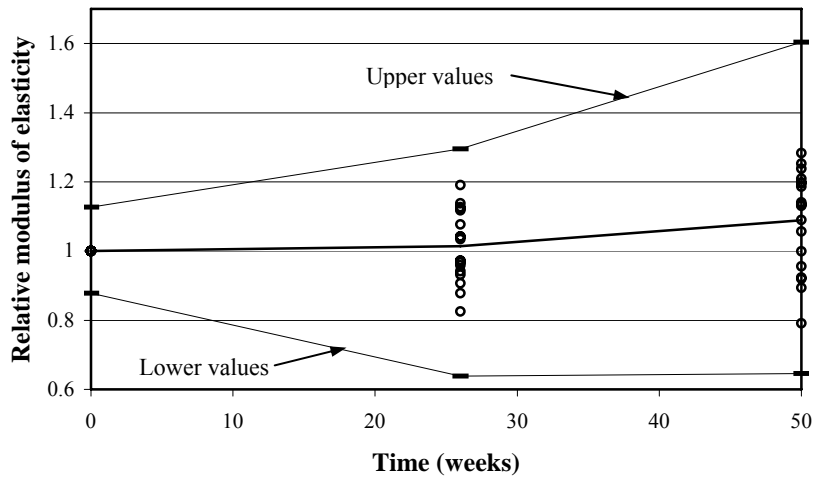


**Figure 34. Summary of Young's Modulus Results.**

Summarizing, the tensile strength values of the GFRP bars studied have a tendency to decrease with exposure time. The overall average tensile strength reductions were 1 percent at 26 weeks and 7 percent at 50 weeks. The Young's modulus of the GFRP bars tested had a tendency to increase with time. The overall average increase of the Young's modulus was 1 percent at 26 weeks and 9 percent at 50 weeks. The test results can be used to make predictions for exposure periods similar to those studied. However, exposure tests carried out over longer periods of time are necessary to make accurate long-term behavior predictions.

### Tension Test of Notched Bars

This test evolved as a result of the need to evaluate the effects of abrasion and other damage to the GFRP bars during transportation and construction. When the bars

are notched, they undergo a reduction in area, which will affect the performance of the bar. The tensile strengths reported hereafter were obtained by dividing the failure load by the reduced area. The formation of a slip surface at the depth of the notch precluded the strains in the core of the bar from being measured. Since the extensometer was placed across the notch, it could only measure the slip at the notch surface and not the strain in the core of the bar. Thus, the Young's modulus could not be determined.

#### *Tensile Strength of Notched Bar Type P*

The tensile strength results of bar type P are shown in [Table 25](#). After 26 weeks of exposure to a high pH solution and room temperature, the notched bars showed a tensile strength reduction of 12 percent, on average, when compared to the unexposed notched bars. The exposed notched tensile strength results have a COV of 31 percent, a very large value when compared with the COV of the tensile strength of the unexposed un-notched bars. The tensile strength of the notched bars without exposure is larger than the tensile strength of the un-notched unexposed bars because small diameter FRP bars have higher tensile strengths. This can be explained considering that a small diameter bar has less probability of having a flaw than a larger diameter bar.

**Table 25. Tensile Strength of Bar Type P Notched.**

Specimen	Un-notched without exposure (psi)	Notched without exposure (psi)	Notched with exposure (psi)
1	86,125	105,864	61,711
2	85,414	113,656	114,279
3	81,286	110,020	114,695
4	87,265	-	-
5	82,851	-	-
Avg.	84,588	109,847	96,895
S. D.	2,456	3,899	30,471
COV	0.03	0.04	0.31

### *Tensile Strength of Notched Bar Type V1*

The tensile strength results of bar type V1 are shown in [Table 26](#). After 26 weeks of exposure to a high pH solution and room temperature, the notched bars showed a tensile strength reduction of 4 percent, on average, when compared with the unexposed notched bars. For this bar type, the maximum COV is 10 percent. It can also be observed from [Table 26](#) that the tensile strength of the notched bars without exposure is larger than the tensile strength of the un-notched bars without exposure. This behavior can be explained as described for bars type P.

**Table 26. Tensile Strength of Bar Type V1 Notched.**

Specimen	Un-notched without exposure (psi)	Notched without exposure (psi)	Notched with exposure (psi)
1	76,393	86,559	77,610
2	93,258	88,896	89,486
3	96,778	98,136	93,992
4	90,766	-	-
5	85,339	-	-
Avg.	88,507	91,197	87,029
S. D.	7,951	6,122	8,463
COV	0.09	0.07	0.10

### *Tensile Strength of Notched Bar Type V2*

The tensile strength results of bar type V2 are shown in [Table 27](#). After 26 weeks of exposure to a high pH solution and room temperature, the notched bars showed an average tensile strength reduction of 3 percent when compared with the unexposed notched bars. The maximum COV was 5 percent for the type V2 notched bars exposed to the high pH solution. For bar type V2, the tensile strength of the unexposed notched specimens is smaller than the tensile strength of unexposed un-notched specimens. It is not clear why the tensile strength of the unexposed notched bars is lower than the tensile strength of the unexposed un-notched bars. There could be error either in the failure load or in the bar area. The reduced bar area was obtained accounting for the notched depth. Both the bar area and the notch depth are not significantly different from the areas and

notched depths of the other bars. The failure load, on the other hand, is quite lower than the failure loads of the other bar types. The average failure loads of bar types P, V1, and V2 are 25.8 kips, 21.0 kips, and 15.5 kips, respectively. Thus, although not reported by Schaefer (2002), failure of the specimens could have initiated at the end grips, causing premature failure of the specimens.

Summarizing, bar type P exhibited an average strength reduction of 12 percent, while bars V1 and V2 showed reductions of only 4 and 3 percent, respectively. Thus, the bars made with polyester resin exhibited reductions in strength three times higher than bars made with vinyl ester resin after 26 weeks of exposure. This indicates that the vinyl ester resin may perform better than polyester resin when damage to the bar occurs. The mean tensile strength of a commercially available vinyl ester resin is 14,000 psi (Dow Chemical Company 2003). The mean tensile strength of a typical polyester resin is 10,500 psi (Lubin 1969). The improved performance of the vinyl ester resin could be due to better interfacial bond strength with the glass fibers and better wetting of the fibers.

**Table 27. Tensile Strength of Bar Type V2 Notched.**

Specimen	Un-notched without exposure (psi)	Notched without exposure (psi)	Notched with exposure (psi)
1	76,670	67,308	66,859
2	77,096	65,561	62,251
3	75,099	63,403	61,330
4	71,673	-	-
5	71,816	-	-
Avg.	74,471	65,424	63,480
S. D.	2,598	1,956	2,962
COV	0.03	0.03	0.05

## **MOISTURE ABSORPTION TEST**

The need to conduct moisture absorption tests on GFRP bars was discussed in [Section II](#), and a test to determine absorption rates as a function of time was described in [Section III](#). The results of the moisture absorption tests on bars with uncapped ends will be presented first. Following this, the results of the moisture absorption tests on bars with capped ends, and a model for prediction of the diffusion into the GFRP bars is presented. Finally, a prediction model to estimate the residual tensile strength of exposed GFRP bars is presented. Specimens with capped and uncapped ends were tested because there is no agreement between manufacturers as to whether the ends of FRP bars should be protected with a resin. The test with capped ends was also necessary because capping the ends of the bar limits the moisture ingress into the bar from the ends, allowing moisture to diffuse into the bar almost exclusively from the bar sides. This condition is more representative of actual field conditions where bars are long, and the moisture absorption that occurs at the ends does not affect the moisture absorption at bar sections far removed from the ends.

### **Test Results for Bars with Uncapped Ends**

The test results of the bars with uncapped ends are summarized in [Table 28](#), where the ratio of the measured wet weight to the dry initial weight is shown. The results shown are the average values obtained from three test specimens. All specimens show an increase in weight (or mass) with time. All specimens from this experiment were tested in shear at the end of the test. The specimens exposed to distilled water and no chlorides displayed the highest moisture absorption. The researchers believe that the surface of bars exposed to an alkaline solution made with calcium hydroxide and those exposed to chlorides exhibit less diffusion because the calcium hydroxide and chloride atoms can block the movement of other atoms into the bar. Therefore, the diffusion coefficient of FRP bars exposed to calcium hydroxide and chloride atoms could be reduced over time. It is believed that this is the reason why the bar specimens exposed to distilled water exhibited the highest moisture absorption values. The relative weights of the specimens

exposed to distilled water, with mean pH values of 7.4 and 7.3, are shown in [Table 28](#). The relative weights of the specimens exposed to a calcium hydroxide solution, with average pH values of 9.1 and 9, are shown in [Table 28](#). In general, smaller diameter bars have higher moisture absorption rates than large diameter bars at a given time. This behavior indicates that small diameter bars will saturate faster than large diameter bars, as expected. The complete data of the uncapped end results are presented in [Table A1](#) of [Appendix A](#).

**Table 28. Average Relative Weight from Test of Bars with Uncapped Ends.**

pH	NaCl content (%)	Bar diameter (in.)	Exposure time (weeks)					
			22		42		48	
			Bar P	Bar V1	Bar V2	Bar P	Bar V1	Bar V2
7.4	0	0.500	-	-	-	1.0032	1.0127	1.0112
		0.625	-	-	-	1.0042	1.0087	1.0052
		0.750	-	-	-	1.0060	1.0058	1.0022
7.3	3.5	0.500	1.0028	1.0077	1.0055	1.0026	1.0092	1.0067
		0.625	1.0021	1.0040	1.0023	1.0021	1.0045	1.0029
		0.750	1.0054	1.0020	1.0016	1.0055	1.0028	1.0020
9.1	0	0.500	1.0030	1.0081	1.0073	1.0027	1.0117	1.0084
		0.625	1.0035	1.0048	1.0040	1.0036	1.0068	1.0049
		0.750	1.0045	1.0021	1.0019	1.0047	1.0041	1.0026
9.0	3.5	0.500	-	-	-	1.0026	1.0088	1.0083
		0.625	-	-	-	1.0025	1.0048	1.0045
		0.750	-	-	-	1.0048	1.0029	1.0023

### Test Results for Bars with Capped Ends

[Table 29](#) summarizes the results of the moisture absorption of the bars with capped ends in distilled water. The distilled water had an average pH value of 7.8. [Table 29](#) shows the ratio of the measured wet weight (or mass) to the dry initial weight (or mass). The moisture absorption is consistently larger for small diameter bars than for large diameter bars for bar types V1 and V2. Bar type P shows the highest moisture absorption for the 0.75-inch diameter bars. The complete data for the capped end specimens in distilled water are presented in [Table A2](#) of [Appendix A](#).

**Table 29. Average Relative Weight from Test of Capped-End Bars in Distilled Water.**

Bar type	Bar diameter (in.)	Exposure time (weeks)					
		0.7	2.4	15.9	79.0	88.7	97.0
P	0.500	1.0000	1.0011	1.0015	1.0023	1.0071	1.0071
	0.625	1.0000	1.0008	1.0011	1.0018	1.0066	1.0066
	0.750	1.0000	1.0018	1.0029	1.0051	1.0102	1.0103
V1	0.500	1.0000	1.0025	1.0040	1.0072	1.0138	1.0139
	0.625	1.0000	1.0016	1.0029	1.0053	1.0115	1.0115
	0.750	1.0000	1.0011	1.0017	1.0027	1.0073	1.0074
V2	0.500	1.0000	1.0028	1.0044	1.0079	1.0136	1.0139
	0.625	1.0000	1.0017	1.0024	1.0040	1.0089	1.0091
	0.750	1.0000	1.0009	1.0013	1.0019	1.0064	1.0064

Table 30 summarizes the results of the moisture absorption of the bars with capped ends in alkaline solution. The alkaline solution had an average pH value of 12.8. Table 30 shows the ratio of the measured wet weight to the dry initial weight. As for the distilled water case, the moisture absorption is invariably larger for small diameter bars than for large diameter bars for bar types V1 and V2. Also, bar type P shows the highest moisture absorption for the 0.75-inch diameter bars, followed by the 0.625-inch diameter bars, and then by the 0.5-inch diameter bars. The complete data for the capped end specimens in alkaline solution are presented in Table A3 of Appendix A.

**Table 30. Average Relative Weight from Test of Capped-End Bars in Alkaline Solution.**

Bar type	Bar diameter (in.)	Exposure time (weeks)					
		0.7	2.4	15.9	79.0	88.7	97.0
P	0.500	1.0000	1.0007	1.0012	1.0021	1.0065	1.0066
	0.625	1.0000	1.0007	1.0011	1.0017	1.0065	1.0066
	0.750	1.0000	1.0011	1.0018	1.0035	1.0082	1.0087
V1	0.500	1.0000	1.0018	1.0035	1.0065	1.0135	1.0135
	0.625	1.0000	1.0006	1.0016	1.0037	1.0096	1.0101
	0.750	1.0000	1.0006	1.0011	1.0018	1.0063	1.0064
V2	0.500	1.0000	1.0016	1.0019	1.0032	1.0096	1.0096
	0.625	1.0000	1.0010	1.0014	1.0019	1.0068	1.0070
	0.750	1.0000	1.0007	1.0009	1.0014	1.0061	1.0062

It can be observed from Tables 29 and 30 that the specimens in the distilled water solutions exhibited higher absorptions than those in the alkaline solution for all bar types and diameters.

The average relative weight results versus the square root of time are plotted in Figures 35 and 36 for the specimens exposed to distilled water and alkaline solution, respectively. In Figures 35 and 36, the labels indicate bar type followed by bar diameter in eighths of an inch. The labels of the ordinates indicate the average weight of five specimens ( $w$ ) expressed as a fraction of the initial (dry) weights ( $w_0$ ). Both figures show that all specimens are either saturated or close to saturation.

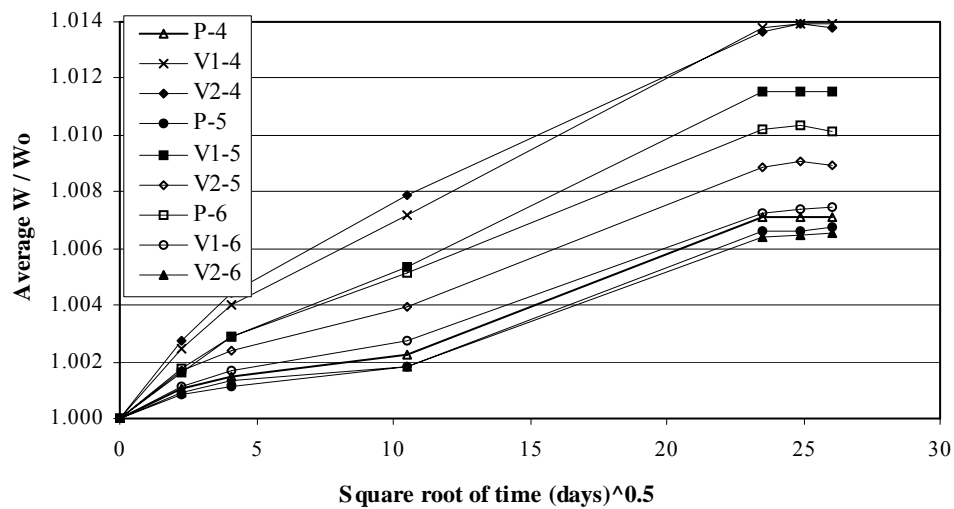


**Figure 35. Average Relative Weight of Specimens in Distilled Water.**

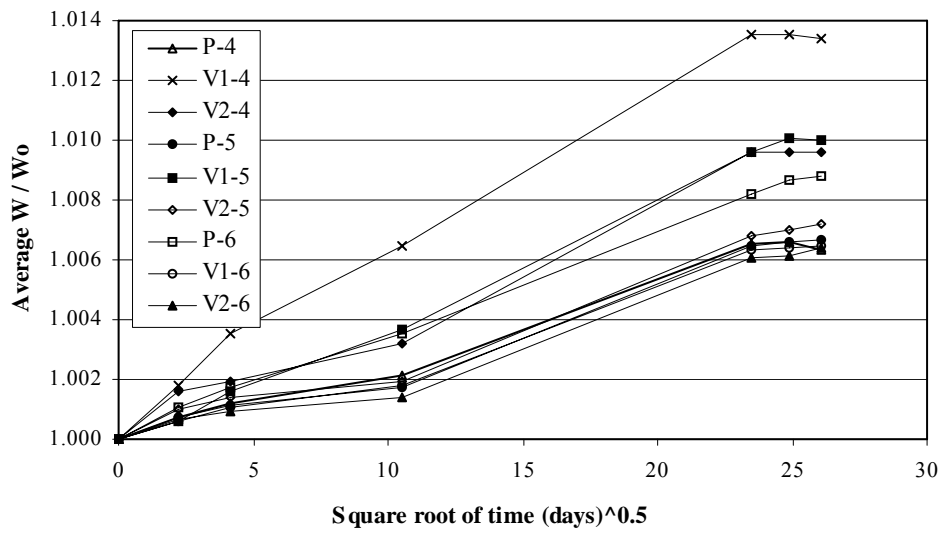


**Figure 36. Average Relative Weight of Specimens in Alkaline Solution.**

It can be seen in Figures 35 and 36 that all of the 0.5-inch diameter bar specimens are saturated. Most of the specimens with 0.625-inch and 0.75-inch diameter bars are close to saturation, although still some increase in moisture was observed, especially for the 0.75-inch diameter bars.

The results from bar types V1 and V2 will be used to compare the moisture absorption of the uncapped-end and capped-end specimens. Comparing the results obtained at 68 weeks of exposure from Table 28 for pH values of 7.4 and 9.1 and no chloride content with the results obtained at 79 weeks of exposure from Tables 29 and 30, it can be seen that the specimens with uncapped ends absorbed more moisture than the specimens with capped ends. Although the results of the uncapped-end specimens were recorded at 68 weeks and the results for the capped-end specimens were obtained at 79 weeks, the uncapped-end specimens showed moisture absorption 2 percent higher, on average. Thus, capping the bar ends should yield absorption rates that are closer to actual absorption rates found in the long bars embedded in concrete elements.

The moisture absorption of the bars will now be modeled to obtain the diffusion coefficient of the GFRP bars. The diffusion coefficient will then be used in a model to predict the tensile strength degradation of GFRP bars. The model to predict the strength degradation of GFRP bars will then be used to predict the tensile strength degradation versus exposure times.

### Diffusion Analysis

Modeling diffusion in GFRP bars is complex because there are several factors that introduce heterogeneity, including the fact that the bar is a composite material, an interface exists between the resin and the fibers, there is an uneven distribution of fibers within the matrix, and voids and fillers are present. Some of these features can be seen in Figures 4 and 5 shown previously. A typical inhomogeneous distribution of fibers within the matrix can be observed in [Figure 37](#).

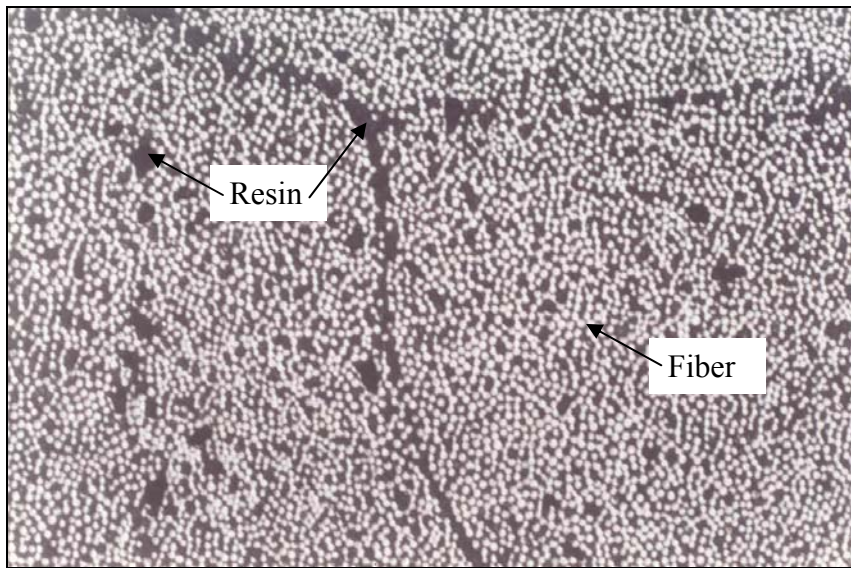


**Figure 37. Heterogeneous Distribution of Fibers within the Matrix.**

Solid polymers do not satisfy some of the basic assumptions made regarding diffusion through a medium according to Neogi (1996). Among the conditions not satisfied are isotropy and homogeneity. Alfrey (1965) identified the first basic type, out of the two known, of non-Fickian sorption behaviors. In Alfrey's sorption experiments for glassy polymers, the moisture gain was found to be proportional to time, instead of being proportional to the square root of time for Fickian behavior. Long and Richman (1960) documented the second type of non-Fickian behavior. In that case, the moisture uptake was found to be sigmoidal. Figure 38 depicts the main types of Fickian and non-Fickian sorption.

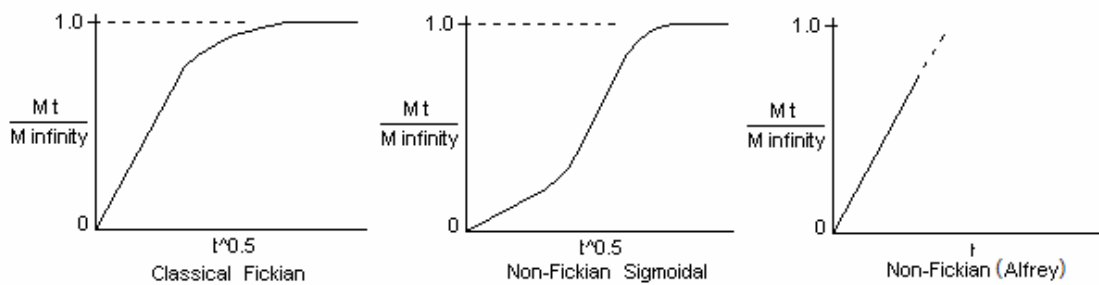


**Figure 38. Main Types of Diffusion.**

In order to determine whether the moisture absorption of GFRP bars can be modeled with Fick's second law of diffusion, the results of the moisture absorption tests of the bars with capped ends will be plotted in different ways. Figures 39 and 40 illustrate the moist weight,  $w$ , expressed as a fraction of the weight at saturation,  $w_{\text{saturation}}$ , for all types of capped bars. In this case, saturation is defined as the moisture absorption level beyond which there is no moisture absorption increase. It can be observed from both figures that moisture absorption in GFRP bars can be approximated with Fick's second law of diffusion as illustrated in Figure 38, since the moisture absorption is approximately proportional to the square root of time up to saturation. It

can be seen from Figures 39 and 40 that, in general, the specimens exposed to the distilled water solution absorbed more moisture than the specimens exposed to the alkaline solution at a given time.

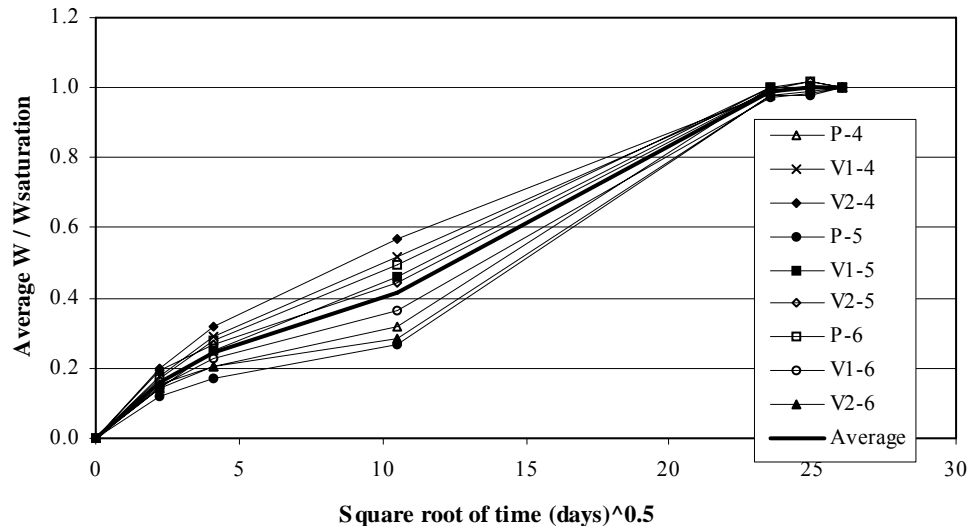


**Figure 39. Weight of Bars in Distilled Water as a Fraction of Weight at Saturation.**

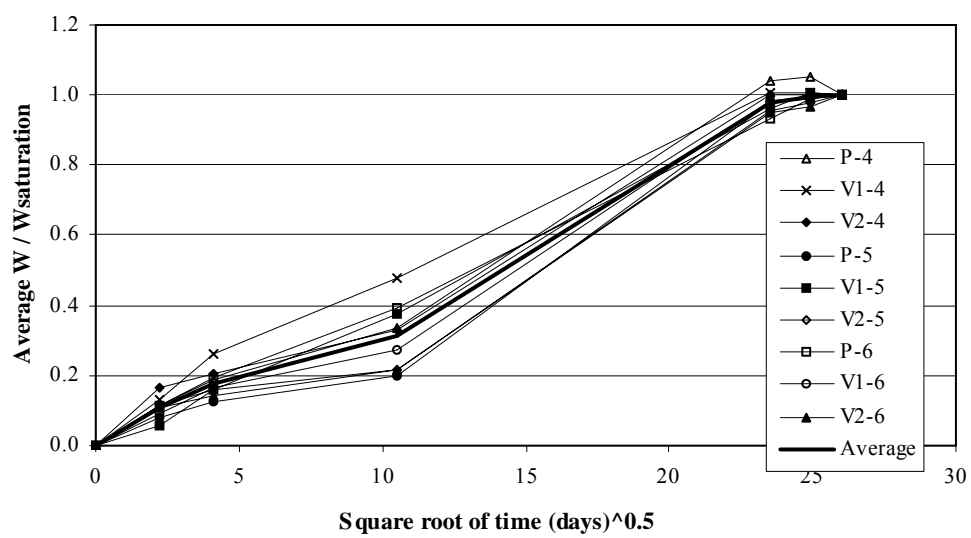


**Figure 40. Weight of Bars in Alkaline Solution as a Fraction of Weight at Saturation.**

To obtain the diffusion coefficient, the equation for Fick's second law for diffusion of a substance into a cylinder can be used as follows:

$$\frac{\partial c}{\partial t} = D \left( \frac{\partial^2 c}{\partial r^2} + \frac{1}{r} \left( \frac{\partial c}{\partial r} \right) \right) \quad (15)$$

A solution to Equation 15 is given by Jost (1952), which lends itself for comparison with experiments where it is typically not easy to measure local concentrations, but rather the total amount of solution taken up by the bar, is as follows:

$$\frac{c_{avg} - c_f}{c_i - c_f} = \sum_{i=1}^{\infty} \frac{4}{\xi_{vi}^2} \exp \left( -\frac{\xi_{vi}^2 D t}{r_o^2} \right) \quad (16)$$

where,

$c_i$  = Initial solution concentration,

$c_f$  = Final solution concentration,

$c_{avg}$  = Average solution concentration,

$\xi_{vi}$  = Roots of the equation  $J_0(x) = 0$ , where  $J_0(x)$  is the Bessel-function of zero order ( $\xi_{vi} = 2.405, 5.520, 8.654, 11.792, 14.931, 18.071\dots$ ),

$r_o$  = Radius of the bar (inch),

$D$  = Diffusion coefficient (inch<sup>2</sup> sec<sup>-1</sup>),

$T$  = Time (sec).

where the average concentration is computed as follows:

$$c_{avg} = \frac{1}{r_o} \int_0^{r_o} c dr \quad (17)$$

where  $c$  is the concentration at a given point in the bar. In the case of a GFRP bar immersed in distilled water,  $c_{avg}$  is the moisture content at time  $t$ , expressed as a fraction of the moisture absorbed at saturation.

The boundary conditions for the equations are:

$$c = c_i = 0 \text{ for } 0 < r < r_o \text{ and } t = 0 \quad (18)$$

$$c = c_f \neq 0 \text{ for } r = r_o \text{ and } t > 0 \quad (19)$$

where  $r$  is a radial distance (*inch*).

Using the first term of the series:

$$\frac{c_{avg} - c_f}{c_i - c_f} \approx \frac{4}{(2.405)^2} \exp\left(-\frac{t}{\tau}\right) \quad (20)$$

where,

$$\tau = \frac{r_0^2}{(2.405)^2 D} \quad (21)$$

For the case of a GFRP bar in distilled water,  $c_f$  is equal to one, the fraction of moisture content at saturation;  $c_i$  is the initial moisture content of the bar, equal to zero, i.e., the bar was dried prior to using it in the moisture absorption test.

Equations 20 and 21 are used to obtain the diffusion coefficients of the bars with capped ends exposed to distilled water. The same equations are used to compute the diffusion coefficients of the bars with capped ends exposed to the alkaline solutions. In the case of the specimens exposed to the alkaline solution, the diffusion coefficient was determined by assuming the average concentration ( $c_{avg}$ ) at a given time to be equal to the weight gain at that time expressed as a fraction of the weight gain at saturation, as it was assumed in the case of the specimens exposed to distilled water. The concentrations  $c_i$  and  $c_f$  are equal to 0 and 1, respectively, as is the case of the distilled water specimens. The diffusion coefficients for the specimens exposed to distilled water and alkaline solution are indicated in [Table 31](#). The diffusion coefficient can be computed at any time. However, the researchers noticed that the diffusion coefficients computed at short exposure times were not realistic, and as the exposure time approached the saturation time, the computed diffusion coefficient was less variable and more realistic as indicated in [Figure 41](#). This could be an indication that the diffusion coefficient is not constant with time. Therefore, the diffusion coefficients were obtained for the value of time

closest to the time at which the specimens reached saturation. The specimens in distilled water have a slightly higher diffusion coefficient.

**Table 31. Diffusion Coefficients.**

Bar type	Diameter (in.)	D (in. <sup>2</sup> /sec)	
		Distilled water	Alkaline solution
P	0.500	9.12E-10	1.61E-10
	0.625	1.65E-09	1.04E-09
	0.750	1.92E-09	1.35E-09
V1	0.500	9.74E-10	3.36E-10
	0.625	4.47E-10	1.02E-09
	0.750	1.74E-09	2.39E-09
V2	0.500	1.68E-11	4.74E-11
	0.625	1.14E-09	1.19E-09
	0.750	8.03E-10	1.85E-09
Average		1.07E-09	1.04E-09
Standard Deviation		6.23E-10	7.79E-10

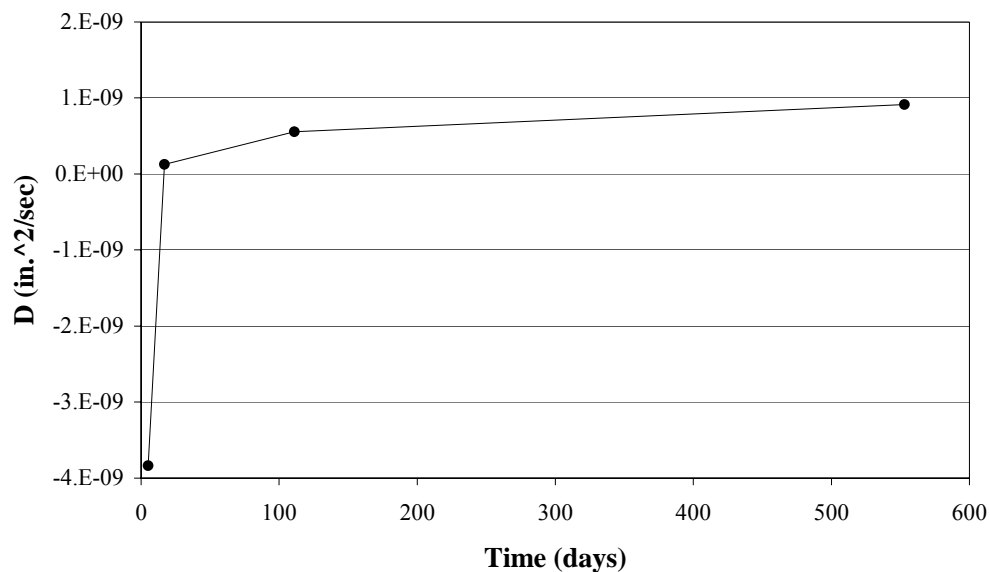


**Figure 41. Typical Trend of Computed Diffusion Coefficients.**

The diffusion coefficients indicated in Table 31 are similar to diffusion coefficients obtained by other authors. Tannous and Saadatmanesh (1999) obtained a diffusion coefficient of  $1.06 \times 10^{-11}$  inch<sup>2</sup>/sec for 0.375-inch diameter GFRP bars exposed to distilled water at 77 °F. Carter and Kibler (1978) reported a diffusion coefficient of  $1.63 \times 10^{-10}$  inch<sup>2</sup>/sec for resin type 5208 at 75 °F. Soles et al. (2000) reported diffusion coefficients that ranged from  $2.5 \times 10^{-8}$  to  $5.8 \times 10^{-8}$  inch<sup>2</sup>/sec for resins with different stiffnesses at 95 °F. Sen et al. (2002) reported diffusion coefficients that ranged from  $1.49 \times 10^{-8}$  to  $1.38 \times 10^{-10}$  inch<sup>2</sup>/sec for 0.375-inch diameter GFRP bars exposed to an alkaline solution with average pH of 13.4.

The diffusion coefficients obtained from Table 31 were used to compute the moisture absorption as a function of time for the bars studied. The results are plotted in Figures 42 and 43. The nomenclature used in Figures 42 and 43 to identify the bar type and size is the same as described previously.

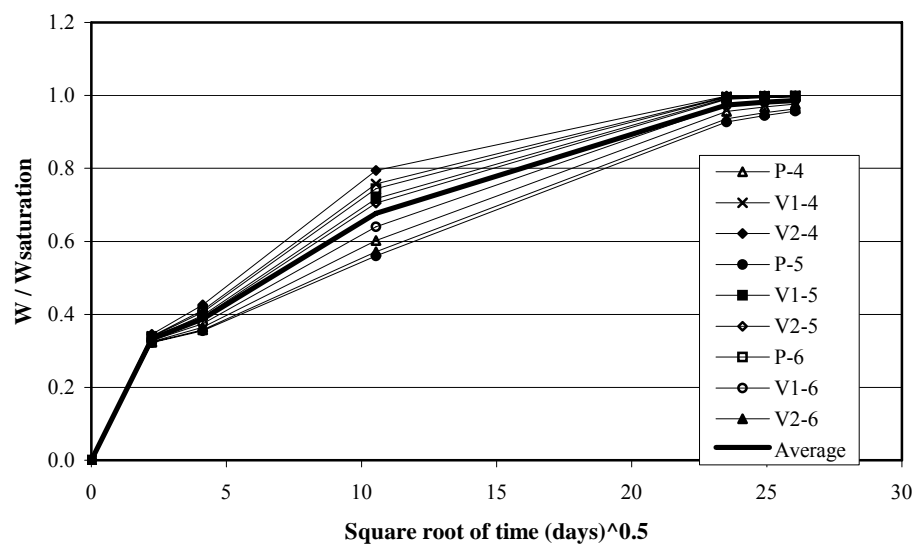


**Figure 42. Predicted Weight Gain for Distilled Water Specimens Using Computed Diffusion Coefficients.**

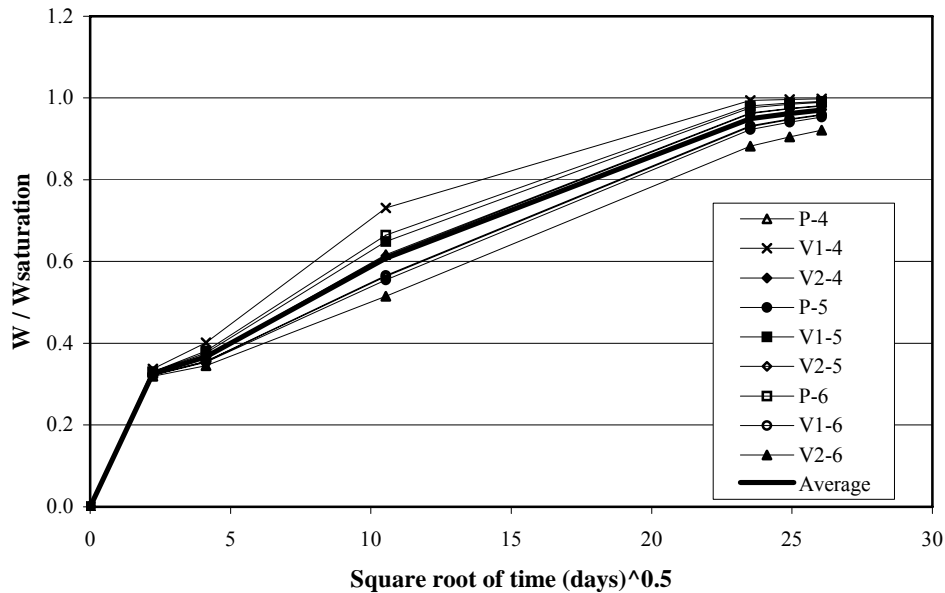


**Figure 43. Predicted Weight Gain for Alkaline Solution Specimens Using Computed Diffusion Coefficients.**

Comparing Figure 39 with Figure 42 and Figure 40 with Figure 43, it can be seen that the average computed weight gain is higher than the mean measured weight gain. This observation is more clear in Figures 44 and 45. Thus, the computed diffusion coefficients predict higher moisture contents than measured values before saturation for all times. The saturation time is the same in the predicted and measured specimens.

The predictions of the tensile strength degradation of the GFRP bars are not significantly affected by the fact that the computed diffusion coefficients predict higher, although conservative, moisture contents than those measured. This observation is adequate, since the time required for saturation of the bars is approximately 550 days (1.5 years), a small fraction of the time structures are intended to last.

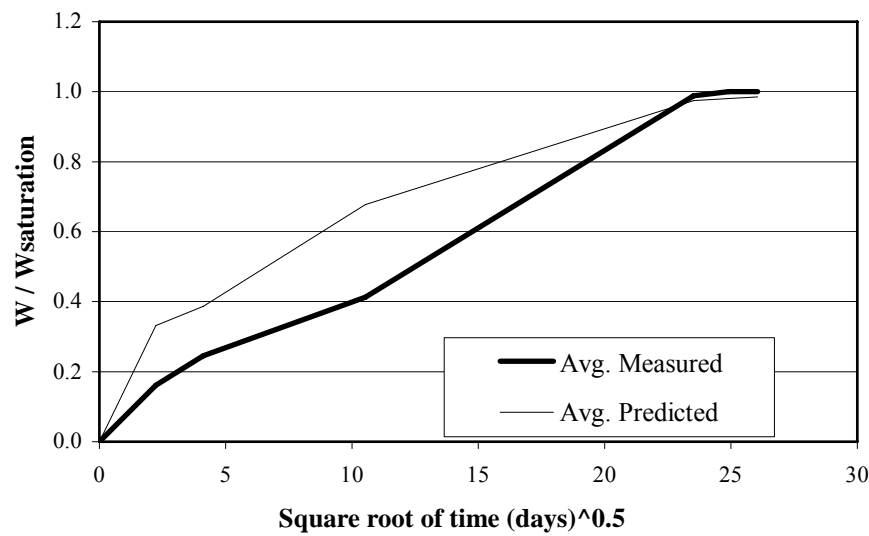


Figure 44. Comparison between Average Predicted and Measured Absorption in Distilled Water.

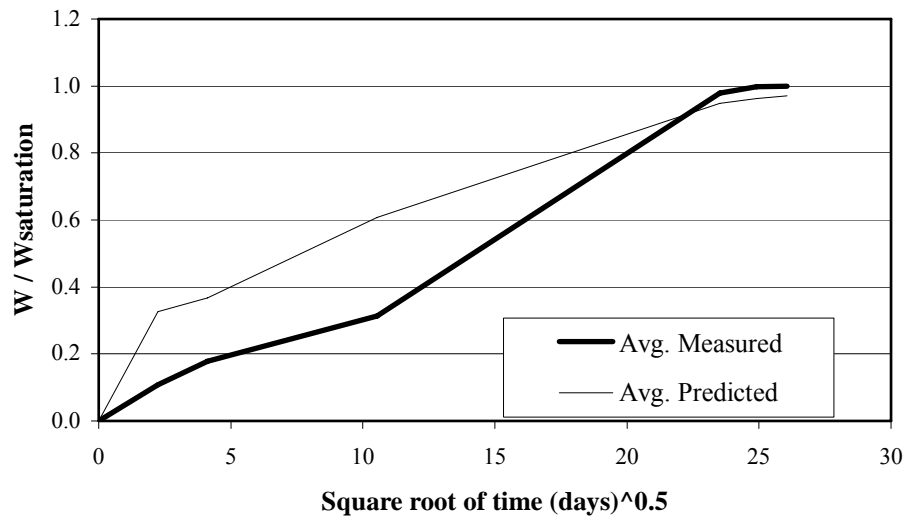


Figure 45. Comparison between Average Predicted and Measured Absorption in Alkaline Solution.

## Tensile Strength Degradation Analysis

To estimate the degradation of GFRP bars over time, the method proposed by Katsuki and Uomoto (1995) will be modified. Katsuki and Uomoto predicted the depth of penetration of a solution into an FRP bar to be:

$$x = \sqrt{2Dct} \quad (22)$$

where,

$x$  = the depth from surface of the bar (mm),

$D$  = the diffusion coefficient of the FRP bar in concrete pore solution ( $\text{mm}^2 \text{ sec}^{-1}$ ),

$c$  = the concentration of the exposure solution (mol/l),

$t$  = time (sec).

The depth  $x$  is illustrated in [Figure 46](#).

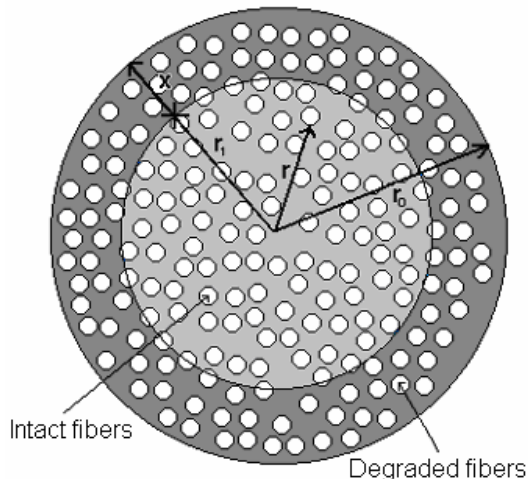


**Figure 46. Schematic of Degradation Model.**

Katsuki and Uomoto (1995) obtained the following expression for the computation of the residual tensile strength:

$$\sigma_t = \left(1 - \frac{\sqrt{2Dct}}{r_0}\right)^2 \sigma_0 \quad (23)$$

where,

- $\sigma_t$  = the tensile strength at any give age (psi),
- $\sigma_0$  = the tensile strength before exposure (psi),
- $r_0$  = *the bar radius (inch).*

The model by Katsuki and Uomoto assumed the fibers located in the region ( $r < r_I$ ) to be intact and the fibers located in the region ( $r_0 > r > r_I$ ) to be completely degraded. This assumption would imply that the whole bar would be entirely deteriorated upon saturation, at approximately 1.5 years. However, glass fibers do not degrade instantaneously as they are exposed to the solution. Therefore, [Equation 23](#) will be modified to account for the fact that time is required to degrade the glass fibers as follows:

$$\sigma_t = \left(1 - \frac{\sqrt{2D\lambda t}}{R_0}\right)^2 \sigma_0 \quad (24)$$

where the terms are as defined earlier and  $\lambda = f(c, t)$ . [Equation 24](#) yields the residual tensile strength using an equivalent depth of penetration. The difference between the new proposed depth of penetration ( $x' = (2D\lambda t)^{1/2}$ ) and  $x$  is that  $x'$  is smaller than  $x$ , since glass fibers do not degrade instantaneously upon contact with a solution. The predicted residual strength will be computed using the overall average diffusion coefficient obtained from the distilled water exposure specimens. The value of  $\lambda$  will be obtained by fitting the predicted residual tensile strength to the overall lowest observed tensile strength obtained from the tension tests for the 0 and 50 weeks exposure times, using least squares. The value determined for  $\lambda$  was 0.006. The predicted residual tensile strengths are plotted in [Figure 47](#) and are labeled “fit to lowest observed values.” [Figure](#)

[47](#) also shows all the data points for the measured relative tensile strengths at 0, 26, and 50 weeks. Since [Equation 24](#) is parabolic, the predicted relative tensile strengths will reach a minimum at a given time and then will increase. Therefore, [Equation 24](#) should be valid only for residual tensile strength predictions up to the time when the minimum relative residual tensile strength is reached. The residual tensile strengths should be considered to remain constant beyond that time.

There are obvious limitations on the validity of the model to predict residual tensile strengths at long periods of time, since the model is based on residual strength data for exposures of only one year. In addition, recent work indicates that the basic assumption by Katsuki and Uomoto that alkali ions can migrate into GFRP bars may not be applicable ([Jones 1998, Dejke 2001](#)). Nevertheless, in the absence of reliable long-term data, the model was used to predict residual relative tensile strengths at exposure times much larger than those covered by the experiments. The residual tensile strengths were predicted to be 0.64, 0.55, 0.49, and 0.44 at 5, 10, 15, and 20 years, respectively.

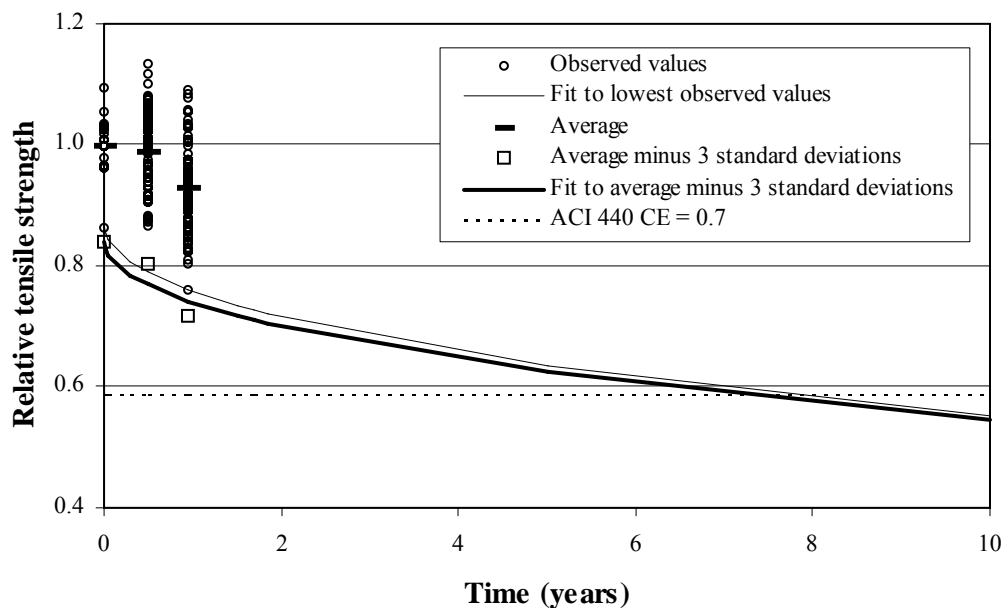


**Figure 47. Measured and Predicted Residual Relative Tensile Strength.**

The ACI 440 (2001) design guidelines recommend using a design tensile strength for the FRP bars equal to:

$$f_{fu} = C_E f_{fu}^* \quad (25)$$

where,

$f_{fu}$  = Design tensile strength of FRP, considering reduction for service environment, *psi*,

$C_E$  = Environmental reduction factor (0.8 and 0.7 for GFRP bars, for concrete not exposed to earth and weather, and concrete exposed to earth and weather, respectively),

$f_{fu}^*$  = Guaranteed tensile strength of an FRP bar defined as the mean tensile strength of a sample of test specimens minus three times the standard deviation ( $f_{fu}^* = f_{u,avg} - 3\sigma$ ) (*psi*).

The overall average and standard deviations of the tensile strength of all the specimens tested were presented in the tension test section. The standard deviations of the relative tensile strength for all the specimens tested at 0, 26, and 50 weeks of exposure were 0.054, 0.063, and 0.070, respectively. The standard deviations were used to compute the guaranteed tensile strength, by subtracting three standard deviations from the average values, at 0, 26, and 50 weeks. The guaranteed relative tensile strengths at 0, 26, and 50 weeks are 0.84, 0.80, and 0.72, respectively. A new value of  $\lambda$  equal to 0.0057 was obtained by fitting a new predicted residual tensile strength to the guaranteed relative tensile strength obtained for the 26- and 50-week exposure times, using least squares. The results are presented in [Figure 47](#) and are labeled “fit to average minus 3 standard deviations.” The residual tensile strengths, relative to the initial tensile strength, at 5, 10, 15, and 20 years were predicted to be 0.64, 0.55, 0.49, and 0.44, respectively. On the other hand, the residual tensile strengths, computed relative to the guaranteed initial tensile strength are 0.74, 0.65, 0.58, and 0.53 at 5, 10, 15, and 20 years, respectively. [Figure 47](#) shows (with a dashed line) the design relative tensile

strength computed following the ACI 440 design guidelines for an environmental reduction factor of 0.7. [Figure 47](#) indicates that the predictions made with the lowest value fit line and with the average minus three standard deviations fit line are similar. [Figure 47](#) also shows that the predicted residual tensile strength and the design strength computed following the ACI 440 design guidelines meet at approximately seven years. This indicates that if the exposure conditions of the test specimens match those of bars embedded in concrete elements in the field, the environmental reduction factor of 0.7 for glass FRP bars given in the ACI 440 design guidelines may be unconservative beyond 7 years assuming the best fit equation can be interpolated beyond one year. A comparison between the results obtained and the ACI 440 design guidelines will be given in [Section V](#).

Sen et al. ([2002](#)) conducted tests on 0.375-inch diameter E-glass vinyl ester bars unstressed and subjected to 10, 15, and 25 percent of the ultimate stress. Several sets of three bars each were exposed to a simulated concrete pore solution with a pH that varied between 13.35 and 13.55. The authors found that the residual tensile strength of exposed specimens with no load was 50 percent of the original tensile strength, on average, after one month of exposure. The residual strength of the specimens stressed at 10 percent of the ultimate original strength showed a residual strength of 40 percent, and the specimens loaded at 25 percent of the initial original strength showed a strength reduction of 100 percent (all of the specimens failed). At six months of exposure, the results obtained were as follows: the unloaded specimens showed average residual tensile strengths of 36 percent, the specimens loaded at 10 percent of the original strength showed average residual tensile strengths of 31 percent, and the specimens loaded at 15 percent of the original strength showed average residual tensile strengths of 8 percent. At nine months of exposure, the unloaded specimens showed average residual strengths of 37 percent, the specimens loaded at 10 percent of the initial ultimate strength showed an average residual strength of 30 percent, and the specimens loaded at 15 percent of the ultimate initial strength showed strength reductions of 100 percent (all

of the specimens failed). It is clear from these results that stress level affects GFRP bars considerably and that using even the lower bound relative strength values may be unconservative.

The residual tensile strengths obtained by Sen et al. (2002) are lower than values obtained in this project. The results of the unloaded test results from Sen et al. and from this project are compared in [Table 32](#). Sen et al. obtained much larger tensile strength degradations than obtained in this project. This may be because Sen and coworkers exposed their specimens to a pH higher than used in this project. Sen and coworkers argue that the concrete pH varies between 12.5 and 13.5, while Mindess and Young (1981) report that concrete pH values typically range between 12 and 12.5. Since pH is based on a logarithmic scale, an increase in pH of one is a ten-fold increase in hydroxyl ions ( $\text{OH}^-$ ). Obviously the concrete pH depends on the concrete mix and raw materials used to make it; however, the value of 13.3 used by Sen et al. could be on the high side. Another reason that contributed to the faster degradation observed by Sen and coworkers is that they tested 0.375-inch diameter specimens, while this project tested 0.625-inch diameter specimens. As indicated in the moisture absorption results, smaller diameter bars will saturate faster than larger diameter bars and, therefore, will degrade faster. Based on this analysis, the results of the unstressed bars tested in this project can be assumed to be an upper bound residual tensile strength.

**Table 32. Comparison of Relative Residual Tensile Strength Results of Unstressed Specimens.**

Project	6 Months		9 or 11.5 Months	
	Avg. pH	Residual tensile strength	Avg. pH	Residual tensile strength
Sen et al. (2002)	13.35	0.36	13.41	0.37 at 9 months
This project (guaranteed strength fit)	12.00	0.77	12.00	0.74 at 11.5 months
This project (smallest observation fit)	12.00	0.79	12.00	0.76 at 11.5 months

The results of the moisture absorption of bars with capped and uncapped ends have been presented. The results show that all specimens were either saturated or close to saturation at approximately 1.5 years. Capping of the moisture absorption specimens is necessary to model more accurately the moisture absorption behavior of GFRP bars used in service conditions. Fick's second law of diffusion can be used to model the moisture absorption of GFRP bars. The solution to the differential equation of diffusion of a solution into an infinitely long cylinder with constant concentration at the surface as presented by Jost (1952) was used to find the diffusion coefficients of the specimens studied. Results indicate that diffusion through GFRP bars takes place at a faster rate when the solution is distilled water when compared with calcium hydroxide exposure solutions. The average diffusion coefficient of the specimens exposed to distilled water was used in a degradation model obtained by modifying the model proposed by Katsuki and Uomoto (1995). This was done to better account for the time required for glass fibers to degrade. Finally, predictions of residual tensile strengths were made using the modified tensile strength degradation model. The limitations of the prediction model are that only one bar size was studied, the specimens were exposed for only 1.5 years, and as described in the [tension test results section](#), a larger number of specimens may be necessary for statistical validation due to the high variability of the tensile strength of GFRP bars.

## DIRECT SHEAR STRENGTH TEST

As noted in [Section II](#), the degradation of the direct shear strength of GFRP bars is an important parameter for design of FRP-reinforced concrete structures that has not yet been characterized. [Section II](#) also describes an application where the shear modulus of elasticity could be used. This section presents the direct shear strength test results, followed by the shear modulus of elasticity test results and by a failure analysis.

The direct shear strength tests were conducted with 0.625-inch diameter bars. As indicated in the uncapped end moisture absorption tests, bar types P, V1, and V2 were

exposed for 48, 68, and 68 weeks, respectively. Bar type P specimens were exposed for only 48 weeks because the exposure test began with the other bars before bar types P were received.

### **Direct Shear Strength Test Results**

Tables 33, 34, and 35 show the shear strength test results for bar types P, V1, and V2, respectively. It can be observed from Tables 33 through 35 that the maximum COV of the shear strength is 8 percent. In general, the coefficients of variation of the shear strength test results are smaller than the coefficients of variation obtained for the tension tests.

**Table 33. Shear Strength Values of Bar Type P.**

Specimen	Unexposed (psi)	Exposed for 48 weeks (psi)			
		pH = 7	pH = 7, Na Cl	pH = 12	pH = 12, Na Cl
1	22,487	22,915	21,130	21,273	20,416
2	22,201	23,058	21,273	22,772	21,487
3	22,344	21,915	21,559	20,631	22,130
4	20,488	-	-	-	-
5	21,915	-	-	-	-
Average	21,887	22,629	21,321	21,559	21,344
S.D.	810	622	218	1,099	866
COV	0.04	0.03	0.01	0.05	0.04

**Table 34. Shear Strength Values of Bar Type V1.**

Specimen	Unexposed (psi)	Exposed for 68 weeks (psi)			
		pH = 7	pH = 7, Na Cl	pH = 12	pH = 12, Na Cl
1	23,415	24,129	22,701	22,201	23,700
2	23,058	21,915	22,344	22,772	24,057
3	23,914	20,559	22,986	21,915	23,058
4	22,986	-	-	-	-
Average	23,343	22,201	22,677	22,296	23,605
S.D.	424	1,802	322	436	506
COV	0.02	0.08	0.01	0.02	0.02

**Table 35. Shear Strength Values of Bar Type V2.**

Specimen	Unexposed (psi)	Exposed for 68 weeks (psi)			
		pH = 7	pH = 7, Na Cl	pH = 12	pH = 12, Na Cl
1	20,916	21,416	20,845	19,988	20,988
2	21,773	23,058	23,058	18,061	20,988
3	21,559	20,060	20,559	21,202	20,773
4	23,058	-	-	-	-
5	21,130	-	-	-	-
Average	21,687	21,511	21,487	19,750	20,916
S.D.	838	1,501	1,368	1,584	124
COV	0.04	0.07	0.06	0.08	0.01

[Figure 48](#) shows a comparison of the direct shear strength results. The ordinate indicates the shear strength results after exposure relative to the unexposed shear strength. It can be observed that the most severe condition is the high pH exposure. In this case, the direct shear strength reductions amount to 2, 4, and 9 percent of the original shear strength values for bar types P, V1, and V2, respectively. As indicated by Paul (1982) all silicate glasses become especially susceptible to decomposition when in contact with a solution with pH values higher than approximately 9 or 10. Thus, larger shear strength degradations are expected to occur in GFRP bars exposed to high pH solutions. Nevertheless, a shear strength increase of approximately 3 percent relative to the original value was recorded for bar type P after 48 weeks of exposure to distilled water, and a relative increase of approximately 2 percent was measured in bar type V1 after 68 weeks of exposure in a high pH solution with chlorides. The apparent shear strength increase may result from the high variability of the mechanical properties of GFRP bars as indicated in the [tension test results section](#).

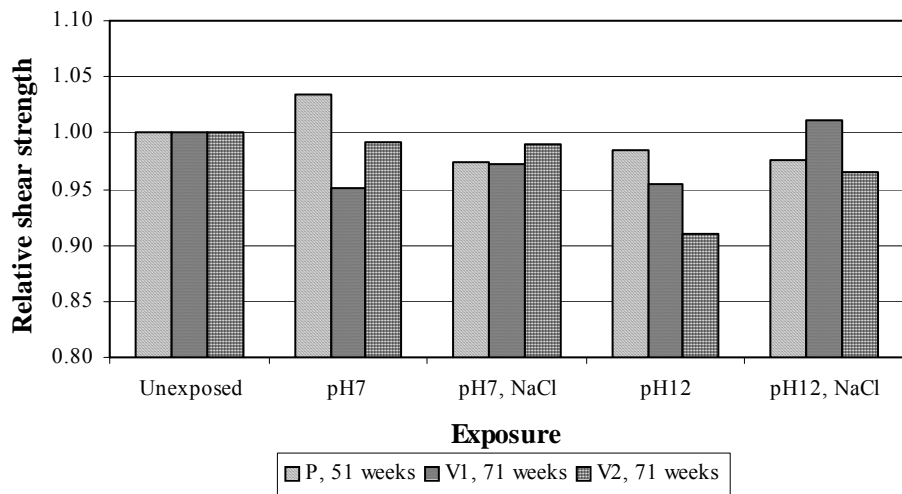


**Figure 48. Relative Shear Strength versus Exposure Condition.**

### Shear Modulus of Elasticity Test Results

Tables 36, 37, and 38 show the shear modulus of elasticity test results for bar types P, V1, and V2, respectively. The shear modulus of elasticity is the slope of the direct shear stress versus the shear strain curve. The shear moduli of elasticity test results have higher variability than the shear strength test results.

**Table 36. Shear Modulus of Elasticity Values of Bar Type P.**

Specimen	Unexposed (psi)	Exposed for 48 weeks (psi)			
		pH = 7	pH = 7, Na Cl	pH = 12	pH = 12, Na Cl
1	2,465	2,432	2,554	1,897	2,369
2	2,513	2,198	2,814	2,131	2,185
3	2,365	1,808	2,233	2,143	2,112
4	2,305	-	-	-	-
5	2,411	-	-	-	-
Average	2,412	2,146	2,534	2,057	2,222
S.D.	82	315	291	139	132
COV	0.03	0.15	0.11	0.07	0.06

**Table 37. Shear Modulus of Elasticity Values of Bar Type V1.**

Specimen	Unexposed (psi)	Exposed for 68 weeks (psi)			
		pH = 7	pH = 7, Na Cl	pH = 12	pH = 12, Na Cl
1	2,446	2,368	2,121	2,526	2,621
2	2,608	2,617	2,884	2,125	2,629
3	2,393	2,340	2,531	2,552	2,413
4	2,911	-	-	-	-
Average	2,590	2,442	2,512	2,401	2,554
S.D.	233	152	382	239	122
COV	0.09	0.06	0.15	0.10	0.05

**Table 38. Shear Modulus of Elasticity Values of Bar Type V2.**

Specimen	Unexposed (psi)	Exposed for 68 weeks (psi)			
		pH = 7	pH = 7, Na Cl	pH = 12	pH = 12, Na Cl
1	2,766	3,195	2,460	2,308	2,628
2	2,866	3,160	2,903	2,629	2,916
3	2,941	2,877	2,910	2,520	2,734
4	2,893	-	-	-	-
5	2,568	-	-	-	-
Average	2,807	3,077	2,758	2,486	2,759
S.D.	148	174	258	163	146
COV	0.05	0.06	0.09	0.07	0.05

A comparison of the average values of the shear modulus of elasticity test results obtained before and after exposure is presented in [Figure 49](#). The ordinate indicates the shear modulus of elasticity of exposed specimens relative to the shear modulus of elasticity of unexposed specimens. Once again, the pH of 12 exposure condition seems to be the most severe condition, resulting in shear modulus of elasticity reductions of 15, 7, and 11 percent for bar types P, V1, and V2, respectively. An increase in shear modulus of elasticity of nearly 10 percent relative to the original value was recorded in bar type V2 after 68 weeks of exposure to distilled water. A relative shear modulus of elasticity increase of 5 percent was found for bar type P after 48 weeks of exposure to a solution made with distilled water and chlorides.

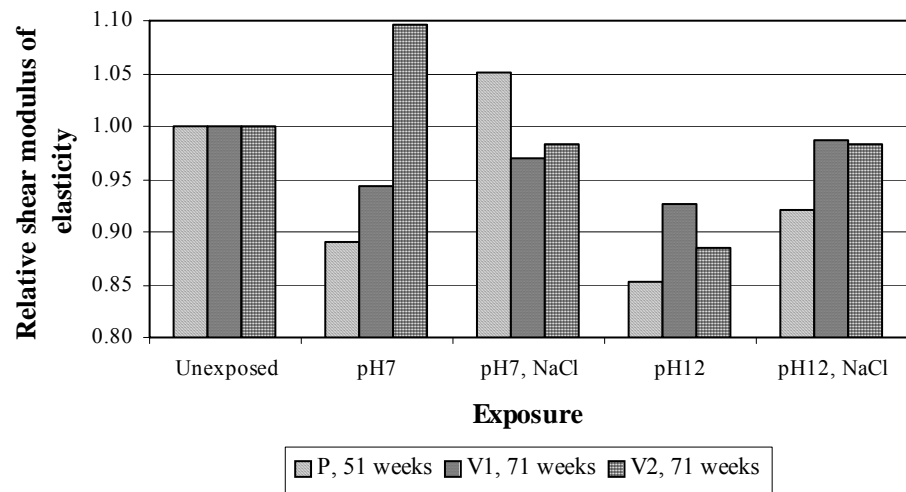


**Figure 49. Relative Shear Modulus of Elasticity versus Exposure Condition.**

### Failure Analysis

In the case of a unidirectional composite subjected to shear forces, failure may occur by matrix shear failure, matrix shear failure with fiber debonding, fiber debonding, or shear rupture of fibers (Agarwal 1990). Figures 50, 51, and 52 illustrate the failure modes of bar types P, V1, and V2, respectively.

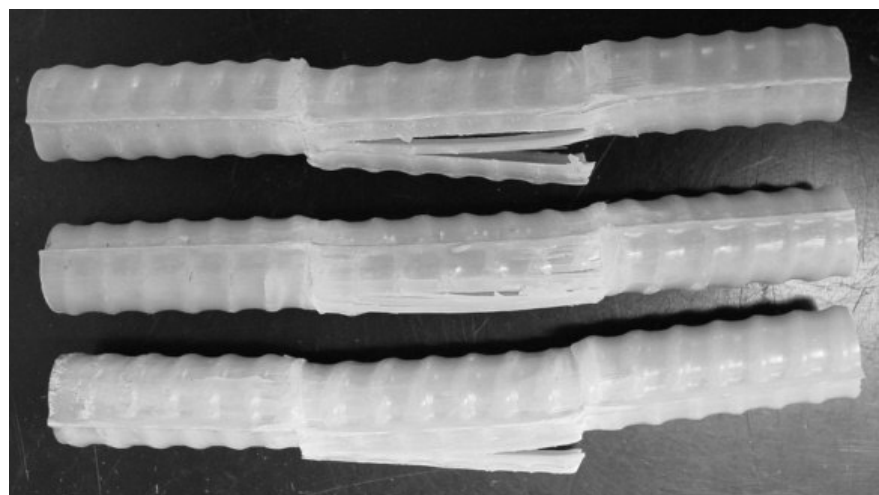


**Figure 50. Failure of Bars Type P.**

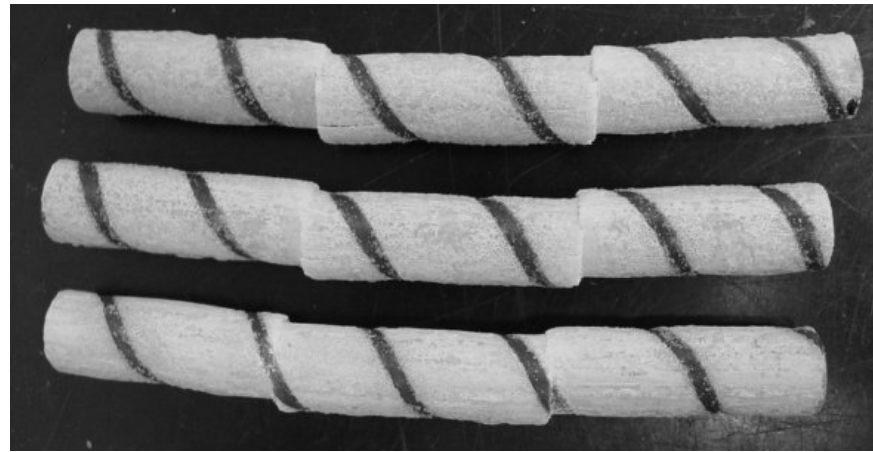


**Figure 51. Failure of Bars Type V1.**

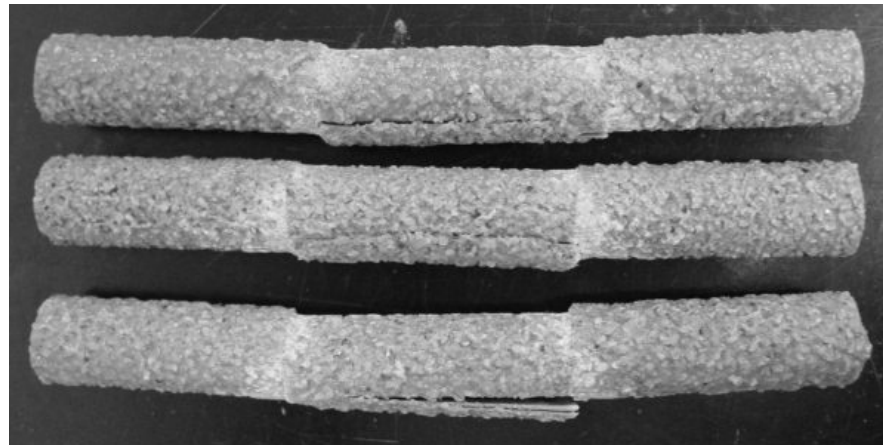


**Figure 52. Failure of Bars Type V2.**

It can be observed in Figures 50 and 52 that bars type P and V2 tend to fail by a combination of constituent debonding and shear rupture of the matrix and the glass fibers. Bars type V1 failed primarily by direct shear, that is to say, mostly by matrix shear failure and fiber rupture as illustrated in Figure 51.

As an application of the use of the shear strength of GFRP bars in design, consider the case of a concrete pavement connected to a bridge deck with GFRP bars

(even though this is not the case for pavement-bridge interfaces in Texas). The connection can be conservatively designed by assuming the shear force transmitted to the pavement by a vehicle will be transferred to the deck solely by shear through the GFRP bars. As such, the shear strength of the barrier can be computed to be:

$$V = A_f N \tau_f \quad (26)$$

where,

$V$  = Shear strength of the barrier (*lb.*),

$A_f$  = FRP bar area (*inch*<sup>2</sup>),

$N$  = Number of FRP bars,

$\tau_f$  = Shear strength of a GFRP bar (*psi*).

From this project, it was found that after 71 weeks of exposure, a degradation of the direct shear strength of the GFRP bars was reduced by as much as 9 percent of the original direct shear strength. Therefore, a direct shear strength reduction factor should be applied to [Equation 26](#) to include the long-term exposure effects in the design of GFRP-reinforced structural elements connected with GFRP bars subjected to direct shear. The proposed equation should consist of an exposure factor,  $k$ , as follows:  $V_{exp} = k A_f N \tau_f$ , where  $k$  represents the degradation as a function of time.

Summarizing, exposing GFRP bars to simulated concrete pore solutions for a period of 68 weeks could lead to reductions in the direct shear strength of the bars as high as 9 percent of the original shear strength value. The shear modulus of elasticity reductions could be as high as 15 percent from the original for some bars after 48 weeks of exposure to simulated concrete pore solutions.

## CREEP TEST

It was discussed in [Section II](#) that a limit on deflections is one of the serviceability requirements that typically governs the design of FRP-reinforced concrete elements. A method currently available for the computation of deflections for FRP-reinforced concrete elements was also reviewed in [Section II](#). It was noted that the method used to compute long-term deflections of FRP-reinforced concrete elements given by the ACI 440 design guidelines does not account for creep of FRP bars. Before presenting the creep test results, some definitions of terms used in this section will be given. This section describes the results of the creep test, followed by a description of a method that can be used in the computation of long-term deflections of FRP-reinforced concrete elements accounting for creep of the FRP bars.

### Definitions

#### *Creep*

The definition of creep given by Shackelford ([1996](#)) is that creep is the plastic (permanent) deformation occurring at high temperature under constant load over a long time period. Neville and Meyers ([1964](#)) defined concrete creep as “an increase with time in the strain of concrete subjected to stress.” Lin and Burns ([1981](#)) define creep as “time-dependent inelastic deformation of concrete or steel resulting solely from the presence of stress and a function thereof.” Gere and Timoshenko ([1990](#)) define creep as the increase in length of a bar loaded with a constant force over time, beyond the initial (elastic) deformation. The definition of creep given by Gere and Timoshenko ([1990](#)) will be used in this section.

#### *Relaxation*

Lin and Burns ([1981](#)) define relaxation as the “time-dependent inelastic deformation of steel resulting from sustained stress and a function thereof.” Gilbert and Mickleborough ([1990](#)) indicated that high-strength steel creeps under high stress and that

the loss of stress in a tendon subjected to a constant strain is known as relaxation. According to Gere and Timoshenko (1990), stretching a wire between two immovable supports will cause an initial stress in the wire, and as time elapses, the stress in the wire gradually diminishes a manifestation of creep, which is called relaxation of the material. The definition of relaxation given by Gere and Timoshenko (1990) will be used in this section.

### Creep Test Results

The criterion used to determine the elastic and creep strains in the GFRP bars tested in this project is illustrated in Figure 53. The magnitudes of the elastic and creep strains at different times for a bar subjected to constant tensile forces are shown in Figure 53. The following nomenclature is used in Figure 53:

$P$	= Force
$L$	= Initial bar length
$L'$	= Final bar length at time $t_1$
$\Delta L$	= Initial elastic elongation of the bar, after the application of force $P$
$\Delta L'$	= Total bar elongation due to creep at time $t_1$
$\varepsilon_e$	= Elastic strain
$\varepsilon_c$	= Creep strain
$\varepsilon_T$	= Total strain
$t$	= Time
$\varepsilon_{eo}$	= Elastic strain at time $t_o$
$\varepsilon_{co}$	= Creep strain at time $t_o$
$\varepsilon_{To}$	= Total strain at time $t_o$
$\varepsilon_{e1}$	= Elastic strain at time $t_1$
$\varepsilon_{c1}$	= Creep strain at time $t_1$
$\varepsilon_{T1}$	= Total strain at time $t_1$
$\sigma$	= Stress

It can be demonstrated in Figure 53 that the elastic strain remains constant over time; the creep strain, initially zero, develops over time, and the total strain increases over time in a tension specimen subjected to constant load. Nádai (1931) reported that the stress in the bar remains essentially constant for small strain values. The true stress should be computed when large strains develop (Nádai 1931).

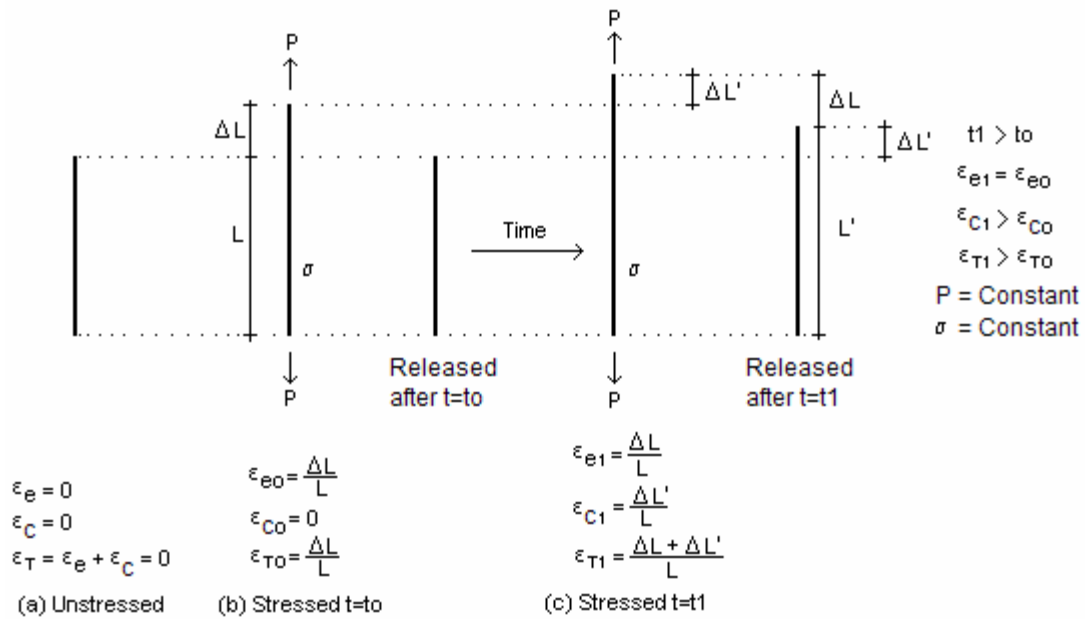
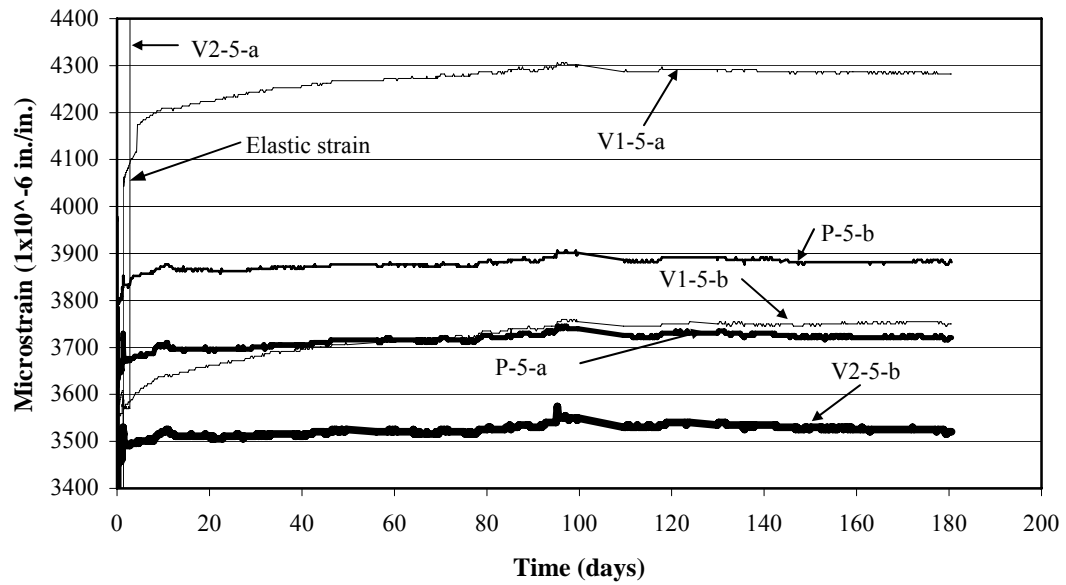


Figure 53. Elastic and Creep Strains of a Bar under Constant Load.

The creep test procedure was described in [Section III](#). Six GFRP bars were placed in creep frames located inside a controlled-environment room with an average temperature of 88 °F and a relative humidity of 67 percent for a period of six months. The specimens were loaded to simulated service load conditions, and a load equivalent to approximately 23 percent of the ultimate tensile load of the GFRP bars was applied to the specimens. The load applied to the bars was 6900 lb. The bars used in the test had a diameter of 0.625 inch. Thus, the stresses present in bars were 20,110 psi, 20,710 psi, and 20,170 psi for specimens with bar types P, V1, and V2, respectively. These stresses correspond to 24, 23, and 27 percent of the ultimate strength of the bar types P, V1, and V2, respectively. Although the ACI 440 design guidelines recommend limiting the stress due to sustained loads to 20 percent of the ultimate strength of the bars, the researchers selected the stress levels indicated to obtain conservative estimates of the creep deformation of the GFRP bars. These stresses are higher than sustained stresses expected under service loading in a bridge deck

Creep strain is the strain increase, with time, recorded beyond the elastic strain. The time-microstrain curves recorded for the samples tested in this project are shown in [Figure 54](#). One microstrain is equal to one millionth of a millimeter per millimeter. For example, 10,000 microstrain is equivalent to a strain of 0.01 inch/inch, or 1 percent. In [Figure 54](#), the specimens are identified by bar type first, followed by nominal bar size in eighths of an inch, and by specimen (either a or b). It can be observed in [Figure 54](#) that all specimens had a relative peak in strain at approximately 95 days. It is not clear why this occurred; however, the strain readings could have been affected by temperature or moisture changes at that time. [Figure 54](#) illustrates that the largest increase in strain rate beyond the initial elastic strain was developed during the first 10 days. After 10 days, the strain increased at a slower rate with some variations. The location of the elastic strain after the load was applied to the bar is indicated in [Figure 54](#) for specimen V1-5-a. The elastic strain was the strain recorded immediately after the loading jack was released and the 500 lb. load was hanging freely from each creep frame. The elastic strains for all specimens are shown in [Table 39](#). The test was run for a period of 180 days. The creep test data are presented in [Table B1](#) of [Appendix B](#).

From the data shown in [Table 39](#), it can be determined that specimens manufactured without fibers wrapped round the bar (P and V2) showed an increase in strain beyond the initial elastic strain on the order of 2 percent. This value was computed by dividing the creep strain by the elastic strain from [Table 39](#). Specimens V1, which were manufactured with fibers wound around the bar, exhibited an increase in strain beyond the initial elastic strain on the order of 6 percent over the six-month period. A similar behavior was reported by Yamasaki et al. (1993) where stranded or braided carbon FRP bars displayed strains from 100 to 300 microstrain larger than straight carbon FRP bars after being subjected to a constant load equal to one-third of the tensile strength of the bars for one year. Sixty-five hours after being loaded, specimen V2-5-b failed by rupture of the bar. Failure of the specimen occurred at the gripping end.



**Figure 54. Creep Test Results.**

**Table 39. Creep Strain of GFRP Bars at Six Months.**

Specimen	Elastic strain (microstrain)	Final strain (microstrain)	Creep strain (microstrain)	Creep strain over elastic strain (%)
P-5-a	3643	3721	78	2.1
P-5-b	3794	3882	88	2.3
V1-5-a	4058	4282	224	5.5
V1-5-b	3521	3755	234	6.6
V2-5-a	3457	3525	68	2.0
V2-5-b	3555	This specimen failed at 65 hours after the test began		

### Time-Dependent Deformation Analysis

The long-term deformation analysis presented here was modified from an analysis used in prestressed concrete elements presented by Gilbert and Mickleborough (1990). The analysis presented is for the computation of the time-dependent strains and curvatures of cracked GFRP-reinforced concrete elements, where creep of the GFRP bars is taken into account. An analogy between deformations of prestressed concrete

elements due to relaxation of the high-strength prestressing steel and the deformations of GFRP-reinforced concrete elements due to creep of GFRP bars will be presented first. The difference between relaxation and creep has been explained in the definitions addressed previously.

#### *Analogy between Deformations of Steel-Prestressed Concrete and GFRP-Reinforced Concrete Elements*

Under constant total strain, high-strength steel relaxes (loses stress) over time. High-strength steel develops permanent deformations due to dislocation glide at high stresses and temperatures below the melting temperature (Courtney 2000). This behavior is illustrated in Figure 55 for a steel tendon that is held at a constant total strain. The terms of Figure 55 are as defined before, and the subscript *r* represents relaxation.  $P_o$  and  $P_1$  are the forces present in the tendon at times  $t_o$  and  $t_1$ , respectively; and  $\sigma_o$  and  $\sigma_1$  are the stresses present in the tendon at times  $t_o$  and  $t_1$ , respectively. It can be observed that the prestressing force and the stresses present in the tendon are reduced due to relaxation. The prestressing force is reduced because the elastic strain is reduced over time. The elastic strain is reduced as the creep strain increases.

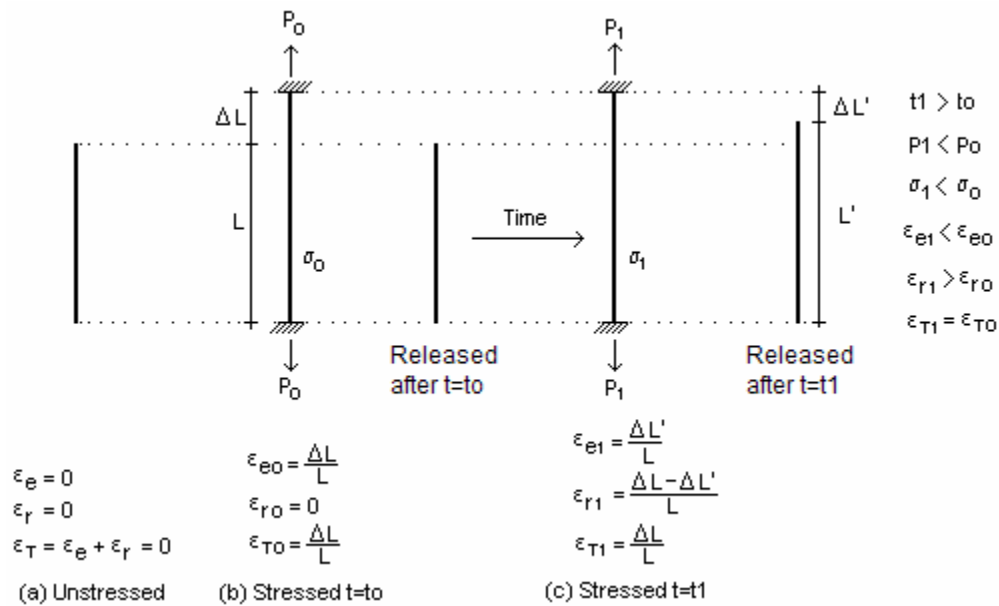


**Figure 55. Relaxation of Prestressing Steel Tendon.**

The same behavior is observed in an imaginary unbonded prestressed concrete beam where shrinkage and creep of the concrete are artificially prevented. Figure 56 illustrates the case where a beam with an unbonded tendon is prestressed and subjected to a distributed load  $w$ . At transfer ( $t = t_o$ ), the strain present in the tendon is the elastic strain ( $\varepsilon_{eo}$ ), the prestressing force is  $P_o$ , and the deflection is  $\Delta_o$ . After an elapsed time,  $\Delta t = t_1 - t_o$ , relaxation of the tendon occurs, and the strain in the tendon consists of an elastic strain component ( $\varepsilon_{eI}$ ) and a relaxation strain component ( $\varepsilon_{rI}$ ), with the total strain ( $\varepsilon_{T1} = \varepsilon_{eI} + \varepsilon_{rI}$ ) remaining constant, as illustrated in part c of Figure 55. As a result of the relaxation of the tendon, the prestressing force is reduced to  $P_1$ , and the deflection increases to  $\Delta_1$ . The nomenclature used in Figure 56 is the same as in Figure 55, and  $\Delta$  is the midspan beam displacement. The strains developed at times  $t_o$  and  $t_1$  in Figure 56 are the same as the strains of Figure 55 for times  $t_o$  and  $t_1$ , respectively.

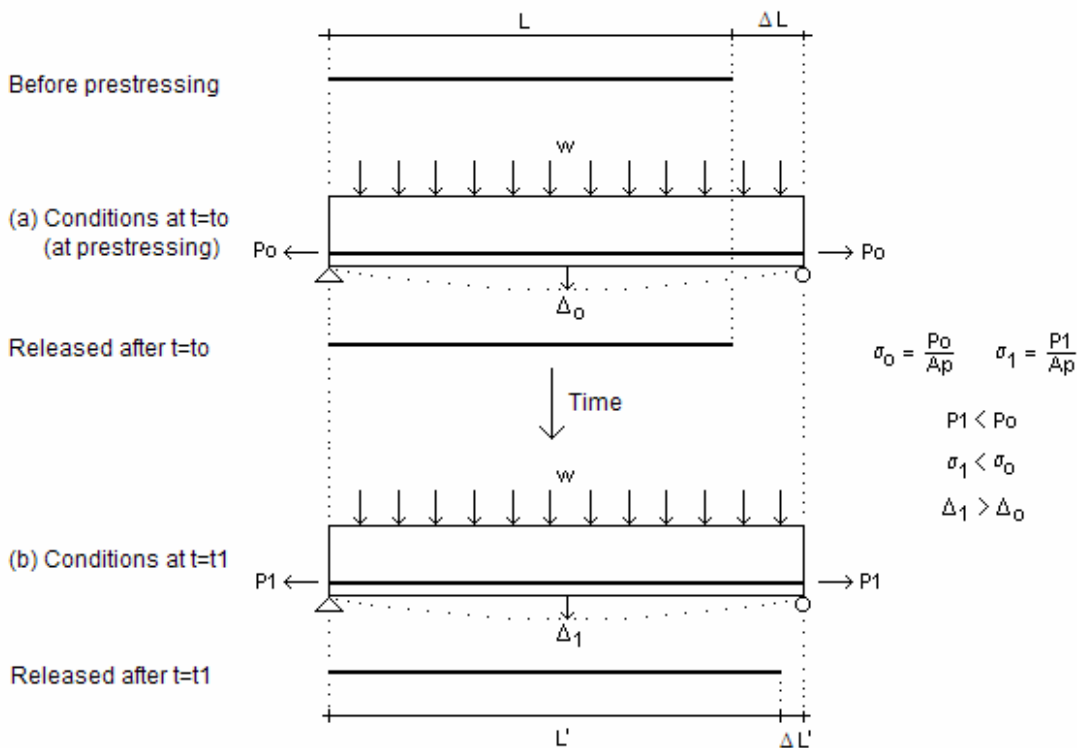
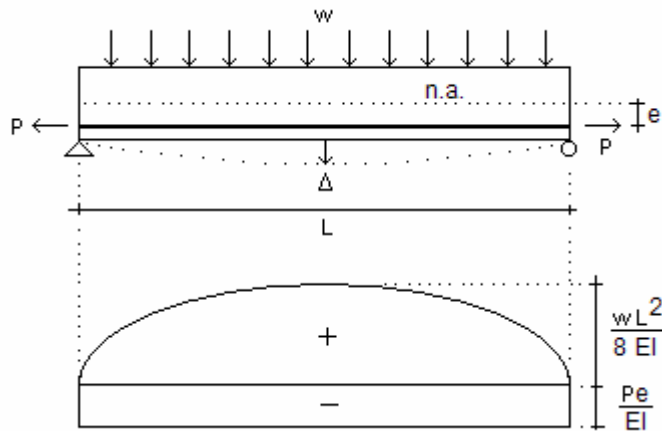


Figure 56. Prestress Losses due to Prestressing Steel Relaxation in a Loaded Beam.

The deflection  $\Delta$  of the prestressed beam shown in [Figure 57](#) can be computed using the moment area method. In [Figure 57](#),  $e$  is the eccentricity of the tendon and  $n.a.$  is the neutral axis location. The  $M/EI$  diagram is illustrated in [Figure 57](#).  $M$  is the bending moment acting at a section on the beam,  $E$  is the modulus of elasticity of the beam, and  $I$  is the moment of inertia of the beam at the same section. Thus, the deflection,  $\Delta$ , can be computed as:

$$\Delta = \left( \frac{2 w L^2}{38 EI} \right) \frac{L}{2} \left( \frac{3L}{8} \right) - \left( \frac{Pe}{EI} \right) \frac{L}{2} \frac{L}{4} = \frac{w L^4}{128 EI} - \frac{Pe L^2}{8 EI} \quad (27)$$

Using [Equation 27](#) to compute the deflections of the beam in [Figure 56](#), it can be found that  $\Delta_I$  is larger than  $\Delta_o$  because the prestressing force  $P_I$  is smaller than the prestressing force  $P_o$ .



**Figure 57. Prestressed Concrete Beam Deflections.**

From [Figure 56](#), the increase of strain over time can be obtained as:

$$\Delta \varepsilon = \varepsilon_r = \frac{\Delta \sigma}{E_s} = \frac{\Delta P}{A_{ps} E_s} \quad (28)$$

where ( $\Delta P = P_o - P_I$ ) is the change in prestressing force,  $A_{ps}$  is the area of prestressing steel, and  $E_s$  is the elastic modulus of steel.

Thus, the loss of prestress can be computed as:

$$\Delta P = \varepsilon_r A_{ps} E_s \quad (29)$$

The prestress losses due to steel relaxation of an actual prestressed concrete beam are different than those obtained with [Equation 29](#) because prestress losses of actual prestressed concrete beams due to relaxation are affected by creep and shrinkage of the concrete, elastic shortening of the concrete section at transfer, type of prestressing reinforcement, and level of prestress. Different equations have been proposed to compute relaxation losses of bonded and unbonded tendons ([Branson 1977](#)).

For pretensioned strands:

$$CR_s = 20,000 - 0.125 (SH + ES + CR_c) \quad (30)$$

For post-tensioned strands:

$$CR_{sp} = 20,000 - 0.125 (0.8 SH + 0.5 ES + CR_c) \quad (31)$$

where,

$CR_s$  = the ultimate losses (in psi) due to relaxation from pretensioning,

$CR_{sp}$  = relaxation from post-tensioning,

$SH$  = shrinkage of the concrete,

$ES$ , = elastic shortening of the section,

$CR_c$  = creep of the concrete .

Nevertheless, it is common to use methods that make no distinction between bonded and unbonded tendons to compute relaxation losses, as the method given by the Precast/Prestressed Concrete Institute ([PCI 1999](#)):

$$RE = [Kre - J (SH + CR + ES)] C \quad (32)$$

where,

$RE$  = the relaxation of tendons,

$Kre$  = is a factor that depends on the grade and type of tendon (stress relieved, low-relaxation strand, etc.),

$J$  = is a factor that depends on the same variables as  $Kre$ ,

$SR$  = is the shrinkage of the concrete,

$CR$  = is the creep of the concrete,

$ES$  = is the elastic shortening of the concrete, and  $C$  depends on the level of prestressing.

In the case of a non-prestressed steel-reinforced concrete section, the strain (and, therefore, the stress) in the steel remains basically unchanged due to long-term loads and the effects of concrete shrinkage and creep (Holloway 1978). Therefore, it can be assumed that creep and shrinkage of the concrete do not affect the strain in the FRP reinforcement. That is, creep of FRP bars due to long-term loads depends only on the stresses of the reinforcement resulting from the sustained loads.

An analysis similar to the analysis presented in Figure 56 for a prestressed concrete beam can be performed with an FRP-reinforced concrete beam, as depicted in Figure 58. All of the terms used in Figure 58 have the same meaning as those in Figure 53, and  $\Delta$  represents the midspan deflection of the beam. The total strain ( $\varepsilon_{To}$ ) present in the beam at time  $t_o$  is equal to the elastic strain ( $\varepsilon_{eo}$ ). After an elapsed time,  $\Delta t = t_I - t_o$ , the FRP reinforcement creeps ( $\varepsilon_{cl}$ ), the elastic strain is now ( $\varepsilon_{el}$ ), and the total strain is the sum of the elastic and creep strains ( $\varepsilon_{TI} = \varepsilon_{el} + \varepsilon_{cl}$ ). The increase of strain at time  $t_I$  due to creep of the FRP bars can be described as an imaginary change in stress:

$$\varepsilon_{cl} = \frac{\Delta L'}{L} = \frac{\Delta \sigma_f}{E_f} \quad (33)$$

where  $\sigma_f$  is the imaginary stress in the FRP reinforcement required to induce an elastic strain equal in magnitude to  $\varepsilon_{cl}$ , and  $E_f$  is the elastic modulus of the FRP reinforcement.

An equivalent imaginary creep loss of prestressing force can be obtained as follows:

$$\Delta P = \Delta \sigma_f A_f \quad (34)$$

where  $A_f$  is the area of the FRP reinforcement.

The equivalent imaginary creep loss of prestressing force can thus be written as:

$$\Delta P = \varepsilon_{cl} E_f A_f \quad (35)$$

As explained in previous paragraphs, the stress in the FRP bar does not increase with time when the bar is subjected to reasonably small strains and, therefore, the stress  $\Delta \sigma_f$  in Equations 34 and 35 is nonexistent. Analyzing the deflections of an FRP-reinforced concrete beam where the effects of creep and shrinkage of the concrete are artificially prevented, it would be concluded that deflections increase over time due to creep of the FRP bars alone, as illustrated in Figure 58. If a prestressing force acting along the axis of the FRP bar shown in Figure 58 at time  $t_1$  was applied to the beam, and if the prestressing force had a magnitude equal to the force  $\Delta P$  computed with Equation 35, the midspan deflection of the beam would be  $\Delta_0$  instead of  $\Delta_1$ . That is, the increase in deflection of the FRP-reinforced concrete beam caused by creep of the FRP bars would be canceled. This means that the deflections of an FRP-reinforced concrete beam can be computed by assuming the FRP bars do not develop any creep when stressed and by adding to the new FRP-reinforced concrete beam an equivalent prestress loss with magnitude  $\Delta P$  obtained with Equation 35.

The equivalent loss of prestressing force can be computed if the creep strain developed in the FRP reinforcement is known along the bar. There is controversial information regarding whether the creep rate of GFRP materials depends on the level of applied stress. Holloway (1978) stated that the magnitude of the creep strain of GFRP materials depends on the magnitude of the stress the composite is subjected to, although

no experimental evidence is provided. Johnston (1979) presents experimental evidence showing that the creep-time behavior of glass fabric/polyester in water at 73.4 °F (23 °C) is different for different applied stress levels. The stress levels presented by Johnston are 40, 50, 55, 60, 65, 70, and 75 percent of the ultimate tensile strength. However, the creep-time curves presented by Johnston could be approximated with straight lines of similar slope for the different stress levels studied. Holmes and Just (1983) present best-fit lines through experimental creep-time observations performed on unidirectional continuously reinforced glass fiber composites. The best-fit lines show approximately the same slope for the creep-time plots at the stress levels of 10.8 ksi and 14.8 ksi. Thus, since the creep strain rate does not seem to change appreciably at different stress levels, it will be assumed to be constant. As such, it will be assumed that the creep strain rate is the same at any section along a GFRP-reinforced concrete beam subjected to a uniformly distributed load. Therefore, the total elongation due to creep ( $\Delta L'$ ) of a GFRP bar subjected to different stress levels along a beam, as shown in Figure 58, can be computed as  $\Delta L' = \varepsilon_{cI} L$ , where  $\varepsilon_{cI}$  is the creep strain at time  $t_I$ . Computing the imaginary creep loss of prestressing force with Equation 35, the method described next can be readily implemented to compute the long-term deflections of GFRP-reinforced concrete elements.

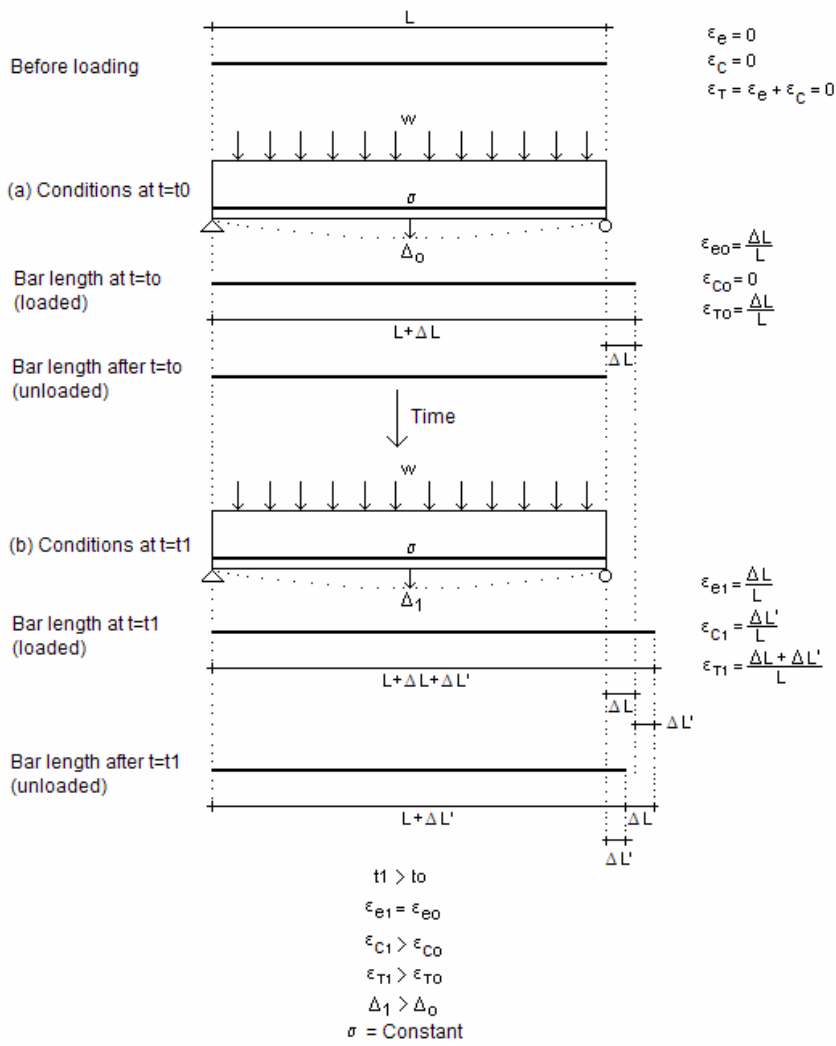
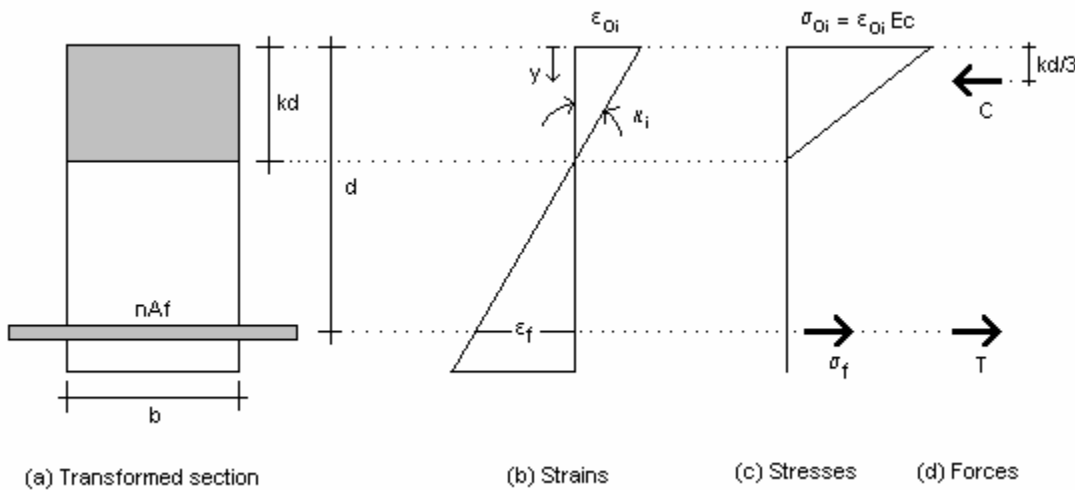


Figure 58. Creep of FRP Reinforcement in a Loaded Concrete Beam.

### Properties of Cracked Cross Sections

An FRP-reinforced concrete cross section with a vertical axis of symmetry will be analyzed. The top surface of the cross section will be used as the reference surface, instead of the neutral axis. This choice of reference surface is used because the position of the neutral axis of the cross section varies with time due to creep and shrinkage of the concrete. Thus, a distance  $y$  measured from the top surface will be used for analysis of the section as indicated in [Figure 59](#). Note that the sign convention used is as follows:  $y$  is negative as shown in the figure;  $\varepsilon_{oi}$  is negative when the concrete is in compression;  $\kappa_i$  (curvature sign) is obtained by dividing  $\varepsilon_{oi}$  by  $k_d$ ; concrete stress,  $\sigma$ , is positive in tension and negative in compression.



**Figure 59. Analysis of a Cracked Cross Section.**

In [Figure 59](#),  $n$  is the short-term modular ratio ( $E_f / E_c$ ), where  $E_f$  is the elastic modulus of the FRP bar and  $E_c$  is the elastic modulus of concrete. The strain at a depth  $y$  from the top surface depends on the top surface strain  $\varepsilon_{oi}$  and the initial curvature  $\kappa_i$ , such that:

$$\varepsilon_i = \varepsilon_{oi} + y\kappa_i \quad (36)$$

Assuming the short-term behavior to be linearly elastic, the initial concrete stress at a depth  $y$  below the top surface is:

$$\sigma_i = E_c \varepsilon_i = E_c (\varepsilon_{oi} + y\kappa_i) \quad (37)$$

The resultant axial force  $N_i$  present in the section can be determined by integrating the stresses over the height of the section as indicated in the following expression:

$$\begin{aligned} N_i &= \int_{y=0}^{y=kd} \sigma_i dA + T \\ N_i &= E_c \varepsilon_{oi} \int_{y=0}^{y=kd} dA + E_c \kappa_i \int_{y=0}^{y=kd} y dA + T \\ N_i &= E_c \varepsilon_{oi} A_c + E_c \kappa_i B_c + T \end{aligned} \quad (38)$$

where,

$$A_c = \int_{y=0}^{y=kd} dA = \text{Area of the transformed section in compression,}$$

$$B_c = \int_{y=0}^{y=kd} y dA = \text{First moment of the transformed area in compression about the top surface,}$$

$$T = \text{Tensile force developed in the FRP bar.}$$

The resultant moment about the top surface is obtained by integrating the stresses about the top surface over the depth of the section, as indicated in [Equation 39](#).

$$\begin{aligned} M_i &= \int_{y=0}^{y=kd} \sigma_i y dA + Td \\ M_i &= E_c \varepsilon_{oi} \int_{y=0}^{y=kd} y dA + E_c \kappa_i \int_{y=0}^{y=kd} y^2 dA + Td \\ M_i &= E_c \varepsilon_{oi} B_c + E_c \kappa_i I_c + Td \end{aligned} \quad (39)$$

where,

$B_c = \int_{y=0}^{y=kd} ydA$  = First moment of the transformed area in compression about the top surface,

$I_c = \int_{y=0}^{y=kd} y^2 dA$  = Second moment of the transformed area in compression about the top surface,

$T$  = Tensile force in the FRP bar,

$d$  = Effective depth of the section.

Equations for the initial top fiber strain and curvature can be obtained in terms of  $N_i$  and  $M_i$  by rearranging Equations 38 and 39:

$$\varepsilon_{oi} = \frac{M_i B_c' - N_i I_c}{E_c (B_c'^2 - I_c A_c)} \quad (40)$$

and

$$\kappa_i = \frac{B_c N_i - A_c' M_i}{E_c (B_c'^2 - I_c A_c)} \quad (41)$$

where

$$B_c' = B_c + \frac{I_c - dB_c}{d(1 - \frac{k}{3})} \quad (42)$$

$$A_c' = A_c + \frac{B_c - dA_c}{d(1 - \frac{k}{3})} \quad (43)$$

To find the depth of the neutral axis, the first moment of the area in tension about the neutral axis is equated to the first moment of the area in compression about the neutral axis. Thus,

$$k = \sqrt{(\rho_f n)^2 + 2\rho_f n - \rho_f n} \quad (44)$$

where,

$\rho_f = \frac{A_f}{bd}$  = FRP reinforcement ratio, and  $b$  and  $d$  are as defined in Figure 59.

### Time-Dependent Analysis of Cracked Cross Sections

The depth of the neutral axis increases with time according to experimental observations (Branson 1977). However, as indicated by Gilbert and Mickleborough (1990), little error is incurred if the depth of the neutral axis is assumed to remain constant with time. This assumption permits the principle of superposition to apply to fully cracked cross sections and, therefore, enables the stresses and strains computed from an elastic analysis to be added to time-dependent stresses and strains. Figure 60 illustrates the initial and time-dependent strain distributions.

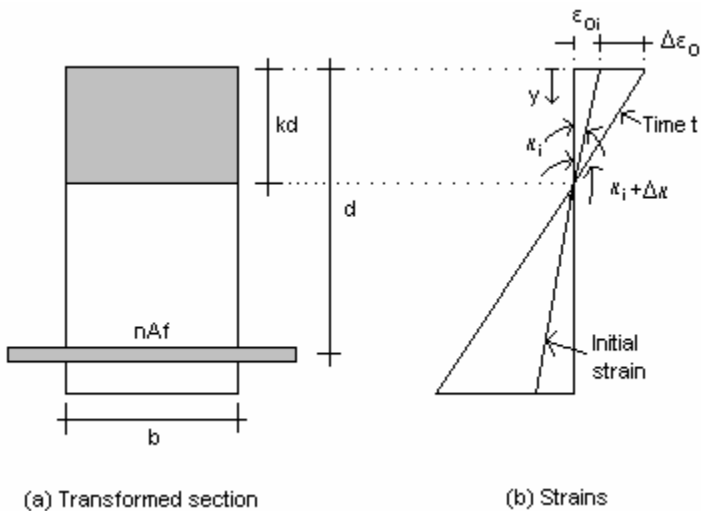


**Figure 60 Initial and Time Dependent Strains and Curvatures.**

The change in the top fiber strain ( $\Delta\epsilon_o$ ) and the change in curvature ( $\Delta\kappa$ ) can be used to determine the time-dependent strain at any distance  $y$  from the top surface of the section ( $\Delta\epsilon$ ):

$$\Delta\epsilon = \Delta\epsilon_o + y\Delta\kappa \quad (45)$$

The magnitude of  $\Delta\epsilon$  is the addition of the following components:

- the free shrinkage strain;

- the creep strain resulting from the initial concrete stress applied at the beginning of the time period, that is  $\varepsilon_c = \Delta\phi\sigma/E_c$ , where  $\Delta\phi$  is the increment of the creep coefficient associated with the time period under consideration;
- the creep and elastic strain resulting from  $\Delta N(t)$  and  $\Delta M(t)$  applied gradually to the section (This term is the contribution to the internal restraint to creep and shrinkage given by the bonded reinforcement.); and
- the tensile creep strain in the FRP bars.

To determine the changes in strain during a given time period, a relaxation procedure proposed by Bresler and Selna (1964) will be used. During a time interval, the strains in the cross section are assumed to remain fixed; that is, the effects of creep and shrinkage on strain are fictitiously prevented. For the total strain to remain constant while having the shrinkage and creep strains change, the elastic component of strain must also change by an equal and opposite amount. Since the elastic strains change, the concrete stress changes as well. This implies that the concrete stresses on the section must be modified due to relaxation. Equilibrium unbalance results from these forces. To restore equilibrium, an axial force  $\delta N$  and a flexural moment  $\delta M$  need to be applied to the section.

If bonded reinforcement did not restrain creep from taking place in the concrete and the concrete stress stayed constant during the period of analysis, the strain at the top fiber would increase by  $\Delta\phi\varepsilon_{oi}$  and the curvature by  $\Delta\phi\kappa_i$ . The forces necessary to keep this deformation from developing are obtained from the following expressions:

$$-\delta N_{concrete-creep} = -E_e \Delta\phi (A_c \varepsilon_{oi} + B_c \kappa_i) \quad (46)$$

$$-\delta M_{concrete-creep} = -E_e \Delta\phi (B_c \varepsilon_{oi} + I_c \kappa_i) \quad (47)$$

where  $A_c$ ,  $B_c$ , and  $I_c$  are the properties of the area in compression of the cracked concrete cross section with respect to the top surface. Since these equations are comprised of only the creep in the concrete, the properties of the concrete section alone are utilized. Since

the restraining forces  $\delta N$  and  $\delta M$  are slowly applied during the period of analysis, the age-adjusted effective modulus  $E_e$  is used:

$$E_e(t, \tau) = \frac{E_c}{1 + \chi \Delta\phi(t, \tau)} \quad (48)$$

where  $\chi$  is an aging coefficient that depends on the age at first loading and the duration of loading. The coefficient  $\chi$  varies between 0.6 and 1.0 and, according to Gilbert and Mickleborough (1990), for most practical purposes can be taken as 0.8. In Equation 48,  $\Delta\phi(t, \tau)$  is the increment of the creep coefficient of the concrete between times  $t$  and  $\tau$ , defined as the ratio of the creep strain to the instantaneous strain and is expressed by:

$$\Delta\phi(t, \tau) = \frac{\varepsilon_c(t, \tau)}{\varepsilon_e} \quad (49)$$

The elements of Equation 49 are illustrated in Figure 61. There are several methods available for the computation of the creep coefficient. The ACI method for estimating the increment of the creep coefficient is given by (Mindess and Young 1981, Gilbert and Mickleborough 1990):

$$\Delta\phi(t, \tau) = \frac{(t - \tau)^{0.6}}{D + (t - \tau)^{0.6}} C_{ult} \quad (50)$$

where  $\Delta\phi(t, \tau)$  is the increment of the creep coefficient between times  $t$  and  $\tau$ ,  $\tau$  is the age of concrete at first loading (in days),  $t - \tau$  is the duration of loading (in days),  $C_{ult}$  is the ultimate creep coefficient, and  $D$  is a constant that is equal to 10 for concrete loaded at an age of 7 days or older. The value of  $C_{ult}$  will be in the range of 1.30 to 4.15, and ACI recommends an average value of 2.35 for evaluation of  $C_{ult}$  if no experimental data are available. The following correction factors (C.F.) for relative humidity and age at loading are recommended by ACI:

$$C.F._{RH} = 1.27 - 0.0067H, H \geq 40\% \quad (51)$$

$$C.F._{age-at-loading} = 1.25t_l^{-0.118} \quad (52)$$

where  $H$  is the relative humidity as a percentage, and  $t_l$  is the age of the concrete at the time of loading in days.

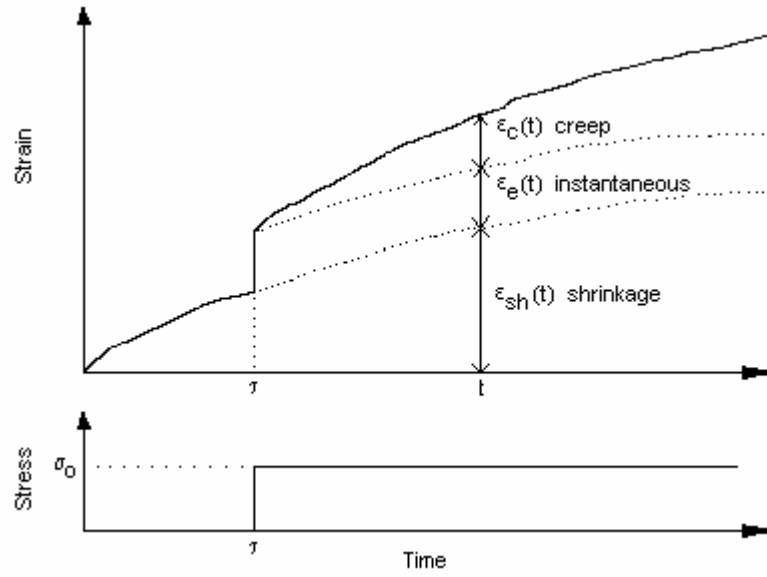


**Figure 61. Elastic, Shrinkage, and Creep Strains Developed in Concrete.**

Shrinkage strain,  $\varepsilon_{sh}$ , develops during the time period of analysis, and there is no curvature induced if the shrinkage is uniform over the height of the section and free from any restraints. The restraining forces necessary to stop this uniform deformation are:

$$-\delta N_{shrinkage} = -E_e \varepsilon_{sh} A_c \quad (53)$$

$$-\delta M_{shrinkage} = -E_e \varepsilon_{sh} B_c \quad (54)$$

The shrinkage strain can be estimated using the ACI method at any time  $t$  after 7 days for moist cured concrete with:

$$(\varepsilon_{sh})_t = \frac{t}{35+t} (\varepsilon_{sh})_{ult} \quad (55)$$

where  $(\varepsilon_{sh})_{ult}$  is the ultimate shrinkage value for drying at 40 percent relative humidity (RH). Corrections for RH are given by:

$$\text{above 80 percent RH } (C.F.)_H = 3.00 - 0.03H \quad (56)$$

$$\text{below 80 percent RH } (C.F.)_H = 1.40 - 0.01H \quad (57)$$

where  $H$  is the relative humidity expressed as a percentage. The value of  $(\varepsilon_{sh})_{ult}$  will fall in the range of  $415$  to  $1070 \times 10^{-6}$ , and ACI recommends a value of  $730 \times 10^{-6}$  when no data are available.

The analogy between a prestressed concrete section and an FRP-reinforced concrete section will be presented next. In a prestressed concrete element, restraining forces are necessary to prevent the relaxation in the tendons from developing. Thus, in an FRP-reinforced concrete element, an equivalent prestressing force  $F$  equal to the force  $\Delta P$  of [Equation 35](#) is required to prevent tensile creep from occurring in the FRP reinforcement. The equivalent restraining forces required to prevent creep in the  $m$  layers of the FRP reinforcement are:

$$-\delta N_{FRP-creep} = \sum_{j=1}^m F_j \quad (58)$$

and

$$-\delta M_{FRP-creep} = \sum_{j=1}^m F_j d_j \quad (59)$$

The total restraining forces are obtained by adding the creep of the concrete, concrete shrinkage, and creep of the FRP reinforcement components:

$$-\delta N = -E_e [\Delta \phi (A_c \varepsilon_{oi} + B_c \kappa_i) + \varepsilon_{sh} A_c] + \sum_{j=1}^m F_j \quad (60)$$

$$-\delta M = -E_e [\Delta \phi (B_c \varepsilon_{oi} + I_c \kappa_i) + \varepsilon_{sh} B_c] + \sum_{j=1}^m F_j d_j \quad (61)$$

The following expressions can be used to obtain the increments of the top fiber strain ( $\Delta \varepsilon_o$ ) and curvature ( $\Delta \kappa$ ) of the section, resulting from the gradual application of the force  $\delta N$  and the moment  $\delta M$ :

$$\Delta \varepsilon_o = \frac{B'_e \delta M - I'_e \delta N}{E_e (B_e^2 - A_e I_e)} \quad (62)$$

$$\Delta \kappa = \frac{B'_e \delta N - A'_e \delta M}{E_e (B_e^2 - A_e I_e)} \quad (63)$$

where  $A_e$ ,  $B_e$ , and  $I_e$  are the area of the age-adjusted transformed section, the first moment of the age-adjusted transformed section about the top surface, and the second moment of the age-adjusted transformed section about the top surface, respectively.  $A_e$ ,  $B_e$ , and  $I_e$  are the properties of the transformed area obtained using the age-adjusted effective modulus,  $E_e$ , in the computation of the transformed area of the bonded reinforcement. Since  $\delta N$  and  $\delta M$  produce elastic and creep strains, the age-adjusted effective modulus is used in Equations 62 and 63.

### *Deflection Computations*

Following the analysis by Gilbert and Mickleborough (1990), by integrating the curvature along a concrete member, the slope  $\theta$  and the curvature  $\kappa$  at any point  $x$  can be computed. Using simple beam theory:

$$\theta = \int \kappa(x) dx \quad (64)$$

$$y = \iint \kappa(x) dx dx \quad (65)$$

Equations 64 and 65 are applicable to elastic and inelastic behavior.

If the curvatures at the supports and midspan are known, the deflection of the GFRP-reinforced concrete element illustrated in Figure 62 can be computed using the following expression:

$$y_c = \frac{L^2}{96} (\kappa_A + 10\kappa_C + \kappa_B) \quad (66)$$

Using the time dependent deformation analysis described assumes that creep of the FRP bars is uniform across the span.

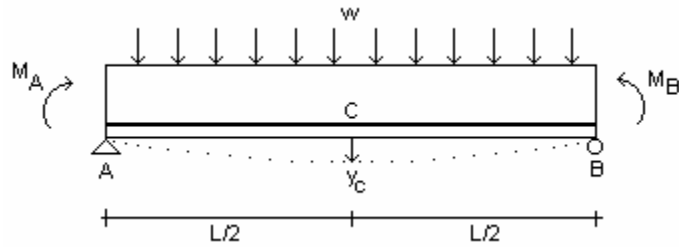


**Figure 62. Deflections of a Simple Beam.**

The change in curvature with time due to creep of concrete, shrinkage, and creep of FRP bars obtained from [Equation 63](#) can be included in [Equation 66](#) to compute the long-term deflections of FRP-reinforced concrete elements.

Some limitations of the work presented here include that the creep tests were conducted on only one bar diameter and at only one stress level, and that only five data points were obtained. In order to fully utilize the method described to compute long-term deflections, more creep tests are required that include different bar sizes and different stress levels with a larger number of specimens. An example is provided in [Section V](#) for completeness using the creep data obtained in the test program.

Summarizing, the results of a creep test for GFRP bars are presented. An analogy between relaxation of prestressing steel tendons and creep of FRP bars is presented. A method to compute the changes in strain and curvature of FRP-reinforced concrete elements over time due to creep of the concrete, shrinkage, and creep of FRP bars also is given. Finally, the use of calculated time-dependent changes in curvature in the computation of deflections of FRP-reinforced concrete elements also is presented.

## **CRACKING OF CONCRETE SLABS TEST**

This section describes the test results of the concrete slabs tests. The need to carry out the tests was described in [Section II](#). The materials used in the test, the test description, and test specimens were described in [Section III](#). This section is divided into three parts. The first part presents and describes the test results. The second part compares the test results and available equations to predict maximum crack width. The last part involves a correlation analysis of the available expressions, resulting in the validation of the expression to predict maximum crack width.

As described in the literature review section, testing of concrete elements with different concrete covers is necessary because crack widths are a function of concrete cover, as well as an evaluation of the correlation between the test results and proposed equations. Limited information on maximum crack width of FRP-reinforced concrete flexural members was available when Equation 8-9b (and 8-9c) of the ACI 440 ([2001](#)) design guidelines was proposed. [Section II](#) presents an expression proposed by Faza and GangaRao ([1993](#)) to compute maximum crack width; however, verification of the goodness of fit of this expression to maximum crack width test data is necessary.

### **Test Results**

This section describes the results of the flexural tests conducted on 36 hybrid epoxy-coated steel (ECS) GFRP-reinforced concrete slabs. The cracking behavior and ultimate loads of the specimens are described first. The GFRP bar stresses, computed from measured GFRP bar strains, and corresponding maximum crack widths will then be presented and described.

As mentioned in [Section III](#), 36 specimens were tested, 12 for each of the nominal covers of 1, 2, and 3 inches. The specimens with 1-inch nominal cover had actual average covers of 1.25 inches when 0.625-inch diameter bars were used and 1.16

inches when 0.75-inch diameter bars were used. The overall average clear concrete cover for the specimens with 1-inch nominal cover was 1.21 inches. The specimens with 2-inch nominal cover had actual average covers of 2.19 inches when 0.625-inch diameter bars were used, and 2.18 inches when 0.75-inch diameter bars were used. The overall average clear concrete cover for the specimens with 2-inch nominal cover was 2.18 inches. The specimens with 3-inch nominal cover had actual average covers of 3.23 inches when 0.625-inch diameter bars were used, and 3.13 inches when 0.75-inch diameter bars were used. The overall average clear concrete cover for the specimens with 3-inch nominal cover was 3.18 inches.

The slabs were loaded at a constant displacement rate until cracking occurred and were then held at constant displacement until crack widths were measured. After measuring crack widths, the displacement increased sequentially at several displacement levels (and, therefore, several load levels) until failure of the specimen occurred. The cracking and ultimate loads for the 36 specimens are presented in [Table 40](#). As observed from the data, the ultimate load of the specimens with smaller cover was the highest. This was expected since the specimens with small cover had a larger effective depth and, therefore, a higher flexural strength than the specimens with large covers. The cracking load was also dependent on concrete cover, being highest for the specimens with the smallest cover. This behavior results from the contribution to the moment of inertia of the transformed section by the tension reinforcement. In [Table 40](#), the specimens are labeled as follows: the bar type is given first, followed by the number of bars, then by the bar size in eighths of an inch, and finally by the specimen (either a or b).

**Table 40. Cracking and Ultimate Loads of Specimens.**

Specimen	Average cover = 1.21 in.		Average cover = 2.18 in.		Average cover = 3.18 in.	
	Cracking load (kips)	Ultimate load (kips)	Cracking load (kips)	Ultimate load (kips)	Cracking load (kips)	Ultimate load (kips)
P-4-5-a	3.5	15.0	3.0	12.0	2.1	7.8
P-4-5-b	2.8	14.2	2.7	9.6	2.2	8.4
V1-4-5-a	3.5	16.1	2.7	10.7	2.6	7.9
V1-4-5-b	3.2	14.4	3.0	10.8	2.2	8.7
V2-4-5-a	3.5	13.3	3.1	12.8	2.2	8.0
V2-4-5-b	3.5	13.9	3.3	9.9	2.3	8.4
P 3-6-a	3.2	13.8	2.7	10.6	2.7	7.8
P-3-6-b	3.2	14.9	2.8	11.1	2.7	8.8
V1-3-6-a	3.2	13.2	2.6	11.4	2.4	9.3
V1-3-6-b	3.3	13.9	3.3	10.5	2.3	8.9
V2-3-6-a	3.4	14.8	3.0	10.8	2.2	8.4
V2-3-6-b	3.5	14.1	2.7	11.7	2.2	9.0
Average	3.3	14.3	2.9	11.0	2.3	8.4
S.D.	0.21	0.80	0.23	0.88	0.22	0.50
COV	0.06	0.06	0.08	0.08	0.09	0.06

Loading of the slabs was stopped approximately eight times after the cracking load was attained to measure the widths of cracks with a crack microscope. The strains recorded during testing of the slabs were converted to stresses using the elastic moduli of the bars. The average values of the moduli of elasticity from each bar type were used in the computations. The computed GFRP bar stresses and the corresponding maximum crack widths ( $W_{max}$ ) observed at those stress levels are illustrated in Tables 41 through 45. Table 41 shows the results for specimens with an average clear concrete cover of 1.21 inches. Tables 42 and 43 show the results for a clear concrete cover of 2.18 inches. Tables 44 and 45, show the results for the specimens with a clear concrete cover of 3.18 inches. In Tables 41 through 45 the top of the column identifies the specimen with the bar type first, followed by the number of bars, followed by the bar diameter in eighths of an inch, and by the specimen (either a or b). For example, specimen V1-4-5-a was made with four-vinyl ester bars type 1 (described in Section III) with a diameter of 0.625 inch and is specimen a. The researchers were unable to download strains from some of the

specimens from the acquisition system, and the data from those specimens are not included in Tables 41 through 45. The labels part a and part b in Tables 42 through 45 indicate that the specimens of parts a and b belong to the same concrete cover group.

**Table 41. Midspan GFRP Bar Stresses and Maximum Crack Widths for 1.21-Inch Cover.**

P-4-5-b		V1-4-5-a		V1-4-5-b		V2-4-5-b		V1-3-6-a		V1-3-6-b		V2-3-6-b	
Stress (psi)	W <sub>max</sub> (in.)												
295	0.000	439	0.000	410	0.000	309	0.000	349	0.000	219	0.000	370	0.000
2,657	0.012	4,515	0.012	9,045	0.008	9,167	0.012	4,742	0.008	2,633	0.008	1,011	0.008
3,204	0.016	5,858	0.016	9,582	0.008	10,536	0.016	6,440	0.012	3,252	0.012	7,584	0.012
4,214	0.016	8,308	0.024	12,679	0.016	14,259	0.020	9,676	0.016	6,393	0.016	10,566	0.016
19,821	0.020	10,923	0.028	15,440	0.020	17,344	0.028	12,419	0.028	9,825	0.024	14,191	0.020
24,900	0.035	17,113	0.039	27,856	0.028	23,201	0.043	19,789	0.039	16,957	0.039	19,986	0.031
29,628	0.043	23,848	0.059	30,660	0.039	30,382	0.039	26,794	0.047	22,535	0.043	26,203	0.035
31,432	0.059	31,386	0.087	31,570	0.055	31,496	0.075	31,268	0.063	31,282	0.047	31,159	0.047

**Table 42. Midspan GFRP Bar Stresses and Maximum Crack Widths for 2.18-Inch Cover (Part A).**

P-4-5-a		P-4-5-b		V1-4-5-a		V1-4-5-b		V2-4-5-a		V2-4-5-b	
Stress (psi)	W <sub>max</sub> (in.)										
195	0.000	37	0.000	143	0.000	157	0.000	105	0.000	151	0.000
311	0.008	110	0.008	224	0.012	168	0.000	197	0.000	165	0.000
3,166	0.012	2,586	0.016	10,662	0.012	196	0.008	238	0.004	15,076	0.016
5,470	0.020	3,233	0.024	12,992	0.020	12,477	0.024	10,791	0.012	16,085	0.016
6,662	0.028	6,353	0.031	17,885	0.035	18,008	0.028	14,499	0.024	19,397	0.016
12,648	0.051	19,857	0.047	23,079	0.047	26,996	0.047	20,357	0.035	24,186	0.035
19,061	0.075	23,892	0.071	31,600	0.067	30,182	0.071	29,286	0.047	29,945	0.047
29,117	0.098	31,148	0.130	31,607	0.071	31,164	0.091	31,392	0.071	31,285	0.063
-	-	-	-	31,614	0.134	-	-	-	-	-	-

**Table 43. Midspan GFRP Bar Stresses and Maximum Crack Widths for 2.18-Inch Cover (PartB).**

P-3-6-a		P-3-6-b		V1-3-6-a		V1-3-6-b		V2-3-6-b	
Stress (psi)	W <sub>max</sub> (in.)								
219	0.000	164	0.000	179	0.000	35	0.000	93	0.000
223	0.012	256	0.000	342	0.004	108	0.000	240	0.004
1,189	0.016	9,897	0.012	1,236	0.008	188	0.008	346	0.012
10,706	0.020	11,414	0.020	1,687	0.016	14,832	0.016	1,260	0.016
13,837	0.028	13,506	0.031	2,896	0.020	16,018	0.024	2,059	0.024
18,012	0.043	16,808	0.047	14,920	0.035	20,437	0.028	14,618	0.051
23,600	0.063	20,094	0.094	20,818	0.051	25,467	0.047	18,996	0.055
31,202	0.094	31,649	0.094	27,910	0.063	31,150	0.063	30,415	0.055
31,180	0.122	-	-	-	-	-	-	-	-

**Table 44. Midspan GFRP Bar Stresses and Maximum Crack Widths for 3.18-Inch Cover (Part A).**

P-4-5-a		P-4-5-b		V1-4-5-a		V1-4-5-b		V2-4-5-a		V2-4-5-b	
Stress (psi)	W <sub>max</sub> (in.)										
85	0.000	22	0.000	61	0.000	47	0.000	87	0.000	102	0.000
339	0.020	306	0.028	140	0.016	27	0.016	148	0.016	166	0.016
4,523	0.035	416	0.039	3,294	0.020	460	0.020	473	0.020	1,607	0.022
6,380	0.047	5,766	0.047	10,021	0.028	1,618	0.031	1,398	0.024	5,596	0.029
16,211	0.094	13,950	0.087	11,387	0.033	5,326	0.083	5,480	0.043	11,717	0.063
22,552	0.106	21,575	0.118	13,491	0.043	11,698	0.094	16,178	0.067	19,450	0.102
27,671	0.138	29,494	0.138	15,509	0.055	18,612	0.146	23,784	0.091	28,207	0.126
31,147	0.177	31,270	0.177	17,677	0.055	-	-	30,964	0.134	31,387	0.146
-	-	-	-	20,202	0.071	-	-	31,528	0.157	-	-
-	-	-	-	24,073	0.094	-	-	-	-	-	-
-	-	-	-	29,323	0.098	-	-	-	-	-	-

**Table 45. Midspan GFRP Bar Stresses and Maximum Crack Widths for 3.18-Inch Cover (Part B).**

P-3-6-a		P-3-6-b		V1-3-6-a		V1-3-6-b		V2-3-6-a		V2-3-6-b	
Stress (psi)	W <sub>max</sub> (in.)										
19	0.000	231	0.000	68	0.000	22	0.000	12	0.000	42	0.000
191	0.000	494	0.025	125	0.008	131	0.016	37	0.000	100	0.008
2,188	0.026	1,229	0.051	4,713	0.020	9,359	0.020	132	0.024	245	0.016
4,376	0.043	8,860	0.102	6,733	0.028	11,239	0.031	2,352	0.028	11,090	0.028
6,065	0.071	11,748	0.134	11,706	0.055	14,842	0.047	5,665	0.055	16,367	0.051
11,389	0.114	20,391	0.154	16,277	0.098	19,082	0.087	22,350	0.087	20,593	0.063
18,719	0.134	24,959	0.177	28,741	0.126	28,206	0.114	28,819	0.102	26,567	0.071
24,469	0.217	-	-	31,240	0.118	31,360	0.134	-	-	31,413	0.106

The results presented in Tables 41 through 45 are summarized in Figures 63, 64, and 65 for the specimens with overall clear covers of 1.21 inches, 2.18 inches, and 3.18 inches, respectively. The specimen designation is as indicated earlier. Similar to the results by Gergely and Lutz (1973), there is considerable scatter in the data. Although, the maximum crack width versus GFRP bar stress shows a non-linear behavior at high stresses for some specimens, a straight line can be used as an approximation to represent the data. It can be seen from Figures 63 through 65 that the maximum crack width of the specimens increases as the concrete cover increases. This behavior is captured by the factor  $\beta$  of Equation 67 shown in the next section.

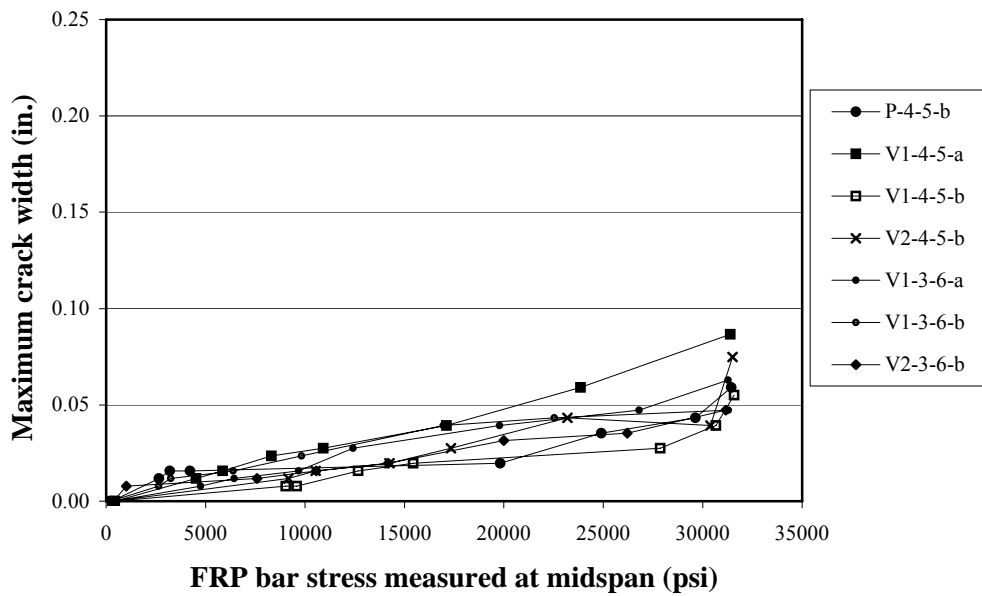


**Figure 63. Stress versus Maximum Crack Width of Specimens with 1.21-Inch Cover.**

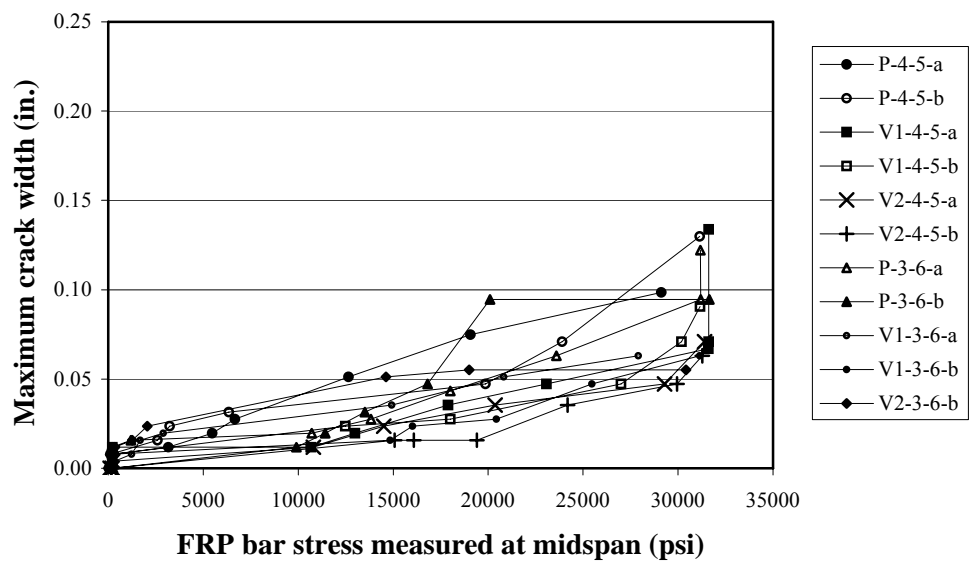


**Figure 64. Stress Versus Maximum Crack Width of Specimens with 2.18-Inch Cover.**

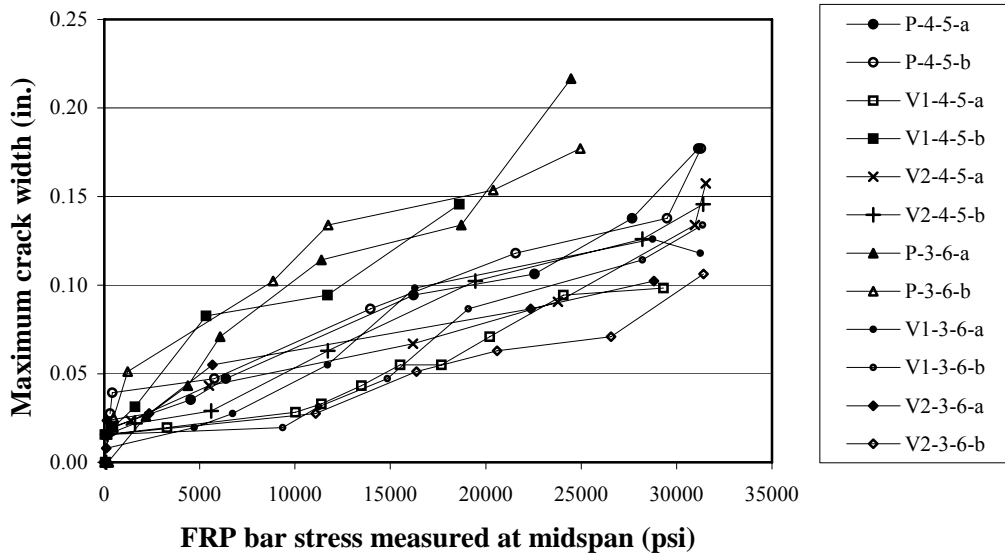


**Figure 65. Stress versus Maximum Crack Width of Specimens with 3.18-Inch Cover.**

### Comparison between Test Results and Available Equations to Predict Maximum Crack Width

The suitability of the expression given by the ACI 440 (2001) design guidelines and the equation given by Faza and GangaRao (1993) to predict the maximum crack width in FRP-reinforced concrete members will be evaluated in this section. A comparison between existing equations and the experimental data will be made, beginning with the Gergely and Lutz (1973) equation:

$$W_{\max} = 0.076\beta \cdot f_s \cdot \sqrt[3]{d_c A} \quad (67)$$

where,

$$\beta = h_2/h_1$$

$h_1$  = Distance from the centroid of the reinforcement to the neutral axis (inch),

$h_2$  = Distance from the extreme tension fiber to the neutral axis (inch),

$f_s$  = Stress in the reinforcement (ksi),

$d_c$  = Bottom cover measured from the center of lowest bar (inch),

$A$  = Twice the difference between the total and effective depths multiplied by the width of the section (effective area of concrete surrounding the main reinforcement) divided by the number of bars ( $\text{inch}^2$ ).

Committee ACI 440 (2001) modified the Gergely and Lutz (1973) equation for FRP-reinforced concrete elements as:

$$W_{\max} = 0.076 \beta \cdot \frac{E_s}{E_f} f_f \cdot \sqrt[3]{d_c A} \quad (68)$$

where all the terms are as defined before and:

$f_f$  = Stress in the FRP reinforcement ( $\text{ksi}$ ),

$E_s$  = Modulus of elasticity of steel ( $29,000,000 \text{ psi}$ ),

$E_f$  = Modulus of elasticity of FRP bars ( $\text{psi}$ ).

The ACI 440 equation was evaluated to estimate the maximum crack width of the specimen with 0.75-inch diameter bars for the three different concrete covers. The values of the variables to be used in the equation will be presented next. The variables were taken as follows:  $E_s = 29,000,000 \text{ psi}$ ,  $E_f = 6,062,000 \text{ psi}$  (average of unexposed elastic modulus from all bar types studied),  $f'_c = 5990 \text{ psi}$ ,  $E_c = 4,412,000 \text{ psi}$ ,  $n_f = E_f/E_c = 1.37$ , the area of four 0.625-inch diameter bars is  $1.48 \text{ inch}^2$ , and the area of three 0.75-inch diameter bars is  $1.35 \text{ inch}^2$ . The average width of the slab is 17.1 inches, and the average slab thickness is 8 inches. The rest of the elements used in the ACI 440 expression are presented in [Table 46](#).

**Table 46. Variables Used in the ACI 440 Expression.**

Bar diameter (in.)	Number of bars	Cover $d_c$ (in.)	Bar area (in. <sup>2</sup> )	Depth d (in.)	$\rho$	k	kd (in.)	$\beta$	A (in. <sup>2</sup> )	$E_s/E_f$
0.625	4	3.56	1.48	4.44	0.0195	0.2062	0.92	2.01	30.39	4.78
0.750	3	3.51	1.35	4.49	0.0176	0.1968	0.88	1.97	39.94	4.78
0.625	4	2.52	1.48	5.48	0.0158	0.1877	1.03	1.57	21.51	4.78
0.750	3	2.56	1.35	5.44	0.0145	0.1806	0.98	1.57	29.12	4.78
0.625	4	1.58	1.48	6.42	0.0135	0.1748	1.12	1.30	13.48	4.78
0.750	3	1.54	1.35	6.46	0.0122	0.1671	1.08	1.29	17.51	4.78

The expression developed by Faza and GangaRao (1993) to predict maximum flexural crack widths in a beam is:

$$W_{\max} = \frac{f_{fs}}{E_f} \frac{2f'_t}{\mu_m} \frac{A}{\pi D} \quad (69)$$

where,

$W_{\max}$  = Maximum crack width (inch),

$$f'_t = 7.5\sqrt{f'_c}$$

- $f'_c$  = Compressive strength of concrete at 28 days (psi),
- $f_{fs}$  = Maximum FRP bar stress at service load level (ksi),
- $E_f$  = Modulus of elasticity of FRP bar (ksi),
- $\mu_m$  = Maximum bond stress (psi),
- $D$  = Bar diameter (inch),
- $A$  = Twice the difference between the total and effective depths multiplied by the width of the section (effective area of concrete surrounding the main reinforcement) divided by the number of bars (inch<sup>2</sup>).

Since the bond strength of the bar is required in Equation 69, the specific value obtained from the bond tests from bar type V2 will be used. The bond strength of 1663 psi for bar V2 was used because it was the value closest to the overall average of all the bond strengths obtained from the specimens that failed in pullout. The overall average

bond strength was 1754 psi. The highest bond stress obtained was 2567 psi, and the lowest was 668 psi. The details of the bond test results are given in the [bond test results section](#) presented later. The values used in [Equation 69](#) are indicated in [Table 47](#).

**Table 47. Values of the Variables Used in the Equation of Faza and GangaRao.**

Nominal cover (in.)	d (in.)	h (in.)	b (in.)	A (in. <sup>2</sup> )	$\mu_m$ (psi)	$f_f$ (psi)	$f_c$ (psi)	$f_t$ (psi)	D (in.)	$E_f$ (psi)
1	6.46	8.00	17.08	52.53	1663	84588	5990	580	0.751	6062157
2	5.44	8.00	17.08	87.37	1663	84588	5990	580	0.751	6062157
3	4.49	8.00	17.08	119.81	1663	84588	5990	580	0.751	6062157

The maximum crack widths computed with the ACI 440 and Faza and GangaRao expressions together with the data from the experiments are illustrated in Figures 66 through 68 for the specimens with overall clear covers of 1.21 inches, 2.18 inches, and 3.18 inches, respectively. Figures 66 through 68 also show the maximum crack width limit for exterior exposure of 0.02 inch recommended by the ACI 440 design guidelines. It can be observed from Figures 66 through 68 that most specimens at low stress levels exceed the ACI 440 crack width limit. The number of maximum crack width observations that exceed the ACI 440 limit tends to decrease as the concrete cover decreases. As noted earlier, maximum crack width is a function of concrete cover and this behavior is taken into account in Equations 67 and 68 by the  $\beta$  factor. This behavior also was noticed in steel-reinforced concrete elements ([Beeby 1978](#)), where it was identified that the width of a crack varies almost linearly from the surface of the reinforcement. As indicated by Beeby ([1978](#)), crack widths are nearly the same at the surface of the reinforcement for different covers, while they are larger at the surface of the concrete for elements with larger covers. Thus, it might be reasonable to use a maximum crack width limit that is a function of concrete cover.

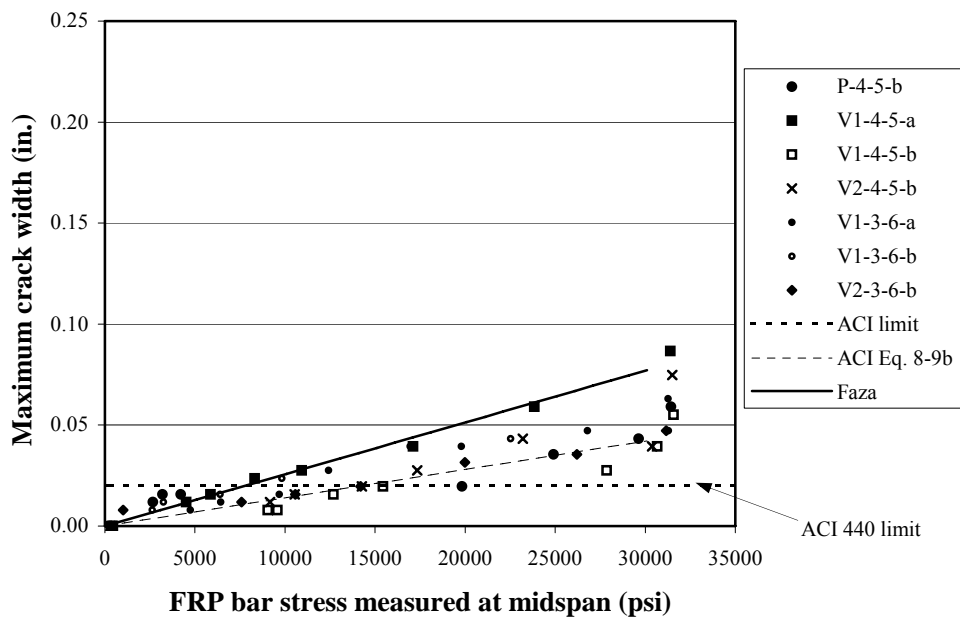


**Figure 66. Comparison of Predicted and Measured Values for Specimens with 1.21-Inch Cover.**

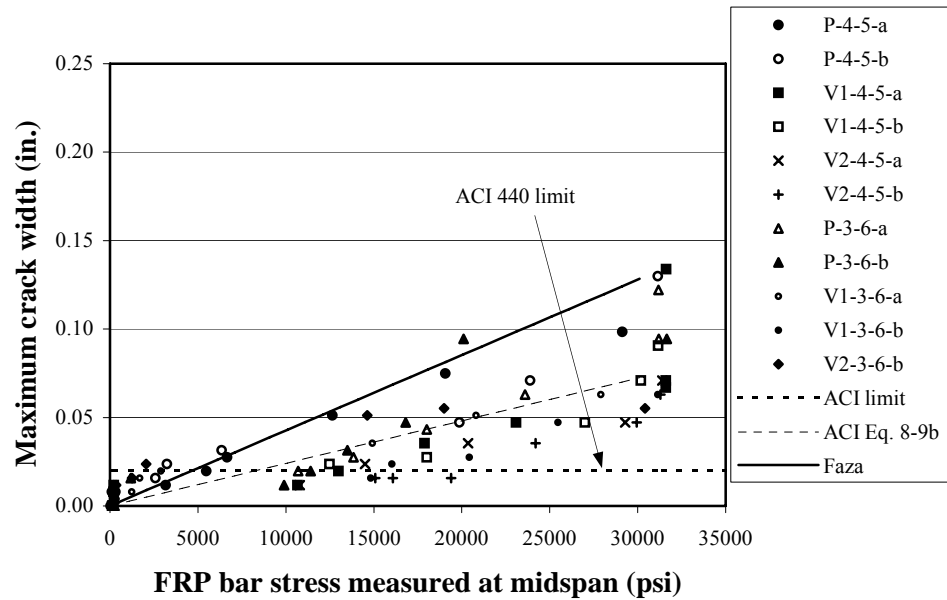


**Figure 67. Comparison of Predicted and Measured Values for Specimens with 2.18-Inch Cover.**

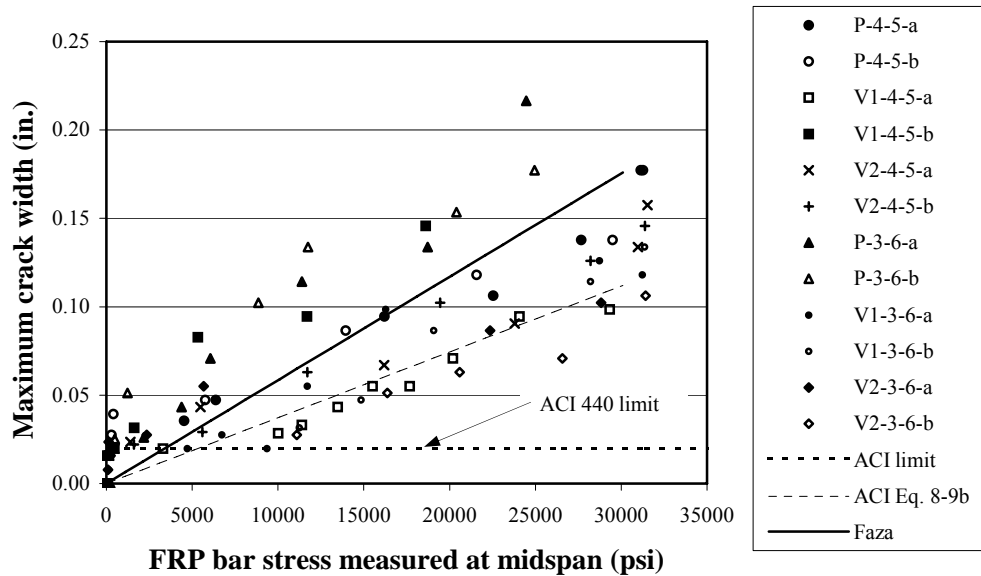


**Figure 68. Comparison of Predicted and Measured Values for Specimens with 3.18-Inch Cover.**

### Correlation of Test and Predicted Results

In order to evaluate the correlation of the equations given by ACI 440 (2001) and Faza and GangaRao (1993), the method of least squares was used. Gergely and Lutz (1973) used a similar statistical analysis to the one used in this project. Thus, a best-fit line was obtained for the observed data. The results are illustrated in Figures 69, 70, and 71 for the specimens with overall clear covers of 1.21 inches, 2.18 inches, and 3.18 inches, respectively. The equation proposed by Faza and GangaRao was observed to be overly conservative and consistently predicted larger maximum crack widths than those predicted by the least squares line for the three concrete covers tested in this project. Since the equation given by ACI 440 predicted maximum crack widths that were closer to the least squares lines, it was decided to evaluate the ACI 440 equation. The objective was to develop (or validate) an expression that could predict maximum crack widths that were closer to the best-fit lines determined from this research. The following modified ACI 440 equation will be studied:

$$W_{max} = C \cdot \beta \cdot f_f \cdot \sqrt[3]{d_c A} \quad (70)$$

where all terms were defined earlier and the coefficient  $C$  needs to be determined.

Equation 70 is plotted with a value of  $C = 0.09$  in Figures 69, 70, and 71. The procedure used to obtain the coefficient  $C$  will be described next.

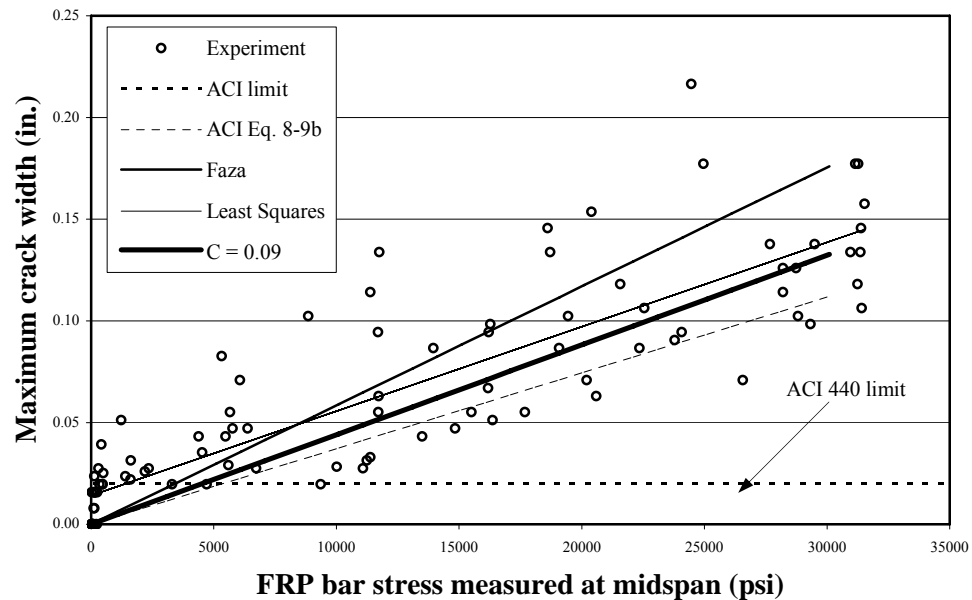


**Figure 69. Comparison of Equations Analyzed for Specimens with 1.21-Inch Cover.**

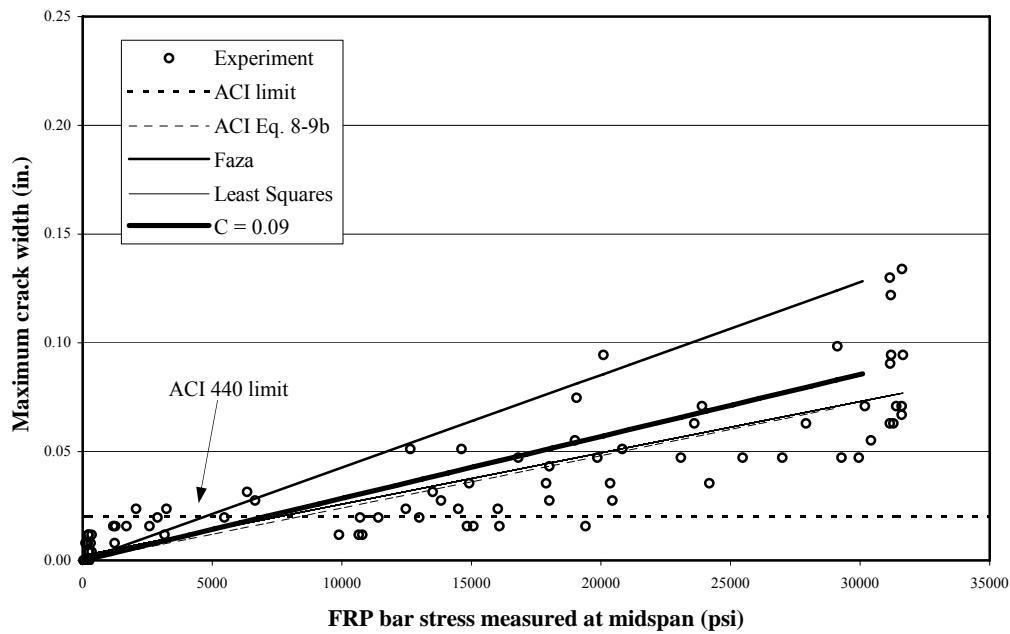


**Figure 70.** Comparison of Equations Analyzed for Specimens with 2.18-Inch Cover.

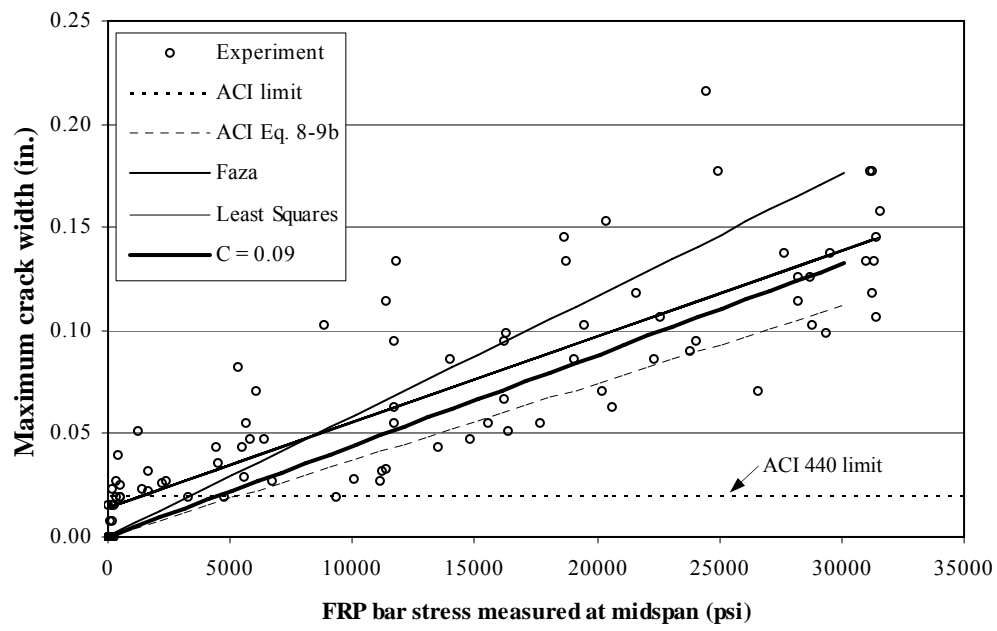


**Figure 71.** Comparison of Equations Analyzed for Specimens with 3.18-Inch cover.

The method of least squares was used to judge how close an expression lay to the least squares line. The residual or error is defined as the deviation between an observation and the value predicted by a regression line  $e_i = (y_{obs} - y_{pred})$  (Johnson and Bhattacharyya 1985). The sum of the squares due to error (SSE) is defined as (Johnson and Bhattacharyya 1985):

$$SSE = \sum e_i^2 \quad (71)$$

The method of least squares minimizes the SSE to obtain the best fitting line to the observed data. Since the regression line obtained by least squares is the line with the smallest SSE, the goodness of fit of the three expressions analyzed to predict maximum crack width will be based on how close their SSE lies to the SSE obtained by the best-fit line equation. Thus, the sum of the squares due to error was obtained for the best-fit line, the ACI 440 (2001) expression, the equation of Faza and GangaRao (1993), and the modified ACI 440 equation. The sums of the errors squared were obtained for each of the three covers studied for all of the equations mentioned. The results of the sum of the errors squared from each cover were normalized to the sum of the errors squared of the least squares line. The numbers obtained from the three covers from all of the equations were then added. Thus, the sum corresponding to the least squares line was 3, one from each cover. The modification proposed for the ACI 440 expression consists in changing the multiplier of 0.076 for a constant  $C$ . Several values were evaluated for the constant  $C$  until the value that gave the lowest SSE results was obtained. The results from the analysis are summarized in Table 48. The sample correlation coefficients ( $R^2$ ) between the FRP bar stress and the maximum measured crack width are 0.81, 0.74, and 0.75 for concrete covers of 1.21 inches, 2.18 inches and 3.18 inches, respectively.

**Table 48. Values of SSE of Several Equations Normalized to SSE of Least Squares Line.**

Equation	Least squares	ACI 440	Faza & Ganga Rao	C									
				0.070	0.080	0.085	0.088	0.089	0.090	0.091	0.092	0.095	0.100
1.21 in. cover	1.00	1.47	3.82	1.84	1.29	1.12	1.06	1.04	1.03	1.02	1.01	1.00	1.05
2.18 in. cover	1.00	1.01	4.70	1.08	1.01	1.07	1.13	1.15	1.18	1.21	1.24	1.34	1.57
3.18 in. cover	1.00	1.56	1.57	1.82	1.42	1.28	1.22	1.21	1.19	1.18	1.17	1.15	1.15
Sum	3.00	4.04	10.08	4.74	3.72	3.47	3.40	3.40	3.39	3.40	3.41	3.49	3.76

From the analysis summarized in [Table 48](#), it appears that [Equation 70](#) with a value of  $C = 0.09$  would make maximum crack width predictions that are closest to the least squares lines fit to the test data, since [Equation 70](#) has a smaller sum than the Faza and GangaRao expressions. In order to verify whether [Equation 70](#) has a higher probability of predicting maximum crack widths than the other expressions, the percentage of observations recorded within a range of  $\pm 30$  percent of all of the equations was determined and compared in [Table 49](#).

**Table 49. Observations within  $\pm 30$  Percent Range<sup>a</sup>.**

Average cover (in.)	Number of observations within +/- 30 % of values predicted by equation			Percentage of total observations within +/- 30 % range		
	ACI 440	Faza	C = 0.09	ACI 440	Faza	C = 0.09
1.21	31	26	34	55	46	61
2.18	45	31	42	50	34	47
3.18	45	42	50	46	43	52

<sup>a</sup> The total number of observations from this research were: 56 for the 1.21 inch cover, 90 for the 2.18 inch cover, and 97 for the 3.18 inch cover.

[Table 49](#) shows that the coefficient,  $C$ , of 0.09 has good correlation with the ACI 440 equation for predicting the maximum crack width for average concrete covers of 1.21, 2.18, and 3.18 inches. Note that in the ACI 440 equation a constant of 0.076 is

used (see [Equation 68](#)). ACI 440 recommends a  $k_b$  factor of 1.2. Multiplying the  $k_b$  factor of 1.2. with the constant 0.076 results in a factor of 0.0912, very similar to the value estimated in this research (i.e.,  $C = 0.09$ ). Following the results from this research, the following equation to predict maximum crack width of FRP-reinforced concrete flexural members is as follows:

$$W_{\max} = 0.09\beta \cdot f_f \cdot \sqrt[3]{d_c A} \quad (72)$$

where all of the terms have been defined earlier.

It should be noted that the best-fit line was used to predict the average maximum crack width, although this is not a conservative approach since 50 percent of cracks will be larger than that predicted with the equation. However, since Gergely and Lutz performed the same analysis for conventionally reinforced concrete sections, the same approach was used in this project.

The applicability of [Equation 72](#) to beam type elements needs verification. However, in developing [Equation 72](#), the research data reported by the studies conducted by Faza and GangaRao ([1993](#)) and by Masmoudi et al. ([1998](#)) were not included for several reasons. The study reported by Faza and GangaRao did not include the size of the specimens, reinforcement type, or test configuration. The research by Masmoudi et al. did not present the data numerically and did not report the stresses corresponding to each maximum crack width observation. Thus, verification of the applicability of the equation proposed in this project could not be made for beams.

Summarizing, measurements of maximum crack width and GFRP reinforcement stress from a large number of tests were compared to existing equations. Using the method of least squares, a new equation that fits the data from this research was determined. This equation needs verification with FRP-reinforced concrete members other than slabs, such as square and T-beams. This project found that the maximum allowable crack width recommended by the ACI 440 document is similar to that found

in this research. Since the maximum crack widths recorded are a function of concrete cover, a larger maximum crack width limit that is a function of concrete cover might be more reasonable.

### **Cyclic Loading of Concrete Beams Test**

[Section II](#) described the previous efforts by researchers devoted to investigating the performance of FRP-reinforced concrete members under cyclic loading. As noted, research is limited in this area and limited tests have been reported on the effects of cyclic loading on the deflections of GFRP-reinforced concrete specimens. The specimens, materials, and setup used in this research were described in [Section III](#). The influence of bar diameter, concrete cover, and bar surface finish on the deflection performance of GFRP-reinforced concrete beams was investigated. Two bar diameters were used: 0.5 inch and 0.75 inch; two concrete covers were investigated: 1.5 inch and 2 inch; and three bar surface types: bars with a ribbed surface, bars with a circular shape finished with a sand coating, and bars with a helical wrapping and sand coating were used. The strength results of the beams tested at a constant load rate will be presented first, followed by the deflections of the beams tested under cyclic loading. Finally, the residual strength of the beams subjected to cyclic loading will be presented.

### **Constant Load Rate Tests**

Twelve beams were first tested at constant load rate in four-point bending to determine their failure loads. The ultimate loads of the beams were necessary to determine the upper loads to be applied to the specimens subjected to cyclic load. The failure loads and failure modes of the beams tested at constant load rate are summarized in [Table 50](#) for the beams reinforced with 0.5-inch diameter bars and [Table 51](#) for the beams reinforced with 0.75-inch diameter bars. The specimen designation is given by the reinforcement type, followed by the bar diameter in eighths of an inch, and by the clear concrete cover in inches. For example, specimen P-6-2 is a beam reinforced with a

bar type P, 0.75 inch in diameter, and a clear concrete cover of 2 inches. Tables 50 and 51 show that the beams reinforced with 0.75-inch diameter bars are 22 percent stronger than the beams reinforced with 0.5-inch diameter bars, on average. Most of the beams with 0.75-inch diameter bars failed by crushing of the concrete, while most of the beams with 0.5-inch diameter reinforcement failed by rupture of the bars. The failure loads showed a COV of 6 percent for the beams reinforced with 0.75-inch diameter bars and 8 percent for the beams reinforced with 0.5-inch diameter bars.

**Table 50. Failure Loads of Beams with 0.5-Inch Diameter Bars.**

Specimen	Failure load (kips)	Failure mode
P-4-2	13.3	Compression
V1-4-2	12.6	Compression followed by tension
V2-4-2	14.6	Tension
P-4-1.5	14.8	Tension
V1-4-1.7	12.2	Tension
V2-4-1.5	13.0	Tension
Average	13.4	
S.D.	1.1	
COV	0.08	

**Table 51. Failure Loads of Beams with 0.75-Inch Diameter Bars.**

Specimen	Failure load (kips)	Failure mode
P-6-2	15.5	Compression
V1-6-2	17.1	Compression
V2-6-2	16.2	Compression
P-6-1.5	17.9	Compression
V1-6-1.5	15.2	Compression
V2-6-1.5	16.2	Tension
Average	16.4	
S.D.	1.0	
COV	0.06	

## Cyclic Load Tests

All 13 beams tested in cyclic loading were cracked under load before the application of the cyclic loading. The beams were subjected to a sinusoidal load with a frequency of 10 Hz. All beams were loaded with two-point loads in four-point bending. The upper load magnitude was 4.1 kips, and the lower load magnitude was 0.2 kips for the beams reinforced with 0.75-inch diameter bars. Thus, the load range was 3.9 kips. The upper load magnitude was 2.1 kips, and the lower load magnitude was 0.2 kips. for the beams reinforced with 0.5-inch diameter bars. Thus, the load range was 1.9 kips. The upper load magnitudes are equivalent to 25 percent and 16 percent of the average failure load of the beams reinforced with 0.75-inch and 0.5-inch diameter bars, respectively. A summary of the reinforcement stresses, computed at midspan using elastic analysis, is presented in [Table 52](#). Average values from all bar types were used in the computation of the area, diameter, modulus of elasticity, and tensile strength of the bars. The stress range for all specimens is approximately 18.9 ksi. Although there appears to be a different load range applied to beams reinforced with 0.75-inch and 0.5-inch bar diameters, there is essentially no difference in the stress ranges applied to the bars. Thus, stress range was not a variable. The measured midspan deflections and the corresponding number of cycles obtained in the cyclic loading tests are summarized in [Tables 53, 54, and 55](#). The labels a, b, and c in [Tables 53, 54, and 55](#) are used only to assign the tables a different name and to indicate that the results of those tables are part of the same test. The specimens are labeled as noted earlier. It should be noted that no companion specimens with steel reinforcement were evaluated.

**Table 52. GFRP Bar Stresses at Midspan.**

Bar diameter (in.)	Cover (in.)	Load (kips)	Stress (psi)	Stress range (psi)	Average stress range (psi)	
0.75	2.0	4.10	19,886	18,916	18,699	
		0.20	970			
	1.5	4.10	18,883	17,962		
		0.20	921			
0.50	2.0	2.10	21,744	18,439	19,186	
		0.20	2,071			
	1.5	2.10	20,667	19,673		
		0.20	1,968			

**Table 53. Number of Cycles and Midspan Beam Deflections (Part A).**

V1-6-1.5		V1-6-2-a		P-4-2-a		V1-6-2-b		V2-6-2	
Number of cycles	Deflection (in.)								
1	0.13	500	0.13	33	0.09	32	0.10	52	0.10
102	0.21	1,000	0.13	100	0.10	100	0.12	103	0.13
649	0.22	10,000	0.15	510	0.11	500	0.13	510	0.13
1,053	0.22	20,000	0.15	1,010	0.11	1,000	0.14	1,010	0.14
9,963	0.24	50,000	0.15	10,510	0.14	199,880	0.15	10,010	0.14
20,019	0.26	100,000	0.15	20,000	0.14	276,880	0.17	20,010	0.14
49,967	0.26	200,000	0.16	50,000	0.15	-	-	49,510	0.14
100,043	0.26	500,000	0.17	103,530	0.15	-	-	99,510	0.14
200,432	0.27	593,000	0.17	201,810	0.26	-	-	199,510	0.13
541,612	0.27	1,000,000	0.23	501,820	0.27	-	-	499,510	0.14
989,500	0.28	-	-	1,000,830	0.28	-	-	997,590	0.31
2,001,644	0.29	-	-	2,026,820	0.34	-	-	2,012,590	0.36
2,841,644	0.29	-	-	-	-	-	-	-	-

**Table 54. Number of Cycles and Midspan Beam Deflections (Part B).**

P-4-2-b		P-6-1.5		V1-4-1.5-b		P-4-1.5	
Number of cycles	Deflection (in.)						
34	0.09	33	0.10	32	0.12	32	0.11
103	0.09	103	0.11	102	0.16	102	0.12
540	0.14	855	0.11	512	0.21	500	0.13
1,040	0.15	1,010	0.13	1,024	0.22	1,000	0.14
9,946	0.17	10,070	0.17	10,033	0.26	10,000	0.14
36,490	0.18	44,390	0.22	49,972	0.27	49,600	0.15
49,990	0.19	85,798	0.22	100,000	0.28	99,840	0.15
100,240	0.21	839,830	0.29	500,670	0.28	675,730	0.15
202,970	0.28	998,240	0.37	1,001,770	0.31	1,001,130	0.17
502,970	0.30	1,989,050	0.40	1,458,020	0.38	2,157,380	0.18
998,670	0.32	3,002,270	0.41	-	-	-	-
1,999,110	0.40	3,933,520	0.41	-	-	-	-
2,269,110	0.41	-	-	-	-	-	-

**Table 55. Number of Cycles and Midspan Beam Deflections (Part C).**

V1-13-38-a		V2-13-50		P-19-50		V2-19-38	
Number of cycles	Deflection (in.)						
10	0.08	29	0.06	32	0.08	33	0.11
109	0.10	89	0.06	100	0.09	103	0.13
509	0.10	440	0.08	200	0.10	550	0.13
1,010	0.11	2,000	0.12	2,040	0.13	1,000	0.18
10,500	0.11	10,000	0.12	10,040	0.14	10,000	0.25
49,500	0.11	50,100	0.12	50,240	0.14	49,960	0.31
99,500	0.12	101,100	0.13	101,240	0.14	76,990	0.32
499,500	0.12	501,100	0.13	501,240	0.15	151,240	0.33
1,001,260	0.12	1,001,100	0.13	1,001,240	0.15	186,240	0.36
1,683,030	0.12	1,996,100	0.13	1,996,240	0.14	500,860	0.42
3,395,850	0.12	-	-	-	-	1,000,860	0.43
4,761,830	0.13	-	-	-	-	1,998,570	0.44
-	-	-	-	-	-	2,163,570	0.44

Beam V1-4-1.5-b is the only specimen that failed during cyclic loading. The beam failure may have been the result of overloading. If a beam moved sideways or the

bearing pads wore out, the testing machine would stop. Beam V1-4-1.5-b was left under cyclic loading overnight. During the night, the testing machine stopped. The next day when the testing machine was restarted, the load ram may have loaded the beam beyond the intended load level, and a cracking noise was heard. It is possible that the beam was not properly seated and aligned after changing the bearing pads before loading was resumed. Cyclic load testing of beam V1-4-1.5-b was stopped at that time. This beam had undergone 1,458,020 cycles before failure occurred. The results from Tables 53, 54, and 55 are shown graphically in Figures 72 and 73.

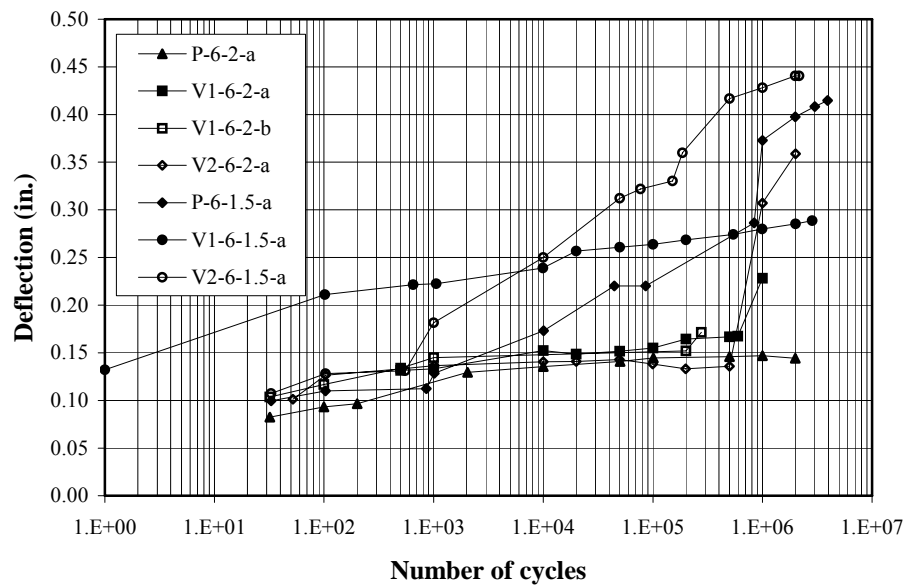


**Figure 72. Cyclic Loading Results of Beams Reinforced with 0.75-Inch Diameter Bars.**

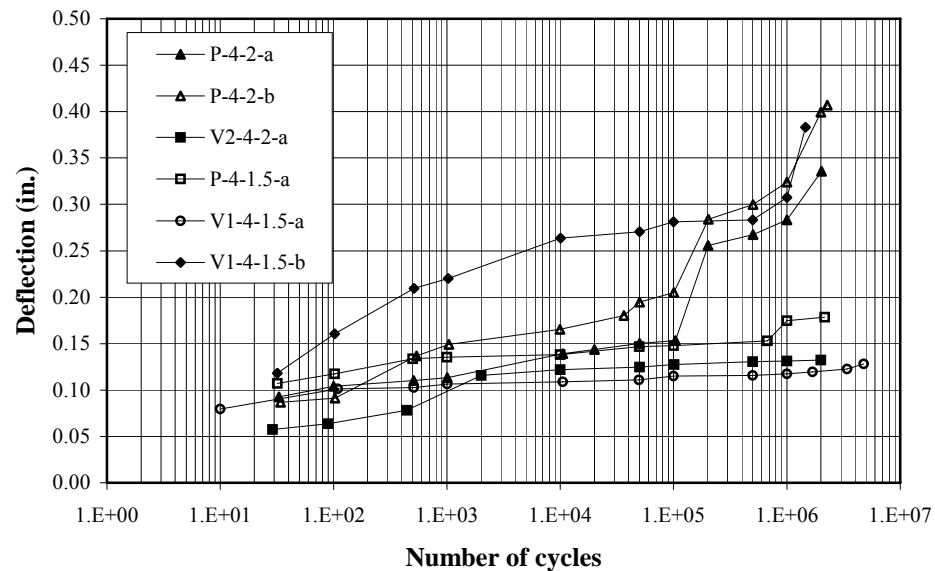


**Figure 73.** Cyclic Loading Results of Beams Reinforced with 0.5-Inch Diameter Bars.

In general, an increase in deflections with number of cycles of loading is observed for all of the specimens. A beam with a 2-inch cover would have a smaller cracked moment of inertia than a section with 1.5-inch cover, all other variables being the same. This factor did not seem to cause a significant influence on the increase in deflections due to cyclic loading as shown in [Figure 74](#). [Figure 74](#) illustrates that beams with concrete covers of 2 inches and 1.5 inches have a similar increase in deflection rate.

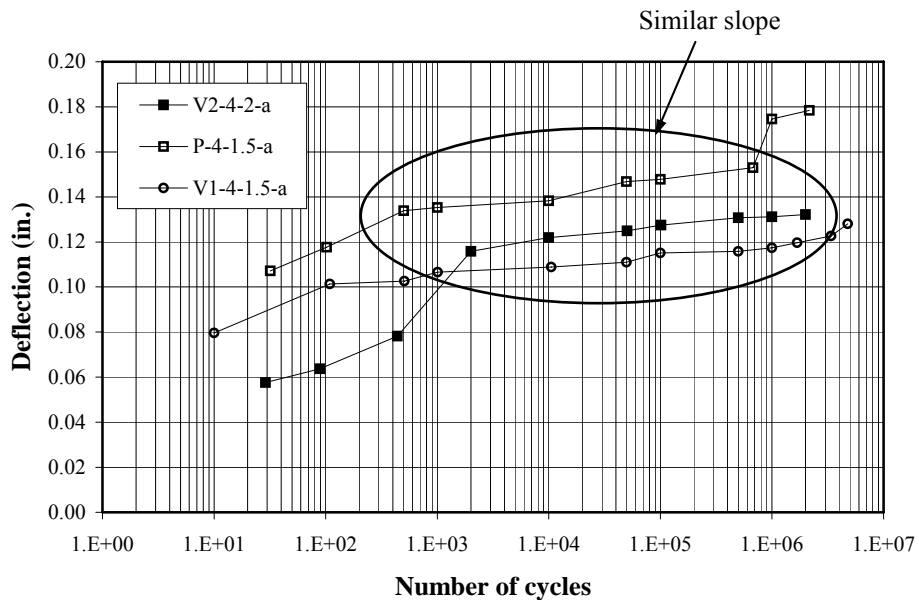


**Figure 74. Influence of Concrete Cover on Rate of Beam Deflection Increase.**

As can be seen in [Figure 74](#), after 1000 cycles, bars with three different surface finishes have essentially the same slope in the deflection versus number of cycles plot. This behavior is an indication that bars with different surface finishes and, therefore, different bond strengths have similar performance under cyclic loading.

The results of all beams are presented in [Figure 75](#) to investigate whether bar size has an influence in beam deflections. As observed from [Figure 75](#), there is no clear difference between the results obtained for the beams reinforced with 0.75-inch diameter bars and the beams reinforced with 0.5-inch diameter bars.

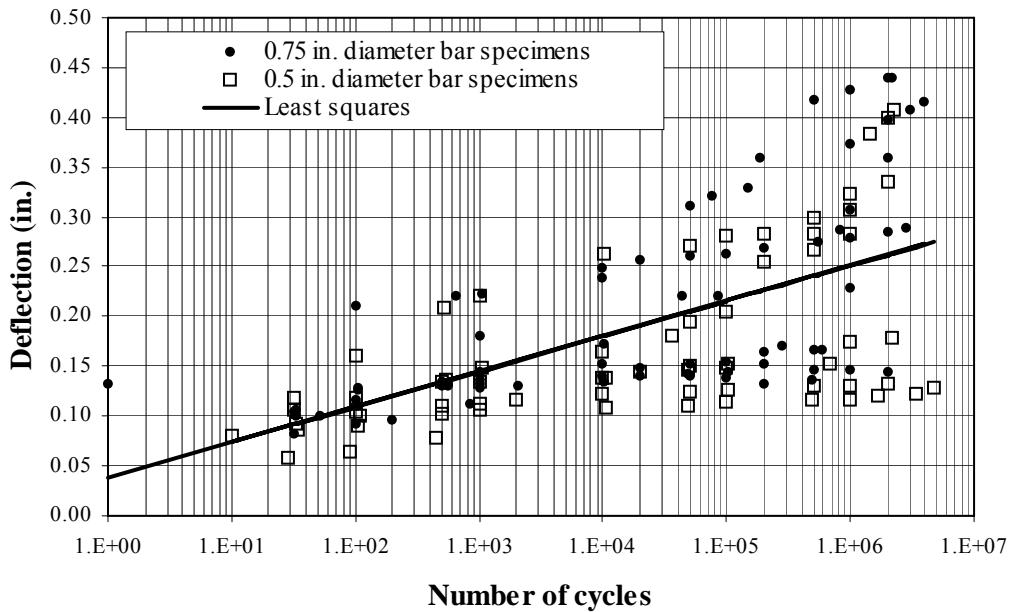


**Figure 75. Deflections of All Specimens.**

A regression analysis of the data resulted in the following equation:

$$y = 0.0154 \ln(n) + 0.0384 \quad (73)$$

where  $y$  is the beam deflection in inches and  $n$  is the number of cycles. The correlation coefficient is  $R^2 = 0.38$ . The slope of Equation 73 may be used to predict the increase of deflections of GFRP-reinforced concrete members under cyclic loading. Thus, for a beam having an initial deflection of 0.038 inch, the increment of deflection can be computed to be 680 percent at 2 million cycles. This shows that deflections of GFRP-reinforced concrete elements may increase considerably due to cyclic loading.

In an effort to obtain a higher correlation coefficient for the data obtained, a new analysis will be made where some of the results will be omitted due to an abrupt increase in deflections (i.e., possibly due to slip) or because the beam deflections differ considerably from the deflections of most of the other beams. Thus, the results of specimens V1-6-1.5-a and V2-6-1.5-a from the 0.75-inch diameter bar group were

omitted. In addition, the data corresponding to specimens V1-6-2-a, V2-6-2-a, and P-6-1.5-a was truncated at 1 million cycles, 1 million cycles, and 10,000 cycles, respectively. Also, the results of specimens P-4-2-b and V1-4-1.5-b from the 0.5-inch diameter bar group were omitted. Additionally specimen P-4-2-a was truncated at 200,000 cycles. The selected data are presented in [Figure 76](#).

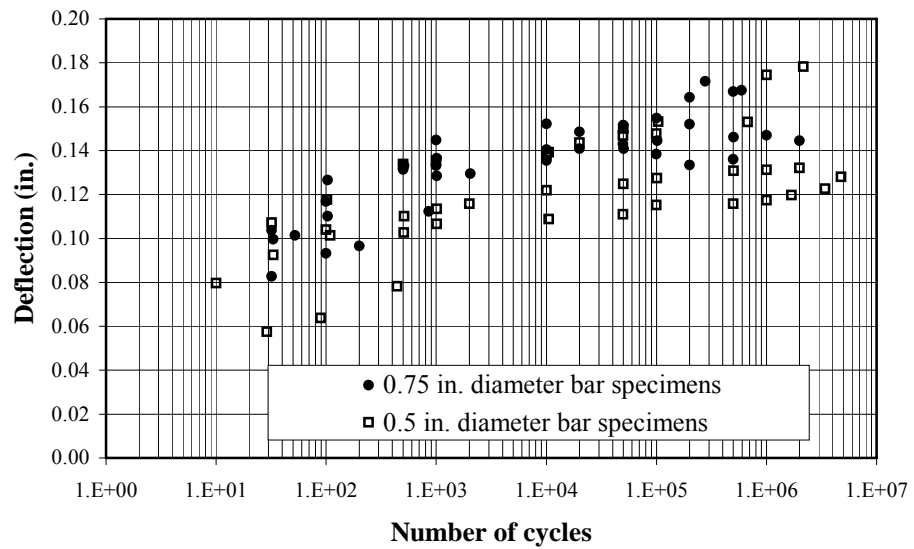


**Figure 76. Selected Deflections of Specimens with 0.5-and 0.75-Inch Diameter Bars.**

There is basically no difference between the deflections obtained for the 0.5-inch and 0.75-inch diameter bar specimens. Therefore, a regression analysis was carried out for the combined data, and the trend line is presented in [Figure 77](#).

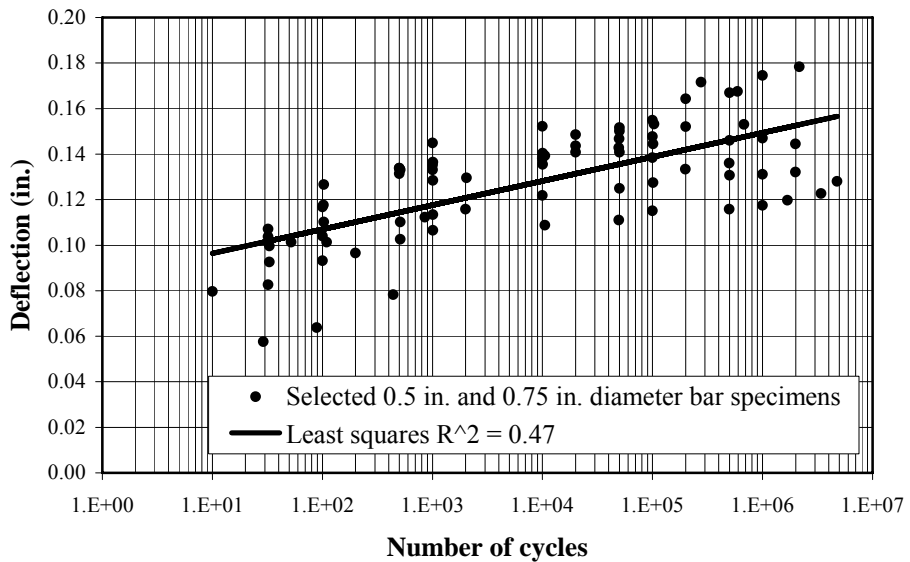


**Figure 77. Regression Analysis Results.**

The correlation coefficient for the combined selected data is  $R^2 = 0.47$ , and the regression equation is:

$$y = 0.0046 \ln(n) + 0.0858 \quad (74)$$

where  $y$  is the beam deflection in inches and  $n$  is the number of cycles.

Although the coefficient of correlation is relatively low, the slope of [Equation 74](#) could still be used to estimate the increase in deflections of a GFRP-reinforced concrete beam due to cyclic loading. The deflections of a beam due to cyclic loading could be estimated to be 0.15 inch after 2 million cycles for an initial deflection of 0.086 inch, using [Equation 74](#). That is a 74 percent increase in deflection relative to the initial elastic deflection. Thus, [Equation 74](#) may be used to compute a lower bound expected deflection for GFRP-reinforced concrete members subjected to cyclic loading.

Elastic short-term deflections of cracked FRP-reinforced concrete beams can be computed using the effective moment of inertia of Equation 8-12a recommended by the ACI 440 (2001) design guidelines:

$$I_e = \left( \frac{M_{cr}}{M_a} \right)^3 \beta I_g + \left[ 1 - \left( \frac{M_{cr}}{M_a} \right)^3 \right] I_{cr} \leq I_g \quad (75)$$

where  $E_s$  and  $E_f$  have been defined previously,

$$\beta = \alpha \left( \frac{E_f}{E_s} + 1 \right)$$

and

$\alpha$  = Bond-dependent coefficient,

$I_e$  = Effective moment of inertia of the section ( $inch^4$ ),

$I_{cr}$  = Cracked moment of inertia of the section ( $inch^4$ ),

$I_g$  = Gross moment of inertia of the section ( $inch^4$ ),

$M_{cr}$  = Cracking moment ( $inch-lb$ ),

$M_a$  = Maximum moment in the member at stage deflection is computed ( $inch-lb$ ).

and

$$I_{cr} = \frac{bk^3 d^3}{3} + nA_f(d - k)^2,$$

$$k = \sqrt{(\rho_f n)^2 + 2\rho_f n - \rho_f n},$$

$$\rho_f = \frac{A_f}{bd},$$

$$n = \frac{E_f}{E_s},$$

$b$  = Width of the section ( $inch$ ),

$d$  = Distance from top of the beam to center of the reinforcement ( $inch$ ),

$A_f$  = Cross-sectional area of the FRP reinforcement ( $inch^2$ ).

The deflections of a cracked FRP-reinforced concrete element subjected to cyclic loading can be obtained by adding to the elastic deflections computed using [Equation 75](#). In this equation,  $m$  is the slope of the deflection versus number of cycles line obtained from the linear regression, and  $n$  is the number of cycles. The deflections predicted with [Equations 73](#) and [74](#) are valid only for an FRP bar stress range of 18.9 ksi. Future tests should include different bar stress ranges to provide the basis for making predictions of the deflection behavior of beams under cyclic loading at different stress ranges.

### **Constant Load Rate after Cyclic Load Tests**

The results from the constant load rate tests include the number of cycles the beam was subjected to, the failure load after constant load rate testing, and the ratio of the failure load due to constant load rate testing after cyclic load was applied to the failure load due to constant load rate without cyclic load. The results are summarized in [Tables 56](#) and [57](#) for specimens with 0.75-inch and 0.5-inch diameter bars, respectively. Specimen P-6-1.5-a was subjected to almost 4 million cycles and had a residual strength of 91 percent of the original strength, while specimen V1-4-1.5-b was subjected to close to 5 million cycles and showed a residual strength of 113 percent of the strength exhibited by the specimen not subjected to cyclic load. The COV of the failure load for the specimens subjected to cyclic loading and reinforced with 0.75-inch diameter bars was 8 percent. The average failure load after cyclic loading for the 0.75-inch diameter specimens was 5 percent higher, on average, than for the specimens not subjected to cyclic loading.

Specimen V1-4-1.5-b offset the average values of the failure load and COV, since it failed during the cyclic loading. The average failure load of the specimens reinforced with 0.5-inch diameter bars and subjected to cyclic loading, computed excluding specimen V1-4-1.5-b, was 13.5 kips. This average value is the same as the average value obtained from the specimens not subjected to cyclic loading. Based on these data, it can be concluded, under the conditions tested, that applying an average of 2

million cycles of loading with a bar stress range of 18.9 ksi did not affect the load capacity of the GFRP-reinforced concrete beams studied.

**Table 56. Failure Loads with and without Cyclic Loading for 0.75-Inch Diameter Bar Specimens.**

Specimen	Number of cycles	P <sub>u</sub> after cyclic loading (kips)	P <sub>u</sub> without cyclic loading (kips)	P <sub>u</sub> after cycling / P <sub>u</sub> without cycling
P-6-2-a	1,196,240	17.7	15.5	1.14
V1-6-2-a	276,880	17.2	17.2	1.00
V1-6-2-b	1,000,000	18.0	17.2	1.05
V2-6-2-a	2,012,590	17.1	16.2	1.05
V2-6-2-b	1,996,450	16.7	16.2	1.03
P-6-1.5-a	3,933,520	16.3	17.9	0.91
V1-6-1.5-a	2,841,644	18.4	15.2	1.21
V2-6-1.5-a	2,163,570	16.4	16.2	1.01
Average	1,927,612	17.2	16.4	1.05
S.D.	-	0.8	-	-
COV	-	0.04	-	-

**Table 57. Failure Loads with and without Cyclic Loading for 0.5-Inch Diameter Bar Specimens.**

Specimen	Number of cycles	P <sub>u</sub> after cyclic loading (kips)	P <sub>u</sub> without cyclic loading (kips)	P <sub>u</sub> after cycling / P <sub>u</sub> without cycling
P-4-20-a	2,026,820	13.6	13.3	1.02
P-4-2-b	2,269,110	13.8	13.3	1.03
V2-4-2-a	1,996,100	12.7	14.6	0.87
P-4-1.5-a	2,157,380	13.7	14.9	0.92
V1-4-1.5-a	4,761,830	13.8	12.2	1.13
V1-4-1.5-b	1,458,080	4.5	12.2	0.37
V2-4-1.5-a	2,014,510	13.1	13.0	1.01
Average	2,383,404	12.2	13.4	0.91
S.D.	4,761,830	3.4	-	-
COV	-	0.28	-	-

From the tests performed in the laboratory, results indicate that surface finish, concrete cover, and bar diameter do not significantly affect the rate of deflection increase of GFRP-reinforced concrete beams. Two best-fit line equations were obtained to predict the deflections of GFRP-reinforced concrete beams for a bar stress range of 18.9 ksi. The application of 2 million cycles of loading does not affect the ultimate capacity of GFRP-reinforced concrete beams. However, the application of 2 million cycles of loading could increase the deflections of GFRP-reinforced concrete beams between 78 and 680 percent from the initial elastic deflection.

## BOND TEST

In the [literature review section](#), it was evident that the degradation of the bond strength of GFRP bars has not been thoroughly evaluated. The applicability of Equation 11-7 from the [ACI 440 \(2001\)](#) design recommendations, used to compute the development length of FRP bars, requires verification for GFRP bars embedded in concrete. This section describes test results that show that the bond strength between GFRP bars and concrete may degrade with time.

Tables [9](#) and [10](#) presented in [Section III](#) describe the number of samples used for the specimens with 0.5-inch and 0.75-inch diameter bars, respectively. As described in [Section III](#), a set of specimens was exposed outdoors, and another set was exposed indoors under high temperature and high humidity conditions. During planning of the test, the researchers believed that a continuously moist and hot environment would accelerate bond degradation to a measurable degree, if any occurred, between the FRP bars and concrete. Thus, some specimens were left outdoors, and some were exposed in the controlled conditions, both for a period of 16 months.

The recorded maximum bond stresses at failure are shown in Tables [58](#) and [59](#). The results presented in Tables [58](#) and [59](#) are average values computed using all of the

test specimens whether they failed by pullout or bar rupture. The results indicate that the bond strength of the bars is either equal to or greater than the recorded bond stress value. The bond strength would be equal to the recorded bond stress when the bar failed by pullout. When the specimen failed by bar rupture, the bond strength would be equal to or greater than the recorded bond stress. Thus, the results presented in Tables 58 and 59 are lower bounds of bond strength. A comparison between the recorded average bond stress values of the indoor specimens made with bar type V1 and a bond length of 5 inches and the outdoor specimens shows that the indoor exposed specimens had a lower bound bond stress of 9 percent less than the value found for the outdoor specimens. Except for the 0.5-inch diameter specimens made with bar type P and a bond length of 5 inches, all specimens subjected to the controlled environment showed higher lower bound bond stress values, on average, than the specimens exposed to the outdoor exposure condition. This could be the result of a tensile strength reduction of the GFRP bars in the indoor condition relative to the outdoor condition, since all the specimens except six ultimately failed by bar rupture.

**Table 58. Average Bond Stresses at Failure for the 0.5-Inch Diameter Bars.**

Bond length (in.)	Outdoor exposure, failure stress (psi)			Indoor exposure, failure stress (psi)		
	Bar P	Bar V1	Bar V2	Bar P	Bar V1	Bar V2
5	2,328	1,775	2,094	2,380	1,625	1,708
15	827	669	690	798	462	643
30	432	-	-	404	305	320

- no data

**Table 59. Average Bond Stresses at Failure for the 0.75-Inch Diameter Bars.**

Bond length (in.)	Outdoor exposure, failure stress (psi)			Indoor exposure, failure stress (psi)		
	Bar P	Bar V1	Bar V2	Bar P	Bar V1	Bar V2
7.5	-	-	-	2,161	1,717	1,721
22.5	-	-	-	673	590	549
45	-	-	-	-	291	291

- no data

Tables 58 and 59 contain the results of specimens that failed by bar rupture as well as by pullout. Only six specimens out of the 38 tested failed by pullout. The average bond stresses at failure of the specimens that failed by pullout will be discussed next. Two 0.5-inch diameter specimens of bar type P exposed outdoors exhibited pullout stresses of 2567 psi and 2484 psi. The average pullout strength for these specimens was 2526 psi. No specimens with 0.5-inch diameter bars and indoor exposure failed by pullout. The average pullout failure stresses of the specimens with 0.75-inch diameter bars are summarized in Table 60. None of the specimens with 0.75-inch diameter bars subjected to outdoor exposure failed by pullout.

**Table 60. Average Pullout Failure Stresses for 0.75-Inch Diameter Bars.**

Bond length (in.)	Indoor exposure, failure stress (psi)		
	Bar P	Bar V1	Bar V2
7.5	2,161 *	-	1,663
22.5	668	-	-
1143 (45)	-	-	-

\*Average of two samples (2246 psi and 2075 psi).

Two of the 20 specimens exposed outdoors experienced pullout failures, while 4 specimens out of the 18 exposed indoors exhibited pullout failures. This could be an indication that the continuously moist concrete environment may degrade the bond strength between GFRP bars and concrete more than the concrete environment of the specimens exposed outdoors. This is the environmental condition typically encountered in concrete bridge decks according to measurements made by Pyé (1998).

Equilibrium of forces in a bond specimen can be determined as follows:

$$\pi D \mu_f l_{bf} = A_f f_{fu} \quad (76)$$

where,

$D$  = Diameter of FRP bar (*inch*),

$\mu_f$  = Average bond strength of FRP bar (*psi*),

$l_{bf}$  = Basic development length of an FRP bar (*inch*),

$f_{fu}$  = Design tensile strength of FRP bar (*psi*).

Rewriting [Equation 76](#):

$$l_{bf} = \frac{A_f f_{fu}}{\pi D \mu_f} \quad (77)$$

or

$$l_{bf} = \frac{D f_{fu}}{4 \mu_f} \quad (78)$$

Using [Equation 78](#), the development length of the specimens that failed in pullout can be computed. The development length can be computed using the unexposed tensile strength of the GFRP bars, assuming that the tensile strength obtained from tension tests on 0.625-inch diameter bars was the same for the 0.5-inch and 0.75-inch diameter bars. The average development length of the specimens made with 0.5-inch diameter type P bars exposed outdoors was 4.3 inches. The development lengths of the specimens with 0.75-inch diameter bars are shown in [Table 61](#).

**Table 61. Computed Development Length for 0.75-Inch Diameter Bars.**

Bond length (in.)	Indoor exposure, development length (in.)		
	Bar P	Bar V1	Bar V2
7.5	7.4	-	8.7
22.5	23.8	-	-
45	-	-	-

The required bond length for the specimens according to [Equation 11-7](#) of the [ACI 440 \(2001\)](#) design guidelines is computed as:

$$l_{bf} = \frac{d_b f_{fu}}{2700} \quad (79)$$

where the terms are as indicated before.

Assuming the tensile strength of the 0.5-inch and 0.75-inch diameter bars to be the same as those of the 0.625-inch diameter bars and substituting the unexposed average tensile strengths of 84,588, 88,507, and 74,471 psi for bar types P, V1, and V2, respectively, in [Equation 79](#), the following development lengths for a 0.5-inch diameter bar are obtained: 15.7 inches, 16.4 inches, and 13.8 inches for bar types P, V1, and V2, respectively. The computed development lengths for the 0.75-inch diameter bars are: 23.5 inches, 24.6 inches, and 20.7 inches for bar types P, V1, and V2, respectively.

Comparing the development lengths obtained from pullout failure stresses and those computed using [Equation 79](#), it can be concluded that the development length required by ACI 440 Equation 11-7 is conservative for all of the 0.5-inch diameter specimens. It can also be observed that the development lengths obtained using ACI 440 Equation 11-7 for bond length would be adequate for the 0.75-inch diameter specimens of bar types V1 and V2. However, it should be noted that one specimen failed at a development length of just 101 percent of that recommended by the design guidelines.

The Japanese Recommendations for Design and Construction of Concrete Structures Using Continuous Fiber Reinforcing Materials ([JSCE 1997](#)) contains a test method to evaluate the bond properties of FRP reinforcement. The specifications indicate that loading of the specimens should be continued until the tendon pulls out of the concrete or the load decreases significantly due to splitting or cracking of the concrete. Obviously, another failure mode not mentioned in the specifications is rupture of the tendon. The Japanese specifications recommend measuring the slippage at the free end of the specimen. Although the Japanese specifications do not specifically classify tendon pulling out of the concrete or concrete splitting as bond failures, they are implied. If the criterion of bar pullout from the concrete in the Japanese specifications is followed, only 6 specimens out of a total of 38 experienced bond failures.

In an unpublished draft of a document by committee ACI 440-K ([2000](#)), a test method for the determination of the bond strength of FRP bars is described. The ACI 440-K test method requires loading the specimen continuously until either rupture of the FRP bar occurs, the enclosing concrete splits, or slippage of at least 0.1 inch occurs at the loaded end of the specimen. The failure criterion of excessive slippage was most likely established because excessive slippage would either lead to large crack widths in a reinforced concrete member, invalidating methods of analysis where perfect bond is assumed, or compromise the safety of the structure. Although the unpublished ACI 440-K recommended test method to measure bond strength does not specifically classify splitting of the concrete or slippage in excess of 0.1 inch as bond failures, it is implied.

The criterion of the unpublished ACI 440-K recommended test methods ([ACI 2000](#)) could be used to analyze the test data obtained in this research. With this method, the displacement at the loaded end limit state criterion is applied to the specimens tested. Using this criterion, it can be concluded that all but one specimen failed in bond. The average slip displacements at the loaded end of the specimens are summarized in Tables [62](#) and [63](#). It can be observed from these that the 0.75-inch diameter bars, on average, slipped a distance of only 44 percent of the slipped distance recorded for the 0.5-inch diameter bars at failure. It can also be seen that the indoor exposed 0.5-inch diameter specimens slipped, on average, 13 percent more than the outdoor specimens, at failure. The data in [Table 62](#) indicate that for type V2 and P bars the average slippage at failure is 30 and 23 percent higher, respectively, for the indoor exposed specimens. On the other hand, for type V1 bars the slip at failure for the indoor exposed specimens was only 78 percent of the slip recorded for outdoor exposed specimens. The fact that the specimens exposed to the controlled environment exhibited larger slip at the loaded end at failure than the specimens exposed outdoors is an indication that the moist and hot environment could degrade the bond between the FRP bars and the concrete more than the outdoor exposure.

**Table 62. Average Slip at Loaded End of 0.5-Inch Diameter Bars at Failure.**

Bond length (in.)	Outdoor exposure, slip (in.)			Indoor exposure, slip (in.)		
	Bar P	Bar V1	Bar V2	Bar P	Bar V1	Bar V2
5	0.40	0.35	0.48	0.61	0.39	0.51
15	0.65	0.36	0.28	0.57	0.18	0.35
30	0.49	-	-	0.66	0.26	0.72
Average	0.52	0.36	0.38	0.61	0.27	0.53

**Table 63. Average Slip at Loaded End of 0.75-Inch Diameter Bars at Failure.**

Bond length (in.)	Indoor exposure, slip (in.)		
	Bar P	Bar V1	Bar V2
7.5	0.24	0.18	0.18
22.5	0.26	0.18	0.17
45	-	0.22	0.21
Average	0.25	0.19	0.19

Typical bar rupture and pullout failures are shown in Figures 78 and 79, respectively.



**Figure 78. Bar Rupture Failure.**



**Figure 79. Pullout Failure.**

Results of the test program indicate that a continuously wet concrete environment may degrade the bond properties of GFRP bars more than an outdoor exposure, with slippage at failure load increasing by as much as 30 percent after 16 months of exposure. Equation 11-7 of the ACI 440 (2001) design guidelines does not take into account degradation of bond strength between concrete and FRP bars. This is important because any bond strength degradation increases the required development length of a reinforcing bar. An analysis of the effects of bond strength degradation in the computation of the development length will be presented in [Section V](#), where the ACI 440 design guidelines are reviewed. The number of specimens that failed in pullout from the indoor exposure group was twice as large as the number of specimens from the outdoor exposure group. It was also found that the larger diameter bars exhibited less slippage than the smaller diameter bars. Equation 11-7 given by the ACI 440 design guidelines to compute bond length may be unconservative, since one specimen failed at the required development length. Furthermore, as explained in [Section V](#), the basic development length computed with ACI 440 Equation 11-7 may provide adequate

development length at the end of the service life of the structure, but it does not provide adequate development length when the structure is put in service. This happens because Equation 11-7 includes FRP bar strength reduction factors that automatically and unconservatively reduce the basic development length. Thus, a higher factor of safety may be necessary. A modification to ACI 440 Equation 11-7 is proposed in [Section V](#) after an analysis of the effects of bond strength degradation and tensile strength degradation on the computation of the development length of an FRP-reinforced concrete element. The ACI 440-K recommended test methods may need to revise the 0.1-inch slip limit at the loaded end of a bond test specimen. If the 0.1-inch slip limit at the loaded end is considered a bond failure criterion, the bond strength results of all but one of the specimens of this experiment have to be categorized as bond failures. This research indicates that the outdoor exposure of some specimens may not be the condition that degrades bond strength between FRP bars and concrete the most. Since the specimens exposed to a high moisture environment showed more bond strength degradation, it is expected that reinforced concrete elements exposed to high moisture environments could exhibit higher bond strength degradation. Also, samples made, cured, and tested in the laboratory may have bond properties that vary from actual bond properties in the field.

## **THERMAL EXPANSION OF CONCRETE SLABS**

The high transverse coefficient of thermal expansion of FRP bars causes concern for cracking in decks. As such, it is important to know the depth of a safe concrete cover to be used with FRP bars in concrete for the typical bar sizes and temperatures expected to develop in a concrete structure. Schaefer ([2002](#)) conducted the thermal expansion tests and obtained the data presented in this section. The data are reanalyzed in this section.

A particular type of structure needs to be selected in order to evaluate the effects of thermal expansion on an FRP-reinforced concrete structure. Thermal expansion can

be a problem for FRP-reinforced concrete elements in bridge structures. Bridge decks experience considerable solar radiation in some regions, and since they are very common structures, a bridge deck was selected as the structural element to study. A bridge deck section 8 inches thick was tested to evaluate the effect of temperature and cover depth on surface cracking.

FRP bars can undergo expansions or contractions without stressing the concrete before the concrete has set. However, once the concrete sets, tensile stresses develop in the concrete as a result of the differential thermal expansion between the FRP bars and the concrete, at temperatures above the temperature present in the concrete at setting. In this project, the temperature at which the specimens set was not measured. However, the specimens were cast on July 13, 2000, when the normal maximum temperature was approximately 95 °F, as recorded by the National Weather Service in Dallas-Forth Worth ([NWSFO 2003](#)). Therefore, the setting temperature of the specimens was assumed to occur at 95 °F.

### **Cracking Temperature of Bar Type P Specimen**

After the heat lamps were turned on, the specimen was visually monitored continuously for surface cracking. For P bar types, cracks were observed for bar cover depths of 1, 2, and 3 inches. These cracks were observed on the surface of the concrete specimen over the bars with cover depths of 1 inch when the temperature on the surface of the center bar was 239 °F. This indicates that an increase of 144 °F from the setting temperature is required to cause cracking. The temperature on the surface of the slab when the specimen cracked for the 1-inch cover depth samples was 292 °F. [Figure 80](#) (modified from Schaefer [\[2002\]](#)) shows the specimen after testing.

Cracks on the specimen with the 2-inch cover depths occurred when the temperature at the surface of the center bar was 206 °F. Thus, a temperature increase of 111 °F at the level of the reinforcement was required to crack the concrete over the FRP

bar. The temperature at the surface of the slab when the specimen cracked on the 2-inch cover depth sample was 292 °F.

Some small cracks were observed on the surface of the slab over the 3-inch cover. The temperature recorded at the depth of the bars was 168 °F. This represents a temperature rise of 73 °F from the setting temperature. The temperature on the surface of the slab when the specimen cracked for the 3-inch cover depth was 292 °F.

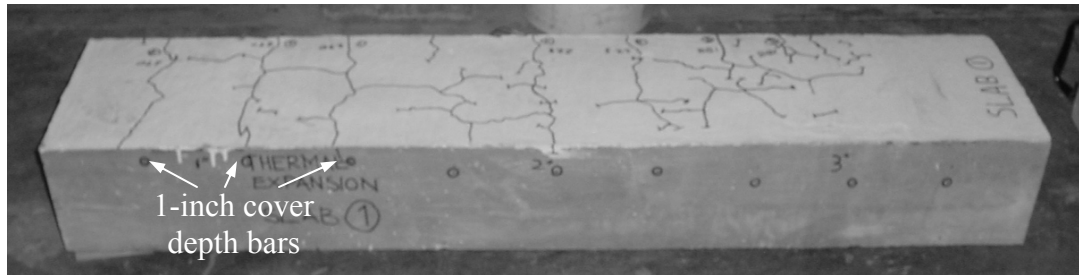


**Figure 80. Specimen with Bars Type P after Testing (Modified from Schaefer [2002]).**

The temperature profile at cracking is shown in [Figure 81](#). These results presented indicate that for the larger covers, smaller temperature differentials are required to crack the slab. However, [Figure 81](#) shows that the temperature is not uniform over the depth of the slab, the temperature being highest at the surface and lowest at the bottom. Thus, cracks developed simultaneously at all three different covers. If the temperature were uniformly distributed, the smallest cover would crack first.

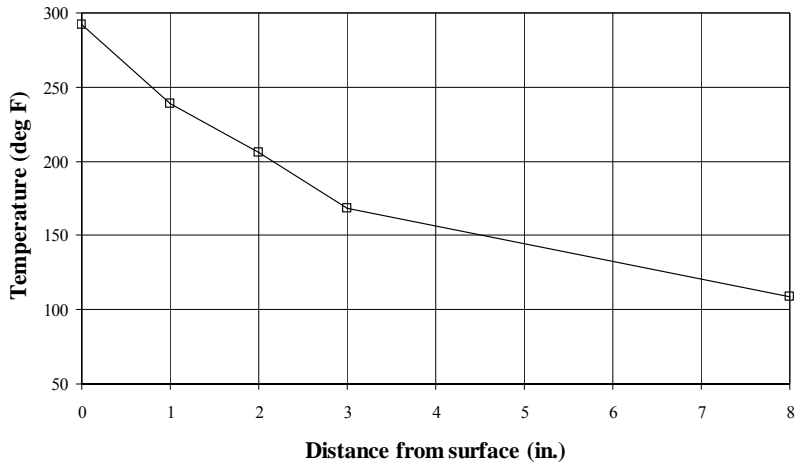


**Figure 81. Temperature Profile of Slab at Cracking for Bars Type P.**

Section 3.16 of the 1992 AASHTO (1992) specifications indicates the range of temperatures for designing concrete structures to be +30 °F and -40 °F in moderate climates and a temperature rise of 35 °F and a temperature fall of 45 °F in cold climates. Section 3.16 of the 1992 AASHTO specifications is intended to be a guide to compute uniform temperature changes in the absence of more precise information for the design of expansion bearings and deck joints. The 1998 AASHTO (1998) specifications cover uniform temperature changes in Section 3.12.2. Section 3.12.2 has a different temperature range requirement. This section requires an upper temperature of 80 °F and a lower temperature of 10 °F for moderate climates and an upper temperature of 80 °F and a lower temperature of 0 °F for cold climate. The 1998 AASHTO specifications indicate that the difference between the upper or lower boundary and the base construction temperature shall be used to compute thermal deformation effects. Both specifications were developed to account for temperature rise and fall relative to the temperature of the concrete when setting occurred. Temperature variations of  $\pm 36$  °F are typical in bridges according to Taly (1998). Therefore, the temperature rise of 73 °F required to cause cracking over the 3-inch cover would typically not occur in a bridge. Based on the results obtained in this project, the use of 1-, 2-, or 3-inch covers for 0.75-

inch diameter (or smaller) FRP bars would not cause a typical concrete bridge deck with 28-day compressive strength of approximately 5880 psi to crack due to thermal expansion. The cracking temperatures are summarized in Figure 82.

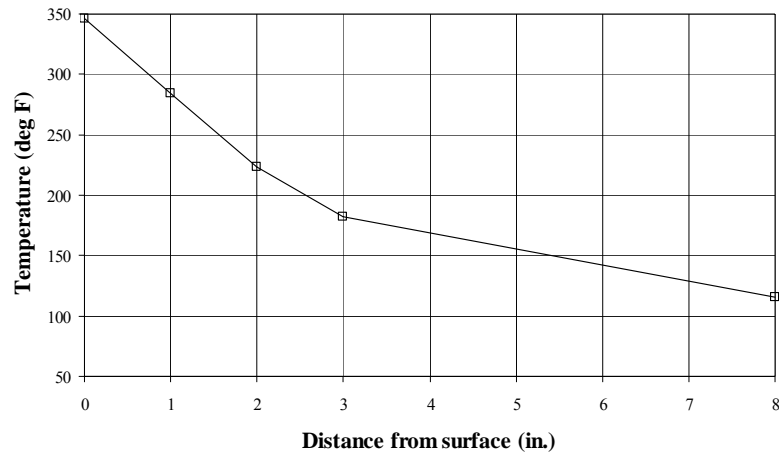


**Figure 82. Temperature Profile of Slab at Cracking for Bars Type V1.**

### Cracking Temperature of Bar Type V1 Specimen

In this specimen, cracks were also observed at cover depths of 1, 2, and 3 inches. The cracks that occurred over the 1-inch cover depth developed when the temperature at the depth of the bar was 284 °F. Thus, a temperature increase of 189 °F from the setting temperature was required to produce cracks over the 1-inch cover depth. Small cracks were detected over the 2-inch cover depth when the temperature at the surface of the bar was 223 °F. Therefore, a temperature increase of 128 °F from the setting temperature was required to produce cracks over the 2-inch cover depth. Cracks appeared on the surface of the slab over the 3-inch cover depth when the temperature at the surface of the bar was 182 °F. This indicates that a temperature increase of approximately 87 °F from the setting temperature is required to produce cracks over the 3-inch cover depth. The

temperature recorded at the surface of the slab at the time the cracks over the three cover depths were observed was 347 °F. Figure 83 (modified from Schaefer [2002]) shows the specimen after testing.

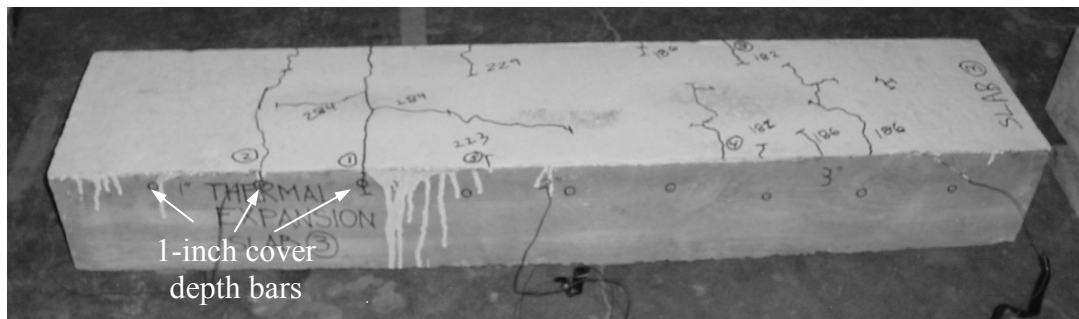


**Figure 83.** Specimen with Bars Type V1 after Testing (Modified from Schaefer [2002]).

The temperature profile of the specimen with bars type V1 is shown in Figure 83. The same observations made earlier regarding temperature distribution for the specimen with bars type P are applicable to the specimen with bars type V1.

A similar analysis to the one performed for the specimen with bars type P would lead to the same conclusions for specimens with bars type V1, since now the smallest temperature increase at which cracking occurred was 87 °F. Thus, concrete covers of 1, 2, and 3 inches would be adequate for GFRP bars with 0.75-inch diameter or smaller to be used in a typical concrete bridge deck with a concrete compressive strength of 5880 psi.

## **Cracking Temperature of Bar Type V2 Specimen**

Cracks were observed over the 1-inch and the 2-inch cover depths for the slab containing V2 bars. A temperature of 264 °F was measured at the surface of the bar with 1-inch cover when cracks developed at the surface of the slab directly over the bars. This

indicates a temperature rise of approximately 169 °F from the setting temperature is required to crack the concrete cover. The surface of the slab developed a small crack directly over the bars with 2-inch cover when the temperature at the surface of the bar was 185 °F. Thus, a temperature rise of approximately 90 °F is required to crack the specimen directly over the bars with 2-inch cover depth. No cracking occurred over the bars with 3-inch cover. Cracking over the bars with 1-inch and 2-inch cover depths occurred when the temperature on the surface of the slab was 327 °F. [Figure 84](#) (modified from Schaefer [2002]) shows the specimen after testing.

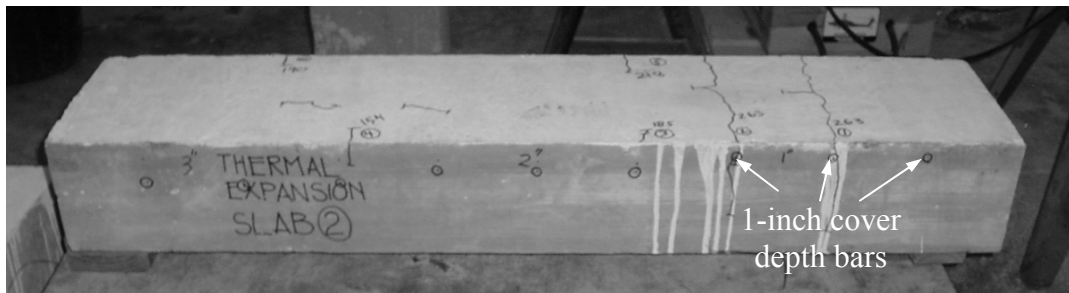


**Figure 84. Specimen with Bars Type V2 after Testing (Modified from Schaefer [2002]).**

The temperature distribution of the specimen with bars type V2 is shown in [Figure 85](#). The observations made earlier regarding temperature distribution across the section for the specimen with bars type P are valid for the specimen with bars type V2.

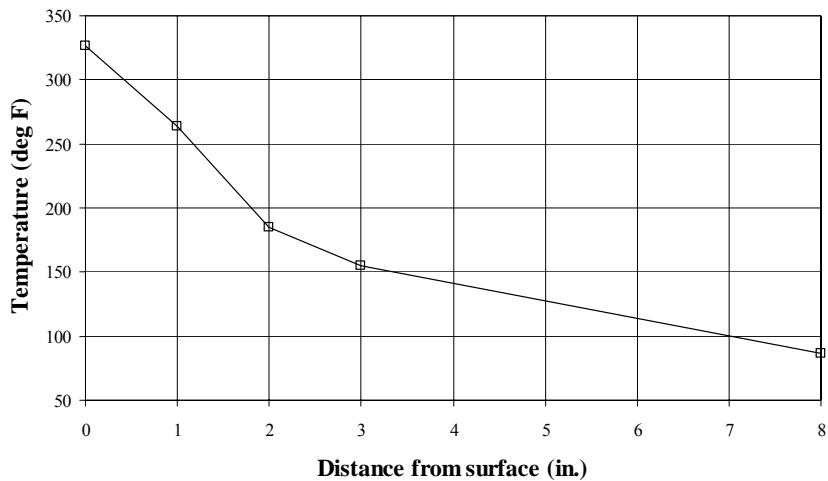


**Figure 85. Temperature Distribution of Slab at Cracking for Bars Type V2.**

Performing the same analysis as for specimens with bars type P and V1 for the specimen with bars type V2, the same conclusions are reached. For the specimen with bars type V2, the approximate minimum temperature increase necessary to cause the concrete cover to crack would be 90 °F. Therefore, concrete covers of 1, 2, and 3 inches would be adequate for 0.75-inch diameter GFRP bars or smaller used in a typical concrete bridge deck with a concrete compressive strength of 5880 psi.

A comparison between the different bar types is made in [Table 64](#). The specimen with bars type P cracked at the lowest temperature, and the specimen with bars type V1 cracked at the highest temperature. For comparison, the specimen with bar types V1 cracked at the 1-inch cover at a temperature 20 °F higher than the cracking temperature of the specimen with bars type V2 for the same cover and at a temperature 45 °F higher than the cracking temperature of the specimen with bars type P for the same cover.

**Table 64. Comparison of Temperatures at Cracking.**

Distance from top surface (in.)	Temperature (deg. F)		
	P	V1	V2
0	292	347	327
1	239	284	264
2	206	223	185
3	168	182	155 *
8	109	116	87

\* No cracking was observed over the 3-inch cover for specimen V2.

The results indicate that a typical 8-inch thick concrete bridge deck reinforced with GFRP bars would not experience cracking on the surface due to thermal expansion for concrete covers of 1, 2, and 3 inches and GFRP reinforcement with a diameter 0.75 inch or smaller. This assertion would be valid for conditions where a temperature rise of less than 54 °F from the concrete setting temperature takes place and the concrete compressive strength is 5880 psi or higher. The results presented in this section are limited to the properties of the materials used in this research program.



## V. REVIEW OF ACI 440 DESIGN GUIDELINES

This section will review the ACI 440 design guidelines as they relate to the results obtained in this research. The ACI 440 design guidelines present information on the history and use of FRP reinforcement, a description of the material properties of FRP, and committee recommendations relative to the construction of concrete structures reinforced with FRP bars. The ACI 440 document also includes recommended materials requirements, construction practices, and design recommendations. Only sections of the ACI 440 design guidelines that could be improved and that are related to the use of FRP bars in bridges will be reviewed. The first section to be reviewed is Section 7.2, Design Material Properties, specifically related to the environmental reduction factors proposed by the guidelines to be applied to the tensile strength of FRP bars reinforced with glass fibers. A review of Section 8.3, Serviceability, follows. The serviceability section will be reviewed in regard to cracking (subsection 8.3.1) and deflections (addressed in subsections 8.3.2 and 8.3.2.3). Section 11.1 regarding the development length of straight bars also will be reviewed. Finally, comments will be provided in regard to minimum concrete cover.

### ACI 440 SECTION 7.2 DESIGN MATERIAL PROPERTIES

This section of the guidelines indicates that the material properties provided by the manufacturer should be reduced to account for long-term exposure to the environment. The guidelines recommend that the tensile strength should be determined by:

$$f_{fu} = C_E f_{fu}^* \quad (80)$$

where,

$f_{fu}$  = Design tensile strength of FRP, considering reduction for service environment (psi),

$C_E$  = Environmental reduction factor,

$f_{fu}^*$  = Guaranteed tensile strength of an FRP bar defined as the mean tensile strength of a sample of test specimens minus three times the standard deviation ( $f_{fu}^* = f_{u,ave} - 3\sigma$ ) (psi),  
 $f_{u,ave}$  = Average tensile strength of FRP bars.

The environmental reduction factors given in the guidelines for GFRP bars are 0.8 and 0.7 for concrete not exposed to earth and weather and for concrete exposed to earth and weather, respectively. The guidelines indicate that the environmental reduction factors are conservative estimates where temperature effects have been considered, as long as the material is not used above the glass transition temperature of the polymer employed to manufacture the bars.

The average tensile strengths of the unexposed specimens of the tension tests in this dissertation are presented in column 2 of [Table 65](#). The unexposed tensile strength standard deviations and guaranteed tensile strengths are indicated in columns 3 and 4, respectively, of [Table 65](#). Also indicated in [Table 65](#) (in columns 5 and 6) are the design tensile strengths as computed using [Equation 80](#). The smallest measured tensile strength from any of the exposure conditions at 50 weeks is shown in column 7 of [Table 65](#). Column 8 presents the guaranteed tensile strength ( $f_{fu}^* = f_{u,ave} - 3\sigma$ ) obtained from the measured exposure data at 50 weeks. Column 9 presents the predicted average residual tensile strength computed using a value of  $\lambda = 0.0057$  (best fit to guaranteed tensile strength) computed using the method described in the tensile strength degradation analysis section of the moisture absorption test results, for a five-year exposure period. Column 10 shows the predicted residual tensile strength using a value of  $\lambda = 0.006$  (curve fit to lowest measured data points) described in the tensile strength degradation analysis section of the moisture absorption test results, for a five-year exposure period.

According to comparisons made with the research conducted by Sen et al. ([2002](#)) in the tensile strength degradation analysis section, the results predicted with [Equation](#)

[24](#) and a value of  $\lambda$  of 0.0057 (best fit to guaranteed tensile strength) can be considered as upper bound residual tensile strengths. The predictions are considered as upper bound residual strength values because the bars were exposed unstressed, and as indicated by Sen and coworkers, the application of a sustained stress to GFRP bars causes larger strength reductions with time than when the bars are unstressed.

**Table 65. Tensile Strength Results and Predicted Values.**

Bar type	Tensile strength (psi)					Smallest 50 weeks $f_u$ (psi)	Guaranteed 50 weeks $f^*_{fu}$ (psi)	Predicted 5 years $f^*_{fu}$ (psi)	Predicted 5 years $f_u$ (psi)
	$f_{u, avg}$ unexp.	S.D. unexp.	$f^*_{fu}$ unexp.	$f_{fu}$ ( $C_E = 0.8$ )	$f_{fu}$ ( $C_E = 0.7$ )				
(1)	(2)	(3)	(4)	(5)	(6)	(7)	(8)	(9)	(10)
P	84,588	2,456	77,219	61,775	54,053	68,616	59,995	52,868	53,798
V1	88,507	7,951	64,655	51,724	45,258	70,969	63,559	55,317	56,290
V2	74,471	2,598	66,676	53,341	46,673	56,609	54,863	46,544	47,363

Comparing the values presented in columns 6 and 8 of [Table 65](#), it can be seen that the values of column 6 are only 11, 40, and 18 percent lower than the values of column 8. The values of  $f_{fu}$  represent the design tensile strength obtained following ACI 440 design guidelines and include an environmental reduction factor for exterior exposure that is intended to account for strength reductions suffered by GFRP bars over the life of the structure. The results shown indicate that the design strength is slightly larger than the guaranteed tensile strength after one year of exposure for bar type P. Since the reductions in strength shown in column 8 were determined for unstressed specimens, it is expected that the guaranteed tensile strength will be lower in actual service conditions, where the GFRP bars are stressed.

A comparison of columns 6 and 9 of [Table 65](#) shows that the five-year predicted guaranteed tensile strengths are equivalent to 0.98, 1.22, and 1.00 of the design strengths presented in column 6. This shows that the GFRP bars studied in this research and using

the predicted degradation model, after five years in service conditions (although unstressed), can have a guaranteed residual tensile strength close to the design strength. As mentioned in the previous paragraph, GFRP bars are expected to have a lower residual tensile strength when they are stressed in service conditions.

Glaser et al. (1983) conducted a 10-year study on the life estimation of S-Glass/epoxy composites under sustained tensile load. The specimens were kept at a temperature between 68 °F and 82 °F and a relative humidity between 24 and 37 percent. The researchers found that the residual tensile strength of the specimens continuously decreased with time, even beyond five years.

Based on the observations of this project, and since the tensile strength of GFRP bars in stressed service conditions is expected to either level off or continue to degrade after one year of exposure, the results indicate that the environmental reduction factors given by the ACI 440 design guidelines may be unconservative.

As indicated in the tensile strength degradation analysis section of the moisture absorption test, it is difficult to make valid predictions for long periods of time with the limited exposure times studied. It is, therefore, necessary to carry out exposure tests over longer periods of time to make reliable long-term behavior predictions. The application of the strength reduction factors is presented in a design example given at the end of this section.

### **ACI 440 SECTION 8.3.1 CRACKING**

The ACI 440 design guidelines indicate that FRP bars are corrosion resistant, and as a result, the maximum crack width limitation can be relaxed when corrosion of the reinforcement is the main reason for crack-width limitations. The guidelines recommend

using maximum crack width limits of 0.02 inch for exterior exposure and 0.028 inch for interior exposure.

The [results section](#) of the cracking of the concrete slabs test indicated that maximum crack width increases with concrete cover. However, as indicated by Beeby (1978), although the crack width on the surface of the concrete is a function of concrete cover, the crack width at the level of the reinforcement could be approximately the same. Thus, it would be appealing to specify a maximum surface crack width limit that is a function of concrete cover if the degradation of the GFRP bar depends on the crack width at the surface of the bar rather than at the surface of the concrete. However, until research that relates the degradation of GFRP bars to crack width at the surface of the concrete and at the surface of the GFRP bar is available, no recommendations can be made.

The ACI 440 design guidelines recommend using Equation 8-9c to estimate the maximum crack width of FRP-reinforced concrete elements. As described in the [results section](#), the constant 0.076 multiplied by a  $k_b$  of 1.2 as shown by the ACI 440 yields a good fit to the experimental data:

$$W_{\max} = 0.09\beta \cdot f_f \cdot \sqrt[3]{d_c A} \quad (81)$$

where the terms are as described in [Section IV](#).

In [Figure 86](#), Equation 81 is compared with ACI 440 Equation 8-9b, the equation proposed by Faza and GangaRao (1993), and the experimental data obtained from this research. Note that the equation by Faza and GangaRao is more conservative, but past practice has been to use the best-fit line equation instead of the more conservative approach. The ACI 440 maximum crack width limit for exterior exposure is also indicated in [Figure 86](#) and provides very similar results to those found in this research.

According to the analysis presented in [Section IV](#), in the cracking of concrete slabs test results, [Equation 81](#) yields a good prediction of average maximum crack width and a better prediction than the work done by Faza and GangaRao ([1993](#)). Previous to this research, limited test results were available on maximum crack width of FRP-reinforced concrete elements, and no analysis had been done to evaluate the correlation between test data and proposed equations. It should be noted that [Equation 81](#) was developed based on experiments on slabs only.

An application of [Equation 81](#) is presented in the design example given at the end of this section. The example presents the maximum crack width computations obtained using [Equation 81](#) and ACI 440 Equations 8-9b and 8-9c shown next:

$$\text{ACI 440 Equation 8-9b} \quad W_{\max} = 0.076 \beta \cdot \frac{E_s}{E_f} f_f \cdot \sqrt[3]{d_c A} \quad (82)$$

$$\text{ACI 440 Equation 8-9c} \quad W_{\max} = \frac{2200}{E_f} \beta \cdot k_b f_f \cdot \sqrt[3]{d_c A} \quad (83)$$

where all terms have been described previously and  $k_b$  is a bond modification factor with a recommended value of 1.2 for bond strength between FRP bars and concrete similar to the bond strength between steel bars and concrete. The results of the design example show that Equations [81](#) and [83](#) yield similar maximum crack widths. In addition, the maximum crack widths obtained with Equations [81](#) and [83](#) are larger, and therefore more conservative, than those obtained with [Equation 82](#).

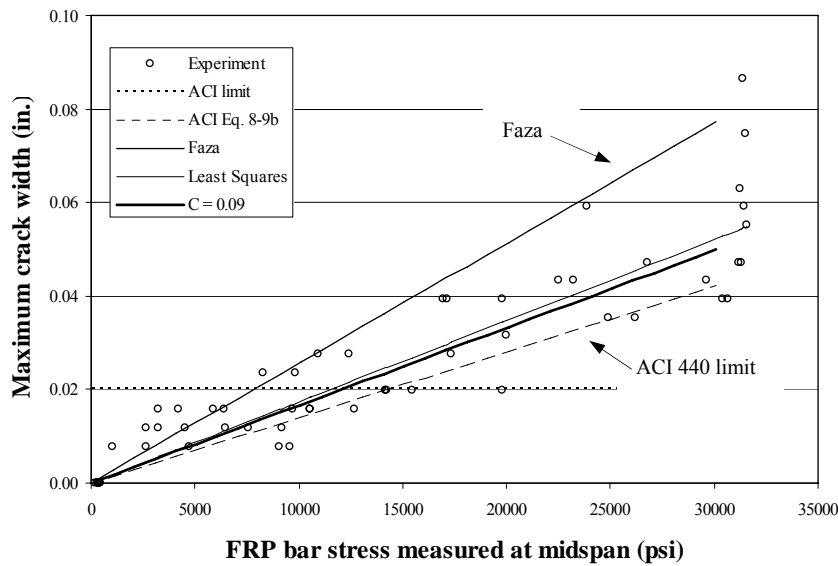


**Figure 86. Comparison between Equation 81 ( $C=0.09$ ) and Other Equations for a 1.21-Inch Cover.**

### ACI 440 SECTION 8.3.2 DEFLECTIONS

The ACI 440 design guidelines require deflections to be limited in FRP-reinforced concrete flexural members. The guidelines follow the deflection limitations of the ACI 318 building code, where the deflections of reinforced concrete elements under immediate and sustained static loads are limited. However, the deflection limitations of the ACI 440 design guidelines and the ACI 318 code do not apply to dynamic loads, such as earthquakes, transient winds, or vibration of machinery.

The results section of the cyclic loading of concrete beam tests indicate that the deflections of beams subjected to 2 million cycles of loading with an FRP bar stress range of 18.9 ksi increased by 78 percent. This increment was computed from a least squares best-fit line to the data. Therefore, the deflection increase due to cyclic loading is significant and should be accounted for in the ACI 440 design guidelines. In the

absence of more test data, [Equation 73](#), shown below as [Equation 84](#), can be used to estimate a lower bound of the increase in long-term deflections due to cyclic loading.

$$y = 0.0046 \ln(n) + 0.0858 \quad (84)$$

where  $y$  is the beam deflection in inches and  $n$  is the number of cycles. The correlation coefficient between beam deflection and the number of cycles is  $R^2 = 0.47$ . The slope of this equation can be used to compute deflections due to cyclic loading of GFRP-reinforced concrete members.

An application of [Equation 84](#) to estimate deflections due to cyclic loading is shown in the example presented at the end of this section. The design example computes the deflections of a GFRP-reinforced concrete beam subjected to dead load and the application of 2 million cycles of an alternating live load. The results show an initial deflection due to dead and live load of 0.37 inch and a final deflection due to dead and live load of 0.47 inch, after 2 million cycles of application of the live load. This represents a 27 percent increase in deflection due to cyclic load application.

### **ACI 440 SECTION 8.3.2.3 CALCULATION OF DEFLECTION (DIRECT METHOD)**

This section of the ACI 440 design guidelines presents a method to compute long-term deflections of FRP-reinforced concrete elements using ACI 440 Equation 8-14:

$$\Delta_{(cp+sh)} = 0.6\xi(\Delta_i)_{sus} \quad (85)$$

where,

$\Delta_{(cp+sh)}$  = Additional deflection due to creep and shrinkage under sustained loads (mm, inch),

$(\Delta i)_{sus}$  = Immediate deflection due to sustained loads (service loads) (mm, inch),

$\xi$  = Time-dependent factor for sustained load defined in the ACI 318 building code (ACI 2000).

As indicated in [Section III](#), [Equation 85](#) can predict smaller deflections than recorded. Perhaps the biggest advantage of [Equation 85](#) is its simplicity. However, [Equation 85](#) does not specifically account for creep of FRP bars. The method described in [Section IV](#) under [creep test](#) for the computation of long-term deflection of FRP-reinforced concrete elements, accounting for creep of FRP bars, is proposed as an alternative to [Equation 85](#). [Equation 86](#) can be used to compute the increment in curvature, and [Equation 87](#) can be used to compute the long-term deflection:

$$\Delta\kappa = \frac{B_e \delta N - A_e' \delta M}{E_e (B_e^2 - A_e I_e)} \quad (86)$$

$$y_c = \frac{L^2}{96} (\kappa_A + 10\kappa_C + \kappa_B) \quad (87)$$

where all the terms have been defined before.

Long-term deflection computations obtained with [Equations 85](#) and [87](#) are shown in the design example presented at the end of this section. The six-month dead load deflections obtained with [Equation 85](#) are 0.2 inch, and the six-month dead load deflections obtained with [Equations 86](#) and [87](#) are 0.61 inch. Thus, the six-month deflection due to dead load computed with the newly proposed method from this research is equal to three times the deflection obtained with ACI Equation 8-14.

## ACI 440 SECTION 11.1 DEVELOPMENT LENGTH OF A STRAIGHT BAR

The development length of a straight bar can be computed with Equation 11-3 of the ACI 440 design guidelines as follows:

$$l_{bf} = \frac{d_b f_{fu}}{4\mu_f} \quad (88)$$

where,

$l_{bf}$  = Basic development length (*inch*),

$d_b$  = Bar diameter (*inch*),

$f_{fu}$  = Design tensile strength of FRP, considering reductions for service environment  
(*psi*),

$\mu_f$  = Bond strength between FRP bar and concrete (*psi*).

The bond test results presented in [Section IV](#) indicate that the bond strength of GFRP bars exposed to an environment with high temperature and moisture was lower than the bond strength of specimens exposed outdoors. In addition, the number of specimens exposed to controlled conditions that failed by pullout was twice as many as the number of specimens from the outdoor exposure group that experienced pullout failures. However, only a small number of samples were studied in this research. The displacement recorded at the loaded end was larger, on average, for the specimens exposed in temperature-and moisture-controlled conditions than for the specimens exposed outdoors. These are indications that bond strength degrades over time. ACI 440 Equation 11-3 recognizes that the tensile strength of FRP bars degrades with time and yields a smaller development length for a smaller tensile strength. Nevertheless, when the bond strength degrades, the development length increases. This fact may make [Equation 88 \(ACI 440 Equation 11-3, 2001\)](#) unconservative. The development length of [Equation 88](#) should depend on the ratio of the rate of tensile strength degradation of FRP bars to the rate of bond strength degradation between the FRP bars and concrete. Additional research is needed to better estimate both the rate of tensile strength degradation in a given environment and the rate of bond degradation in the same environment. Perhaps the simplest way to account for the bond strength degradation would be to apply an environmental reduction factor to the bond strength.

The bond strength of FRP bars in concrete depends on the compressive strength of concrete, and tests have determined the denominator of [Equation 88](#) to be approximately 2850 psi. The ACI 440 design guidelines propose using Equation 11-7:

$$l_{bf} = \frac{d_b f_{fu}}{2700} \quad (89)$$

If the basic development length of an FRP bar is computed with [Equation 89](#) (above), the bar should have adequate development length at the end of its service life, since [Equation 89](#) includes an environmental reduction factor ( $C_E$ ) in  $f_{fu}$ . But, the bond length should be enough to develop the full strength of the bar when the bar is put in service ( $f_{u,ave}$ ), as well as the strength of the bar when it is close to the end of its service life ( $f_{fu}$ ). Therefore, the basic development length obtained would be insufficient to develop the guaranteed tensile strength ( $f_{fu}^* = f_{u,ave} - 3 \sigma = f_{fu} / C_E$ ) or the average tensile strength ( $f_{u,ave}$ ) of the FRP bar when the structure is put in service. The terms  $f_{fu}$ ,  $f_{fu}^*$ ,  $f_{u,ave}$ , and  $C_E$  were defined at the beginning of this section.

Until sufficient data are available to determine the rate of degradation of the tensile strength and the rate of degradation of the bond strength, the average tensile strength should be used in the computation of the basic development length of FRP bars, without reducing it by three standard deviations and without the application of the environmental reduction factor as used in [Equation 89](#). Thus, this research recommends that the following equation be used to compute the basic development length and should replace ACI 440 Equation 11-7:

$$l_{bf} = \frac{d_b f_{u,ave}}{2700} \quad (90)$$

where the terms are as defined before and  $f_{u,ave}$  is the average tensile strength of FRP bars.

The design example presented at the end of this section shows the basic development lengths computed using Equations 89 and 90. [Equation 89](#) yields a basic development length of 17 inches, and [Equation 90](#) yields a basic development length of 26.4 inches. Thus, [Equation 90](#) can yield basic development lengths 55 percent larger than those obtained with [Equation 89](#).

## **MINIMUM CONCRETE COVER**

The results of the thermal expansion of the concrete slabs test indicate that using 0.75-inch diameter GFRP bars in 8 inch concrete bridge decks with clear covers of 1, 2, and 3 inches would not crack under a temperature increase of 54 °F from the concrete setting temperature, for a concrete compressive strength of 5880 psi or higher. The fact that 0.75-inch diameter GFRP bars could be safely used in concrete elements subjected to temperature increases smaller than 54 °F for 1, 2, and 3 inch concrete covers could be used in the ACI 440 design guidelines to determine minimum concrete cover requirements. The concrete covers of 1-, 2-, and 3-inches are equivalent to 1.33, 2.66, and 4 bar diameters, respectively. From the results of this research, it cannot be determined whether the minimum concrete cover of 1 bar diameter recommended by the ACI 440 design guidelines does not have problems with cracking due to thermal expansion. However, it can be concluded from the results of this research that a minimum concrete cover of 1.33 bar diameters would not cause thermal expansion problems for typical bridge decks under normal environmental conditions.

## **INTRODUCTION TO DESIGN EXAMPLE**

This section presents a design example that includes the recommended modifications and/or verifications to the ACI 440 design guidelines. A simply supported beam subjected to distributed dead and live loads is designed for strength. The resulting design section is then checked to satisfy deflection, maximum crack width, and creep rupture stress limits. The basic development length is also computed. Finally, the beam deflections due to 2 million cycles of live load application are estimated.

## DESIGN EXAMPLE

### Objective

Design a simply supported rectangular concrete beam with a span of 14 ft. The beam will be in the exterior of a structure. The beam should carry a service live load of  $w_{LL} = 1.2$  kips/ft and a superimposed dead load of  $w_{SDL} = 0.6$  kips/ft. The deflection of the beam at six months should not exceed  $l/240$ , and the instantaneous live load deflection should not exceed  $l/360$ . GFRP bars will be used to reinforce the beam. The average tensile strength of the GFRP bars is  $f_{u,ave} = 96,000$  psi, the standard deviation is (S.D.) = 2500 psi, and the guaranteed tensile strength is  $f^*_{fu} = 88,500$  psi. Other material properties are:  $E_f = 6,279,000$  psi and  $f'_c = 4000$  psi. Assume the beam has adequate shear strength. Assume the beam will be cured for 7 days and first loaded at 14 days of age. Compute the basic development length of the FRP reinforcement. Estimate the beam midspan deflection after 2 million cycles of loading due to an alternating live load. [Figure 87](#) shows a design based on ACI 440 guidelines and based on results from this research.

<b>Design based on ACI 440.1R-03 design guidelines</b>	<b>Design based on results from this research project</b>
<p><b>1. Estimate the beam size.</b></p> <p>Estimate the depth of a simply supported reinforced concrete beam from Table 9.5(a) of the ACI 318 code. Deflections, however, need to be checked.</p> $h \geq \frac{l}{16}$ $h \geq \frac{(14 \text{ ft})(12 \frac{\text{in.}}{\text{ft}})}{16} = 10.5 \text{ in.}$ <p>Since GFRP bars have lower stiffness than steel bars, greater depth than steel-reinforced concrete may be required for deflection control</p> <p>Try <math>h = 16</math> inches Try <math>b = 10.5</math> inches</p>	<p><b>1. Estimate the beam size.</b></p> <p>Estimate the depth of a simply supported reinforced concrete beam from Table 9.5(a) of the ACI 318 code. Deflections, however, need to be checked.</p> $h \geq \frac{l}{16}$ $h \geq \frac{(14 \text{ ft})(12 \frac{\text{in.}}{\text{ft}})}{16} = 10.5 \text{ in.}$ <p>Since GFRP bars have lower stiffness than steel bars, greater depth than steel-reinforced concrete may be required for deflection control</p> <p>Try <math>h = 16</math> inches Try <math>b = 10.5</math> inches</p>
<p><b>2. Factored load</b></p> <p>Compute the distributed dead load: <math>w_{DL} = w_{SDL} + w_{SW}</math>.</p> $w_{DL} = 600 \frac{\text{lb}}{\text{ft}} + \frac{(10.5 \text{ in.})(16 \text{ in.})}{\left(12 \frac{\text{in.}}{\text{ft}}\right)^2} (150 \text{ pcf}) = 775 \frac{\text{lb}}{\text{ft}}$ <p>Compute the total factored load <math>w_u = 1.4w_{DL} + 1.7w_{LL}</math>.</p> $w_u = 1.4\left(0.775 \frac{\text{kip}}{\text{ft}}\right) + 1.7\left(1.2 \frac{\text{kip}}{\text{ft}}\right) = 3.13 \frac{\text{kip}}{\text{ft}}$	<p><b>2. Factored load</b></p> <p>Compute the distributed dead load: <math>w_{DL} = w_{SDL} + w_{SW}</math>.</p> $w_{DL} = 600 \frac{\text{lb}}{\text{ft}} + \frac{(10.5 \text{ in.})(16 \text{ in.})}{\left(12 \frac{\text{in.}}{\text{ft}}\right)^2} (150 \text{ pcf}) = 775 \frac{\text{lb}}{\text{ft}}$ <p>Compute the total factored load <math>w_u = 1.4w_{DL} + 1.7w_{LL}</math>.</p> $w_u = 1.4\left(0.775 \frac{\text{kip}}{\text{ft}}\right) + 1.7\left(1.2 \frac{\text{kip}}{\text{ft}}\right) = 3.13 \frac{\text{kip}}{\text{ft}}$

**Figure 87: Design Example.**

<b>Design based on ACI 440.1R-03 design guidelines</b>	<b>Design based on results from this research project</b>
<p><b>3. Compute the design strength.</b></p> <p>For a beam located in an exterior space an environmental reduction factor (<math>C_E</math>) of 0.7 is used. The design rupture strength is:</p> $f_{fu} = C_E f_{fu}^*$ $f_{fu} = (0.7)(88.5 \text{ ksi}) = 62.0 \text{ ksi}$	<p><b>3. Compute the design strength.</b></p> <p>For a beam located in an exterior space an environmental reduction factor (<math>C_E</math>) of 0.70 is used. The design rupture strength is:</p> $f_{fu} = C_E f_{fu}^*$ $f_{fu} = (0.7)(88.5 \text{ ksi}) = 62.0 \text{ ksi}$
<p><b>4. Determine the area of GFRP bars required for flexural strength.</b></p> <p>Factored moment demand at midspan:</p> $M_u = \frac{w_u l^2}{8}$ $M_u = \frac{(3.13 \frac{\text{kip}}{\text{ft}})(14 \text{ ft})^2}{8} = 76.6 \text{ kip} \cdot \text{ft}$ <p>Balanced reinforcement ratio:</p> $\rho_{fb} = 0.85 \frac{f_c'}{f_{fu}} \beta_1 \frac{E_f \varepsilon_{cu}}{E_f \varepsilon_{cu} + f_{fu}}$ $\rho_{fb} = 0.85 \frac{4}{62.0} (0.85) \frac{(6279)(0.003)}{(6279)(0.003) + 62.0}$ $\rho_{fb} = 0.0109$ <p>For a failure controlled by concrete crushing, the reinforcement ratio should be at least <math>1.4 \rho_{fb}</math>. If <math>\rho_f \geq 1.4 \rho_{fb}</math>, the strength reduction factor is 0.70.</p>	<p><b>4. Determine the area of GFRP bars required for flexural strength.</b></p> <p>Factored moment demand at midspan:</p> $M_u = \frac{w_u l^2}{8}$ $M_u = \frac{(3.13 \frac{\text{kip}}{\text{ft}})(14 \text{ ft})^2}{8} = 76.6 \text{ kip} \cdot \text{ft}$ <p>Balanced reinforcement ratio:</p> $\rho_{fb} = 0.85 \frac{f_c'}{f_{fu}} \beta_1 \frac{E_f \varepsilon_{cu}}{E_f \varepsilon_{cu} + f_{fu}}$ $\rho_{fb} = 0.85 \frac{4}{62.0} (0.85) \frac{(6279)(0.003)}{(6279)(0.003) + 62.0}$ $\rho_{fb} = 0.0109$ <p>For a failure controlled by concrete crushing, the reinforcement ratio should be at least <math>1.4 \rho_{fb}</math>. If <math>\rho_f \geq 1.4 \rho_{fb}</math>, the strength reduction factor is 0.70.</p>

Figure 87: Design Example. (Continued)

Design based on ACI 440.1R-03 design guidelines	Design based on results from this research project
$1.4\rho_{fb} = 0.0152$ <p>Try using 6-No. 6 bars with a cover of 1.5 inch and No. 3 stirrups:</p> $d = 16 \text{ in.} - 1.5 - 0.375 - (0.743/2) = 13.75 \text{ in.}$ $A_f = 0.433 \text{ in.}^2 (6) = 2.60 \text{ in.}^2$ $\rho_f = \frac{A_f}{bd}$ $\rho_f = \frac{2.60 \text{ in.}^2}{10.5 \text{ in.} (13.75 \text{ in.})} = 0.0180 > 1.4\rho_{fb} \therefore \phi = 0.7$ <p>Find the FRP bar stress when the ultimate strain of 0.003 in the concrete is reached:</p> $f_f = \sqrt{\frac{(E_f \varepsilon_{cu})^2}{4} + \frac{0.85\beta_1 f_c'}{\rho_f} E_f \varepsilon_{cu} - 0.5E_f \varepsilon_{cu}} \leq f_{fu}$ $f_f = \sqrt{\frac{[6279(0.003)]^2}{4} + \frac{0.85(0.85)(4)}{0.0180} (6279)(0.003) - 0.5(6279)(0.003)}$ $f_f = 46.4 \text{ ksi} < f_{fu} = 62 \text{ ksi} \therefore \text{Failure occurs indeed by concrete crushing.}$	$1.4\rho_{fb} = 0.0152$ <p>Try using 6-No.6 bars with a cover of 1.5 inch and No. 3 stirrups:</p> $d = 16 \text{ in.} - 1.5 - 0.375 - (0.743/2) = 13.75 \text{ in.}$ $A_f = 0.433 \text{ in.}^2 (6) = 2.60 \text{ in.}^2$ $\rho_f = \frac{A_f}{bd}$ $\rho_f = \frac{2.60 \text{ in.}^2}{10.5 \text{ in.} (13.75 \text{ in.})} = 0.0180 > 1.4\rho_{fb} \therefore \phi = 0.7$ <p>Find the FRP bar stress when the ultimate strain of 0.003 in the concrete is reached:</p> $f_f = \sqrt{\frac{(E_f \varepsilon_{cu})^2}{4} + \frac{0.85\beta_1 f_c'}{\rho_f} E_f \varepsilon_{cu} - 0.5E_f \varepsilon_{cu}} \leq f_{fu}$ $f_f = \sqrt{\frac{[6279(0.003)]^2}{4} + \frac{0.85(0.85)(4)}{0.0180} (6279)(0.003) - 0.5(6279)(0.003)}$ $f_f = 46.4 \text{ ksi} < f_{fu} = 62 \text{ ksi} \therefore \text{Failure occurs indeed by concrete crushing.}$

Figure 87: Design Example. (Continued)

Design based on ACI 440.1R-03 design guidelines	Design based on results from this research project
Nominal Moment capacity:	Nominal Moment capacity:
$M_n = \rho_f f_f \left(1 - 0.59 \frac{\rho_f f_f}{f_c'}\right) b d^2$	$M_n = \rho_f f_f \left(1 - 0.59 \frac{\rho_f f_f}{f_c'}\right) b d^2$
$M_n = (0.0180)(46.4) \left[1 - 0.59 \frac{(0.0180)(46.4)}{4}\right] (10)(13.75)^2$	$M_n = (0.0180)(46.4) \left[1 - 0.59 \frac{(0.0180)(46.4)}{4}\right] (10)(13.75)^2$
$M_n = 1385 \text{ kip} \cdot \text{in.} = 115.4 \text{ kip} \cdot \text{ft}$	$M_n = 1385 \text{ kip} \cdot \text{in.} = 115.4 \text{ kip} \cdot \text{ft}$
Provided moment capacity:	Provided moment capacity:
$\phi M_n \geq M_u$	$\phi M_n \geq M_u$
$\phi M_n = (0.7) 115.2 \text{ kip} \cdot \text{ft} = 80.8 \text{ kip} \cdot \text{ft}$	$\phi M_n = (0.7) 115.2 \text{ kip} \cdot \text{ft} = 80.8 \text{ kip} \cdot \text{ft}$
$\phi M_n = 80.8 \text{ kip} \cdot \text{ft} \geq M_u = 76.6 \text{ kip} \cdot \text{ft} \therefore \text{The section has adequate flexural strength.}$	$\phi M_n = 80.8 \text{ kip} \cdot \text{ft} \geq M_u = 76.6 \text{ kip} \cdot \text{ft} \therefore \text{The section has adequate flexural strength.}$
Minimum reinforcement:	Minimum reinforcement:
$A_{f,\min} = \frac{5.4 \sqrt{f_c'}}{f_{fu}} b_w d$	$A_{f,\min} = \frac{5.4 \sqrt{f_c'}}{f_{fu}} b_w d$
The minimum reinforcement requirement does not need to be checked because the section is over-reinforced.	The minimum reinforcement requirement does not need to be checked because the section is over-reinforced.

Figure 87: Design Example. (Continued)

Design based on ACI 440.1R-03 design guidelines	Design based on results from this research project
<p><b>5. Check the short-and long-term deflections of the beam,</b></p> <p><i>Short-term deflection</i></p> <p>Gross moment of inertia of the beam:</p> $I_g = \frac{bh^3}{12}$ $I_g = \frac{(10.5 \text{ in.})(16 \text{ in.})^3}{12} = 3584 \text{ in.}^3$ <p>Modular ratio:</p> $n_f = \frac{E_f}{E_c} = \frac{E_f}{57000\sqrt{f'_c}}$ $n_f = \frac{6279000 \text{ psi}}{57000\sqrt{4000 \text{ psi}}} = 1.74$ <p>Neutral axis depth:</p> $k = \sqrt{2\rho_f n_f + (\rho_f n_f)^2} - \rho_f n_f$ $k = \sqrt{2(0.0180)(1.74) + [(0.0180)(1.74)]^2} - (0.0180)(1.74)$ $k = 0.221$ $I_{cr} = \frac{bd^3}{3} k^3 + n_f A_f d^2 (1-k)^2$	<p><b>5. Check the short-and long-term deflections of the beam,</b></p> <p><i>Short-term deflection</i></p> <p>Gross moment of inertia of the beam:</p> $I_g = \frac{bh^3}{12}$ $I_g = \frac{(10.5 \text{ in.})(16 \text{ in.})^3}{12} = 3584 \text{ in.}^3$ <p>Modular ratio:</p> $n_f = \frac{E_f}{E_c} = \frac{E_f}{57000\sqrt{f'_c}}$ $n_f = \frac{6279000 \text{ psi}}{57000\sqrt{4000 \text{ psi}}} = 1.74$ <p>Neutral axis depth:</p> $k = \sqrt{2\rho_f n_f + (\rho_f n_f)^2} - \rho_f n_f$ $k = \sqrt{2(0.0180)(1.74) + [(0.0180)(1.74)]^2} - (0.0180)(1.74)$ $k = 0.221$ $I_{cr} = \frac{bd^3}{3} k^3 + n_f A_f d^2 (1-k)^2$

Figure 87: Design Example. (Continued)

Design based on ACI 440.1R-03 design guidelines	Design based on results from this research project
$I_{cr} = \frac{(10)(13.75)^3}{3}(0.221)^3 + 1.74(2.60)(13.75)^2(1 - 0.221)^2$	$I_{cr} = \frac{(10)(13.75)^3}{3}(0.221)^3 + 1.74(2.60)(13.75)^2(1 - 0.221)^2$
$I_{cr} = 613 \text{ in.}^4$	$I_{cr} = 613 \text{ in.}^4$
<p>Compute the reduction coefficient for deflections using <math>\alpha_b = 0.50</math> for FRP bars having the same bond strength as steel bars:</p>	<p>Compute the reduction coefficient for deflections using <math>\alpha_b = 0.50</math> for FRP bars having the same bond strength as steel bars:</p>
$\beta_d = \alpha_b \left( \frac{E_f}{E_s} + 1 \right)$	$\beta_d = \alpha_b \left( \frac{E_f}{E_s} + 1 \right)$
$\beta_d = 0.50 \left( \frac{6279 \text{ ksi}}{29000 \text{ ksi}} + 1 \right) = 0.608$	$\beta_d = 0.50 \left( \frac{6279 \text{ ksi}}{29000 \text{ ksi}} + 1 \right) = 0.608$
<p>Moment due to dead load plus live load:</p>	<p>Moment due to dead load plus live load:</p>
$M_{DL+LL} = \frac{w_{DL+LL} \cdot l^2}{8}$	$M_{DL+LL} = \frac{w_{DL+LL} \cdot l^2}{8}$
$M_{DL+LL} = \frac{\left(0.775 \frac{\text{kip}}{\text{ft}} + 1.2 \frac{\text{kip}}{\text{ft}}\right)(14 \text{ ft})^2}{8} = 48.4 \text{ kip} \cdot \text{ft}$	$M_{DL+LL} = \frac{\left(0.775 \frac{\text{kip}}{\text{ft}} + 1.2 \frac{\text{kip}}{\text{ft}}\right)(14 \text{ ft})^2}{8} = 48.4 \text{ kip} \cdot \text{ft}$
<p>Cracking moment:</p>	<p>Cracking moment:</p>
$M_{cr} = \frac{f_r I_g}{y_t} = \frac{7.5 \sqrt{f_c} I_g}{\frac{h}{2}}$	$M_{cr} = \frac{f_r I_g}{y_t} = \frac{7.5 \sqrt{f_c} I_g}{\frac{h}{2}}$

Figure 87: Design Example. (Continued)

Design based on ACI 440.1R-03 design guidelines	Design based on results from this research project
$M_{cr} = \frac{7.5\sqrt{4000 \text{ psi}}(3584 \text{ in.}^4)}{16 \text{ in.}} \left( \frac{1 \text{ kip}}{1000 \text{ lb}} \right) \left( \frac{1 \text{ ft}}{12 \text{ in.}} \right) = 17.7 \text{ kip} \cdot \text{ft}$	$M_{cr} = \frac{7.5\sqrt{4000 \text{ psi}}(3584 \text{ in.}^4)}{16 \text{ in.}} \left( \frac{1 \text{ kip}}{1000 \text{ lb}} \right) \left( \frac{1 \text{ ft}}{12 \text{ in.}} \right) = 17.7 \text{ kip} \cdot \text{ft}$
<p>Cracked moment of inertia:</p>	<p>Cracked moment of inertia:</p>
$(I_e)_{DL+LL} = \left( \frac{M_{cr}}{M_{DL+LL}} \right)^3 \beta_d I_g + \left[ 1 - \left( \frac{M_{cr}}{M_{DL+LL}} \right)^3 \right] I_{cr}$	$(I_e)_{DL+LL} = \left( \frac{M_{cr}}{M_{DL+LL}} \right)^3 \beta_d I_g + \left[ 1 - \left( \frac{M_{cr}}{M_{DL+LL}} \right)^3 \right] I_{cr}$
$(I_e)_{DL+LL} = \left( \frac{17.7}{48.4} \right)^3 (0.608)(3584) + \left[ 1 - \left( \frac{17.7}{48.4} \right)^3 \right] (613)$	$(I_e)_{DL+LL} = \left( \frac{17.7}{48.4} \right)^3 (0.608)(3584) + \left[ 1 - \left( \frac{17.7}{48.4} \right)^3 \right] (613)$
$(I_e)_{DL+LL} = 690 \text{ in.}^4$	$(I_e)_{DL+LL} = 690 \text{ in.}^4$
<p>Midspan deflection due to dead and live load:</p>	<p>Midspan deflection due to dead and live load:</p>
$(y_i)_{DL+LL} = \frac{5w_{DL+LL} \cdot l^4}{384E_c(I_e)_{DL+LL}}$ $(y_i)_{DL+LL} = \frac{5(0.775 \frac{\text{kip}}{\text{ft}} + 1.2 \frac{\text{kip}}{\text{ft}})(14 \text{ ft})^4 (12 \frac{\text{in.}}{\text{ft}})^3}{384(3605 \text{ ksi})(695 \text{ in.}^4)} = 0.69 \text{ in.}$	$(y_i)_{DL+LL} = \frac{5w_{DL+LL} \cdot l^4}{384E_c(I_e)_{DL+LL}}$ $(y_i)_{DL+LL} = \frac{5(0.775 \frac{\text{kip}}{\text{ft}} + 1.2 \frac{\text{kip}}{\text{ft}})(14 \text{ ft})^4 (12 \frac{\text{in.}}{\text{ft}})^3}{384(3605 \text{ ksi})(695 \text{ in.}^4)} = 0.69 \text{ in.}$
<p>Midspan deflections due to dead load alone and live load alone:</p>	<p>Midspan deflections due to dead load alone and live load alone:</p>
$(y_i)_{DL} = \frac{w_{DL}}{w_{DL+LL}} (y_i)_{DL+LL}$	$(y_i)_{DL} = \frac{w_{DL}}{w_{DL+LL}} (y_i)_{DL+LL}$

Figure 87: Design Example. (Continued)

Design based on ACI 440.1R-03 design guidelines	Design based on results from this research project
$(y_i)_{DL} = \frac{0.775 \frac{\text{kip}}{\text{ft}}}{0.775 \frac{\text{kip}}{\text{ft}} + 1.2 \frac{\text{kip}}{\text{ft}}} (0.69 \text{ in.}) = 0.27 \text{ in.}$	$(y_i)_{DL} = \frac{0.775 \frac{\text{kip}}{\text{ft}}}{0.775 \frac{\text{kip}}{\text{ft}} + 1.2 \frac{\text{kip}}{\text{ft}}} (0.69 \text{ in.}) = 0.27 \text{ in.}$
$(y_i)_{LL} = \frac{w_{LL}}{w_{DL+LL}} (y_i)_{DL+LL}$	$(y_i)_{LL} = \frac{w_{LL}}{w_{DL+LL}} (y_i)_{DL+LL}$
$(y_i)_{LL} = \frac{1.2 \frac{\text{kip}}{\text{ft}}}{0.775 \frac{\text{kip}}{\text{ft}} + 1.2 \frac{\text{kip}}{\text{ft}}} (0.69 \text{ in.}) = 0.42 \text{ in.}$	$(y_i)_{LL} = \frac{1.2 \frac{\text{kip}}{\text{ft}}}{0.775 \frac{\text{kip}}{\text{ft}} + 1.2 \frac{\text{kip}}{\text{ft}}} (0.69 \text{ in.}) = 0.42 \text{ in.}$
Allowable instantaneous live load deflection:	Allowable instantaneous live load deflection:
$(y_i)_{LL} = \frac{l}{360}$	$(y_i)_{LL} = \frac{l}{360}$
$0.42 \text{ in.} < \frac{(14 \text{ ft})(12 \frac{\text{in.}}{\text{ft}})}{360} = 0.47 \text{ in.} \therefore \text{O.K.}$	$0.42 \text{ in.} < \frac{(14 \text{ ft})(12 \frac{\text{in.}}{\text{ft}})}{360} = 0.47 \text{ in.} \therefore \text{O.K.}$
Long-term deflection:	Long-term deflection due to dead load:
$\xi = 1.25$ (ACI 318 for a duration of six months)	Compute initial top fiber strain and curvature at midspan.
$\lambda = 0.60\xi$	Area of transformed section in compression:
$\lambda = 0.60(1.25) = 0.75$	$A_c = bkd = (10.5 \text{ in.})(0.221)(13.75 \text{ in.}) = 31.9 \text{ in.}^2$
Compute six-month deflection and compare to allowable:	First moment of area of transformed section in compression about top surface:
$y_{LT} = (y_i)_{LL} + \lambda(y_i)_{DL}$	
$y_{LT} = (0.42 \text{ in.}) + 0.75(0.27 \text{ in.}) = 0.62 \text{ in.}$	$B_c = b \frac{(kd)^2}{2} = (10.5 \text{ in.}) \frac{[(0.221)(13.75 \text{ in.})]^2}{2} = 48.5 \text{ in.}^3$

Figure 87: Design Example. (Continued)

Design based on ACI 440.1R-03 design guidelines	Design based on results from this research project
<p>Allowable long-term deflection:</p> $y_{LT} \leq \frac{l}{240}$ $0.62 \text{ in.} < \frac{(14 \text{ ft})(12 \frac{\text{in.}}{\text{ft}})}{240} = 0.70 \text{ in.} \therefore \text{OK}$	<p>Moment of inertia of transformed section in compression about top surface:</p> $I_c = b \frac{(kd)^3}{12} + b \frac{(kd)^2}{2}$ $I_c = (10.5 \text{ in.}) \frac{[(0.221)(13.75 \text{ in.})]^3}{12} + (10.5 \text{ in.}) \frac{[(0.221)(13.75 \text{ in.})]^2}{4}$ $I_c = 98.3 \text{ in.}^4$ $A'_c = A_c + \frac{B_c - dA_c}{d(1 - \frac{k}{3})}$ $A'_c = 31.9 \text{ in.}^2 + \frac{48.5 \text{ in.}^3 - (13.75 \text{ in.})(31.9 \text{ in.}^2)}{13.75 \text{ in.}(1 - \frac{0.221}{3})} = 1.27 \text{ in.}^2$ $B'_c = B_c + \frac{I_c - dB_c}{d(1 - \frac{k}{3})}$ $B'_c = 48.5 \text{ in.}^3 + \frac{98.3 \text{ in.}^4 - (13.75 \text{ in.})(48.5 \text{ in.}^3)}{13.75 \text{ in.}(1 - \frac{0.221}{3})} = 3.86 \text{ in.}^3$ <p>Moment due to dead load:</p> $M_{DL} = \frac{w_{DL} \cdot l^2}{8}$

Figure 87: Design Example. (Continued)

Design based on ACI 440.1R-03 design guidelines	Design based on results from this research project
	$M_{DL} = \frac{(0.775 \frac{\text{kip}}{\text{ft}})(14 \text{ ft})^2}{8} = 19.0 \text{ kip} \cdot \text{ft}$ <p>Initial top fiber strain and curvature at midspan:</p> $\varepsilon_{oiC} = \frac{19 \text{ kip} \cdot \text{ft} \left( \frac{12 \text{ in.}}{1 \text{ ft}} \right) (3.86 \text{ in.}^3)}{3605 \text{ ksi} \left[ (48.5 \text{ in.}^3)^2 - (98.3 \text{ in.}^4)(31.9 \text{ in.}^2) \right]} = -3.12 \times 10^{-4} \text{ in./in.}$ $\kappa_{ic} = \frac{-(1.27 \text{ in.}^2)(19 \text{ kip} \cdot \text{ft}) \left( \frac{12 \text{ in.}}{1 \text{ ft}} \right)}{3605 \text{ ksi} \left[ (48.5 \text{ in.}^3)^2 - (98.3 \text{ in.}^4)(31.9 \text{ in.}^2) \right]} = 1.02 \times 10^{-4} \text{ in.}^{-1}$ <p>Check curvature:</p> $\kappa_{ic} = \frac{M_i}{E_c I_{cr}} = \frac{19 \text{ kip} \cdot \text{ft} \left( \frac{12 \text{ in.}}{1 \text{ ft}} \right)}{(3605 \text{ ksi})(613 \text{ in.}^4)} = 1.03 \times 10^{-4} \text{ in.}^{-1} \therefore \text{OK}$ <p>Check top fiber strain:</p> $\varepsilon_{oiC} = -k_{ic}kd = -(1.02 \times 10^{-4} \text{ in.}^{-1})(0.221)(13.75 \text{ in.})$ $\varepsilon_{oiC} = -3.10 \times 10^{-4} \text{ in./in.} \therefore \text{OK}$ <p>Creep coefficient at six months: Assume <math>C_{ult} = 2.35</math>.</p> $\Delta\phi(t, \tau) = \frac{(t - \tau)^{0.6}}{D + (t - \tau)^{0.6}} C_{ult}$

Figure 87: Design Example. (Continued)

Design based on ACI 440.1R-03 design guidelines	Design based on results from this research project
	$\Delta\phi(180,14) = \frac{(180-14)^{0.6}}{10 + (180-14)^{0.6}} (2.35) = 1.60$ <p>Choose an aging coefficient <math>\chi = 0.8</math>, as recommended by Gilbert and Mickleborough:</p> <p>Shrinkage strain at six months: Assume the beam was cured for 7 days.</p> $(\varepsilon_{sh})_t = \frac{t}{35+t} (\varepsilon_{sh})_{ult}$ <p>Assume <math>(\varepsilon_{sh})_{ult} = -730 \times 10^{-6}</math></p> $(\varepsilon_{sh})_{180-7} = \frac{(180-7)}{35+(180-7)} (-730 \times 10^{-6}) = -6.07 \times 10^{-4} \text{ in./in.}$ <p>Obtain an equivalent imaginary creep loss of prestressing force at six months.</p> <p>As explained in the creep test results section, the creep strain can be assumed to be independent of stress. Thus, for a beam with a distributed load, the creep strain will be assumed to be constant over the full length of the 14-ft span.</p> <p>The creep strain at six months of <math>234 \times 10^{-6}</math> inch/inch from specimen V1-5-b of the creep test will be used.</p>

Figure 87: Design Example. (Continued)

Design based on ACI 440.1R-03 design guidelines	Design based on results from this research project
	<p>Thus, the equivalent imaginary creep loss of prestressing force is:</p> $F = \Delta P = -\varepsilon_c E_f A_f = -234 \times 10^{-6} \frac{\text{in.}}{\text{in.}} (6279 \text{ ksi}) (2.60 \text{ in.}^2) = -3.82 \text{ kip}$ <p>Age-adjusted effective modulus:</p> $E_e(t, \tau) = \frac{E_c}{1 + \chi \Delta \phi(t, \tau)}$ $E_e(t, \tau) = \frac{3605 \text{ ksi}}{1 + (0.8)(1.60)} = 1591 \text{ ksi}$ <p>Total restraining forces at midspan:</p> $-\delta N = -E_e [\Delta \phi (A_c \varepsilon_{oiC} + B_c \kappa_{iC}) + \varepsilon_{sh} A_c] + \sum_{j=1}^m F_j$ $A_c \varepsilon_{oiC} + B_c \kappa_{iC} = (31.9 \text{ in.}^2) (-3.12 \times 10^{-4}) + (48.5 \text{ in.}^3) (1.02 \times 10^{-4} \text{ in.}^{-1})$ $A_c \varepsilon_{oiC} + B_c \kappa_{iC} = -5.0 \times 10^{-3} \text{ in.}^2$ $\Delta \phi (A_c \varepsilon_{oiC} + B_c \kappa_{iC}) + \varepsilon_{sh} A_c = 1.6 (-5.0 \times 10^{-3} \text{ in.}^2) + (-6.07 \times 10^{-4}) (31.9 \text{ in.}^2)$ $\Delta \phi (A_c \varepsilon_{oiC} + B_c \kappa_{iC}) + \varepsilon_{sh} A_c = -0.0273 \text{ in.}^2$ $-\delta N = -1579 \text{ ksi} (-0.0273 \text{ in.}^2) - 3.82 \text{ kip}$ $-\delta N = 39.3 \text{ kip}$

Figure 87: Design Example. (Continued)

Design based on ACI 440.1R-03 design guidelines	Design based on results from this research project
	$-\delta M = -E_e [\Delta\phi(B_c \varepsilon_{oi} + I_c \kappa_i) + \varepsilon_{sh} B_c] + \sum_{j=1}^m F_j d_j$ $B_c \varepsilon_{oiC} + I_c \kappa_{iC} = (48.5 \text{ in.}^3)(-3.12 \times 10^{-4}) + (98.3 \text{ in.}^4)(1.02 \times 10^{-4} \text{ in.}^{-1})$ $B_c \varepsilon_{oiC} + I_c \kappa_{iC} = -5.11 \times 10^{-3} \text{ in.}^3$ $\Delta\phi(B_c \varepsilon_{oiC} + I_c \kappa_{iC}) + \varepsilon_{sh} B_c = 1.6(-5.11 \times 10^{-3} \text{ in.}^3) + (-6.07 \times 10^{-4})(48.5 \text{ in.}^3)$ $\Delta\phi(B_c \varepsilon_{oiC} + I_c \kappa_{iC}) + \varepsilon_{sh} B_c = -0.0376 \text{ in.}^3$ $Fd = (-3.82 \text{ kip})(13.75 \text{ in.})\left(\frac{1 \text{ ft}}{12 \text{ in.}}\right) = -4.38 \text{ kip} \cdot \text{ft}$ $-\delta M = -1579 \text{ ksi}(-0.0376 \text{ in.}^3)\left(\frac{1 \text{ ft}}{12 \text{ in.}}\right) - 4.38 \text{ kip} \cdot \text{ft}$ $-\delta M = 0.57 \text{ kip} \cdot \text{ft}$ <p>Properties of age-adjusted transformed section:</p> <p>Area of age-adjusted transformed section:</p> $A_e = bkd + n_{fe} A_f$ $n_{fe} = \frac{E_f}{E_e} = \frac{6279 \text{ ksi}}{1579 \text{ ksi}} = 3.98$ $A_e = (10.5 \text{ in.})(0.221)(13.75 \text{ in.}) + 3.98(2.6 \text{ in.}^2) = 42.2 \text{ in.}^2$

Figure 87: Design Example. (Continued)

Design based on ACI 440.1R-03 design guidelines	Design based on results from this research project
	<p>First moment of area of age-adjusted transformed section about top of surface:</p> $B_e = b \frac{(kd)^2}{2} + n_{fe} A_f d$ $B_e = (10.5 \text{ in.}) \frac{[(0.221)(13.75 \text{ in.})]^2}{2} + 3.98(2.6 \text{ in.}^2)(13.75 \text{ in.}) = 191 \text{ in.}^3$ <p>Moment of inertia of transformed section in compression about top of surface:</p> $I_e = b \frac{(kd)^3}{12} + b \frac{(kd)^2}{2} + n_{fe} A_f d^2$ $I_e = (10.5 \text{ in.}) \frac{[(0.221)(13.75 \text{ in.})]^3}{12} + (10.5 \text{ in.}) \frac{[(0.221)(13.75 \text{ in.})]^2}{4}$ $+ 3.98(2.6 \text{ in.}^2)(13.75 \text{ in.})^2$ $I_e = 2054 \text{ in.}^4$ $A'_e = A_e + \frac{B_e - dA_e}{d(1 - \frac{k}{3})}$ $A'_e = 42.2 \text{ in.}^2 + \frac{191 \text{ in.}^3 - (13.75 \text{ in.})(42.2 \text{ in.}^2)}{13.75 \text{ in.}(1 - \frac{0.221}{3})} = 11.6 \text{ in.}^2$

Figure 87: Design Example. (Continued)

Design based on ACI 440.1R-03 design guidelines	Design based on results from this research project
$B'_e = B_e + \frac{I'_e - dB_e}{d\left(1 - \frac{k}{3}\right)}$ $B'_e = 191 \text{ in.}^3 + \frac{2054 \text{ in.}^4 - (13.75 \text{ in.})(191 \text{ in.}^3)}{13.75 \text{ in.}\left(1 - \frac{0.221}{3}\right)} = 146 \text{ in.}^3$ <p>Time-dependent increments of curvature and top surface strain at midspan:</p> $\Delta\varepsilon_{oc} = \frac{\delta MB'_e - \delta NI'_e}{E_e (B_e^2 - I_e A_e)}$ $\Delta\varepsilon_{oc} = \frac{(-0.57 \text{ kip}\cdot\text{ft})\left(\frac{12 \text{ in.}}{1 \text{ ft}}\right)(146 \text{ in.}^3) - (-39.4 \text{ kip})(2054 \text{ in.}^4)}{1579 \text{ ksi} \left[ (191 \text{ in.}^3)^2 - (2054 \text{ in.}^4)(42.2 \text{ in.}^2) \right]}$ $\Delta\varepsilon_{oc} = -1.01 \times 10^{-3}$ $\Delta\kappa_c = \frac{B_e \delta N - A'_e \delta M}{E_e (B_e^2 - I_e A_e)}$ $\Delta\kappa_c = \frac{(191 \text{ in.}^3)(-39.4 \text{ kip}) - (11.6 \text{ in.}^2)(-0.57 \text{ kip}\cdot\text{ft})\left(\frac{12 \text{ in.}}{1 \text{ ft}}\right)}{1579 \text{ ksi} \left[ (191 \text{ in.}^3)^2 - (2054 \text{ in.}^4)(42.2 \text{ in.}^2) \right]}$ $\Delta\kappa_c = 9.39 \times 10^{-5} \text{ in.}^{-1}$ $\varepsilon_{oc} = \varepsilon_{oci} + \Delta\varepsilon_{oc} = -1.31 \times 10^{-3} \text{ in./in.}$	

Figure 87: Design Example. (Continued)

Design based on ACI 440.1R-03 design guidelines	Design based on results from this research project
	<p>Final curvature and top surface strain at midspan:  <math>\kappa_c = \kappa_{ic} + \Delta\kappa = 1.96 \times 10^{-4} \text{ in.}^{-1}</math></p> <p>Initial top fiber strain and curvature at left support:</p> $\varepsilon_{oiL} = \frac{M_i B_c - N_i I_c}{E_c (B_c^2 - I_c A_c)} = 0 \text{ since } M_i = 0 \text{ and } N_i = 0$ $\kappa_{iL} = \frac{B_c N_i - A_c M_i}{E_c (B_c^2 - I_c A_c)} = 0 \text{ since } M_i = 0 \text{ and } N_i = 0$ <p>Total restraining forces at left support:</p> $-\delta N = -E_e [\Delta\phi (A_c \varepsilon_{oiL} + B_c \kappa_{iL}) + \varepsilon_{sh} A_c] + \sum_{j=1}^m F_j$ $-\delta N = -E_e (\varepsilon_{sh} A_c) + \sum_{j=1}^m F_j$ $-\delta N = -1579 \text{ ksi} [(-6.07 \times 10^{-4})(31.9 \text{ in.}^2)] - 3.82 \text{ kip} = 26.8 \text{ kip}$ $-\delta M = -E_e [\Delta\phi (B_c \varepsilon_{oiL} + I_c \kappa_{iL}) + \varepsilon_{sh} B_c] + \sum_{j=1}^m F_j d_j$ $-\delta M = -E_e (\varepsilon_{sh} B_c) + \sum_{j=1}^m F_j d_j$ $-\delta M = -1579 \text{ ksi} [(-6.07 \times 10^{-4})(48.5 \text{ in.}^3)] \left(\frac{1 \text{ ft}}{12 \text{ in.}}\right) - 4.38 \text{ kip} \cdot \text{ft}$ $-\delta M = -0.50 \text{ kip} \cdot \text{ft}$

Figure 87: Design Example. (Continued)

Design based on ACI 440.1R-03 design guidelines	Design based on results from this research project
	<p>Time-dependent increments of curvature and top surface strain:</p> $\Delta\epsilon_{oL} = \frac{\delta MB_e' - \delta NI_e}{E_e (B_e^2 - I_e A_e)}$ $\Delta\epsilon_{oL} = \frac{(0.50 \text{ kip} \cdot \text{ft}) \left(\frac{12 \text{ in.}}{1 \text{ ft}}\right) (146 \text{ in.}^3) - (-26.8 \text{ kip})(2054 \text{ in.}^4)}{1579 \text{ ksi} \left[ (191 \text{ in.}^3)^2 - (2054 \text{ in.}^4)(42.2 \text{ in.}^2) \right]}$ $\Delta\epsilon_{oL} = -7.02 \times 10^{-4}$ $\Delta\kappa_L = \frac{B_e \delta N - A_e' \delta M}{E_e (B_e^2 - I_e A_e)}$ $\Delta\kappa_L = \frac{(191 \text{ in.}^3)(-26.8 \text{ kip}) - (11.6 \text{ in.}^2)(0.50 \text{ kip} \cdot \text{ft}) \left(\frac{12 \text{ in.}}{1 \text{ ft}}\right)}{1579 \text{ ksi} \left[ (191 \text{ in.}^3)^2 - (2054 \text{ in.}^4)(42.2 \text{ in.}^2) \right]}$ $\Delta\kappa_L = 6.50 \times 10^{-5} \text{ in.}^{-1}$ <p>Final curvature and top surface strain at left support:</p> $\epsilon_{oL} = \epsilon_{oiL} + \Delta\epsilon_{oL} = -7.02 \times 10^{-4} \text{ in./in.}$ $\kappa_L = \kappa_{iL} + \Delta\kappa_L = 6.50 \times 10^{-5} \text{ in.}^{-1}$ <p>Initial top fiber strain and curvature at right support:</p> $\epsilon_{oiR} = 0, \kappa_{iR} = 0$

Figure 87: Design Example. (Continued)

<b>Design based on ACI 440.1R-03 design guidelines</b>	<b>Design based on results from this research project</b>
	<p>Final curvature and top surface strain at left support:</p> $\varepsilon_{oR} = -7.02 \times 10^{-4} \text{ in./in.}$ $\kappa_R = 6.50 \times 10^{-5} \text{ in.}^{-1}$ <p>Compute midspan deflection at six months due to dead load:</p> $(y_{LT})_{DL} = \frac{L^2}{96} (\kappa_L + 10\kappa_C + \kappa_R)$ $(y_{LT})_{DL} = \frac{[(14 \text{ ft})(\frac{12 \text{ in.}}{1 \text{ ft}})]^2}{96} (6.50 \times 10^{-5} \text{ in.}^{-1} + 10(1.02 \times 10^{-4}) + 6.50 \times 10^{-5} \text{ in.}^{-1})$ $(y_{LT})_{DL} = 0.61 \text{ in.}$ <p><i>Total six-month deflection at midspan:</i></p> $y_{LT} = (y_i)_{LL} + (y_{LT})_{DL}$ $y_{LT} = 0.41 \text{ in.} + 0.61 \text{ in.} = 1.03 \text{ in.}$ <p>Allowable long-term deflection:</p> $y_{LT} \leq \frac{l}{240}$ $1.03 \text{ in.} > \frac{(14 \text{ ft})(12 \frac{\text{in.}}{\text{ft}})}{240} = 0.70 \text{ in.} \therefore \text{N.G.}$ <p>Before redesigning the section, check the maximum crack width.</p>

**Figure 87: Design Example. (Continued)**

Design based on ACI 440.1R-03 design guidelines	Design based on results from this research project
<p><b>6. Check the maximum crack width.</b>  Compute the stress level in the FRP bars under dead load plus live load (service conditions):</p> $f_f = \frac{M_{DL+LL}}{A_f d \left(1 - \frac{k}{3}\right)}$ $f_f = \frac{48.4 \text{ kip} \cdot \text{ft} \left(\frac{12 \text{ in.}}{1 \text{ ft}}\right)}{(2.60 \text{ in.}^2) 13.75 \text{ in.} \left(1 - \frac{0.221}{3}\right)} = 17.5 \text{ ksi}$ <p>Find the effective tension area of concrete:</p> $\beta = \frac{h - kd}{d - kd}$ $\beta = \frac{16 \text{ in.} - 0.221(13.75 \text{ in.})}{13.75 \text{ in.} - 0.221(13.75 \text{ in.})} = 1.21$ $d_c = \text{cover} + \text{stirrup size} + \frac{1}{2}d_b$ $d_c = 1.5 \text{ in.} + 0.375 + \frac{1}{2}(0.743 \text{ in.}) = 2.25 \text{ in.}$ $A = \frac{2(h-d)b}{\text{No. bars}}$ $A = \frac{2(16 \text{ in.} - 13.75 \text{ in.})(10.5 \text{ in.})}{6} = 7.86 \text{ in.}^2$	<p><b>6. Check the maximum crack width.</b>  Compute the stress level in the FRP bars under dead load plus live load (service conditions):</p> $f_f = \frac{M_{DL+LL}}{A_f d \left(1 - \frac{k}{3}\right)}$ $f_f = \frac{48.4 \text{ kip} \cdot \text{ft} \left(\frac{12 \text{ in.}}{1 \text{ ft}}\right)}{(2.60 \text{ in.}^2) 13.75 \text{ in.} \left(1 - \frac{0.221}{3}\right)} = 17.5 \text{ ksi}$ <p>Find the effective tension area of concrete:</p> $\beta = \frac{h - kd}{d - kd}$ $\beta = \frac{16 \text{ in.} - 0.221(13.75 \text{ in.})}{13.75 \text{ in.} - 0.221(13.75 \text{ in.})} = 1.21$ $d_c = \text{cover} + \text{stirrup size} + \frac{1}{2}d_b$ $d_c = 1.5 \text{ in.} + 0.375 + \frac{1}{2}(0.743 \text{ in.}) = 2.25 \text{ in.}$ $A = \frac{2(h-d)b}{\text{No. bars}}$ $A = \frac{2(16 \text{ in.} - 13.75 \text{ in.})(10.5 \text{ in.})}{6} = 7.86 \text{ in.}^2$

Figure 87: Design Example. (Continued)

<b>Design based on ACI 440.1R-03 design guidelines</b>	<b>Design based on results from this research project</b>
<p>Compute the maximum crack width using ACI 440.1R-03 Equation 8-9b:</p> $w = 0.076\beta \frac{E_s}{E_f} f_f \sqrt[3]{d_c A}$ $w = 0.076(1.21) \frac{29000}{6279} (17.5 \text{ ksi}) \sqrt[3]{(2.25 \text{ in.})(7.86 \text{ in.}^2)}$ $w = 19 \text{ mils} < 20 \text{ mils} \therefore \text{OK}$	<p>Compute the maximum crack width using Equation 81 from this research:</p> $W_{\max} = 0.09\beta \cdot f_f \cdot \sqrt[3]{d_c A}$ $W_{\max} = 0.09(1.21) \frac{29000}{6279} (17.5 \text{ ksi}) \sqrt[3]{(2.25 \text{ in.})(7.86 \text{ in.}^2)}$ $W_{\max} = 23 \text{ mils} > 20 \text{ mils} \therefore \text{N.G. Redesign the beam.}$
<p>Compute the maximum crack width using ACI 440.1R-03 Equation 8-9c, using the recommended value of <math>kb = 1.2</math>:</p> $w = \frac{2200}{E_f} \beta k_b f_f \sqrt[3]{d_c A}$ $w = \frac{2200}{6279} (1.21)(1.2)(17.5 \text{ ksi}) \sqrt[3]{(2.25 \text{ in.})(7.86 \text{ in.}^2)}$ $w = 23 \text{ mils} > 20 \text{ mils} \therefore \text{N.G.}$	
<p><b>5a. Check the short-and long-term deflections of the beam.</b></p> <p>The beam is adequate for short-term and long-term deflections.</p>	<p><b>5a. Check the short-and long-term deflections of the beam.</b></p> <p>Try <math>h = 19</math> inches.</p> $\rho_f = \frac{A_f}{bd}$ $\rho_f = \frac{2.60 \text{ in.}^2}{10.5 \text{ in.}(16.75 \text{ in.})} = 0.0148 < 1.4\rho_{fb} = 0.0152 \therefore \phi = 0.7$

Figure 87: Design Example. (Continued)

Design based on ACI 440.1R-03 design guidelines	Design based on results from this research project
	<p>Moment capacity:  <math>\phi M_n = 113.7 \text{ kip} \cdot \text{ft} \geq M_u = 77.7 \text{ kip} \cdot \text{ft} \therefore \text{OK}</math></p> <p>Live load deflection:  <math>(y_i)_{LL} = 0.22 \text{ in.} &lt; 0.47 \text{ in.} \therefore \text{OK}</math></p> <p>Total long-term deflection:  <math>(y)_{LT} = 0.67 \text{ in.} \leq \frac{l}{240} = 0.70 \text{ in.} \therefore \text{OK}</math></p>
<p><b>6a. Check the maximum crack width.</b>  The beam is adequate per ACI Equation 8-9b.  Try <math>h = 19</math> inches.  Compute the maximum crack width using ACI 440.1R-03 Equation 8-9c, using the recommended value of <math>kb = 1.2</math>:  <math>w = 18.6 \text{ mils} &lt; 20 \text{ mils} \therefore \text{OK}</math></p>	<p><b>6a. Check the maximum crack width.</b>  Compute the maximum crack width using Equation 81 from this research:  <math>W_{max} = 18.4 \text{ mils} &lt; 20 \text{ mils} \therefore \text{OK}</math></p>
<p><b>7. Check the creep rupture stress limit.</b>  Moment due to sustained load:  <math>M_s = M_{DL}</math>  <math display="block">M_s = \frac{0.808 \frac{\text{kip}}{\text{ft}} (14 \text{ ft})^2}{8} = 19.8 \text{ kip} \cdot \text{ft}</math></p>	<p><b>7. Check the creep rupture stress limit.</b>  Moment due to sustained load:  <math>M_s = M_{DL}</math>  <math display="block">M_s = \frac{0.808 \frac{\text{kip}}{\text{ft}} (14 \text{ ft})^2}{8} = 19.8 \text{ kip} \cdot \text{ft}</math></p>

Figure 87: Design Example. (Continued)

<b>Design based on ACI 440.1R-03 design guidelines</b>	<b>Design based on results from this research project</b>
<p>Sustained stress in the FRP bars:</p> $f_{f,s} = \frac{M_s}{A_f d \left(1 - \frac{k}{3}\right)}$ $f_f = \frac{19.8 \text{ kip} \cdot \text{ft} \left(\frac{12 \text{ in.}}{1 \text{ ft}}\right)}{(2.6 \text{ in.}^2) 16.75 \text{ in.} \left(1 - \frac{0.203}{3}\right)} = 5.85 \text{ ksi}$ <p>Check the stress limit for GFRP bars:</p> $f_{f,s} \leq 0.20 f_{fu}$ $5.85 \text{ ksi} \leq 0.20(62 \text{ ksi}) = 12.4 \text{ ksi} \therefore \text{O.K.}$	<p>Sustained stress in the FRP bars:</p> $f_{f,s} = \frac{M_s}{A_f d \left(1 - \frac{k}{3}\right)}$ $f_f = \frac{19.8 \text{ kip} \cdot \text{ft} \left(\frac{12 \text{ in.}}{1 \text{ ft}}\right)}{(2.6 \text{ in.}^2) 16.75 \text{ in.} \left(1 - \frac{0.203}{3}\right)} = 5.85 \text{ ksi}$ <p>Check the stress limit for GFRP bars:</p> $f_{f,s} \leq 0.20 f_{fu}$ $5.85 \text{ ksi} \leq 0.20(62 \text{ ksi}) = 12.4 \text{ ksi} \therefore \text{O.K.}$
<p><b>8. Compute the basic development length.</b></p> <p>Use ACI Equation 11-7:</p> $l_{bf} = \frac{d_b f_{fu}}{2700} = \frac{(0.743 \text{ in.})(62000 \text{ psi})}{2700} = 17 \text{ in.}$	<p><b>8. Compute the basic development length.</b></p> <p>Use Equation 90 from this research:</p> $l_{bf} = \frac{d_b f_{u,ave}}{2700} = \frac{(0.743 \text{ in.})(96000 \text{ psi})}{2700} = 26.4 \text{ in.}$
<p><b>9. Compute additional deflections due to cyclic loading.</b></p> <p>ACI 440.1R-03 does not account for deflections due to cyclic loading.</p>	<p><b>9. Compute additional deflections due to cyclic loading.</b></p> <p>Assume the cyclic loading will be due to live load alone. Thus, use the slope of Equation 84 from this research, and use the initial deflection due to dead load and live load.</p>

Figure 87: Design Example. (Continued)

Design based on ACI 440.1R-03 design guidelines	Design based on results from this research project
	<p>Initial deflection due to dead load and live load:</p> $(y_i)_{DL+LL} = \frac{5w_{DL+LL} \cdot l^4}{384E_c(I_e)_{DL+LL}}$ $(y_i)_{DL+LL} = \frac{5(0.808 \frac{\text{kip}}{\text{ft}} + 1.2 \frac{\text{kip}}{\text{ft}})(14 \text{ ft})^4 (12 \frac{\text{in.}}{\text{ft}})^3}{384(3605 \text{ ksi})(1299 \text{ in.}^4)} = 0.15 \text{ in.} + 0.22 \text{ in.}$ $(y_i)_{DL+LL} = 0.37 \text{ in.}$ <p>Lower bound beam deflection due to 2 million cycles of application of live load:</p> $y = 0.0046 \text{ in.} \ln(n) + 0.37 \text{ in.}$ $y = 0.0046 \text{ in.} \ln(2000000) + 0.37 \text{ in.} = 0.47 \text{ in.}$

Figure 87: Design Example. (Continued)

As a result of this review, the following changes are proposed to the ACI 440 document. A reevaluation of the environmental reduction factors is proposed, since this research showed that they could be unconservative. [Equation 81](#) is proposed to replace ACI 440 Equation 8-9a. This research also proposes the deflections of GFRP-reinforced concrete elements induced by cyclic loading to be accounted for in the ACI 440 design guidelines. The method presented in [Section IV](#) under creep test is proposed as an alternative to Equation 8-14 of the ACI 440 design guidelines. [Equation 88](#) is proposed to replace Equation 11-7 of the ACI 440 design guidelines. Finally, the minimum cover of 1 bar diameter recommended by the ACI 440 design guidelines cannot be verified for adequacy using this research. However, a cover of 1.33 bar diameters has been shown by this research to have no cracking problems due to thermal expansion.



## **VI. PROPOSED REVISIONS TO THE AASHTO LRFD BRIDGE DESIGN SPECIFICATIONS**

### **INTRODUCTION**

This section presents a review of the 1998 AASHTO LRFD bridge design specifications ([1998](#)) and recommends changes based on the results of this and other research related to the use of non-prestressed GFRP bars to reinforce concrete structures. This section presents a brief introduction followed by a description of the AASHTO sections that may need to be modified to include the design of concrete elements reinforced with FRP bars. The sections of the AASHTO specifications that do not need to be modified are not listed in this section.

The 1998 AASHTO LRFD bridge design specifications do not include recommendations for the design of concrete structures reinforced with GFRP bars. Because the results obtained by this research and by the studies referenced are limited to the conditions and exposures evaluated in this research, extreme care should be taken when designing GFRP-reinforced concrete elements that will be subjected to different conditions. It should be noted that these recommendations are proposed based on the research to date and in most cases more work is needed before implementing such modifications. A review of the applicable sections is presented next. Note that the section numbers listed below are the section numbers from the 1998 AASHTO LRFD bridge design specifications.

### **PROPOSED REVISIONS**

#### **1. Add to Section 1.3.3 Ductility**

This section of the code requires the bridge to develop significant and visible inelastic deformations at the strength and extreme event limit states. Since GFRP bars

exhibit linearly elastic behavior up to failure, GFRP-reinforced concrete elements do not exhibit significant ductility. Naaman and Jeong (1995) indicated that although FRP-reinforced concrete beams may deform considerably before failure, they elastically store most of the energy imposed on them during loading. Thus, since inelastic deformations are required by the code, either GFRP bars should not be used or GFRP bars should be used in combination with other systems or materials to provide ductility. Alternatively, the code may develop non-ductile behavior requirements for GFRP-reinforced concrete elements.

## **2. Add to Section 2.5.2.1.1 Materials**

The degradation of GFRP reinforcement should be accounted for in design. The tensile strength of GFRP bars can degrade in the concrete. The durability of FRP-reinforced concrete structures can be affected by several environmental factors such as: acids, alkalis, high temperatures, ultraviolet radiation, organic solvents, and oxygen or ozone (Bakht et al. 2000). The bond strength between GFRP bars and concrete can degrade with time in high-temperature moist conditions.

## **3. Add to Section 3.10.1 General**

The fact that FRP-reinforced concrete elements are non-ductile should be considered when performing a seismic design.

## **4. Notice for Section 4.6.2 Approximate Methods of Analysis**

This section may require modifications because FRP-reinforced concrete elements with a given amount and distribution of reinforcement and a given geometry have lower stiffness than steel-reinforced concrete elements having the same geometry and amount and configuration of reinforcement.

## **5. Notice for Section 5 Concrete Structures**

The ACI 440.1R-03 ([2003](#)) design and construction guidelines should be adopted for this section. However, special care must be taken to ensure that these equations and factors apply to the conditions at the actual structures' location because it has been determined that environmental conditions do affect the performance of GFRP reinforcing bars. Special consideration should be given to the subsections addressed in the following proposed revisions.

## **6. Add to Section 5.4 Material Properties**

Consideration should be given in this section to the material properties of GFRP bars such as tensile strength, accounting for environmental reduction factors, as already discussed in the ACI 440.1R-03 design and construction guidelines, coefficient of thermal expansion of the FRP bars, creep of FRP bars, deflections due to cyclic loading, and deterioration of bond strength between GFRP bars and concrete. A description of the durability and reactivity of fibers and resins to different environmental conditions given in the Canadian Bridge Design code provisions for fiber-reinforced structures could be included in this section ([Bakht et al. 2000](#)). A summary of the deleterious effects of several environments on fibers and matrices as described by Bakht et al. ([2000](#)) is given next:

- *Water*: Polymeric fibers and matrices absorb moisture. Moisture absorption softens the polymers. There are not sufficient data for the rate of deterioration of carbon and glass fibers.
- *Weak acids*: Bridges in industrialized areas may be exposed to weak acids from acid rain and carbonization, with pH values between 4 and 7. Weak acids can attack glass fibers and polyester matrices.
- *Strong acids*: Accidental spillage may cause strong acids to come in contact with bridge components. Strong acids can attack glass fibers, aramid fibers, and polyester and epoxy matrices.

- *Weak alkalis*: Concrete containing pozzolans can have pH values between 7 and 10. Weak alkalis such as these materials can attack glass fibers and polyester matrices.
- *Strong alkalis*: Typical Portland cement concretes have pH values greater than 10 and can cause degradation of glass fibers. Strong alkalis can attack glass fibers, aramid fibers, and polyester matrices.
- *High temperatures*: Carbon and glass fibers are resistant to high temperatures. However, high temperatures adversely affect aramid fibers and polymeric matrices.
- *Ultraviolet radiation*: Carbon and glass fibers are resistant to ultraviolet radiation. However, ultraviolet radiation adversely affects aramid fibers and polymeric matrices.

## **7. Move Section 5.4.4 Prestressing Steel to Section 5.4.5**

## **8. Move Section 5.4.5 Posttensioning Anchorages and Couplers to Section 5.4.6**

## **9. Move Section 5.4.6 Ducts to Section 5.4.7**

## **10. Add Section 5.4.4 FRP Reinforcement**

### **11. Add Section 5.4.4.1 General**

The design tensile strength of GFRP bars should be taken from the ACI 440.1R-03 design and construction guidelines as shown previously in [Equation 1](#):

$$f_{fu} = C_E f_{fu}^*$$

### **12. Add Section 5.4.4.2 Modulus of Elasticity**

The modulus of elasticity of FRP bars should be the average value reported from proper testing or by the manufacturer.

### **13. Add to Section 5.5.3.2 Reinforcing Bars**

The results of the cyclic load tests conducted in this research indicate that the flexural strength of GFRP-reinforced concrete beams show no significant degradation after the application of 4 and 5 million cycles of an alternating load with a GFRP bar stress range of 18.9 ksi. The fatigue capacity of FRP bars to be used in a bridge should be validated by further tests.

### **14. Add Section 5.5.4.2.4 FRP Construction**

The resistance factors recommended by the ACI 440.1R-03 design and construction guidelines should be used in this section. The resistance factors for flexure are:

$$\phi = 0.50 \text{ for } \rho_f \leq \rho_{fb}$$

$$\phi = \frac{\rho_f}{2\rho_{fb}} \text{ for } \rho_f < \rho_{fb} < 1.4\rho_{fb} \quad (92)$$

$$\phi = 0.70 \text{ for } \rho_f \geq 1.4\rho_{fb}$$

The resistance factor for shear should be the same as the factor used in the ACI 318 (2000) building code ( $\phi = 0.85$ ).

### **15. Add Section 5.7.3.2.5 FRP-Reinforced Concrete Elements**

The equations for flexural resistance given in the ACI 440.1R-03 design and construction guidelines should be used in this section. The reinforcement ratio ( $\rho_f$ ) and the balanced reinforcement ratio ( $\rho_{fb}$ ) for GFRP-reinforced sections can be computed with Equations 13 and 14, respectively:

$$\rho_f = \frac{A_f}{bd} \quad (93)$$

$$\rho_{fb} = 0.85\beta_1 \frac{f_c'}{f_{fu}} \frac{E_f \varepsilon_{cu}}{E_f \varepsilon_{cu} + f_{fu}} \quad (94)$$

where,

- $A_f$  = Area of FRP reinforcement ( $inch^2$ ),  
 $a$  = Depth of equivalent rectangular stress block ( $inch$ ),  
 $b$  = Width of section ( $inch$ ),  
 $d$  = Effective depth of the section ( $inch$ ),  
 $\varepsilon_{cu}$  = Ultimate strain in concrete,  
 $\beta_1$  = Factor taken as 0.85 for values of  $f'_c$  up to and including 4 ksi. Above 4 ksi, the factored is reduced linearly at a rate of 0.05 for each 1 ksi in excess of 4 ksi, but should not be smaller than 0.65,  
 $f_{fu}$  = Design tensile strength of FRP reinforcement ( $ksi$ ),  
 $f'_c$  = Design compressive strength of concrete ( $ksi$ ),  
 $E_f$  = Modulus of elasticity of FRP bars ( $ksi$ ).

When the reinforcement ratio is below the balanced ratio, FRP rupture is the failure mode; otherwise, concrete crushing is the failure mode.

The ACI 440.1R-03 design and construction guidelines recommend the following equations to compute the nominal flexural capacity when the reinforcement ratio is greater than the balanced ratio:

$$M_n = A_f f_f \left( d - \frac{a}{2} \right) \quad (95)$$

$$a = \frac{A_f f_f}{0.85 f'_c b} \quad (96)$$

$$f_f = \left( \sqrt{\frac{(E_f \varepsilon_{cu})^2}{4} + \frac{0.85 \beta_1 f'_c}{\rho_f} E_f \varepsilon_{cu}} - 0.5 E_f \varepsilon_{cu} \right) \leq f_{fu} \quad (97)$$

where,

- $M_n$  = Nominal flexural capacity ( $kip.inch$ ),  
 $f_f$  = Stress in the FRP reinforcement ( $ksi$ ).

When the reinforcement ratio is smaller than the balanced ratio, the ACI 440.1R-03 design and construction guidelines recommend the following equation to compute the nominal flexural capacity:

$$M_n = 0.8A_f f_{fu} \left( d - \frac{\beta_1 c_b}{2} \right) \quad (98)$$

$$c_b = \left( \frac{\varepsilon_{cu}}{\varepsilon_{cu} + \varepsilon_{fu}} \right) d$$

Where  $\varepsilon_{fu}$  is the ultimate strain in the GFRP reinforcement and all other terms were previously defined.

## 16. Add to Section 5.7.3.3.2 Minimum Reinforcement

For FRP-reinforced concrete elements in which failure is controlled by FRP rupture, the minimum area of FRP reinforcement should be as recommended by the ACI 440.1R-03 design and construction guidelines:

$$A_{f,min} = \frac{5.4\sqrt{f_c}}{f_{fu}} b_w d \geq \frac{360}{f_{fu}} b_w d \quad (99)$$

This requirement is intended to prevent flexural failure upon concrete cracking.

## 17. Add to Section 5.7.3.4 Control of Cracking by Distribution of Reinforcement

This section should use the allowable crack width for FRP-reinforced concrete elements as recommended by the ACI 440.1R-03 design and construction guidelines. The allowable maximum crack widths are 0.028 inches for interior exposure and 0.020 inches for exterior exposure.

Maximum crack widths can be estimated using the following equation, validated in this project and presented earlier as [Equation 2](#):

$$W_{max} = 0.09\beta \cdot f_f \cdot \sqrt[3]{d_c A} \quad (100)$$

## 18. Add to Section 5.7.3.5 Moment Redistribution

Following the ACI 440.1R-03 design and construction guidelines, since GFRP-reinforced concrete elements exhibit linear elastic behavior up to failure, moment redistribution should not be considered for GFRP-reinforced concrete.

## 19. Add to Section 5.7.3.6.2 Deflection and Camber

Deflection and camber of GFRP-reinforced concrete elements should consider GFRP creep. Equations 8-12a and 8-12b as recommended by the ACI 440.1R-03 design and construction guidelines to compute instantaneous deflections should be used:

$$I_e = \left( \frac{M_{cr}}{M_a} \right)^3 \beta I_g + \left[ 1 - \left( \frac{M_{cr}}{M_a} \right)^3 \right] I_{cr} \leq I_g \quad (101)$$
$$\beta = \alpha \left( \frac{E_f}{E_s} + 1 \right)$$

where,

$I_{cr}$  = cracked moment of inertia of the section ( $\text{inch}^4$ ),

$I_g$  = Gross moment of inertia of the section ( $\text{inch}^4$ ),

and all other terms have been defined previously.

The long-term deflections can be computed using Equation 8-14, provided by the ACI 440.1R-03 design and construction guidelines and shown previously as [Equation 6](#):

$$\Delta_{(cp+sh)} = 0.6\xi(\Delta_i)_{sus} \quad (102)$$

Alternatively, the change in curvature due to long-term loading can be computed using the following equation, shown earlier as [Equation 7](#):

$$\Delta\kappa = \frac{B_e \delta N - A_e \delta M}{E_e (B_e^2 - A_e I_e)} \quad (103)$$

and the long-term deflections can be computed by substituting [Equation 7](#) into [Equation 8](#):

$$y_c = \frac{L^2}{96} (\kappa_A + 10\kappa_C + \kappa_B) \quad (104)$$

Cyclic loading of concrete beam tests shows that deflections due to cyclic loading can increase by 78 percent due to cyclic loading and should be included in the computation of deflections due to live load.

The slope of [Equation 5](#) can be used to compute the lower bound deflection increments due to the application of cyclic load:

$$y = 0.0046 \ln(n) + 0.0858 \quad (105)$$

## **20. Add to Section 5.8.2.5 Minimum Transverse Reinforcement**

The requirements for minimum transverse reinforcement provided by the ACI 440.1R-03 design and construction guidelines should be adopted in this section. The minimum transverse reinforcement for FRP-reinforced concrete sections is:

$$A_{fv,min} = \frac{50b_w s}{f_{fv}} \quad (106)$$

where,

- $A_{fv,min}$  = Minimum area of transverse FRP reinforcement (*inch*<sup>2</sup>),
- $b_w$  = Width of section (*inch*),
- $s$  = Spacing of stirrups (*inch*),
- $f_{fv}$  = Stress level in the FRP shear reinforcement at ultimate (*ksi*).

According to the ACI 440.1R-03 design and construction guidelines, the stress level in the FRP shear reinforcement at ultimate should be limited to the following value to avoid failure at the bent portion of the FRP stirrup:

$$f_{fv} = 0.002E_f \leq f_{fb} \quad (107)$$

where  $f_{fb}$  is the strength of a bent portion of an FRP stirrup (*ksi*).

## 21. Add to Section 5.8.3.3 Nominal Shear Resistance

The neutral axis depth of cracked FRP-reinforced concrete sections is smaller than that for steel-reinforced concrete elements due to the lower stiffness of FRP bars when compared to steel bars ([ACI 2000](#)). Thus, the contribution to shear strength by aggregate interlock, dowel action, and shear of compressed concrete are lower for FRP-reinforced concrete members than for steel-reinforced concrete members. This section should adopt the recommendations of the ACI 440.1R-03 design and construction guidelines for shear design of FRP-reinforced concrete members.

The ACI 440.1R-03 design and construction guide recommendations for the shear force taken by the concrete should be used:

$$V_{c,f} = \frac{\rho_f E_f}{90\beta_1 f_c} V_c \quad (108)$$

where the terms are as defined before and  $V_c$  is the nominal shear force provided by the concrete for steel-reinforced concrete members as given in the ACI 318 code ([2000](#)). The value of  $V_{c,f}$  should not be larger than  $V_c$ .

The required spacing and area of shear reinforcement when stirrups are used perpendicular to the member are:

$$\frac{A_{fv}}{s} = \frac{(V_u - \phi V_{c,f})}{\phi \cdot f_{fv} d} \quad (109)$$

where the terms have been defined before and,

$A_{fv}$  = Area of shear reinforcement ( $\text{inch}^2$ ),

$V_u$  = Factored shear force at section ( $\text{kips}$ ).

## 22. Add to Section 5.10.2.1 Standard Hooks

The recommendation of ACI 440.1R-03 design and construction guidelines for a minimum tail length of 12 bar diameters should be used in this section.

### **23. Add to Section 5.10.2.3 Minimum Bend Diameters**

The minimum ratio of radius of bend to bar diameter of three for FRP stirrups, as recommended by the ACI 440.1R-03 design and construction guidelines, should be considered in FRP-reinforced concrete elements.

### **24. Add to Section 5.10.7 Transverse Reinforcement for Flexural Members**

A maximum spacing for transverse reinforcement of  $d/2$  or 24 inches, as recommended by the ACI 440.1R-03 design and construction guidelines, should be considered in this section.

### **25. Add to Section 5.10.8 Shrinkage and Temperature Reinforcement**

The ACI 440.1R-03 design and construction guidelines recommended minimum reinforcement ratio for temperature and shrinkage  $\rho_{f,ts}$  should be used in this section (but need not be more than 0.00036):

$$\rho_{f,ts} = 0.0018 \frac{60,000}{f_{fu}} \frac{E_s}{E_f} \geq 0.0014 \quad (110)$$

### **26. Notice for Section 5.10.11 Provisions for Seismic Design**

Since GFRP reinforcement is non-ductile, provisions should be taken in the design of GFRP-reinforced concrete elements where ductility is required.

### **27. Add to Section 5.11.2.1.1 Tension Development Length**

This research recommends that the basic development length of GFRP-reinforced concrete elements be computed with the following equation, shown earlier as [Equation 11](#):

$$l_{bf} = \frac{d_b f_{u,ave}}{2700} \quad (111)$$

## **28. Add to Section 5.11.2.1.2 Modification Factors that Increase $l_d$**

The ACI 440.1R-03 design and construction guidelines recommend a modification factor of 1.3 for top bars to obtain the development length of an FRP bar ( $l_{df}$ ).

## **29. Add to Section 5.11.2.4.1 Basic Hook Development Length**

The recommended development length for a bent bar provided by the ACI 440.1R-03 design and construction guidelines should be used in this section. The development length for hooked bars is determined as follows:

$$l_{bhf} = 2000 \frac{d_b}{\sqrt{f'_c}} \cdot for \cdot f_{fu} \leq 75,000 \text{ psi}$$

$$l_{bhf} = \frac{f_{fu}}{37.5} \frac{d_b}{\sqrt{f'_c}} \cdot for \cdot 75,000 \text{ psi} < f_{fu} < 150,000 \text{ psi} \quad (112)$$

$$l_{bhf} = 4000 \frac{d_b}{\sqrt{f'_c}} \cdot for \cdot f_{fu} \geq 150,000 \text{ psi}$$

The development length computed with [Equation 28](#) should not be less than 12  $d_b$  or 9 inches.

## **30. Add to Section 5.11.5.3.1 Lap Splices in Tension**

There is limited research in this area. However, the ACI 440.1R-03 design and construction guidelines recommend using values of 1.3  $l_{df}$  for class A and 1.6  $l_{df}$  for class C splices (as defined by AASHTO). Since the value of 1.7  $l_d$  for class C splice recommended by AASHTO is more conservative, it is advisable to use that value to compute the development length of spliced FRP bars.

## **31. Add to Section 5.12 Durability**

This section should give special consideration to the durability of GFRP reinforcement. Refer to the new proposed section 5.4 Material Properties (recommended by this research to be added to the AASHTO LRFD specifications) for a brief

description of environmental effects on GFRP bars. A summary of the deleterious effects of several environments on fibers and matrices as described previously is repeated next:

- *Water*: Moisture absorption softens the polymers. There are not sufficient data for the rate of deterioration of carbon and glass fibers.
- *Weak acids*: Weak acids can attack glass fibers and polyester matrices.
- *Strong acids*: Strong acids can attack glass fibers, aramid fibers, and polyester and epoxy matrices.
- *Weak alkalis*: Weak alkalis can attack glass fibers and polyester matrices.
- *Strong alkalis*: Strong alkalis can attack glass fibers, aramid fibers, and polyester matrices.
- *High temperatures*: Carbon and glass fibers are resistant to high temperatures. Nevertheless, high temperatures adversely affect aramid fibers and polymeric matrices.
- *Ultraviolet radiation*: Carbon and glass fibers are resistant to ultraviolet radiation. However, ultraviolet radiation adversely affects aramid fibers and polymeric matrices.

### **32. Add to Section 5.12.3 Concrete Cover**

This section of the code specifies a minimum cover for exterior exposure of 2 inches. The recommended covers should consider the fact that a 1-inch cover for a concrete deck with compressive strength of approximately 5.88 ksi and a 0.75-inch diameter bar does not cause cracking due to thermal expansion. This implies that, according to this research, a cover of 1.33 bar diameters is adequate to avoid cracking due to thermal expansion for typical conditions encountered by bridge superstructures. The 2-inch cover should be adequate for elements reinforced with 0.75-inch and smaller diameter bars. The cover depth design of elements exposed to direct solar radiation reinforced with bar diameters larger than 0.75 inch should be supported by tests.



## **VII. CONCLUSIONS, RECOMMENDATIONS, AND FUTURE WORK**

### **CONCLUSIONS AND RECOMMENDATIONS**

A comprehensive research program has been performed on the characteristics of GFRP bars and GFRP-reinforced concrete specimens. The research has identified key issues that needed to be addressed. These issues are:

- the evaluation of the tensile strength degradation of GFRP bars with time after exposure to simulated concrete pore solutions,
- the evaluation of the deterioration of the direct shear strength of GFRP bars exposed to simulated concrete pore solutions,
- the estimation of the creep-induced deflections of GFRP-reinforced concrete elements,
- the evaluation of the maximum crack widths of GFRP-reinforced concrete elements,
- the evaluation of the deflections of GFRP-reinforced concrete elements due to cyclic loading,
- the study of the degradation of the bond strength between GFRP bars and concrete, and
- the evaluation of the cracking of GFRP-reinforced concrete elements due to thermal expansion.

The tensile strength of GFRP bars degrades with time while in contact with simulated concrete pore solution. The tensile strength degraded as much as 24 percent after 50 weeks of exposure for bars exposed to a high pH solution and high temperature environment. Overall, the mean tensile strength degraded 1 percent at 26 weeks and 7 percent at 50 weeks of exposure. In general, the modulus of elasticity of the GFRP bars

studied tends to increase with exposure time. The modulus of elasticity increased, on average, 1 percent at 26 weeks and 9 percent at 50 weeks.

The applicability of Fick's second law to model the diffusion of a solution into a GFRP bar was verified. A model was developed to predict the tensile strength degradation of GFRP bars, using the results of the tension tests and the diffusion coefficients obtained from moisture absorption tests. The strength degradation model predicts an upper bound residual strength for stressed GFRP bars. In [Section V](#), a comparison made between the predicted residual tensile strength at five years and the design tensile strength computed using the ACI 440 design guidelines strength reduction factors showed that the environmental reduction factors may be unconservative. Although the strength degradation model for GFRP bars from this research may not actually predict the degradation of other FRP bars (especially carbon or aramid FRP bars), the research conducted by Glaser et al. ([1983](#)) has verified that the tensile strength of GFRP bars continues to decrease with time, even beyond five years. It should also be noted that the bars evaluated by Glaser et al. may not represent more modern GFRP bars. Thus, the conclusion that the strength reduction factors given by the ACI 440 design guidelines may be unconservative could be realistic, especially for GFRP bars under stress (any practical GFRP-reinforced concrete member). A strength reduction factor for use in the design of GFRP-reinforced concrete members cannot be recommended based on these results due to the limited exposure times.

Results from this research indicate that the direct shear strength of GFRP bars could be reduced as much as 9 percent when exposed to simulated concrete pore solutions for a period of 68 weeks. Results also indicate that the shear stiffness could be reduced as much as 15 percent for some bars after 48 weeks of exposure to simulated concrete pore solutions. The direct shear strength is a material parameter that is necessary for the computation of the strength of construction joints such as joints in

precast elements, pavements joints, and joints between a bridge barrier and a bridge deck.

GFRP bars can creep between 2 and 6 percent over six months, when stressed at 23 percent of the ultimate strength of the bar. Although the stress evaluated in this research is higher than allowed in the ACI 440 design guidelines, this stress level was evaluated to be conservative. The method presented to compute the long-term deflections of FRP-reinforced concrete elements accounting for creep and shrinkage of the concrete and creep of the FRP bars is the only existing alternative to the current existing ACI 440 method to compute long-term deflections of FRP-reinforced concrete elements. The method provided by the ACI 440 design guidelines to compute long-term deflections of FRP-reinforced concrete elements has been shown to make non-conservative predictions. In the design example presented at the end of [Section V](#), it was shown that the method proposed in this research, for the computation of long-term deflections, can predict deflections two times higher at six months than those obtained with the current method recommended by the ACI 440 design guidelines under the conditions tested. The use of the method of analysis proposed in this research should be considered for implementation in the ACI 440 design guidelines and the AASHTO code.

Tests on GFRP-reinforced concrete slabs led to the development of an expression that better predicts the maximum crack width than Equation 8-9b given in the ACI 440 design guidelines. The ACI 440 maximum crack width limits should be a function of concrete cover. The equation developed in this project for the prediction of maximum crack width of FRP-reinforced concrete elements should be implemented into the ACI 440 design guidelines and the AASHTO LRFD specifications. It should be mentioned that the proposed equation was developed using only 0.625-inch and 0.75-inch diameter GFRP bars. The equation will need verification with FRP bars reinforced with aramid or carbon fibers.

Cyclic loading tests on GFRP-reinforced concrete beams show that deflections can be increased between 78 and 680 percent when the beams are loaded for 2 million cycles and the GFRP bar stress range is 18.9 ksi. This research made evident the importance of deflections of GFRP-reinforced concrete elements induced by cyclic loading. Thus, deflections due to cyclic loading should be considered in the design of GFRP-reinforced concrete flexural elements. The surface finish of the bar and concrete cover did not seem to make a difference in the deflections recorded, although further work is needed to validate this. This research also found that the residual flexural strength of GFRP-reinforced concrete beams is basically not affected by cyclic loading at GFRP bars stresses of approximately 21 percent of the average GFRP bar strength for up to 5 million cycles of loading.

Bond tests on GFRP bars embedded in concrete exposed to a moist, elevated temperature environment showed reduced bond strength values after 16 months of exposure. Although all tests exceeded ACI 440 bond requirements, some results were very close to the limits. As a result of this investigation, it was found that Equation 11-7 of the ACI 440 design guidelines may be unconservative. Thus, a conservative modification is proposed to Equation 11-7 of the ACI 440 design guidelines for the computation of the basic development length. The proposed modification consists of replacing the design tensile strength ( $f_{tu}$ ) in the numerator of ACI 440 Equation 11-7 by the average tensile strength ( $f_{u,ave}$ ).

Tests on GFRP-reinforced concrete slabs subjected to heat indicate that a typical 8-inch thick concrete deck reinforced with 0.75 inch diameter bars and a concrete compressive strength of 5880 psi and concrete covers of 1, 2, and 3 inches could stand a temperature increase of 54 °F without cracking. Thus, concrete covers of 1.33 bar diameters are not expected to result in cracking due to differential thermal expansion between GFRP bars and concrete for typical bridge decks under normal conditions.

Similar results may be obtained from carbon FRP bars, but aramid FRP bars are expected to induce larger thermal expansion stresses in the concrete than GFRP bars.

## FUTURE WORK

An investigation that exposes GFRP bars over longer periods of time, preferably under different stress levels, is required in order to make reliable, long-term residual tensile strength predictions and to obtain adequate environmental strength reduction factors.

Additional long-term creep tests on FRP bars reinforced with glass, aramid, and carbon fibers with different bar diameters and under different stress levels are necessary.

An investigation of the influence of an applied stress range on the cyclic loading induced deflections of FRP-reinforced concrete members could help develop a general expression for the computation of cyclic loading induced deflections in those structures.

The degradation of the bond strength between concrete and GFRP bars needs to be investigated further. Experimental research is required in this area, especially long-term bond strength tests in order to determine whether the bond strength of GFRP bars degrades faster than their tensile strength.

As with most research, a more comprehensive test program is needed to statistically validate results from this research program.



## REFERENCES

- AASHTO, *Standard Specifications for Highway Bridges*, 15<sup>th</sup> Edition, American Association of State Highway and Transportation Officials, Washington, D.C., 1992, 923 pp.
- AASHTO, *LRFD Bridge Design Specifications*, Customary U.S. Units, Second Edition, American Association of State Highway and Transportation Officials, Washington, D.C., 1998, 987 pp.
- ACI Committee 318, “Building Code Requirements for Structural Concrete (ACI 318-95) and Commentary (318R-95),” American Concrete Institute, Farmington Hills, Michigan, 1996, 369 pp.
- ACI 440-K-Draft 5, “Recommended Test Methods for FRP Rods and Sheets,” Personal Collection, 2000(a).
- ACI Committee 318, “Building Code Requirements for Structural Concrete (ACI 318-99) and Commentary (318R-99),” American Concrete Institute, Farmington Hills, Michigan, April 2000 (b), 391 pp.
- ACI Committee 440, “Guide for the Design and Construction of Concrete Reinforced with FRP Bars,” American Concrete Institute, Farmington Hills, Michigan, May 2001, 41 pp.
- ACPA, “Pavement Technology Fundamentals: Load Transfer,” Pavement Technology, American Concrete Pavement Association,  
<http://www.pavement.com/PavTech/Tech/Fundamentals/fundloadtran.html>, Accessed on May 10, 2003.
- Adams, P. B., “Glass Corrosion: A Record of the Past? A Predictor of the Future?,” *Journal of Non-Crystalline Solids*, V. 67, Nos. 1–3, 1984, pp. 193–205.
- Agarwal, B. D., and Broutman, L. J., *Analysis and Performance of Fiber Composites*, Second Edition, John Wiley and Sons, New York, 1990, 449 pp.

## REFERENCES (cont.)

- Aiello, M. A., "Concrete Cover Failure in FRP-reinforced Concrete Beams under Thermal Loading," *Journal of Composites for Construction*, ASCE, V. 3, No. 1, February 1999, pp. 46–52.
- Al-Dulaijan, S., Nanni, A., Al-Zaharani, M., Bakis, C., and Boothby, T., "Bond Evaluation of Environmentally Conditioned GFRP/Concrete Systems," *Proceedings, 2<sup>nd</sup> Conference on Advanced Composite Materials in Bridge Structures*, M. El-Badry, Ed., Canadian Society for Civil Engineering, Montréal, Canada, 1996, pp. 845–852.
- Alfrey, T., "Glassy Polymer Diffusion Is Often Tractable," *Chemical and Engineering News*, V. 43, No. 41, October 11, 1965, pp. 64–70.
- ASTM C 39-96, "Standard Test Method for Compressive Strength of Cylindrical Concrete Specimens," *Annual Book of ASTM Standards*, Section 4 Construction, V. 04.02, Philadelphia, Pennsylvania, 1998, pp. 17–21.
- ASTM C 78-75, "Standard Test Method for Flexural Strength of Concrete (Using Simple Beam with Third-Point Loading)," *Annual Book of ASTM Standards*, Part 14, Philadelphia, Pennsylvania, 1975, pp 38–40.
- ASTM C 496-96, "Standard Test Method for Splitting Tensile Strength of Cylindrical Concrete Specimens," *Annual Book of ASTM Standards*, Section 4 Construction, V. 04.02, Philadelphia, Pennsylvania, 1998, pp. 265–268.
- ASTM E 122-72, "Standard Recommended Practice for Choice of Sample Size to Estimate the Average Quality of a Lot or Process," *Annual Book of ASTM Standards*, Part 41, Philadelphia, Pennsylvania. 1975, pp. 89–94.
- Bakht, B., Al-Bazi, G., Banthia, N., Cheung, M., Erki, M. Faoro, M., Machida, A., Mufti, A. A., Neale, K. W., and Tadros, G., "Canadian Bridge Design Code Provisions for Fiber-Reinforced Structures," *Journal of Composites for Construction*, ASCE, February 2000, pp. 3–15.

## REFERENCES (cont.)

- Beeby, A. W., "Corrosion of Reinforcing Steel in Concrete and Its Relation to Cracking," *The Structural Engineer*, V. 56, No. 3, March 1978, pp. 77–81.
- Beer, F. P., and Johnston, E. R., *Mechanics of Materials*, McGraw Hill, New York, 1981, 616 pp.
- Benmokrane, B., Masmoudi, R., Chekired, M., Rahman, H., Debbache, Z., and Tadros, G., "Design, Construction, and Monitoring of Fiber Reinforced Polymer Reinforced Concrete Bridge Deck," *ACI Fourth International Symposium Fiber Reinforced Polymer Reinforcement for Reinforced Concrete Structures*, American Concrete Institute, Farmington Hills, Michigan, 1999, pp. 87–101.
- Branson, D. E., *Deformation of Concrete Structures*, McGraw Hill, New York, 1977, 546 pp.
- Bresler, B., and Selna, L., "Analysis of Time-Dependent Behavior of Reinforced Concrete Structures," *Symposium on Creep of Concrete*, American Concrete Institute, SP-9, Detroit, Michigan, 1964, pp. 115–128.
- Brown, V. L., "Sustained Load Deflections in GFRP-Reinforced Concrete Beams," *Proceedings of the Third International Symposium on Non-Metallic (FRP) Reinforcement for Concrete Structures* (FRPRCS-3), Japan Concrete Institute, Sapporo, Japan, V. 2, 1997, pp. 495–502.
- Carter, H. G., and Kibler, K., "Langmuir-Type Model for Anomalous Moisture Diffusion in Composite Resins," *Journal of Composite Materials*, V. 12, April 1978, pp. 118–131.
- Castro, P., and Carino, N., "Tensile Strength and Nondestructive Testing of FRP Bars," *Journal of Composites for Construction*, ASCE, V. 2, No. 1, February 1998, pp. 17–27.
- Courtney, T. H., *Mechanical Behavior of Materials*, McGraw Hill, Boston, 2000, 733 pp.

## REFERENCES (cont.)

- Deitz, D., "GFRP-reinforced Concrete Bridge Decks," Ph.D. Dissertation, University of Kentucky, Lexington, Kentucky, 1998.
- Dejke, V., "Durability of FRP Reinforcement in Concrete – Literature Review and Experiments," Ph.D. Dissertation, Department of Building Materials, Chalmers University of Technology, Göteborg, Sweden, 2001.
- Epoxy Vinyl Ester Resin, Derakane Momentum 640-900, Dow Chemical Company, <http://www.dow.com/derakane/prod/dm-640-900.htm>, Accessed on May 10, 2003.
- Faza, S. S., and GangaRao, H. V. S., "Theoretical and Experimental Correlation of Behavior of Concrete Beams Reinforced with Fiber Reinforced Plastic Rebars," *Fiber-Reinforced-Plastic Reinforcement for Concrete Structures, ACI Publication SP-138A*, A. Nanni and C. W. Dolan, Eds., American Concrete Institute, Farmington Hills, Michigan, 1993, pp. 599–614.
- Gentry, T. R., and Husain, M., "Thermal Compatibility of Concrete and Composite Reinforcement," *Journal of Composites for Construction*, ASCE, V. 3, No. 2, May 1999, pp. 82–86.
- Gere, J. M., and Timoshenko, S. P., *Mechanics of Materials*, Third Edition, PWS Publishing Company, Boston, 1990, 807 pp.
- Gergely, P., and Lutz, L. A., "Maximum Crack Width in Reinforced Concrete Flexural Members, Causes, Mechanism and Control of Cracking in Concrete," *ACI Publication SP-20*, American Concrete Institute, Detroit, Michigan, 1973, pp. 87–117.
- Gilbert, R. I., and Mickleborough, N. C., *Design of Prestressed Concrete*, Unwin Hyman, London, 1990, 504 pp.
- Girifalco, L. A., *Atomic Migration in Crystals*, Blaisdell Publishing Company, New York, 1964, 162 pp.

## REFERENCES (cont.)

- Gisiner, L., and Bradberry, T., Personal Communications, Bridge Design Department, Texas Department of Transportation, Austin, Texas, January 14, 2003.
- Glaser, R. E., Moore, R. L., and Chiao, T. T., "Life Estimation of an S-Glass/Epoxy Composite Under Sustained Tensile Loading," *Composites Technology Review*, V. 5 No. 1, ASTM, Spring 1983, pp.21–26.
- Gurtin, M. E., and Yatomi, C., "On a Model for Two Phase Diffusion in Composite Materials," *Journal of Composite Materials*, V. 13, April 1979, pp. 126–130.
- Holloway, L., *Glass Reinforced Plastics in Construction: Engineering Aspects*, John Wiley and Sons, New York, 1978, 228 pp.
- Holmes, H., and Just, D. J., *GRP in Structural Engineering*, Applied Science Publishers, London, Great Britain, 1983, 298 pp.
- Hughes Brothers, "GFRP Rebar Project Listing,"  
<http://www.hughesbros.com/RebMainchhtml>, Accessed on May 10, 2002.
- Iwamoto, K., Uchita, Y., Takagi, N., and Kojima, T., "Flexural Fatigue Behavior of Prestressed Concrete Beams Using Aramid-Fiber Tendons," *Proceedings, ACI International Symposium, Fiber-Reinforced-Plastic Reinforcement for Reinforced Concrete Structures*, American Concrete Institute, Detroit, Michigan, 1993, pp. 509–523.
- Japan Society of Civil Engineers, "Recommendation for Design and Construction of Concrete Structures Using Continuous Fiber Reinforcing Materials," Concrete Engineering Series 23, A. Machida, Ed., Research Committee on Continuous Fibre Reinforcing Materials, Japan Society of Civil Engineers, Tokyo, Japan, 1997.
- Johnson, R., and Bhattacharayya, G., *Statistics Principles and Methods*, John Wiley and Sons, New York, 1985, 524 pp.
- Johnston, A. F., *Engineering Design Properties of GFRP*, The British Plastics Federation, London, Great Britain, 1979, 181 pp.

## REFERENCES (cont.)

- Jones, F. R. "Design Composites for Durability in Aqueous and Corrosive Environments," Design Cost Effective Composites, W. Banks, Ed., University of Sheffield, United Kingdom, 1998, pp.65-81.
- Jost, W., *Diffusion in Solids, Liquids, Gases*, Academic Press Inc., New York, 1952, pp. 558.
- Kaddour, A. S., Al-Salehi, F. A. R., Al-Hassani, S. T. S., and Hinton, M. J., "Simultaneous Determination of In-Plane Shear and Transverse Moduli of Unidirectional Composite Laminae at Different Strain Rates and Temperatures," *Composites Science and Technology*, V. 53, No. 4, 1995, pp. 431–444.
- Kage, T., Masuda, Y., Tanano, Y., and Sato, K., "Long-term Deflection of Continuous Fiber Reinforced Concrete Beams," *Non-Metallic (FRP) Reinforcement for Concrete Structures, Proceedings of the Second International RILEM Symposium (FRPRCS-2)*, L. Taerwe, Ed., E and FN Spon, London, Great Britain, 1995, pp. 251–258.
- Katsuki, F., and Uomoto, T., "Prediction of Deterioration of FRP Rods due to Alkali Attack," *Non-Metallic (FRP) Reinforcement for Concrete Structures, Proceedings of the Second International RILEM Symposium (FRPRCS-2)*, L. Taerwe, Ed., E and FN Spon, London, Great Britain, 1995, pp. 82–89.
- Lin, T. Y., and Burns, N. H., *Design of Prestressed Concrete Structures*, Third Edition, John Wiley and Sons, New York, 1981.
- Long, F. A., and Richman, D., "Measurement of Concentration Gradients for Diffusion of Vapors in Polymers," *Journal of the American Chemical Society*, V. 82, No. 3, February 15, 1960, pp. 509–519.
- Lubin, G., *Handbook of Fiberglass and Advanced Plastics Composites*, Polymer Technology Series of the Society of Plastic Engineers, Van Nostrand Reinhold Company, New York, 1969, 894 pp.

## REFERENCES (cont.)

- MacGregor, J. G., *Reinforced Concrete Mechanics and Design*, Second Edition, Prentice Hall, Englewood Cliffs, New Jersey, 1992, 848 pp.
- Mashima, M., and Iwamoto, K., "Bond Characteristics of FRP Rod and Concrete after Freezing and Thawing Deterioration," *Proceedings, ACI International Symposium, Fiber-Reinforced-Plastic Reinforcement for Reinforced Concrete Structures, American Concrete Institute*, Detroit, Michigan, 1993, pp. 51–69.
- Masmoudi, R., Benmokrane, B., and Chaallal, O., "Cracking Behavior of Concrete Beams Reinforced with FRP Rebars," *Proceedings of the First International Conference on Composite in Infrastructure, ICCI '96*, Tucson, Arizona, 1998, pp. 374–388.
- Michaluk, C. R., Rizcalla, S. H., Tadros, G., and Benmokrane, B., "Flexural Behavior of One-Way Concrete Slabs Reinforced by Fiber Reinforced Plastic Reinforcements," *ACI Structural Journal*, V. 95, No. 3, May-June 1998, pp. 353–365.
- Mindess, S., and Young, J. F., *Concrete*, Prentice Hall, Englewood Cliffs, New Jersey, 1981, 671 pp.
- Naaman, A., and Jeong, S., "Structural Ductility of Concrete Beams Prestressed with FRP Tendons," *Non-Metallic (FRP) Reinforcement for Concrete Structures, Proceedings of the Second International RILEM Symposium (FRPRCS-2)*, L. Taerwe, Ed., E and FN Spon, London, Great Britain, 1995, pp. 379–386.
- Nádai, A., *Plasticity: A Mechanics of the Plastic State of Matter*, McGraw Hill, New York, 1931, 349 pp.
- Nawy, E. G., and Neuwerth, G. E., "Behavior of Fiber Glass Reinforced Concrete Beams," *Journal of the Structural Division, ASCE*, V. 97, No. ST9, September 1971, pp. 22032215.
- Neogi, P., Ed., *Diffusion in Polymers*, Marcel Decker, New York, 1996, pp. 173–209.

Neville, A. M., and Meyers, A. L., "Creep of Concrete: Influencing Factors and Prediction," *Symposium on Creep of Concrete*, American Concrete Institute, SP-9, Detroit, Michigan, 1964, pp. 1–31.

NWSFO, "Temperature Records for the Month of July of 2000," National Weather Service Forecast Office, Forth Worth, Texas,  
<http://www.srh.noaa.gov/fwd/CLIMO/dfw/normals/dfw07nrm.html>, Accessed on May 10, 2003.

Nystrom, L., "Engineer's Predictions Dismal for Nation's Highways and Bridges,"  
<http://www.research.vt.edu/resmag/sc2001/weyers.html>, Accessed on January 20, 2003.

Park, R., and Paulay, T., *Reinforced Concrete Structures*, John Wiley and Sons, New York, 1975, 769 pp.

Paul, A., *Chemistry of Glasses*, Chapman and Hall, London, Great Britain, 1982, 293 pp.

PCI, *PCI Design Handbook, Precast and Prestressed Concrete*, Precast/Prestressed Concrete Institute, Chicago, Illinois, 1999.

Pyé, W. A. "Field Performance of Epoxy-Coated Reinforcing Steel in Virginia Bridge Decks," Ph.D. Dissertation, Virginia Polytechnic Institute and State University, Blacksburg, Virginia, September 1998.

Rahman, A. H., Kingsley, C. Y., and Taylor, D. A., "Thermal Stresses in FRP-Reinforced Concrete," *Annual Conference of the Canadian Society for Civil Engineering*, Ottawa, Ontario, Canada, June 1–3, 1995, pp. 605–614.

Rossier, J., "Photoablated Polymer Microsystems for Electro- and Biochemical Analyses," Chapter II, Ph.D. Dissertation, Ecole Polytechnique Fédérale de Lausane, Laboratoire d'Electrochimie Physique et Analytique, Switzerland,  
[http://dcwww.epfl.ch/le/Theses\\_PDF/These\\_Rossier/Chapter\\_II.pdf](http://dcwww.epfl.ch/le/Theses_PDF/These_Rossier/Chapter_II.pdf), Accessed on May 10, 2003.

## REFERENCES (cont.)

- Schaefer, B., "Thermal and Environmental Effects on Fiber Reinforced Polymer Reinforcing Bars and Reinforced Concrete," M.S. Thesis, Texas A&M University, May 2002.
- Schmuck, F., and de Tourreil, C., "Brittle Fractures of Composite Insulators: An Investigation of Their Occurrence and Failure Mechanism and a Risk Assessment," <http://www.corocam.com/papers/Paper%206501.pdf>, Accessed on May 10, 2003.
- Sen, R., Mullins, G., and Salem, T., "Durability of E-Glass Vinylester Reinforcement in Alkaline Solution," *ACI Structural Journal*, V. 99, No. 3, May-June 2002, pp. 369–375.
- Shackelford, J. F., *Introduction to Materials Science for Engineers*, Fourth Edition, Prentice Hall, Englewood Cliffs, New Jersey, 1996, 670 pp.
- Soles, C. L., Chang, F. T., Gidley, D. W., and Yee, A. F., "Contribution of the Nanovoid Structure to the Kinetics of Moisture Transport in Epoxy Resins," *Journal of Polymer Science: Part B: Polymer Physics*, V. 38, No. 5, March 2000, pp 776–791.
- Taly, N., *Design of Modern Highway Bridges*, McGraw Hill, New York, 1998, 1352 pp.
- Tannous F. E., and Saadatmanesh, H., "Durability of AR Glass Fiber Reinforced Plastic Bars," *Journal of Composites for Construction*, February 1999, pp. 12–19.
- Trejo, D., Aguiñiga, F., Buth, E. C., Yuan, R., James, R. W., Keating, P. B., "FRP Reinforcing Bars in Bridge Decks: State of the Art Review," Texas Transportation Institute, Research Report 1520-2, November 2000, 143 pp.
- Ueda, T., Sato, Y., Kakuta, Y., Imamura, A., and Kanematsu, H., "Failure Criteria for FRP Rods Subjected to a Combination of Tensile and Shear Loads," *Non-Metallic (FRP) Reinforcement for Concrete Structures, Proceedings of the Second International RILEM Symposium (FRPRCS-2)*, L. Taerwe, Ed., E and FN Spon, London, Great Britain, 1995, pp. 26–33.

## **REFERENCES (cont.)**

- Vijay, P. V., and GangaRao, H. V. S., "Creep Behavior of Concrete Beams Reinforced with GFRP Bars," *International Conference (CDCC '98)*, Sherbrooke, Quebec, Canada, August 5-7, 1998, pp. 661–667.
- Watstein, D., and Bresler, B., *Bond and Cracking in Reinforced Concrete, Reinforced Concrete Engineering*, V. 1, John Wiley and Sons, New York, 1974, 529 pp.
- Weyers, R. E., Wyoleta P., Sprinkel, M. M., and Kirkpatrick, T. J., "Bridge Deck Cover Depth Specifications – Ensuring Adequate Cover for Reinforcement Corrosion," *Concrete International*, V. 25, No. 2, February 2003, pp. 61–64.
- Yamasaki, Y., Masuda, Y., Tanano, H., and Shimizu, A., "Fundamental Properties of Continuous Fiber Bars," *Proceedings, ACI International Symposium, Fiber-Reinforced-Plastic Reinforcement for Reinforced Concrete Structures*, American Concrete Institute, Detroit, Michigan, 1993, pp. 715–730.
- Yunovich, M., and Thompson, N. G., "Corrosion of Highway Bridges: Economic Impact and Control Methodologies," *Concrete International*, Farmington Hills, Michigan, January 2003, pp. 52–57.

## APPENDIX A: ABSORPTION DATA

**Table A1. Moisture Absorption of Uncapped End Specimens.**

pH	Na Cl content (%)	Bar diameter (in.)	Specimen	Exposure time (weeks)					
				22	42	42	48	68	68
				Bar P	Bar V1	Bar V2	Bar P	Bar V1	Bar V2
7.4	0	0.500	1	-	-	-	1.0031	1.0133	1.0137
			2	-	-	-	1.0028	1.0130	1.0104
			3	-	-	-	1.0036	1.0120	1.0095
		0.625	1	-	-	-	1.0032	1.0093	1.0052
			2	-	-	-	1.0050	1.0083	1.0056
			3	-	-	-	1.0043	1.0086	1.0048
		0.750	1	-	-	-	1.0072	1.0063	1.0020
			2	-	-	-	1.0049	1.0053	1.0023
			3	-	-	-	1.0060	1.0059	1.0022
7.3	3.5	0.500	1	1.0022	1.0075	1.0063	1.0022	1.0086	1.0062
			2	1.0036	1.0076	1.0038	1.0029	1.0096	1.0055
			3	1.0027	1.0081	1.0064	1.0026	1.0095	1.0085
		0.625	1	1.0018	1.0044	1.0017	1.0021	1.0050	1.0028
			2	1.0021	1.0039	1.0028	1.0021	1.0042	1.0029
			3	1.0025	1.0036	1.0023	1.0021	1.0042	1.0029
		0.750	1	1.0056	1.0019	1.0015	1.0052	1.0026	1.0021
			2	1.0059	1.0023	1.0016	1.0062	1.0028	1.0019
			3	1.0047	1.0018	1.0016	1.0052	1.0029	1.0018
9.1	0	0.500	1	1.0033	1.0084	1.0074	1.0028	1.0113	1.0083
			2	1.0024	1.0075	1.0049	1.0026	1.0104	1.0070
			3	1.0032	1.0084	1.0095	1.0027	1.0135	1.0100
		0.625	1	1.0026	1.0041	1.0036	1.0028	1.0063	1.0045
			2	1.0023	1.0041	1.0048	1.0024	1.0066	1.0054
			3	1.0055	1.0060	1.0036	1.0056	1.0076	1.0048
		0.750	1	1.0044	1.0017	1.0019	1.0047	1.0033	1.0026
			2	1.0044	1.0020	1.0017	1.0046	1.0033	1.0024
			3	1.0047	1.0026	1.0020	1.0049	1.0058	1.0027
9.0	3.5	0.500	1	-	-	-	1.0031	1.0093	1.0076
			2	-	-	-	1.0024	1.0084	1.0080
			3	-	-	-	1.0022	1.0087	1.0093
		0.625	1	-	-	-	1.0028	1.0052	1.0046
			2	-	-	-	1.0023	1.0050	1.0048
			3	-	-	-	1.0026	1.0043	1.0040
		0.750	1	-	-	-	1.0043	1.0030	1.0024
			2	-	-	-	1.0048	1.0024	1.0022
			3	-	-	-	1.0053	1.0032	1.0023

**Table A2. Moisture Absorption of Capped End Specimens in Distilled Water.**

Bar type	Bar diameter (in.)	Specimen	Exposure time (weeks)					
			0.7	2.4	15.9	79.0	88.7	97.0
P	0.500	1	1.0011	1.0017	1.0022	1.0072	1.0072	1.0075
		2	1.0011	1.0016	1.0024	1.0071	1.0069	1.0071
		3	1.0011	1.0014	1.0024	1.0073	1.0073	1.0070
		4	1.0011	1.0013	1.0021	1.0069	1.0072	1.0069
		5	1.0011	1.0013	1.0021	1.0070	1.0070	1.0070
	0.625	1	1.0008	1.0011	1.0020	1.0067	1.0067	1.0069
		2	1.0008	1.0010	1.0018	1.0065	1.0065	1.0067
		3	1.0006	1.0010	1.0016	1.0065	1.0065	1.0067
		4	1.0008	1.0013	1.0018	1.0068	1.0068	1.0068
		5	1.0010	1.0013	1.0020	1.0067	1.0067	1.0069
	0.750	1	1.0023	1.0036	1.0069	1.0118	1.0116	1.0118
		2	1.0013	1.0021	1.0041	1.0087	1.0085	1.0090
		3	1.0017	1.0029	1.0049	1.0103	1.0106	1.0102
		4	1.0012	1.0020	1.0034	1.0084	1.0089	1.0080
		5	1.0022	1.0039	1.0063	1.0118	1.0119	1.0118
V1	0.500	1	1.0026	1.0042	1.0079	1.0147	1.0147	1.0147
		2	1.0027	1.0040	1.0072	1.0143	1.0146	1.0146
		3	1.0029	1.0045	1.0073	1.0139	1.0141	1.0141
		4	1.0024	1.0043	1.0069	1.0131	1.0131	1.0131
		5	1.0018	1.0032	1.0066	1.0129	1.0132	1.0132
	0.625	1	1.0013	1.0027	1.0050	1.0115	1.0115	1.0115
		2	1.0014	1.0029	1.0055	1.0116	1.0116	1.0116
		3	1.0017	1.0029	1.0056	1.0118	1.0118	1.0118
		4	1.0017	1.0028	1.0050	1.0113	1.0113	1.0113
		5	1.0020	1.0031	1.0055	1.0115	1.0115	1.0115
	0.750	1	1.0010	1.0018	1.0027	1.0071	1.0071	1.0071
		2	1.0013	1.0015	1.0025	1.0070	1.0072	1.0074
		3	1.0015	1.0020	1.0031	1.0079	1.0079	1.0083
		4	1.0010	1.0016	1.0027	1.0074	1.0075	1.0075
		5	1.0008	1.0016	1.0025	1.0069	1.0072	1.0072
V2	0.500	1	1.0030	1.0047	1.0087	1.0147	1.0150	1.0150
		2	1.0030	1.0045	1.0080	1.0140	1.0138	1.0135
		3	1.0025	1.0045	1.0068	1.0121	1.0126	1.0126
		4	1.0025	1.0040	1.0075	1.0133	1.0138	1.0138
		5	1.0027	1.0042	1.0082	1.0140	1.0145	1.0142
	0.625	1	1.0017	1.0025	1.0040	1.0089	1.0091	1.0089
		2	1.0015	1.0020	1.0037	1.0087	1.0092	1.0090
		3	1.0017	1.0025	1.0042	1.0091	1.0094	1.0089
		4	1.0020	1.0024	1.0043	1.0092	1.0092	1.0092
		5	1.0017	1.0025	1.0037	1.0084	1.0087	1.0085
	0.750	1	1.0006	1.0010	1.0015	1.0063	1.0063	1.0063
		2	1.0011	1.0011	1.0019	1.0064	1.0065	1.0067
		3	1.0010	1.0017	1.0027	1.0069	1.0069	1.0070
		4	1.0010	1.0013	1.0020	1.0065	1.0065	1.0065
		5	1.0010	1.0014	1.0012	1.0058	1.0060	1.0060

**Table A3. Moisture Absorption of Capped End Specimens in Alkaline Solution.**

Bar type	Bar diameter (in.)	Specimen	Exposure time (weeks)					
			0.7	2.4	15.9	79.0	88.7	97.0
P	0.500	1	1.0008	1.0011	1.0021	1.0067	1.0067	1.0054
		2	1.0008	1.0011	1.0022	1.0066	1.0068	1.0068
		3	1.0005	1.0011	1.0019	1.0059	1.0059	1.0059
		4	1.0005	1.0014	1.0022	1.0068	1.0068	1.0068
		5	1.0008	1.0013	1.0022	1.0067	1.0067	1.0067
	0.625	1	1.0008	1.0011	1.0016	0.0000	0.0000	0.0000
		2	1.0008	1.0013	1.0018	1.0066	1.0066	1.0067
		3	1.0007	1.0010	1.0016	1.0063	1.0067	1.0067
		4	1.0007	1.0010	1.0018	1.0065	1.0065	1.0067
	0.750	1	1.0007	1.0015	1.0034	1.0068	1.0076	1.0076
		2	1.0007	1.0010	1.0025	1.0069	1.0075	1.0075
		3	1.0012	1.0021	1.0042	1.0090	1.0093	1.0095
		4	1.0019	1.0033	1.0057	1.0106	1.0108	1.0108
		5	1.0006	1.0009	1.0019	1.0078	1.0081	1.0085
V1	0.500	1	1.0024	1.0043	1.0075	1.0155	1.0155	1.0155
		2	1.0013	1.0026	1.0050	1.0118	1.0118	1.0115
		3	1.0008	1.0027	1.0056	1.0128	1.0128	1.0126
		4	1.0027	1.0045	1.0077	1.0146	1.0146	1.0146
		5	1.0018	1.0037	1.0066	1.0129	1.0129	1.0129
	0.625	1	1.0003	1.0016	1.0036	1.0091	1.0094	1.0093
		2	1.0003	1.0008	1.0024	1.0080	1.0085	1.0086
		3	1.0008	1.0021	1.0048	1.0106	1.0112	1.0109
		4	1.0005	1.0016	1.0032	0.0000	0.0000	0.0000
		5	1.0009	1.0020	1.0044	1.0107	1.0112	1.0112
	0.750	1	1.0002	1.0006	1.0013	1.0057	1.0057	1.0057
		2	1.0006	1.0014	1.0020	1.0066	1.0067	1.0066
		3	1.0007	1.0010	1.0021	1.0066	1.0069	1.0069
		4	1.0008	1.0011	1.0016	1.0063	1.0064	1.0065
		5	1.0007	1.0013	1.0020	1.0064	1.0064	1.0066
V2	0.500	1	1.0015	1.0017	1.0030	1.0102	1.0102	1.0102
		2	1.0017	1.0022	1.0037	1.0099	1.0099	1.0099
		3	1.0018	1.0018	1.0030	1.0093	1.0093	1.0093
		4	1.0015	1.0018	1.0033	1.0095	1.0095	1.0095
		5	1.0015	1.0022	1.0030	1.0092	1.0092	1.0092
	0.625	1	1.0009	1.0011	1.0017	1.0065	1.0065	1.0066
		2	1.0011	1.0017	1.0023	1.0069	1.0074	1.0074
		3	1.0011	1.0015	1.0019	1.0068	1.0069	1.0073
		4	1.0009	1.0015	1.0020	1.0071	1.0072	1.0075
		5	1.0009	1.0011	1.0018	0.0000	0.0000	0.0000
	0.750	1	1.0007	1.0009	1.0013	1.0063	1.0064	1.0066
		2	1.0007	1.0010	1.0014	1.0061	1.0062	1.0067
		3	1.0007	1.0009	1.0014	1.0060	1.0060	1.0061
		4	1.0007	1.0009	1.0015	1.0060	1.0061	1.0063
		5	1.0008	1.0009	1.0013	1.0060	1.0061	1.0062



## APPENDIX B: CREEP TEST DATA

**Table B1. Creep Test Data.**

Time (days)	Strain (microstrains = $1 \times 10^{-6}$ in./in.)						Time (days)	Strain (microstrains = $1 \times 10^{-6}$ in./in.)						
	Specimen							Specimen						
	V1-5-a	V1-5-b	P-5-a	P-5-b	V2-5-a	V2-5-b		V1-5-a	V1-5-b	P-5-a	P-5-b	V2-5-a	V2-5-b	
0.000	-5	-39	-15	-25	-19	-20	1.37	39	3579	3721	3848	3579	3521	
0.003	-5	-44	-15	-29	-20	-20	2.13	4077	3579	3672	3833	3569	3491	
0.007	-5	-39	-15	-29	-20	-20	5.2	4180	3613	3687	3857	9995	3501	
0.010	-5	269	-15	-29	-20	-20	10.2	4209	3638	3701	3872	9995	3521	
0.014	-10	3447	-15	-29	-24	-20	15.1	4214	3648	3696	3867	9995	3511	
0.017	-10	3491	-20	-29	-20	-20	20.1	4224	3662	3696	3862	9995	3511	
0.021	-10	3516	-15	-29	-20	-20	24.9	4233	3672	3696	3862	9995	3511	
0.024	-5	3496	-15	-29	-20	-20	29.8	4243	3682	3701	3867	9995	3511	
0.028	10	3496	-15	-29	-20	-20	34.8	4253	3691	3706	3872	9995	3516	
0.031	3901	3506	-15	-29	-20	-20	39.8	4253	3696	3706	3872	9995	3511	
0.035	3940	3501	-5	-29	-20	-20	44.8	4263	3701	3711	3872	9995	3521	
0.038	3945	3506	1538	-29	-20	-20	49.8	4268	3706	3716	3877	9995	3525	
0.042	3955	3511	3638	-29	-20	-20	60.8	4273	3716	3716	3872	9995	3521	
0.045	3960	3516	3633	-29	-20	-20	65.0	4273	3716	3711	3877	9995	3516	
0.049	3955	3511	3633	-24	-20	-15	67.5	4273	3716	3711	3872	9995	3516	
0.052	3955	3511	3638	-29	-20	-20	70.6	4282	3721	3721	3882	9995	3525	
0.056	3960	3511	3638	-29	-20	-15	75.6	4277	3721	3711	3872	9995	3516	
0.063	3960	3516	3643	-29	15	-15	80.3	4287	3735	3726	3887	9995	3530	
0.069	3965	3516	3647	-24	3550	-15	85.2	4292	3740	3726	3887	9995	3530	
0.076	3965	3516	3643	-29	3555	166	89.9	4287	3740	3726	3882	9995	3530	
0.083	3965	3516	3647	-24	3564	78	94.8	4297	3745	3735	3897	9995	3540	
0.090	3970	3521	3647	-29	3564	78	99.4	4302	3760	3740	3897	9995	3550	
0.097	3970	3516	3647	-24	3564	117	113.8	4287	3745	3721	3882	9995	3530	
0.10	3970	3521	3647	-24	3564	142	118.6	4292	3750	3731	3892	9995	3535	
0.11	3970	3521	3647	-24	3564	103	123.4	4292	3750	3735	3892	9995	3540	
0.12	3975	3521	3652	-24	3564	3086	133.6	4292	3755	3731	3887	9995	3535	
0.13	3975	3521	3647	-24	3564	3472	138.3	4292	3750	3731	3887	9995	3535	
0.13	3975	3521	3643	-24	3564	3472	143.1	4287	3750	3726	3887	9995	3530	
0.14	3975	3525	3647	298	3564	3481	148.9	4287	3750	3721	3882	9995	3530	
0.15	3975	3521	3652	3799	3564	3481	153.9	4287	3750	3721	3882	9995	3525	
0.15	3975	3521	3652	3794	3560	3472	158.6	4287	3750	3726	3882	9995	3525	
0.16	3975	3521	3648	3799	3565	3462	163.6	4287	3755	3721	3882	9995	3525	
0.29	1777	3584	3643	3794	3555	3452	168.6	4282	3755	3721	3882	9995	3525	
0.53	1773	3584	3652	3804	3560	3472	174.0	4287	3755	3726	3887	9995	3525	
0.54	1773	3579	3648	3799	3560	3467	179.0	4282	3750	3716	3882	9995	3521	
0.75	1768	3594	3652	3804	3555	3462	183.9	4282	3755	3726	3887	9995	3525	
0.95	1768	3604	3652	3804	3560	3467	188.9	4282	3755	3731	3892	9995	3530	
1.16	1768	3608	3667	3823	3579	3501	-	-	-	-	-	-	-	

